Microstructured glazing for daylighting, glare protection, seasonal thermal control and clear view

THÈSE N^O 6465 (2015)

PAR

André Gabriel KOSTRO

EPFL

ÉCOLE POLYTECHNIQUE
FÉDÉRALE DE LAUSANNE

Suisse
2015

If your mental attitude is positive,
even when threats abound, you won't lose your inner peace.
On the other hand, if your mind is negative, marked by fear,
suspicion and feelings of helplessness, even among your best friends,
in a pleasant atmosphere and comfortable surroundings, you won't be happy.
— Dalai Lama

To my lovely children...

Acknowledgements

Acknowledgements

vi

Abstract

The appropriate choice of the type of glazing and glazed area in a façade depends on many factors. They include amongst other criteria: location, orientation, climatic condition, energetic efficiency, usage of the building, required user comfort, and the architectural concept. All requirements can not be fulfilled at all times and priorities have to be set to find a compromise between occupant comfort, design objective, cost and energetic efficiency. On the south façade of high-rise buildings in particular, it is a challenge to have simultaneously large glazed area, no glare, no excessive cooling loads, a clear view and sufficient natural light flux. In Switzerland, electric lighting, heating and air conditioning account for about 74% of the total energy demand in private housing (dominated by heating : 70%) and 32% of the overall Swiss electricity usage (dominated by lighting :13%) [Prognos et al., 2013]. This energy consumption can be strongly influenced by using the most appropriate fenestration system [Grynning et al., 2014, Florides et al., 2002, Danny et al., 2008].

CFSPro stands for complex fenestration systems profile ray tracing optimisation and is the name of the software developed during this thesis to engineer new complex fenestration system (CFS). A mixed dimensionality approach was used to achieve a very fast and accurate ray tracing of any lamellar structure that has a two dimensional profile. The originality of the implemented Monte Carlo ray tracing algorithm is the separation of intersection and interaction. Intersections are computed using only the two dimensions of the profile, the complexity of the algorithm is thereby significantly decreased and the computational speed is increased. With these optimisations, the user interface can give an instantaneous idea of the light path and interactions in the modelled system. This visualisation and the proposed performance indicators such as the distribution of transmitted solar radiation and angular dependent transmittance can be used to design new CFSs. The software provides all the mentioned results in the user interface where the different designs can be compared, making the optimisation process of a profile with a defined objective very intuitive. The model also calculates an accurate bidirectional transmission distribution function (BTDF) that is used in combination with Radiance to obtain a rendering of the daylighting distribution in an office space. For the study of daylight performance, these Radiance simulations can be used to obtain indicators such a the daylight factor and daylight autonomy (DA). Finally, to estimate the thermal performances, a simple nodal thermal model was added to simulate the temperature evulotion and the thermal loads in a given office.

A glazing combining several functions and that can contribute to significantly reduce energy consumption in buildings with favourably oriented glass façades was developed using this

Abstract

novel ray tracing approach. It was designed to obtain a strongly angular dependent transmission and a specific angular distribution of transmitted light. The engineered geometry provides elevated daylight illuminance by redirecting the incoming light towards the depth of the room. This redirection simultaneously protects occupants from direct sunlight and reduces the risk of glare. For an optimised usage of available solar radiation, the transmission of direct sunlight is maximised in winter and minimised in summer. Thereby heating loads in winter and cooling loads in summer are reduced. Taking advantage of the changing elevation of the sun between seasons, such a seasonal variation can be created by a strongly angular dependent transmittance. This novel glazing will combine the functions of daylighting, glare protection, and seasonal thermal control.

A fabrication process was identified and samples of embedded micromirrors were produced to demonstrate the feasibility. The fabrication of such structures required several steps. The fabrication of a metallic mould with a relative high aspect ratio and mirror polished surfaces is followed by the production of an intermediate polydimethylsiloxane (PDMS) moulds that was subsequently used to replicate the structure with a ultraviolet (UV) curable polymer. Selected facets of these samples were then coated with a thin film of highly reflective material in a physical vapour deposition process. Finally, the structures were filled with the same polymer to integrated the mirrors.

The samples were characterised during the various fabrication steps using scanning electron microscopy (SEM), energy-dispersive X-ray (EDX) spectroscopy , confocal microscopy and profilometry. A miniature goniophotometer was built to assess the performance of the structured glazing. The final samples redirect up to 70% of the light flux and are very transparent when looking through at normal incidence

Keywords : *Complex fenestration system, Daylighting, Thermal control, Ray tracing, Microstructure, Thin film, Imprint lithography, Glare control, Smart glass*

Zusammenfassung

Die richtige Wahl einer Verglasung hängt von vielen Parametern ab. Unter anderem ist die Orientierung der Fassade wichtig, die geographische Lage, das Klima, die erwünschte energetische Effizienz, die Nutzung des Gebäudes und die Integration im architekturellen Konzept des Gebäudes. Alle Ziele können gleichzeitig nicht erfüllt werden, und Prioritäten müssen gesetzt werden, um ein Gleichgewicht zwischen Design, Komfort und Effizienz zu finden. Auf Südfassaden in Gebäuden mit einem hohem Verglasungsanteil zum Beispiel ist es schwierig, gleichzeitig das ausgieblig vorhandene natürliche Tageslicht zu nutzen ohne Blendeffekte zu verursachen. Anderseits ist es auch schwierig, die hohen natürlichen thermische Gewinne zu nutzen und gleichzeitig eine Sommerliche Überhitzung zu vermeiden. In der Schweiz machen Heizen, Klimatisieren und Beleuchten in privaten Haushältern etwa 74% des energetischen Bedarfs aus (hauptsächlich Heizung : 70%), und 32% des schweizerischen elektrischen Bedarfs (hauptsächlich Beleuchtung: 13%)[Prognos et al., 2013]. Dieser energetische Verbrauch kann durch die Anwendung sorgfältig ausgewählter Fenster stark gesenkt werden [Grynning et al., 2014, Florides et al., 2002, Danny et al., 2008].

CFSPro ist das Akronym für "complex fenestration system ray tracing profile optimisation" , der Name der Software, die im Rahmen dieser Dissertation entwickelt wurde. Das Programm wurde für das Design und die Studie innovativer Verglasung entwickelt. Um die Strahlverfolgung möglichst schnell durchzuführen, wurde ein multi-dimensionaler Algorithmus entwickelt. Dieser Algorithmus ermöglicht das Finden von Schnittpunkten in zwei Dimensionen. Da es sich um zweidimensionale Profile handelt, ist dieses Vorgehen geeignet und schneller als in drei Dimensionen. Die Reflexion oder Brechung des Lichtstrahls an den Schnittpunkten ist hingegen dreidimensional behandelt. Mit einer solchen Methode können die Strahlen direkt verfolgt und angezeigt werden und das optische Verhalten der untersuchten Geometrie leichter verstanden werden. Zusätzlich werden auch noch verschiedene Leistungskennzahlen gegeben um das winkelabhängige Verhalten des Systems abzuschätzen. Die winkelabhängige Transmissions Verteilung wird berechnet. Durch diese Simulation kann auch die sogenannte bidirectional transmission distribution function (BTDF) berechnet werden, um die winkelabhängige Lichtstrahlung des Systems zu beschreiben. Diese Beschreibung kann dann mittels anderer Software wie Radiance benutzt werden, um eine Tageslichtbewertung zu simulieren. Dies ergibt eine Bildsynthese und auch die quantitative information der Beleuchtungsstärke in einem Raum. So kann der Tageslichtfaktor ermittelt werden und mit jährlichen Berechnungen auch die Tageslichtautonomie (DA). Ein vereinfachtes thermisches Modell wurde einbezogen, um den Temperaturverlauf zu verfolgen. So kann die Wirkung der Verglasung auf

Abstract

das thermische Verhalten des Gebäudes abgeschätzt werden.

Ausgehend von dieser Software wurde im Rahmen dieser Dissertation ein neuer Typ von innovativer Verglasung entwickelt. Diese neue Verglasung hat eine starke winkelabhängige Transmission: Strahlung die unter einem höherem Winkel einfällt, wird stark reflektiert, für niedrige Winkel aber nicht. Weil sich die Höhe der Sonne über das Jahr stark ändert, kann somit eine Jahreszeit abhängige Dynamik entstehen. Im Winter wird die Sonnenstrahlung hereingelassen, im Sommer aber reflektiert. Zusätzlich, und für bessere Tageslichtnutzung, wird das Licht auch umgelenkt und in die Tiefe des Raumes geleitet. Gleichzeitig entsteht auch ein Blendschutz für das direkte Sonnenlicht.

Dieses neues System wurde nicht nur mittels Computer Simulation untersucht, sondern auch im Labor hergestellt. Für die Herstellung der vorgeschlagenen verkapselten Spiegel mussten verschiedene Methoden entwickelt und angewandt werden. Diverse Profile wurden mit verschiedenen Fabrikationsprozessen hergestellt, sie wurden dann mittels einer PDMS Form in einen aushärtbaren Kunststoff geprägt. Die Verhärtung dieses Kunststoffes erfolgt durch UV Bestrahlung. Die somit erhaltene Mikrostruktur wurde dann mit einer dünnen reflektiven Schicht beschichtet. Diese Beschichtung erfolgte durch Vakuum Verdampfung von Aluminium oder Silber. Um diese Spiegel zu verkapseln, wurde der selbe Kunststoff wie zuvor benutzt. Es wurde so demonstriert, dass die Miniaturisierung der Strukturen die Transparenz des Systems verbessert und dass Tageslichtlenkung durch verkapselte Spiegel möglich ist. Für das Blockieren von ausgewählten Winkeln werden streifenförmige Reflektoren benötigt, diese wurden durch Lithographie hergestellt.

Die Ergebnisse aller Etappen des Herstellungsprozesse wurden mit verschiedenen optischen Techniken charakterisiert. Rasterelektronenmikroskopie, optische Mikroskopie und konfokale Mikroskopie wurden benutzt, um die Oberflächen zu charakterisieren und das Profil der verschiedenen Strukturen zu ermitteln. Verschiedene Profilometriemessungen wurden auch durchgeführt. Weiterhin wurde auch ein Messgerät hergestellt, um das winkelabhängige Verhalten zu messen: die Transmissionsverteilung kann mit dem Miniaturgoniophotometer gemessen werden.

Slagworte: *Komplexe Verglasungssysteme, Tageslichtnutzung, Thermische Kontrolle, Sonnenschutz, Strahlverfolgung, Mikrostrukturen, Dünne Schichten, Replikation, Blendschutz, Intelligentes Glas*

Résumé

Le choix du type de vitrage et de la surface de vitrage sur une façade dépend de nombreux paramètres. Entres autres, la localisation du site, le climat de la région et l'orientation de la façade jouent un rôle important. L'efficacité énergétique désirée, le type de bâtiment, le niveau de confort visé et le concept architectural du bâtiment entre aussi en ligne de compte. Les objectifs de confort, d'efficacité, de coût de construction et de design ne peuvent pas toujours être atteints simultanément et des compromis doivent être fait. En particulier, sur une façade sud fortement vitrée, il est difficile d'avoir à la fois des niveaux d'éclairage naturels élevés et une vue vers l'extérieur sans avoir de problèmes d'éblouissement. Dans cette situation, d'un point de vue thermique, il est difficile de jouir des gains thermiques élevés requis en hiver sans avoir de problèmes de surchauffe en été. En Suisse, l'éclairage, le chauffage et la climatisation représentent 74% de la consommation énergétique dans le secteur résidentiel (principalement pour le chauffage, 70%). Ces besoin représentent 32% de la consommation électrique suisse (dominé par l'éclairage)[Prognos et al., 2013]. Cette consommation énergétique peut être diminuée par un choix judicieux des éléments de vitrage [Grynning et al., 2014, Florides et al., 2002, Danny et al., 2008].

CFSPro est l'acronyme pour "complex fenestration systems profile ray tracing optimisation", le logiciel développé dans le cadre de cette thèse pour l'étude et le design de systèmes de vitrages complexes. Un algorithme mêlant l'approche tri- et bi-dimensionnelle pour un tracé de rayon plus rapide a été développé. L'originalité du tracé de rayons Monte Carlo ainsi développé est de séparer les intersections des interactions. Les intersections sont calculées dans les deux dimensions du profil alors que les interactions sont calculées en utilisant des vecteurs tri-dimensionnels. Cette approche permet de réduire significativement la complexité du tracé de rayon et d'accélérer le calcul jusqu'à offrir une visualisation en direct des chemins pour de nombreux rayons. Cette visualisation, ainsi que les indicateurs de performance calculés de manière quasi instantanée, offrent une bonne base pour la compréhension du système étudié ainsi que pour son optimisation. Ces indicateurs de performance sont la distribution du rayonnement transmis et la transmittance en fonction de l'angle incident. Pour l'étude de l'impact sur la thermique du bâtiment, des indicateurs plus complets tels que les gains thermiques horaires et les charges thermiques résultantes sont calculées par un modèle thermique simplifié. Pour l'évaluation de l'éclairement dans l'espace, des rendus avec Radiance, le facteur lumière du jour et des métriques dynamiques tel que le DA sont aussi donnés. Ces derniers sont basés sur une BTDF calculée par tracé de rayons.

Un nouveau type de vitrage complexe a été développé dans le cadre de cette thèse grâce à cet

Abstract

outil. Ce système offre simultanément une forte dépendance de l'angle pour la transmittance et une forte redirection de la lumière. La dépendance angulaire de la transmittance permet d'obtenir une dynamique saisonnière des gains thermiques basé sur la hauteur changeante du soleil, en été le rayonnement est bloqué pour éviter la surchauffe alors qu'en hiver, le rayonnement est transmis pour réduire la charge de chauffage. La redirection, quand à elle, permet de guider la lumière plus en profondeur dans la pièce et d'élever le niveau d'éclairement dans les parties reculées de la pièce. La redirection évite aussi un éblouissement par le rayonnement direct.

Ce nouveau concept de vitrage avancé a été étudié par simulation et des échantillons ont étés produits en laboratoire afin de vérifier certaines hypothèses. Il a ainsi été démontré qu'en encapsulant des miroirs de taille micrométriques, il est possible de rediriger la lumière et de conserver une transparence à travers le système. Différentes formes ont été fabriquées dans un moule métallique puis répliquées dans une résine photo-polymérisée et transparente. Pour la réplication, un moule intermédiaire en PDMS est utilisé pour un bon démoulage et pour sa transparence. Certaines faces des structures ainsi obtenues ont ensuite été revêtues d'une couche mince réfléchissante d'aluminium ou d'argent. Cette couche a été déposée par évaporation sous vide. Les structures ainsi miroités ont finalement été noyées dans la même résine que celle utilisée pour la réplication afin d'obtenir des miroirs encapsulés. L'effet de blocage de certain angles d'incidence peut être obtenu en plaçant une bande de miroirs au point focal d'un miroir parabolique encapsulé. Ces miroirs striés on été fabriqués par lithographie "lift-off".

Les échantillons ont été caractérisés aux différents stades de la fabrication à l'aide de différentes techniques pour contrôler la fabrication et optimiser les processus. La microscopie electronique à balayage ainsi que la microscopie confocale et optique ont été utilisées pour observer les états de surfaces et obtenir le profil de ces structures. Différentes techniques de profilometrie ont aussi été utilisées. Finalement un goniophotomètre miniature a été développé pour mesurer la transmittance en fonction de l'angle ainsi que la distribution du rayonnement transmis. Les derniers echantillons produits redirigent une grand partie du flux lumineux (plus de 70%) et sont très transparents à incidence normale.

Mots-clés: *Système de vitrage complexe, Éclairage naturel, Contrôle thermique, Tracé de rayons, Microstructure, Couche mince, Réplication, Protection contre l'éblouissement, Vitrage intelligent*

Contents

Contents

Contents

Contents

List of Figures

List of Tables

Acronyms

Ag	silver
Al	aluminium
$a - S_i - H$	hydrogenated amorphous silicon
$a - S_i$	amorphous silicon
2D	two dimensional
3D	three dimensional
AFM	atomic force microscopy
ALSA	Advanced Linux Sound Architecture
BIOP	BioImaging and Optics Platform
BRDF	bidirectional reflection distribution function
BSDF	bidirectional scattering distribution function
BSP	binary space partitioning
BSSDF	bidirectional surface scattering distribution function
BTDF	bidirectional transmission distribution function
CaTd	cadmium teluride
CFS	complex fenestration system
CFSPro	Complex Fenestration System Ray tracing Profile Optimisation
CGI	CIE glare index
CIE	International Commission on illumination
CIGS	coper indium galium selenide
CIME	Interdisciplinary Centre for Electronic Microscopy
CMi	Center of MicroNanoTechnology
COP	coefficient of performance
CPC	compound parabolic concentrator
CPU	central processing unit
CVD	chemical vapour deposition
DA	daylight autonomy
DF	daylight factor
DGI	daylight glare index
DGP	daylight glare probability
DI	deionised
DIN	Deutsches Institut für Normung
DMA	dynamic mechanical analysis

dpi	dots per inch
EDM	electrical discharge machining
EDX	energy-dispersive X-ray
Empa	Swiss Federal Laboratory for Material Science and Technology
EPFL	Ecole Polytechnique Federale de Lausanne
EXIF	exchangeable image file format
Fiji	Fiji Is Just ImageJ
FWHM	full width at half maximum
GA	genetic algorithm
GUI	graphical user interface
HAZ	heat affected zone
HBP	hyperbranched polymers
HF	hydrofluoric acid
HVAC	heating, ventilation, and air conditioning
IEA	International Energy Agency
IES	Illuminating Engineering Society
IMT	Institute of Microstructure Technology
IR	Infrared
ISE	Institute for Solar Energy Systems
KIT	Karlsruhe Institute of Technology
KOH	potassium hydroxide
LBNL	Lawrence Berkeley National Laboratory
LED	light-emitting diode
LESO-PB	Solar Energy and Building Physics Laboratory
LPMC	Laboratory of Physics of Complex Matter
LPN	Laboratory of Physics of Nanostructures
LTC	Laboratory of Polymer and Composite Technology
NIL	nanoimprint lithography
NIR	Near infrared (IR-A, 0.75-1.4 μm)
NRC	National Research Council
PC	polycarbonate
PC	polycarbonate
PCT	Patent Cooperation Treaty
PDMS	polydimethylsiloxane
PLD	pulsed laser deposition
PLL	phase locked loop
PMMA	polymethyl methacrylate
POR	projected obstructed ratio
PR	photoresist
PV	photovoltaic
PVB	polyvinyl butyral
PVD	physical vapour deposition

rpm	rotations per minute
SEM	scanning electron microscopy
SHGC	solar heat gain coefficient
SWIR	Short-wavelength infrared (IR-B, 1.4-3 μm)
T(θ)	transmittance depending on incoming angle
TD	transmission distribution
TDF	transmission distribution function
TIC	Tribology and Interfacial Chemistry Group
TPO	trimethylbenzoyl phosphine oxide
UDI	useful daylight illuminance
UGR	unified glare rating
UNIL	Université de Lausanne
UV	ultraviolet
UVNIL	ultraviolet nanoimprint lithography
VCP	visual comfort probability
WWR	window to wall surface ratio
XML	extensible markup language

List of Symbols

α	Attenuation coefficient of light in an absorbing medium	$[\,cm^{-1}\,]$
β	Effective deposition angle	$[\,°\,]$
$°$	Angular measure	$[\,-\,]$
$°C$	Unit of temperature	$[\,C\,]$
$°K$	SI Unit of temperature	$[\,K\,]$
γ	Sample tilt angle	$[\,°\,]$
E_v	Illuminance	$[\,lux\,]$
E_e	Irradiance	$[\,W \cdot m^2\,]$
κ	Extinction coefficient of light in an absorbing medium	$[\,-\,]$
L_v	Luminance	$[\,cd \cdot m^{-2}\,]$
μm	Unit of length	$[\,\mu m\,]$
Ω	Unit of electrical resistance	$[\,\Omega\,]$
A	Optical absorptance	$[\,-\,]$
η	Optical admintance	$[\,-\,]$
R	Optical reflectance	$[\,-\,]$
T	Optical transmittance	$[\,-\,]$
L_e	Radiance	$[\,W \cdot sr^{-1} \cdot m^2\,]$
Ra	Unit of roughness	$[\,\mu m\,]$
J_{SC}	Short circuit current of a PV cell	$[\,A\,]$
m^2	Unit of surface	$[\,m^2\,]$
$\parallel$	Subscript for parallel polarisation	$[\,-\,]$
$\perp$	Subscript for perpendicular polarisation	$[\,-\,]$
T	Temperature	$[\,°K\,]$
θ_i	Angle to normal of a surface of an incident light ray	$[\,°\,]$
θ_o	Angle to normal of a surface of an outgoing (transmitted or reflected) light ray	$[\,°\,]$
θ_t	Angle to normal of a surface of a transmitted light ray	$[\,°\,]$
τ_e	Fraction of transmitted energy over the solar spectrum	$[\,-\,]$
τ_v	Fraction of transmitted energy over the visible spectrum	$[\,-\,]$
V	Unit of electrical potential	$[\,V\,]$
W	Unit of power	$[\,W\,]$
Wh	Unit of energy	$[\,Wh\,]$

1 Introduction

1.1 Context

Windows are a major element in buildings and can cover nearly 100 % of a building façade in modern constructions. Besides aesthetic motivations, large glazed areas create bright spaces; and sound levels of natural light in offices reduce general sickness [Begemann et al., 1997]. In particular, sufficient daylight exposure synchronises the circadian system with beneficial effect on sleep quality, mood, and cognitive performance [Gooley et al., 2001, Webb, 2006, Münch and Bromundt, 2012]. Hence glazing has become an elegant structural element that creates comfortable and healthy working or living spaces. But excessive sunlight or strong contrast luminance can also become a problem and cause glare to the occupant [Wienold, 2009]. Shading elements have been introduced to manage this inconvenience but they introduced an other problem: the blind control. If users instinctively close blinds to eliminate an inconvenience, the re-opening of blinds is not an automatism for most of them [James and Bahaj, 2005]. Regarding daylight, the usage of large glazed areas in buildings is hereby double edged. With large window to wall surface ratios (WWRs) thermal confort becomes of importance as well.

Being a major part of the building envelope and with the growing importance of energy management and low carbon emissions, glazed areas are subjected to important energetic constraints. Single glazed windows, that insulate from the exterior as much as an oiled paper window, have been the weak part of a building shell for centuries. Meanwhile, noble gas filled double glazing with low emissivity coatings have become the standard for a low heat transfer coefficient (U value), good insulation and reduced energy losses. In combination with the solar gains linked to the transparency of windows, these properties apply mainly during the heating season when outdoor temperatures are lower than inside and insufficient insulation causes heat losses. In the hot season however, large surfaces of transparent material cause high thermal gains due to transmitted radiation that create the necessity for cooling when combined with well-insulating building envelopes. These gains can be reduced with solar protection glazing by lowering its solar heat gain coefficient (SHGC). To keep reasonable illuminance, the glass can be coated with specially designed stacks of thin films to create an

interface with a selective spectral transmittance as described for example in [Oelhafen, 2007]. In the visible range of the spectrum the transmittance is maximised; it is minimised in the infrared and ultraviolet.

Such state-of-the-art glazing may have a positive impact on health and for the reduction of lighting and cooling loads [Danny et al., 2008]. But a large visible transmittance τ_v can still be a problem and cause glare and visual discomfort for occupants. On the other hand, a low energy transmittance τ_e suppresses solar gains that would be of great use to reduce energy consumption during the heating season. The energetic and photometric performances of a fenestration system are becoming central and important issues for architects. But with such contradictory effects, the right compromise between sound illuminance, visual comfort, electricity savings, usage of solar gains in winter and solar control in summer is not easy to find. In addition there are numerous families of solutions available to architects for a good light management. At most latitudes, an overhanging balcony on a south façade offers a great seasonal solar protection: in winter the sun is low and hits the window, in summer the sun is high and the balcony creates a shading element for the window. Also, many different types of blinds prevent glare while keeping reasonable daylight provisions. Furthermore, automated blinds and shading elements have been introduced to adapt to changing exterior conditions without the need for a highly conscious occupant who constantly adapts the blind position [Daum and Morel, 2010]. Finally, a great number of advanced or complex fenestration systems (CFS) were proposed in the past decade: electrochromic windows, gasochromic windows, laser cut panels, microscopic blinds, prismatic structures, etc. However, these solutions all have their drawbacks, costs and cannot be applied in all situations.

It is clear that a smart management of the available renewable resources is interesting: appropriate illuminances are enjoyable, prevent the so-called "sick building syndrome" [James and Bahaj, 2005] and decrease the energy demand due to electric lighting by a factor of three [Linhart and Scartezzini, 2010]. And an optimal exploitation of solar radiation can reduce heating costs in winter and cooling loads in summer. To the best of the authors knowledge, a static CFS that combines the advantages of daylighting, glare protection, seasonal thermal control and clear view does not exist up to today. The work presented in this thesis is an attempt to get closer to such an ideal system.

1.2 Motivation

For latitudes between $40°N$ and $55°N$, the solar annual solar radiation reaching the surface of the earth is generally between 1000 and $1800 kWh/m^2$ [US Department of Energy, 2014]. The heating loads per area of living space are in the order of $40 kWh/m^2$. For a single family home with $75m^2$ of roof and $150m^2$ floor area, the available radiation ($135MWh$) is thus far beyond the heating loads ($6MWh$). This radiation is spectrally distributed from ultraviolet to infrared as shown shown in Figure 1.1. With about 53% in the visible range the daylighting provision is also high. According to Reinhart, the outdoor illuminance is sufficient between 90% and
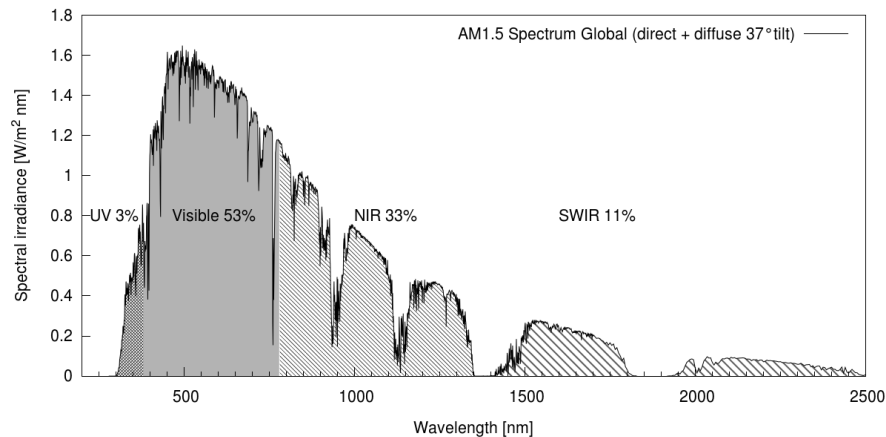
Figure 1.1 – AM1.5 solar spectrum for global radiation.

100% of the time within 9am and 5pm for all latitudes below 50° (where 93% of the world's population live) [Reinhart, 2014a, p. 47]. It is hereby obvious that solar radiation is available in sufficient quantity to directly provide daylight for visual tasks and energy required for space heating. The difficult task is to use it appropriately to avoid glare while providing sufficient task illuminance when possible and to prevent overheating in summer yet have sufficient solar gains in winter. To reach this set of objectives, advanced optical systems providing simultaneously transparency, angular dependent transmittance and light redirection by the means of embedded micromirrors are investigated. This type of approach is interesting for the following reasons:

- By redirecting light, sunbeams can be diffused and spread over a selected range of angles in an opposite direction. This is particularly suitable for a better use of daylight in buildings. Redirected, diffuse light is well suited for most office work tasks and contributes to a more comfortable and healthy environment.

- When sunlight is redirected and diffused, glare is reduced.

- Because the solar elevation changes over the year, angular dependent transmittance can result in a seasonal behaviour. Used in a window with the appropriate angular transmittance, this protects from overheating in summer and maintains solar gains in winter.

- The embedded mirrors can be almost horizontal and their projected height is very small compared to the gap between two mirrors. Therefore at angles close to the normal, light rays are only partly influenced by the structures and traverses mainly the transparent medium.

- Because the micromirrors are embedded, the faces of the medium they are in are flat and parallel, thus the system is imaging with a straight light rays transmission.

3

- Miniaturised, these mirrors can have a height in the range of $10 - 50\mu m$ making them hardly visible. These properties ensures not only translucency but high transparency and enable a view through the system.

- The system can potentially be produced as embedded microstructures in a film with a total thickness below the millimetre. A film of this dimension can be laminated with a glazing. Such films can potentially be produced inexpensively in a roll to roll or web process. This would provide a low cost solution for the glazing industry.

- The system may be combined with selective coatings to obtain wavelength dependent transmittance, for example to achieve an optimised ratio between visible light and solar radiation.

1.3   Method

Various geometries were investigated; an overview of existing designs offering daylight, thermal control, glare protection is presented in Chapter 2. In order to ease the design and evaluate optical performances of envisaged structures, an advanced ray-tracing program was specially developed. This program facilitates the search for new solutions, the study of parametrised laminar structures and the optimisation of the latter parameters. This software and some of the studied structures will be described in Chapter 3. The making of embedded micromirrors requires several steps including the fabrication of a mould with the structure, replication of the structure, alignment of optical components, thin film coating and embedding. The steps of the fabrication process and the corresponding experimental methods and tools are presented in Chapter 4. Many of the used methods had to be developed. The methods used for the characterisation of produced samples are introduced in Chapter 5. They include topographical measures, scanning electron microscopy, optical microscopy and confocal microscopy for the observation of samples but also goniophotometric measurements. The simulation results are presented in Chapters 6 whereas the experimental results obtained with these methods are introduced in Chapter 7. Finally the results, remaining problems and outlook are discussed in Chapter 8.

1.4 Hypothesis

The following hypothesis were accordingly formulated in the framework of this thesis:

- **Redirection of light rays increases the daylight provision when far from the windows and reduces glare risks.**

- **Angular dependent transmittance of light rays creates an intrinsic seasonal thermal control.**

- **A low impact on transparency at viewing angles can be reached with horizontal elements and parallel surfaces.**

- **Ray tracing simulation can be used to design and optimize a novel static optical system combining these three aspects.**

- **The miniaturisation of structures can ease the integration and increase the visual contact with the exterior.**

- **This optical system can be fabricated using a combination of advanced micro fabrication techniques.**

.

2 State of the Art

In this chapter the state of the art in the field of optical devices used for daylighting and seasonal thermal control will be presented. Conventional solutions are presented first, categorised regarding their main functionality as they mostly serve a single purpose. Microstructured devices, introduced more recently are then presented separately in greater detail. Most solutions have major drawbacks regarding the complex objective set in this thesis but their understanding was crucial to propose a new approach.

2.1 Daylighting devices

Glazing has been a light source and a link to the outer world in buildings since the Roman empire, long before the existence of glass, oiled paper windows were extensively used in Asia and animal skins in Europe. Windows with glass panes were initially expensive and small; they became the standard solution for windows in European homes only in the 17th century. Since then extraordinary progress has been made and a great variety of novel systems have been introduced in the past decades to increase the daylight illuminance. The daylight factor (DF) is the ratio between the interior illuminance and the exterior horizontal illuminance for an unobstructed standard overcast sky. Assuming a required task illuminance of $300\,lux$ and a mean daylight factor of 2% in a building, daylight is appropriate to lit the workplane when the outdoor horizontal illuminance is larger than $15,000\,lux$. It was shown that this condition is met for over 80% of the time between 9 am and 5 pm for latitudes below 50° [Reinhart, 2014a]. This means there is a possibility for daylight to become the main source of light in buildings; providing a strong motivation to develop new approaches. Generally this topic was covered in the International Energy Agency (IEA) Task 21 "Daylight in buildings". Many of the technologies presented below are listed in the sourcebook issued from this task [Ruck et al., 2000]. Currently an other IEA task is focusing on "Advanced lighting solutions for retrofitting buildings", investigating efficient daylighting and electrical lighting strategies.

(a) Ray tracing of a laser cut panel for an incident angle of 30°. The tilted rectangles represent the cuts, light rays are reflected at the interface due to total internal reflection.

(b) Ray tracing of a prismatic structure as proposed by 3M™ for example. Rays are mostly reflected back in the direction they came from. This is due to total internal reflection at the interface.

Figure 2.1 – Ray tracing of complex fenestration systems: a laser cut panel and a prismatic pane, both rely on the total internal reflection.

2.1.1 Light redirecting translucent structures

Various CFSs use physical phenomena to redirect light. With horizontal cuts made into an acrylic panel as shown in Figure 2.1a, normal incident light rays are simply transmitted while higher angles create grazing incidence within the panel and total internal reflectance occurs at the air-glass interface. This device known as laser cut panel was suggested by [Edmonds, 1993]. Only light rays hitting this interface above the critical angle are reflected, for other angles the light is refracted through the different elements. This device protects from glare and redirects daylight into the depth of the room as it can be observed in Figure 2.2a. For better redirection, the cuts are usually tilted by a few degrees. The main drawbacks of this design are that it does not provide solar protection and that because of the thickness of the cuts, transparency is reduced. One more example of such a static light redirecting system is the Lumitop™ glazing by St-Gobain (see Figure 2.2b). It "traps" daylight rays into banana shaped elements to guide them upwards. These advanced glazings are partially transparent and often placed in the upper third of the window in order to preserve the view in the outside in the bottom part. They do not protect from excessive solar gains in summer and blinds have to be installed on the lower part to avoid glare.

2.1.2 Blinds

Various types of mobile blinds and sun shadings have been introduced to prevent glare risks. They permit to adapt to changing conditions all along the year by opening, closing or tilting the blinds. Over time, designers have optimised the shape and materials of shading elements to combine protection with comfortable daylight conditions. Recently, split blinds with different

(a) Photograph of a a class room with a laser cut panel installed in the top part of a window.

(b) Photograph of the Lumitop™ glass (in the upper section of the window only).

Figure 2.2 – Illustration of various state of the art daylighting systems using redirection of light.

inclination angles have been introduced. They allow to separately control the upper part and lower part of the blinds. The latter provide a dynamic control at a relatively low cost and a robust system to separately control daylight, view and thermal contributions. In summer, the upper part may then be used for daylighting while the lower part reduces glare and overheating risks. An other interesting solutions is provided by perforated blades (Durlum GmbH), when closed they maintain a view to the outside and some daylight flux yet they maintain their solar protective role. The blinds proposed by RETROSolar™ achieve simultaneously redirection of light and blocking at certain incidence angles but require a form of control, they are described in more detail later.

2.1.3 Dynamic systems

Lately, recent technology has been applied to create windows with variable opacity. The family of called *smart glass* rely on thermochromism, electrochromism, gasochromism, suspended particles, liquid crystals and micro-blinds to provide this effect. Electrochromism directly uses the physical properties of some materials that reversibly change colour when a electrical voltage is applied, the colour changes slowly but remains in its state without current. Reverse current has to be applied to regain full transparency. In gasochromism an electrochrome, usually a metal oxide, interacts with an oxidising or reducing gas (commonly oxygen and hydrogen) to produce a reversible colour changes. Likewise thermochromism relies on temperature change; interestingly this could provide a self regulating device as the transparency needs to be reduced in hot conditions [Zhou et al., 2013]. The main drawbacks of these solutions are the long switching time, the high cost, the extra installation considerations (wiring, power supply) and control system to work properly.

(a) Photograph of the LESO-PB south façade.
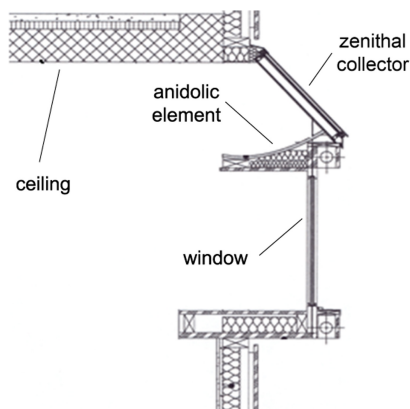
(b) Schematic of the façade concept with a normal window and an anidolic element.
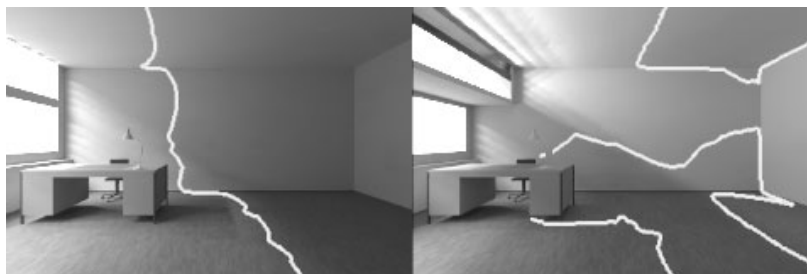
(c) Radiance rendering of typical office with such an anidolic element.

Figure 2.3 – A complex architectural concept using large anidolic mirrors to create well daylit spaces: the façade of the LESO-PB building , photograph and schematic. In (c) the Radiance rendering of an office is compared with and without the anidolic system [Courret, 1999]

2.1.4 Architectural integration

Multiple other architectural solutions can be found to handle daylight properly; these are generally the best and smartest solutions. Anidolic systems with large reflective surfaces have been developed at Ecole Polytechnique Federale de Lausanne (EPFL) [Courret et al., 1998, Scartezzini and Courret, 2004]. Such systems have been in use for several years at the Solar Energy and Building Physics Laboratory (LESO-PB) on the south façade of the laboratory's experimental building (see Figure 2.3), and have proven their potential for visual comfort and energy savings [Scartezzini and Courret, 2002]. The overhanging part with the anidolic mirror simultaneously offers protection for the window in the lower part that provides mostly the view to the outside. Other designs such as light ducts are using anidolic reflectors to guide light rays deep into the space. Zenital openings with diffusing or redirecting elements can also be used to increase daylight illuminance far from windows on the upper levels of a buildings. The Bartenbach licht labor [Bartenbach, 2014] has been a pioneer in matters of daylight and beside the numerous proposed solution, the interesting construction of it's offices is also a example of how to provide comfortable and well daylit spaces. In one office, reflection of light on a pond's water surface is used to create an indirect daylight flux with added moving caustics

effects. The drawback of such architectural solutions is that they often require complex and non standard building procedures along with increased cost and high expertise in the design phase.

2.2 Seasonal thermal control

From an energy perspective, the thermal properties of a window need to be considered to assess their implication on the energy balance of a building. As it has been introduced, ideal windows bring in a large quantity of daylight; but with a large daylight flux comes a large quantity of solar energy, especially in summer. These solar gains will heat up the inner space if they are transmitted. In buildings with highly glazed façades, the solar gains can raise the room temperature by several degrees and lead to overheating problems in summer. On the other hand these gains are welcome in winter where the heating loads can be suppressed completely for most climates by the appropriate choice of g/U value ratio, window orientation and dimension [Manz and Menti, 2012].

2.2.1 Solar control glazing
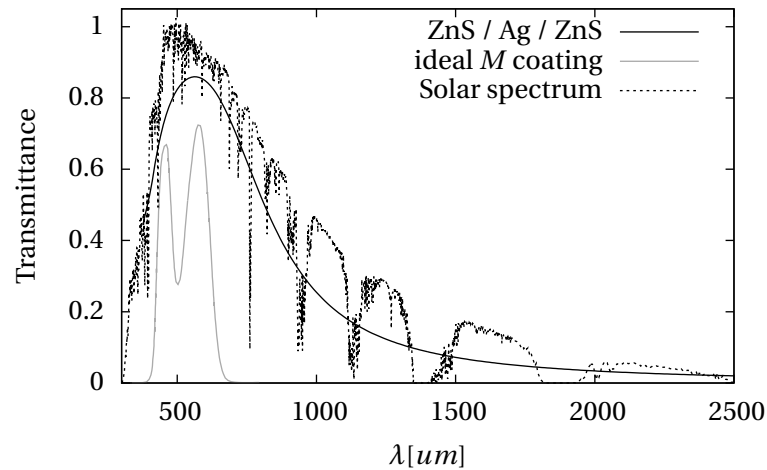
Figure 2.4 – Simulated transmittance of a simple [ZnS / Ag / ZnS] solar control coatings described in [Leftheriotis et al., 2000] and a more refined theoretical transmittance as described in [Oelhafen, 2007]. The normalised spectral distribution of the solar radiation (AM1.5) is shown for comparison.

Thin films or sometimes additives can be used to reduce the solar energy transmittance of a glazing by increasing reflectance or absorptance, such devices are called solar protective glazing or solar control glazing. In particular, thin film coatings can be used to offer high transmittance in the visible range of the spectrum but low transmittance in the infrared range. Hereby the thermal gains are reduced but most of the visible spectrum is still transmitted. A multilayer thin film coating is applied to the glass to create an interferometric filter, the thickness of each layer is typically smaller than a micrometer and at each interface the reflected

wave undergoes a phase shift. Waves reflected from the different interfaces will interfere, constructively or destructively depending on the wavelength. Traditionally a Gaussian like distribution in the visible range cuts down excessive solar gains due to the infra-red and ultraviolet radiation. In Figure 2.4, the transmittance of a ZnS/Ag/ZnS coating as described in [Leftheriotis et al., 2000] was computed with TFCalc. Recent studies show that the transmitted spectrum can be optimised and that with an 'M' shaped transmittance spectrum, an energy load coefficient of τ_e / τ_v = 0.33 can theoretically be reached [Oelhafen, 2007]. First sun protection glazing based on this principle have been realised [Mack, 2008] with an energy load coefficient within 0.34 and 0.40; the latter offers a sound colour neutrality in transmittance and angular stability of reflected colour. Such coatings however offer no seasonal dynamics; solar gains are also mitigated in winter when they are most desired. They have a slight angular dependency but the variations are not significant for low angles and redirection is inexistent. Stronger angular dependence can be reached using angular deposition of metallic coatings as described by Smith G.B. [Smith et al., 1997, Jahan and Smith, 2007]. Such depositions can create columnar structures under particular conditions. This structure creates an angular selectivity but the variation of transmittance is very gradual. With a maximal transmittance of 70% at 60° for example, 10% transmittance is reached only at −60°, in a very progressive way.

2.2.2 Sun rays blocking devices

Various designs use different prismatic structures to create angular dependent transmittance. The oldest might be the one described in an early French patent [Vieri, 1981]. The entry surface is made of prisms and the exit surface is flat. Using this design the light rays incoming on the device at a large incident angle are refracted at the front surface and the angle on the back surface is then larger than the critical angle. Because of the difference in refraction indexes, total internal reflection occurs. The exit surface of the prism is placed so that this reflected light is easily transmitted (low incoming angle). Symmetric 90° prisms can also be used to reflect light impinging at normal incidence. In this case the flat panel surface is the first interface and the prisms are placed on the backside where total internal reflection occurs, this type of prism is illustrated in Figure 2.1b. For application requiring the blocking of a larger range of angles, this devices requires sun tracking because the blocking range is usually narrow. Such devices transmit light rays only outside this angular range. For fenestration applications, the main drawback of this design is that the panels are not transparent because of the prismatic structures. They distort the image and can not be seen through. Also the overall transmittance is not very high and the sun rays are transmitted as a bright parallel beam and not diffused. An other interesting approach uses lenses combined with a reflecting surface to block light at a selected angle [Kuhke, 1991]. The lenses focus daylight at different locations of the backside regarding the incoming angle; if a mirror is placed in the focal point, light rays from this angle are blocked.

(a) Example of architectural integration of KoolShade™ and KoolGlass™ solar protection at the UNIL campus in Lausanne, Switzerland.

(b) Detail of the KoolShade™ exterior shading elements.

(c) Detail of the KoolGlass™ glazing and illustration of transparency.
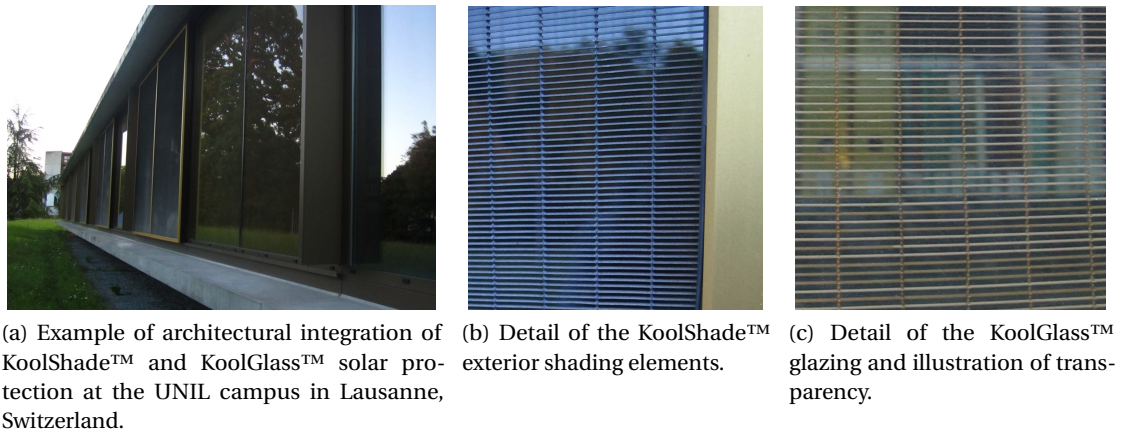
Figure 2.5 – Illustration of KoolShade and KoolGlass products in application at UNIL.

2.2.3 KoolShade

KoolShade™ and KoolGlass™ are products that create an angular dependence using tiny metallic louvres at a fixed angle. The blinds are often black but the colour can be changed to obtain other aesthetic appearances as in a building of the Université de Lausanne (UNIL) depicted in Figure 2.5. In the canton of Fribourg, the novel building of the Association du Centre Professionnel Cantonal was fitted with KoolGlass™ panes of multiple colours. They prevent glare and strongly reduce solar gains all over the year. The main drawback is that solar gains in winter are also reduced. The micro louvres are tilted at 30° and block nearly all the sunlight incoming at angles greater than 45°. Because they are placed outside the window, they radiate less heat into the room than usual blinds, which are often still used indoor. Because of it's small size, with 700 micro louvres per meter, the device is partially transparent. In this system however, the transmitted daylight is not redirected. These blinds are mostly used externally (brand name: KoolShade™) but they may also be laminated in polyvinyl butyral (PVB) between two windows (brand name: KoolGlass™). In this case, the progression from partially transmitting to fully blocking state with changing is slower than when used externally. This may be better suited depending on the climate. This application shows how important it is to place the shading system in the right place and how smaller scale can increase clear views. It also illustrates the relevance of placing a device within a transparent medium to influence the angular properties.

2.2.4 Architectural solutions

As in the perspective of daylighting, architectural design can offer significant improvement of the situation from a perspective of seasonal thermal control. The use of vegetation for example can provide solar protection in summer when trees are fully grown and allow important solar gains in winter when leaves have fallen off [De Abreu and Labaki, 2011]. Overhanging balconies or roof edges take advantage of the changing sun elevation to modulate thermal

gains over the course of the year. When dimensioned accordingly, they provide shading for elevated solar positions in summer and let the winter radiation through the windows. Natural and forced ventilation can also be used to take advantage of the temperature difference between night and day.

2.2.5   Dynamic systems

The dynamic technologies mentioned for daylighting can also be used for thermal control. Glazings with changing SHGC are often named *smart glass*, but without an "intelligent" control they are useless. Choosing not only the required illuminance but also the amount of needed thermal gains requires an even more complex control system depending on the user requirements, indoor and outdoor temperatures, task illuminance, available solar radiation, thermal mass of the building and even to some extent the meteorological forecasts. Amongst other techniques, neural networks have been used [Morel et al., 2001] to achieve this control and adapt to the buildings specificities. Other advanced dynamic systems such as the GlassX™ glazing relying on phase change materials were studied in the review by [Jelle et al., 2012].

2.3   Microstructures

This separate section focuses on the miniaturisation of optical devices that has been made possible at relatively low cost recently. An important field of application lays in the area of consumer electronics such as for flat displays where microstructures enhance directionality of the display and increase its luminosity.

2.3.1   Light redirection

(a) Photograph of the device profile (center), with micrographs of the exterior (left) and interior (right) facing surfaces.

(b) Raytracing of the redirection principle at play in the microstructure proposed by Klammt *et al.*
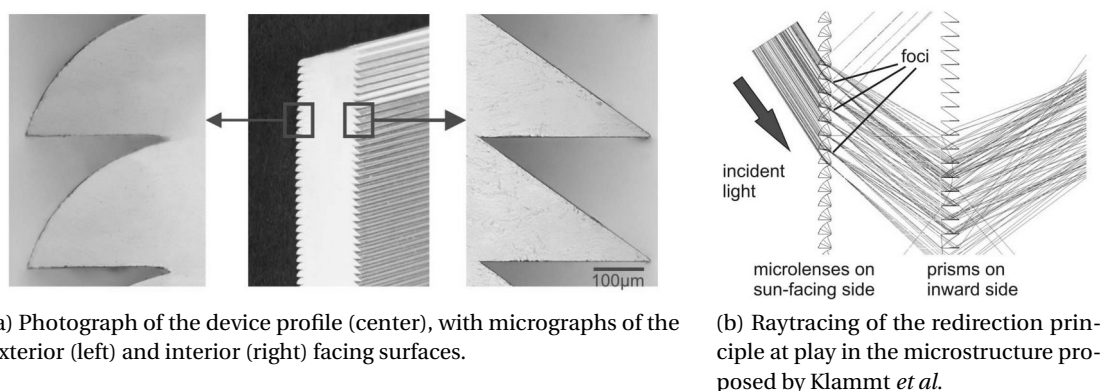
Figure 2.6 – Illustration of the daylighting device proposed by Klammt *et al.* [Klammt et al., 2012]

The redirection provided by different refractive indices in laser cut panels was introduced

earlier; the same effect is obtained on a smaller scale in a plastic film commercialised under the name of SerraGlaze™ canopy system. More complex designs such as the one proposed by S. Klammt and A. Neyer use an asymmetric microstructure to redirect light rays [Klammt et al., 2012]. As illustrated in Figures 2.6a and 2.6b, on the first face, a succession of quarters of a circle capture a maximum of light flux even for large angles of incidence. The horizontal part at the bottom of the quarter of circle reflects light rays on the basis of total internal reflection. These lenses also redistribute a parallel beam aver a range of angles. On the inner side, the horizontal flat surface of the prismatic structures further increases the proportion of light rays redirected upward by total internal reflection and the tilted surface contributes to refract rays in a more horizontal direction as well as increase the transmittance (lower incoming angle with respect to the normal). This design is very efficient at redirecting large portion of the incoming light flux from all angles and has a high transmittance for elevated angles. The transmitted light flux is mainly distributed around 30° upward to improve daylighting conditions. However, this structure achieves neither solar protection nor transparency.

2.3.2 Angular dependent transmittance

Prismatic film and holographic optical elements (HOE) use the combination of geometry and refractive index difference between air and glass or some acrylic glass to obtain an angular dependent behaviour. In holographic elements, the dimensions of structures are generally smaller: they rely purely on diffraction to generate angular dependent transmission or reflection. Rays may be selected from a certain angle, redirected at certain angles only or even focused for certain angles [Müller, 1994]. Various prisms exist at macroscopic scale but miniaturisation of the structures reduces the quantity of material significantly and hereby also the price. A prismatic sheet structured with periodic 90° pyramids for example can be applied like a cap above a window and will reflect normal and near normal incident light rays while other directions are transmitted. These blocking systems have the inconvenience that they operate only for a limited set of angles, they therefore have to be mounted on tracking systems. To extend the blocked range, a microstructure with a parabolic shape as in compound parabolic concentrators (CPCs) (Figure 2.7b) was proposed by Bühler in his thesis [Bühler, 2003]. In this case a reflective coating was added at the exit opening of the CPC and the reflected range is increased to about 15° each side around the normal.

Finally as illustrated in Figure 2.7a taken from the study of [Walze et al., 2005], horizontal flat surfaces in triangular prisms can be used to redirect light rays for certain angles only. By changing the slope of the non horizontal facet of the prism, the range of angle inducing total internal reflection on the horizontal surface can be modified. These angular behaviours of microstructures can be used for daylighting purposes but also seasonal thermal control. However, these devices are asymmetric: one side is flat and the other is structured to provide the tilted or bended surfaces with refractive index difference. This distorts the outside view and creates a duplicate image because the refraction occurring at one interface is not cancelled by the refraction at the other interface. Furthermore, the variations in the index of refraction over
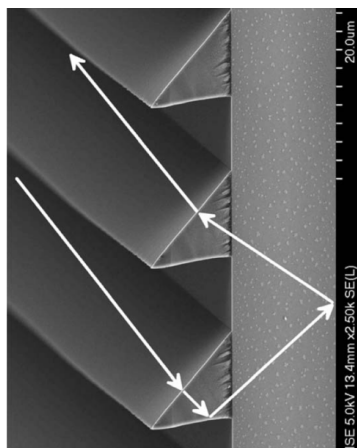
(a) Micrograph of a microstructure for blocking of selected angles with illustrated path of light in blocking situation.
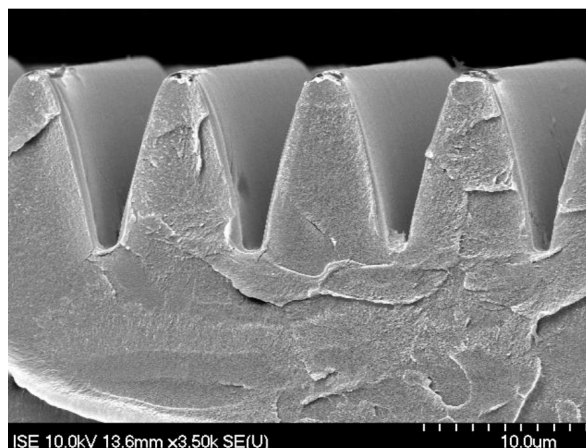
(b) Structure using CPC for light concentration or blocking if a mirror coating is deposited on the top of the structure (light flux incoming on bottom side).

Figure 2.7 – Illustration of advanced microstructures proposed by Walze *et al.* [Walze et al., 2005] and Bühler [Bühler, 2003].

the visible range diffracts colours of a direct sunbeam at different angles creating a rainbow like coloured patterns. In this research the authors also concluded that when reaching dimensions below some tens of micrometers, diffraction effects increase and further distort the view through the system by creating multiple ghost images.

2.3.3 Combination of microstructures with thin films

On a microscopic scale, the Fraunhofer Institute for Solar Energy Systems (ISE) studied coated microstructures to achieve a more advanced control and reduce the diffraction effects [Walze et al., 2005]. Different types of coatings were successfully deposited on selected facets of the microstructures. Researchers attempted to reduce the ghost image created be the refraction on micro prisms with an absorbing coating. Reflective coating were demonstrated to offer the same advantage than absorbing coatings. Additionally the authors changed the angular dependent behaviour. Switchable coatings were also used to control and modify the behaviour of the system. The drawbacks are similar to those of all prismatic structures mentioned above, additionally it can be concluded from this work that when optimising a geometry, one must have the means to fabricate it accurately, variation between the design and the reality can induce very different performances.

2.3.4 Microblinds

Lately dynamic devices relying on microstructured thin film coatings were introduced, B. Lamontagne *et al.* at the National Research Council (NRC) Ottawa in Canada proposed

micro-blinds [Lamontagne and Py, 2006, Lamontagne et al., 2009]. These micro-blinds are electro-statically activated curling electrodes of about 100 micrometers. A multilayer coating is deposited and patterned using lithography. The stressed layer is deposited on top of a sacrificial layer that is later removed in areas where the blinds will curl. By applying an electrical voltage, the stress is reduced and blinds are uncurled. This is a dynamic system that can be used to control the tranmission of daylight, it is similar to an electrochromic glazing but the switching time is decreased and typically in the order of milliseconds (compared to minutes for electrochromic glazing).

2.4 Combined solutions

Few concepts offer a combination of solar protection, daylight provision and clear view. In particular the two following devices come close to an ideal solution.

2.4.1 Advanced blinds

The various blinds proposed by RETROSolar™ are an example of advanced sun shadings aiming at the complex set of objective of this thesis. Köster H. proposed and patented several novel types of blinds [Köster, 1995, Köster, 2011]. One of these blinds has a complex profile combining a W shaped part and a parabolic part as illustrated in Figure 2.8a). The second and fourth faces of the W block direct sunlight whereas the parabolic part redirects it. For larger angles of incidence $(50° - 90°)$, the blocking effect of these two surfaces is increased by their growing projected surface in these directions. For more horizontal angles $(30° - 50°)$, the parabolic surface is dominant and light rays are mostly redirected. Finally for horizontal angles, the projected height of the relatively flat profile of the blinds represents only about one third of the period; this provides a sound transparency. This design provides both redirection and angular dependent transmittance but the complex profile increases the fabrication cost of such blinds. To be protected from wind and dust, and to avoid unwanted solar gains if placed inside, such blinds should be placed between two glass panes within a triple glazing. This creates very thick and expensive windows. Finally mechanical parts are subject to be damaged and prevent the system from working accordingly.

2.4.2 Dual pane structured window

W. Lorenz proposed a system using two symmetric prismatic glass panes to combine solar control and daylighting provisions [Lorenz, 2001a, Lorenz, 2001b, Lorenz, 1998]. The working principle is illustrated in figure 2.8b were it can be observed that on one of the panes, one face of the prism is coated with a reflective coating. The two panes are then assembled and an air gap is kept between them. This air gap plays the angular selective role in the system. When light rays are reflected on the coated face of the prism, they will be reflected by the second face only if the angle is larger than the total internal reflection angle. The use of two complementary

(a) Photographs and schematic representations of the functioning principle of RetroLux™ blinds from the product description [RetroSolar, 2014]. Part of the blind is used to redirect light (the parabolic surface) and the rest is used to block light from elevated angles on incidence. This creates a combination of daylit space and solar protection.

(b) Illustration of the principle proposed by Lorenz [Lorenz, 2001a]. The s_a surface is reflectively coated and the air gap between f_a and f_b creates total internal reflection for selected angles. All refracted angles above ζ_1 will be reflected by this air gap. Depending on the inclination of the s and f surfaces, ζ_1 can be modified. Note that the illustrated path can be followed backwards.

Figure 2.8 – Existing solution combining daylighting, glare protection, seasonal thermal control and clear view

asymmetric 90° prismatic structures preserves transparency because interfaces in the light path are parallel by pairs and interactions cancel out. The main drawback of this design achieving both redirection and angular dependent transmittance is that it requires relatively large elements and a complicated assembly to preserve a parallel air pocket between the two elements. To the knowledge of the author, despite its invention a decade ago, this system was never commercialised.

2.5 Technological gap - Ideal glazing concept

It was found that there are very few existing products offering an optimal combination of thermal and daylighting control. To the best of the authors knowledge all are either dynamic, very complex or expensive. This doctoral thesis attempts to propose a static system offering an optimal combination of these objectives by adapting the CFS to the type of building, the orientation of the façade, the type of architectural element (window or overhanging shading element) and the latitude on earth. The principles of such a glazing are illustrated in Figure 2.9. Such a static device will not be as adaptable to the changing climatic conditions than a dynamic device that can potentially set the admitted light and thermal flux between zero and maximum at any moment. However the simplicity of the device (no moving parts, reduced size), the absence of control strategy and potentially the reduced costs make a static solution desirable in many cases.

A good starting point can be drafted by learning from existing devices, from this state of the art it can be concluded that:

- The angular variation of the solar elevation can provide seasonal thermal control.

- The redirection of light rays can improve daylight provision while simultaneously reducing glare risks.

- The redirection of rays by reflection (not refraction) reduces the "rainbow" effect.

- If the redirecting surface is curved, direct sunlight can be converted to diffuse daylight.

- Miniaturisation of structures increase transparency, ease architectural integration and may also reduce cost on the long term.

- Thin film coatings can be used on selected facets of a microstructure by angular deposition.

This base of knowledge supports the hypothesis formulated in the introduction of this thesis.
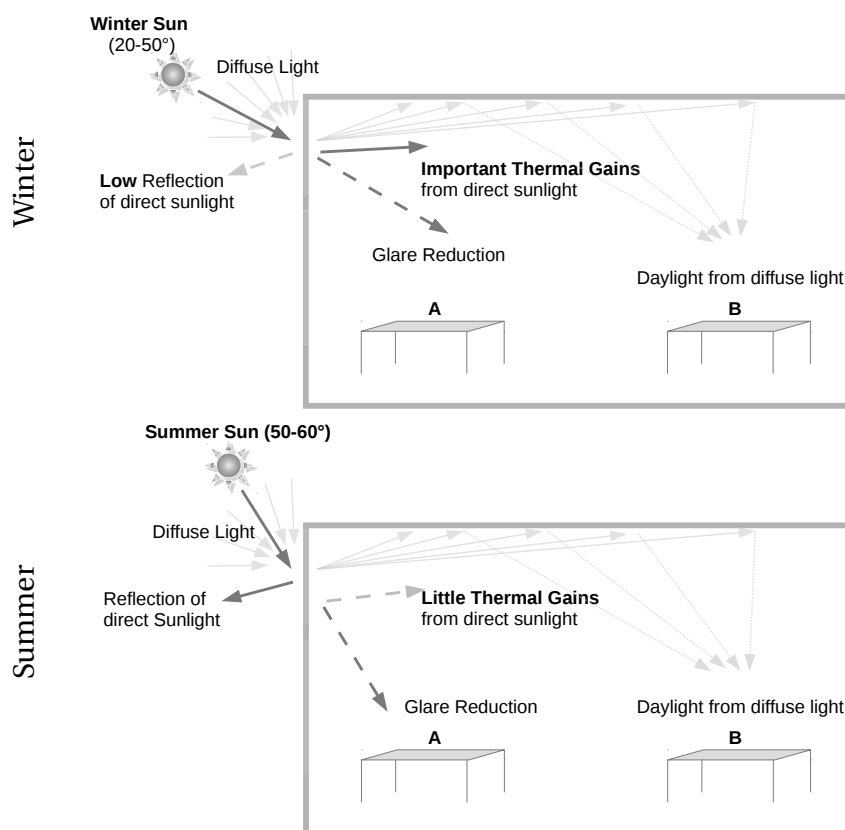
Figure 2.9 – Illustration of the working principle of the an ideal CFS for daylighting, glare protection and seasonal thermal control and view.

3 Development of a Simulation Framework

In order to investigate complex fenestration systems and because existing simulation tools did not provide satisfaction, a custom ray tracing program was developed by the candidate. The goals were to easily design new optical system geometries and parametrise them; easily variate and compare the effect of the parameters; visually assess the propagation of light rays through the system; provide very fast visual response to improve the design; enable the use of thin films and spectral properties of materials; easily compare multiple systems regarding different criteria; produce usable bidirectional scattering distribution functions (BSDFs) for rendering of daylighting in rooms with a software such as Radiance; and finally, offer metrics for the assessment of thermal and daylighting performances. The concepts of the developed model and the said performance indicators will be introduced on this chapter.

3.1 Simulation principles

Ray tracing software is often used [Wittkopf et al., 2010, Andersen et al., 2005] to calculate the BSDF of CFSs but no dedicated tool was found for the modelling of CFS taking into account complex geometrical features, advanced material-dependent features such as wavelength depend refractive indices, as well as thin films interferences. Also, existing commercial tools provide a complete three dimensional (3D) characterisation but their usage is time consuming and their output is not adapted to the evaluation and comparison of CFSs performances. For these reasons, a simple and efficient ray tracing tool for the study of laminar structures was developed with the possibility to directly compare glazing related performances and modulate designs in the graphical user interface (GUI). In this section the simulation principles, the original concepts used in the algorithm and in the user interface of the software are described.

3.1.1 Monte Carlo technique

Monte Carlo algorithms are of stochastic nature and they are used to solve complex physical or mathematical problems. When the number of variables in a system is large and the solution

can not be found analytically, computer simulations using many random events give an accurate estimate of the solution. In a typical Monte Carlo algorithm, random draws define a chain of local events characterising the global event and leading to a final state. Each draw follows a given distribution being representative of the corresponding event. By repeating this succesion of random events numerous times, a probability distribution of the final states is obtained. The accuracy of this result depends on how well the problem is described and on the number of random draws. In the case of optical systems, every physical phenomena (reflection, refraction, absorption) occurs randomly according to the probability distribution given by the corresponding physical laws. For this software, these physical laws at play will be described in Section 3.2.

3.1.2 Ray tracing

Ray tracing is a technique issued from geometrical optics to model the path taken by light in an environment by following rays of light. It may be used in the design of lenses, sets of lenses in microscopes, telescopes, reflectors and other optical devices. It is also an approach for graphical rendering in computer graphics and is used to produce realistic illumination of virtual scenes. Virtual reality is a large field of application for ray tracing; it is used in flight, surgery and other simulators to render scenes and objects with the added realism provided by the features of illumination (shadows, glare, caustics, etc.). In many cases, when the aim is to render a scene, reverse ray tracing is applied. Following the path of rays backwards, from the eye-point outwards, guarantees that only rays that reach the field of view are computed. A large set of existing software use more or less physically accurate ray tracing rendering to simulate the behaviour of light in complex environment. Amongst many, Radiance offers complete and flexible tools for the use of architects to render construction projects and obtain physically sound information such as illuminance levels. More specifically and in relation to complex fenestration systems, rooms with different types of windows and electric lighting sources can be modelled in Radiance to study indoor illuminance, whether it is natural or artificial, direct or indirect [Ward et al., 2011, Kämpf and Scartezzini, 2011, Laouadi et al., 2007]. This however requires an accurate definition of the studied window or light fitting. Such detailed description have to be obtained using physical measurements or more specific software.

In the case of CFS design and optimisation, particular care has to be taken to model accurately the different interactions at play. In general, the physical accuracy of ray tracing techniques is increased by modelling different aspects of light transport. An example of such properties that are however not relevant for CFSs is subsurface light transport: certain light diffusing materials might reflect light rays that were first transmitted and then scattered within the material, therefore the point of reflection might be different from the point of entry of a ray. This can be modelled using a bidirectional surface scattering distribution function (BSSDF) [Jensen et al., 2001] and is useful to provide added realism in the rendering of translucent materials such as paper, skin, milk, cheese, etc. but also in simulations for medical applications. To illustrate this subsurface scattering, one might think of the effect created when covering

a flashlight with a finger; the whole finger appears glowing. An other example is the photo luminescence which needs to be modelled when studying photo luminescent concentrators [Schuler et al., 2008]. In the scope of this thesis, thin films, geometry, material properties and interfaces between materials are considered to compute the path of light rays and to accurately simulate reflection, refraction and absorption. The related models will be described in Section 3.2.

3.1.3 Mixed dimensionality concept

A two dimensional (2D) description of the optical design is sufficient for most existing CFS products because they can be described as 2D extruded profiles. In a pure 2D ray tracing of such a profile, with no scattering, transmittance is modelled accurately for zero degree azimuth because the rays are then always in the plane the profile was defined in. In other words, the profile is extruded in a direction normal to the plane of reflection. Out of this plane the error is cumulated after each reflections and refractions, for complex geometries with several interactions, the error is therefore increased. For a small deviation from this plane, the azimuth angle has little influence on the distribution of transmittance. However, the error grows exponentially for larger azimuth angles. For example, with a mirror embedded in a transparent material, using 2D only for reflection and refraction introduces errors of 20% in the angular distribution when the azimuth angle is 40°. This is not acceptable for an evaluation of annual energy transmittance that relies on three dimensional Bidirectional Transmission and Reflection Distribution Functions (BTDF and BRDF). For an evaluation of daylighting performances using a rendering software such as Radiance, complete and accurate BTDFs are also required. For these reasons, the third dimension has to be considered.
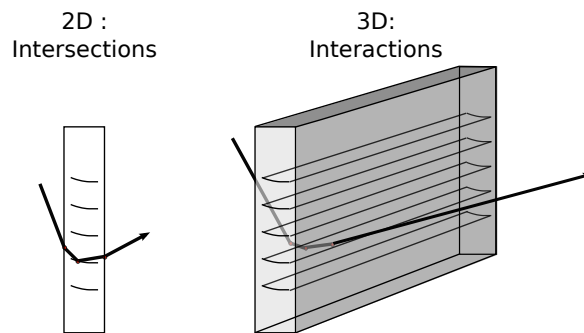
Figure 3.1 – Illustration of the mixed dimensionality concept for ray tracing of profile defined geometries. Intersections are accurately modelled in 2D using the x and y components of the vector. Interactions such as reflection, refraction and absorptions are modelled in three dimensions.

In the proposed algorithm, all intersections are computed in 2D. If a profile is defined in the x and y coordinates, the intersections are computed accurately in this plane using the x, y coordinates of the ray direction vector; the only loss of information in this process is
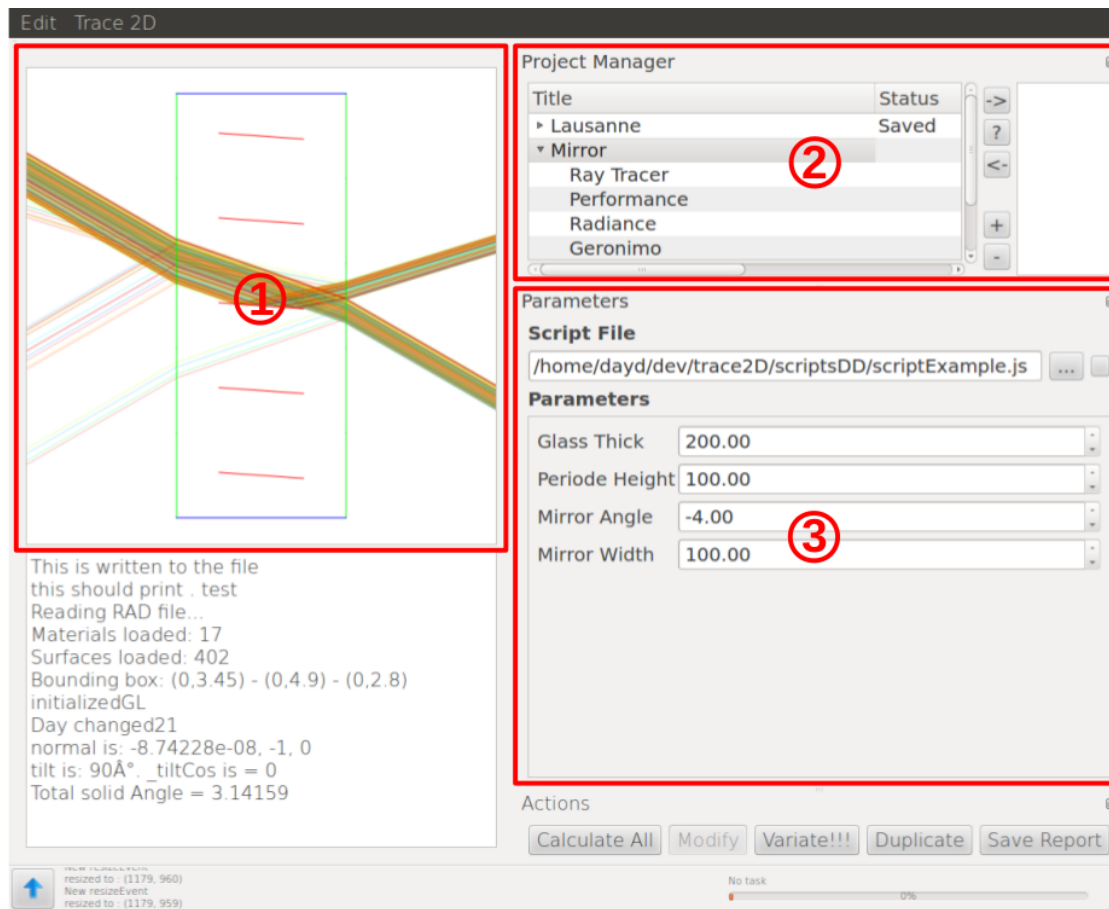
Figure 3.2 – Screenshot of the graphical user interface. ① shows the output, in this case ray tracing of a collimated 30° beam on embedded mirrors as described in the script in Figure 3.3. ② Project List and performance indicators. ③ Parameters created in the script.

the z coordinate of the intersection. This information can be calculated once the distance in the projection plane is known, but it is of little use since the main interest is in the angular distribution of the transmittance. The z coordinate only affects the result in the boundary area of the system and such boundary areas represent a fraction of the device; particularly when the feature is much smaller than the system. Finding intersections between lines in two dimensions is very fast and can be efficiently done using a binary space partitioning (BSP) tree [Ize et al., 2008]. BSP is a process commonly used in computer graphics to accelerate rendering, collision detection, geometrical operations or other problems handling complex spacial scenes. These operations are accelerated by the added spacial information provided by the partition. Such partition algorithms are of the "divide and conquer" type and generally reduce complexity by a $log(n)$ factor for n elements when compared to the simple iteration through all elements. In the BSP tree, the objects are organised regarding a recursive subdivision of space. In the case of Complex Fenestration System Ray tracing Profile Optimisation (CFSPro) for example, this subdivision is done depending on whether other interfaces are on the right or on the left hand side of a surface's vector. The interfaces are recursively placed

```
// Define materials.
include("materials.js");
mAir = tracer.newAirMaterial();

// Parameters loaded in the graphical interface:
parameters.group(Geometry);
glassThick = parameters.getDouble("Glass Thick", 200, 1, 10000);
periode = parameters.getDouble("Periode Height", 200, 1, 10000);
mirrorAngle = parameters.getDouble("Mirror Angle", -10, -60, 60);
mirrorWidth = parameters.getDouble("Mirror Width", 100, 1, 10000);

y = 0;

// Loop to create 5 embedded mirrors with the specified parameters.
for (i=0;i<5;i++)
{
        // front side glass interface
        tracer.addGlass(0, y, 0, y+periode, mAir, mBk7);

        // mirror vector
        vx = mirrorWidth * Math.cos(mirrorAngle * Math.PI / 180) / 2;
        vy = mirrorWidth * Math.sin(mirrorAngle * Math.PI / 180) / 2;

        // the mirror itself
        tracer.addMirror( glassThick/2 - vx, y + periode/2 - vy,
                          glassThick/2 + vx, y + periode/2 + vy, mBk7);

        // back side glass interface
        tracer.addGlass(glassThick, y, glassThick, y+periode, mBk7, mAir);

        y += periode;
}

// Border conditions :reports ray to other side.
tracer.addTeleporters(0, 0, glassThick, 0, y);

// Create a parameterized light source.
// parameters belong to an other group, they will be displayed eles where.
parameters.group(Sky);
elev = parameters.getDouble("Elevation Min", -80, -180, 180);
azi = parameters.getDouble("Azimuth", 0, -90, 90);
tracer.setDistribLightSource([0], [0, y], [0], [elev], [azi], [400, 1000]);
```

Figure 3.3 – Example of a script to draw five embedded flat mirrors in a transparent medium. The parameters for this script are glass thickness, periodicity of mirrors, mirror width and tilt angle. When a value is introduced with the `parameters.getDouble()` function, the associated field appears in area ③ of the GUI (Figure 3.2) with the specified name. The optical properties of the material "mBk7" are loaded from the "materials.js" file.

in a binary tree depending on their relative position and might be split in two if they are part left, part right. All children of a leaf in the left branch of the tree are on the left hand side, all children in the right branch are on the right hand side of this interface. The tree should be well balanced to increase the performance significantly, this balancing has to be done in a preprocess. When searching for intersections, the relative position of the ray and the tree root node can be used to determine if the left and/or right branches should be explored. This search is applied recursively until the end of the tree. When a single structure is composed of many interfaces, the speed of computation can be increased by performing the ray tracing only for a representative cell of the system, rays exiting the cell from the bottom are reintroduced at an equivalent position on the top of the cell.

For interactions all three dimensions are used. Reflection, refraction and absorption are pre-

cisely modelled using tree dimensional vector calculus following physical laws as described later. Also, for the modelling of thin films, 3D vectors are used in combination with a matrix approach for the calculation of reflection, refraction and absorptions as described in Section 3.2.3. The principles of such a mixed dimensionality approach are illustrated in Figure 3.1.

3.1.4 Script based description of geometry and parameters

Besides accurate physical modelling and calculations, the developed software was also meant to be an intuitive and flexible design tool. For intuitive development, structures can be parametrised and the parameters can be modified in the graphical user interface (GUI) with a direct rendering of the resulting distribution of rays. The GUI can be used to modify the incidence angle of the beam and visualise the angular distribution of transmitted and reflected light flux. To provide flexibility, each design is based on a text file containing a geometrical description using a set of parameters. These scripts can make use of the basic JavaScript programming language such as `for` and `while` loops, `if - then - else` statements, mathematical operators as well as more advanced data structures such as arrays. In addition to the JavaScript language, functions specific to ray tracing are implemented to add interfaces, define materials and light sources. Another set of instructions was defined to add parameters, these are directly included in the graphical interface. Hereby almost any 2D extruded structure can be defined, modified and visualised. Part of the GUI is hereby created depending on the script (part ③ in Figure 3.2) For example, the file describing a glass with integrated flat mirrors introduces the parameters for mirrors width, tilt and periodicity as well as glass thickness. It then contains a scripted description of the interfaces between the bulk material and air and were to include the mirrors as defined by the parameters. The light source can also be defined in the script and parametrised using an other group of parameters, the latter parameters will appear in the GUI. The script for this example is shown in Figure 3.3 and the corresponding GUI in Figure 3.2.

3.1.5 Project optimisation oriented GUI

In the process of designing a solution, new concepts need to be tested and parameters optimised. To facilitate the study and optimisation of CFS complying with multiple requirements, the graphical user interface of the software was built around a list of projects and their variations. Projects are organised in a tree structure, each variation of a project becomes its child in this tree. This structure shown in area ② of Figure 3.2, gives a rapid overview and history of designs. As mentioned in Section 3.1.4 the projects are described by a JavaScript containing both the geometry of the design and the list of parameters. Each of these parameters can than be modified individually in part ③ of the GUI and the resulting ray path visualised immediately in part ①. In Figure 3.2, the displayed parameters correspond to those introduced by the script of Figure 3.3. Different indicators of the performances can also be visualised in part ① of the GUI for each design. For a meaningful comparison and optimisation, a design can be varied according to a single parameter. The different variations appear as sub projects

in the tree structure. they can be varied again or discarded. By selecting several projects in area ② of the GUI, their performances can be directly compared in area ① regarding different criteria. These criteria include transmission distribution of solar radiation; transmittance depending on incident angle; daylighting performances and thermal performances. These are as described later in Sections 3.3 and 3.4. This approach proved to be very useful to understand how complex geometries affect ray paths depending on the incidence angle and was used to invent and optimise an original design described in Chapter 6.

3.1.6 Genetic algorithms

Genetic algorithms are commonly used to find an optimal solution to intricate problems depending on numerous parameters. The principles of genetic algorithms are inspired by natural selection. Solution are represented by individuals and the parameters are represented by alleles. Like in the natural evolution process, individuals of a generation mix their alleles when mating to form the next generation. A fitness function is defined to select the best individuals of each generation and eliminate the weaker ones. Mutations and crossovers are used to introduce variations, they are suited to escape local minima. Such a genetic algorithm was implemented using the *GAlib* library developed by Matthew Wall from MIT [Wall, 2014].

The genetic algorithm was tested on a theoretical anti-reflective coating. The coating was defined, simulated and optimised for minimum reflection in the visible range with a classical software for thin film design (TFCalc). It is a 4 layer coating on a glass substrate with alternate low and high refraction indices (starting from the glass substrate, alternating layers with $n = 2.2$ and $n = 1.38$). The thickness of the 4 layers were then randomised and the genetic algorithm was used to find optimal layer thickness. Figure 3.4 shows the "individual" with the best reflection spectra from generations 1, 6 and 10.
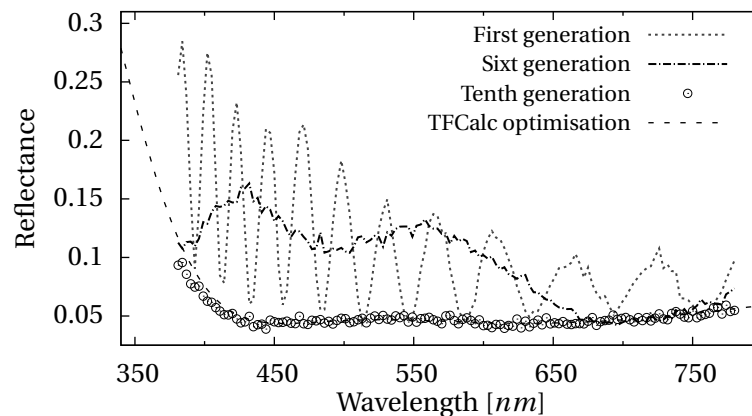
Figure 3.4 – Convergence of a population towards an optimised four layer anti-reflective coating using a genetic algorithm and ray tracing. Starting with fully randomised thicknesses, after ten generations the result is comparable to the optimisation obtained with TFCalc.

3.2 Physical models

The different physical laws used to model the complex optical systems studied in this work are described in the present section.

3.2.1 Refraction and reflection (Snell-Descartes and Fresnel laws)

Refraction is a well-known phenomenon changing the direction of light rays at the interface between two different mediums. This phenomenon is due to a change of the speed of light in the medium and the angle of refraction is defined by the Snell-Descartes law:

$$n_i \sin(\theta_i) = n_t \sin(\theta_t) \tag{3.1}$$

where n_i and n_t are the refractive indices of the materials on the incoming and transmitted side of the interface respectively. The angles to the normal: θ_i and θ_t are the incoming and transmitted angles respectively. The values for the refraction indices are not always constant and can vary strongly depending on the wavelength of light. Therefore the refraction index of each material should be defined using sufficient values for the different wavelengths of interest. Indeed, depending on the modelled geometry and considered angle, a very small variation of the refractive indexes can change the light path by some degrees and hereby disperse colours. When $n_i > n_t$ and beyond the critical angle $\theta_c = \arcsin(n_t/n_i)$, total internal reflection occurs. Let $\vec{v}$ be the normalised direction of propagation of the light ray and $\vec{n}$ the normal to the interface (with $\vec{n} \cdot \vec{v} < 0$), then the vectorial calculus for a reflected ray $\vec{v}_r$ is:

$$\vec{v}_r = \vec{v} - 2\vec{n}\,(\vec{v} \cdot \vec{n}) \tag{3.2}$$

In agreement with what is described in [Glassner, 1989], the corresponding vectorial calculus for a refracted ray $\vec{v}_t$ was found to be:

$$n_r = \frac{n_i}{n_t} \tag{3.3a}$$

$$\cos\theta_i = -\,\vec{n} \cdot \vec{v} \tag{3.3b}$$

$$\cos\theta_t = \sqrt{1 - n_r^2\,(1 - \cos\theta_i{}^2)} \tag{3.3c}$$

$$\vec{v}_t = n_r \vec{v} + \left(n_r \cos\theta_i - \cos\theta_t\right)\vec{n} \tag{3.3d}$$

The Snell-Descartes law defines the refracted angle but as it is stated by the Fresnel equations,

refraction does not occur for the totality of the incident light beam, part of this beam is reflected. The reflected proportion depends on the incident angle and the refractive index of the materials at each side of the interface. It also depends on the polarisation of light but when the simulation does not take polarisation into account, the mean value between orthogonally and parallel polarised light beam is normally used. The Fresnel equations (3.4a) to (3.4c) give the ratio of reflected and refracted light in a beam [Born and Wolf, 1999]. The index of refraction of a material is given by $\tilde{n} = n - i\kappa$. These equations consider only the real part of the reflective index and are valid [Chang et al., 2005] for low absorption cases $\kappa/n \ll 1$. Because a Monte Carlo approach was used and only a single ray is modelled at a time, a random number between 0 and 1 is drawn at every intersection with an interface; if it is greater than the reflected fraction of light R, the photon is refracted, else it is reflected.

$$R_\perp = r_\perp^2 = \left| \frac{n_i \cos\theta_i - n_t \cos\theta_t}{n_i \cos\theta_i + n_t \cos\theta_t} \right|^2 \tag{3.4a}$$

$$R_\parallel = r_\parallel^2 = \left| \frac{n_i \cos\theta_t - n_t \cos\theta_i}{n_i \cos\theta_t + n_t \cos\theta_i} \right|^2 \tag{3.4b}$$

$$R = \frac{R_\perp + R_\parallel}{2} \tag{3.4c}$$

3.2.2 Absorption (Beer Lambert law)

An other central phenomenon that has to be modelled in optics is the absorption of light by the medium. This phenomenon is essential to simulate polymers and glasses that can have non negligible absorption towards the ultraviolet end of the spectrum. When a material is absorbing, the intensity of a light beam diminishes exponentially with the distance in the material as defined by the Beer Lambert law (3.5) [Born and Wolf, 1999].

$$I(x) = I_0 \, e^{-\alpha x}, \qquad \alpha = \frac{4\pi\kappa}{\lambda}. \tag{3.5}$$

where α is the attenuation coefficient and depends on the extinction coefficient κ of the material and the wavelength of light. This law defines the intensity at a given distance inside the material; it can also be considered as the probability distribution function for the penetration depth inside the material. For each photon the method of the inverse function can be used to generate a random penetration depth inside the medium:

$$d = \frac{-ln(1-y)}{\alpha}, \qquad y \in [0,1]. \tag{3.6}$$

Drawing a random penetration depth for each photon and providing their number is large enough, will result in a beam intensity according to the expected law at any depth in the material. This approach was chosen rather than having a discrete space where the photons have a probability to be absorbed at each step of their travel through the material. If the distance to the next intersection (this distance has to be computed in 3D) is larger than the free path d defined using (3.6) and a random number y, the ray is considered absorbed. This approach may seem inappropriate because one might think each ray "gets new chances" after reaching an interface. It does, but this is justified by the fact that reaching the interface can be seen as the realisation of an event with a given probability: the probability of randomly drawing a distance higher than the distance to the interface is equal to the probability of reaching the interface. Because in a Monte Carlo approach probabilities of each event are multiplied to get the probability of a state, this approach is justified.

3.2.3 Optical modelling of thin film interference

The coating of glass with thin metallic or dielectric layers to obtain anti-reflective properties or to create optical filters is common in the glazing industry and in research laboratories. These coatings rely on wavelength dependent constructive and destructive interferences. Because most modern glazing and some complex fenestration system include such thin film coatings, a thin film calculation was included in the model. The Fresnel equations for the calculation of reflectance and transmittance of thin films are derived from Maxwell equations. To simplify the equations, the optical admittance η for parallel (3.7a) and perpendicular (3.7b) polarisation are introduced as well as the phase thickness δ (3.7c) for each layer:

$$\eta_\parallel = \frac{n - i\kappa}{\cos(\theta_i)} \tag{3.7a}$$

$$\eta_\perp = (n - i\kappa)\cos(\theta_i) \tag{3.7b}$$

$$\delta = \frac{2\pi \tilde{n} d \cos(\theta_i)}{\lambda} \tag{3.7c}$$

Following the description of Macleod [Macleod, 2001] a characteristic matrix can be used to compute reflectance, transmittance and absorptance:

$$\begin{pmatrix} B \\ C \end{pmatrix} = \begin{pmatrix} \frac{E_a}{E_m} \\ \frac{H_a}{E_m} \end{pmatrix} = \left\{ \prod_{r=1}^{q} \begin{bmatrix} \cos(\delta_r) & \frac{i\sin(\delta_r)}{\eta_r} \\ i\eta_r \sin(\delta_r) & \cos(\delta_r) \end{bmatrix} \right\} \cdot \begin{pmatrix} 1 \\ \eta_m \end{pmatrix} \tag{3.8}$$

where E is the electric field and H the magnetic field, r the index of the different layers in the stack, a the index of the first layer and m the index for the substrate. δ is the phase thickness and η the optical admittance introduced previously. They can then be used to compute the reflectance R, transmittance T and eventual absorptance A as follows:

$$R = \left(\frac{\eta_0 - \frac{C}{B}}{\eta_0 + \frac{C}{B}}\right) \cdot \left(\frac{\eta_0 - \frac{C}{B}}{\eta_0 + \frac{C}{B}}\right)^* \tag{3.9}$$

where $*$ denotes the complex conjugate and η_0 the optical admittance of the incident medium (with no absorption).

$$T = \frac{I_k}{I_i} = \frac{Re(\eta_m)(1-R)}{Re(BC^*)} \tag{3.10}$$

where m is the exit medium, finaly:

$$A = 1 - R - T \tag{3.11}$$

The optical admittance η has different values for perpendicular and parallel polarised light; all derived values can therefore be computed for both polarisations. The final two values for A, R and T are combined, weighted depending on the polarisation state. In this simulation tool, non polarised light is considered and the mean of both values is used at each interface. If the light beam is polarised, the new polarisation state after the thin films stack must be computed. For accurate calculations and interface modelling, the complex refraction index of the used materials need to be defined with spectral values.

3.2.4 Modelling of the annual sky irradiance distribution

The Meteonorm climate model [Meteonorm, 2012] gives time-distributed values of temperatures as well as global and direct solar irradiance values based on location and measurements from nearby meteorological stations. The Perez model [Perez et al., 1993] was implemented using to provide radiance values for each direction of the sky vault at a given time depending on the horizontal global and direct solar irradiances. With this model, hourly radiance values for a discretisation of the hemisphere can be computed depending on the location, orientation of the window and its eventual tilt angle. The luminance values can be derived from the radiance values using the luminous efficacy from this same model. The hemisphere centred around the normal to the considered surface is discretised by subdividing it into patches. This may be done following the Tregenza [Tregenza, 1987] or Klems [Klems, 1993, Klems, 1994] sky subdivision. For the study of strongly angular dependent effects, patches may in turn be split in 4, 16 or 64 [Bourgeois et al., 2008]. This is mainly useful to increase the resolution of the direct contribution when a single representation is used for direct and diffuse irradiances.

A subdivision with regular angular intervals may also be used; however, the solid angles of the different patches then vary strongly and the resolution is uneven. To keep data concise, the Klems subdivision is generally the preferable approach for CFSs. It is better suited than the Tregenza subdivision because the number of patches is greater close to the normal and reduced towards grazing angles. Indeed, a contribution from grazing incidence is often less important because of higher reflectance. For structured surfaces, however, this is not the case and it might be preferable to use a Tregenza subdivision, prioritising equal distribution of solid angles for all patches. Both distributions were implemented for the diffuse contribution of the sky vault. The ground contributes by reflecting the radiation from the sky in an isotropic way and with a certain reflectance, also referred to as the albedo. The albedo is typically between 0.15 and 0.4 but can reach higher values for snow or water. To take into account the direct part, the sun position is used to determine the radiance impinging the window depending on the angle the sun makes with the normal. The position is calculated using the solar equations for elevation and azimuth. They directly depend on the time of the day and the latitude of the considered location. The Perez model can be used to derive the direct illuminance from the sun irradiance using the direct luminous efficacy. These somewhat longer calculations of the times series of direct and diffuse daylight are carried out once only and stored in a file for future use. This model and the details of its implementation are further described in Annexe A.

3.3   Analysis of angular behaviour

To find a suitable design reaching a complex set of objectives (daylighting, glare protection, seasonal thermal control and transparency) performance indicators had to be established. Through the study of existing solutions it appeared that two angular dependent behaviours are always observed in devices achieving one or several of these objectives. The first is the transmittance depending on the incoming angle; the second is the redirection of light rays and a particular angular distribution of the transmitted radiation. In addition, when using a discretised hemisphere, the map from incoming zone to transmission distribution over outgoing zones can be synthesised in a matrix representation. These representations are presented and commented in this section.

3.3.1   Transmittance depending on incoming elevation

In order to design structures with a changing seasonal transmittance relying on the different solar elevation, it is straightforward to look at the transmittance depending on the incoming elevation angle. Additionally, to get an estimate of the daylighting performances, the latter transmittance can be subdivided depending on the outgoing elevation angle. Light rays reaching a window from the top half of the hemisphere are normally transmitted in the bottom half of the hemisphere on the inner side of the window (hereafter T_{down}). For the same situation, CFSs may redirect light towards the upper half of this hemisphere (hereafter T_{up}). T_{up} obviously is contributing to daylighting in the depth of the room more significantly than
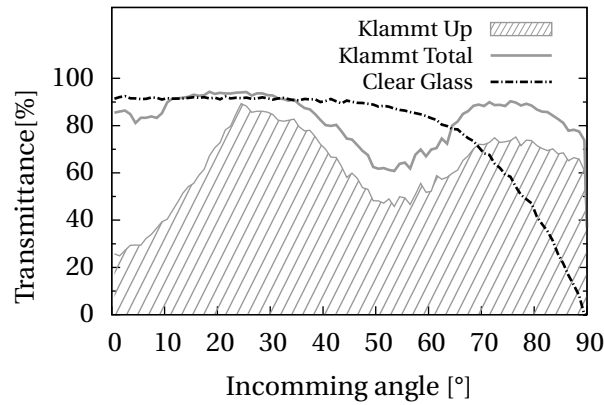
Figure 3.5 – Simulated transmittance depending on the incoming angle for a daylighting system proposed by Klammt *et al.* [Klammt et al., 2012]. The solid line represents total transmittance and the patterned area represents the fraction of transmittance that is transmitted upwards and will thereby contribute more significantly to daylighting. The transmittance of a clear glass is shown for reference.

T_{down}. For the analysis of CFSs with both seasonal thermal and daylighting control, T_{down} and T_{up} as well as the total transmittance (T_{tot}) are computed depending on θ_{in}. The outgoing azimuth is discarded in the output but the transmittance can be computed for any incoming azimuth range. By default it is given for an isotropic elevation distribution and an incoming azimuth of 0° but can also be computed for a distribution corresponding to a International Commission on illumination (CIE) standard overcast sky. The performance of a state of the art microstructure proposed by Klammt *et al.* [Klammt et al., 2012] is illustrated in Figure 3.5. The latter microstructure is very efficient at redirecting light from all angles and redirects about 75% of the transmitted light beam; but it is translucent and not transparent. This representation is particularly useful when modifying design parameters or when considering new geometries. The curves can be compared within the graphical interface and the effect of each parameter can be directly observed.

3.3.2 Polar transmission distribution

In Section 3.3.1 the transmittance was considered regarding the incoming light ray elevation mainly for the study of seasonal thermal control. This gave an idea of the daylighting performance from a qualitative point of view (by comparing T_{tot}, T_{up} and T_{down}). For a more quantitative study of daylighting performances the software plots the distribution of transmitted light rays in polar plots. The representation can be given for single incoming ray angles but for a more realistic study, the transmission distribution is computed for a standard overcast sky distribution, as described by the CIE. The ground contribution is defined as a reflection of the total sky irradiance with a user specified *albedo* as multiplying factor. This reflection is Lambertian and the radiance of the ground is therefore constant in all direction. The *albedo* was set to 0.2 in the selected examples. The incoming distribution of light coming
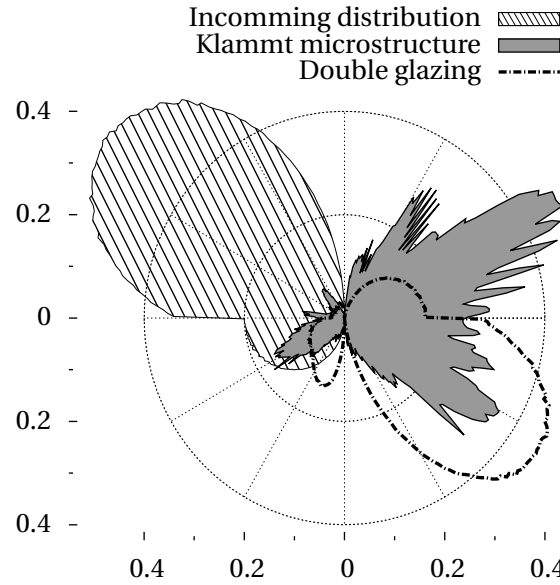
Figure 3.6 – Polar transmission distribution of the daylighting system developed by Klammt *et al.* under a standard CIE overcast sky. The transmission distribution of a clear glass is shown for reference. All units are in percent per bin of 1°.

from the ground does not appear constant in the polar plot because it has to be weighted by the cosine of the angle with the normal: identical radiance does not produce the same irradiance on the surface depending on the direction because the visible surface per solid angle is much greater for larger angles of incidence. Additionally, the solid angle of the ground area is much greater for low elevation angles than for high elevation angles, this makes an other cosine factor come into play. The performances of the structure developed by Klammt *et al.* are shown in Figure 3.6.

3.3.3 Spectral transmittance

A more quantitative evaluation of radiometric transmittance implies to consider the spectral transmittance (T_{tot}, T_{up} and T_{down}), reflectance and absorptance. They may also be studied depending on the incoming angle of light rays. This information can be useful if a structured surface is combined with a thin film coating showing specific spectral properties. In such a case, the ratio between photometric and radiometric transmittance may differ depending on the incoming or outgoing angle of the light beam.

3.3.4 Bidirectional transmission distribution function (BTDF)

For a quantitative study of seasonal thermal and daylighting control, the performances should be studied regarding specific moments and seasons and also be weather dependent. At each time of the day, day of the year and depending on the weather, the sky radiance and luminance

distribution changes and offer a completely different distribution of solar radiation; this has to be taken into account in the design of a complex fenestration system. It is inefficient to compute the transmission distribution for each possible type of sky; this would results in long simulations and large datasets. For this reason, the transmission distribution function is computed once and can then be multiplied by the incoming radiance distribution for the considered location to get the transmitted distribution for a particular type of sky at a given moment. To obtain a high accuracy with reasonable central processing unit (CPU) time, the problem is separated in diffuse and direct components. This separation is made for the BTDF, for the sky distribution and for the matrix computations described later. This way, the sometimes sharp features of both the CFS and the sky are considered when they matter most (direct component) and later combined with the more general features of the diffuse component. Such an approach was recently introduced for dynamic daylight analysis [McNeil, 2013]; the presented methods were inspired by this approach. They were adapted to be applied also to solar gains, to reduce the number of multiplication steps by separating direct and diffuse solar radiation from the start on, and to decrease matrix size by removing zero values.
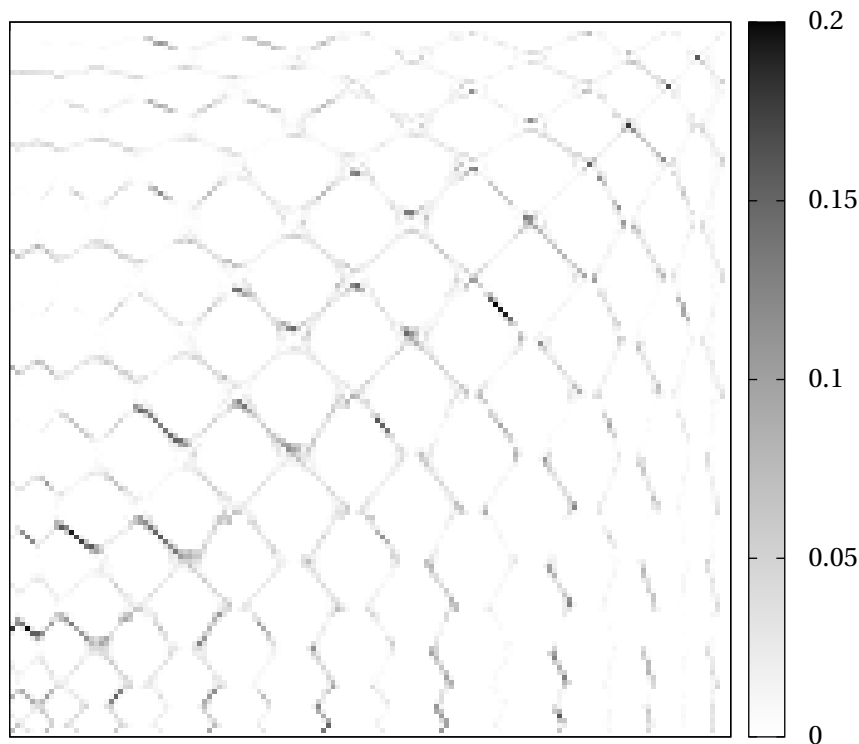
Figure 3.7 – Matrix representation of transmission distribution. The incoming zone is given in rows and outgoing zone in columns.

To reach this objective, a flexible representation was implemented to store different BTDFs format, including Tregenza and Klems. It allows to produce a series of transmission distribution functions (TDFs) at hourly time steps for the direct contribution, using a chosen division

of the hemisphere on the interior of the window and a given time interval to compute the distribution for the corresponding solar positions (usually one hour or less). A BTDF matrix for the distribution of direct radiation over patches of the hemisphere, at each time of the year (and corresponding sun position) is hereby obtained. Likewise, for the diffuse contribution, a TDFs for each incoming zone is computed using a given division of choice for the whole hemisphere. A BTDF matrix linking the zones on the interior and exterior sides of the CFS is hereby obtained (see example in Figure 3.7). This implementation permits to create other representations such as the one used in the Illuminating Engineering Society (IES) standard. An extensible markup language (XML) file following the Window 6 standard [LBNL, 2008] can also be created. These files are compatible with Radiance and can be used to render scenes and perform dynamic daylight analysis of spaces. The tensor tree representation proposed by the authors of Radiance [Ward et al., 2012] was also considered but not implemented yet.

The computed BTDF for diffuse radiation may be visualised as a matrix as shown in Figure 3.7 but this representation is not easy to interpret. Alternately, it can be read using the BSDF Visualiser from the Lawrence Berkeley National Laboratory (LBNL). This tool provides an interactive visualisation where the incoming patch can be selected to display the transmittance / reflectance distribution over outgoing patches. An example of such a visualisation is given in Figure 3.8.
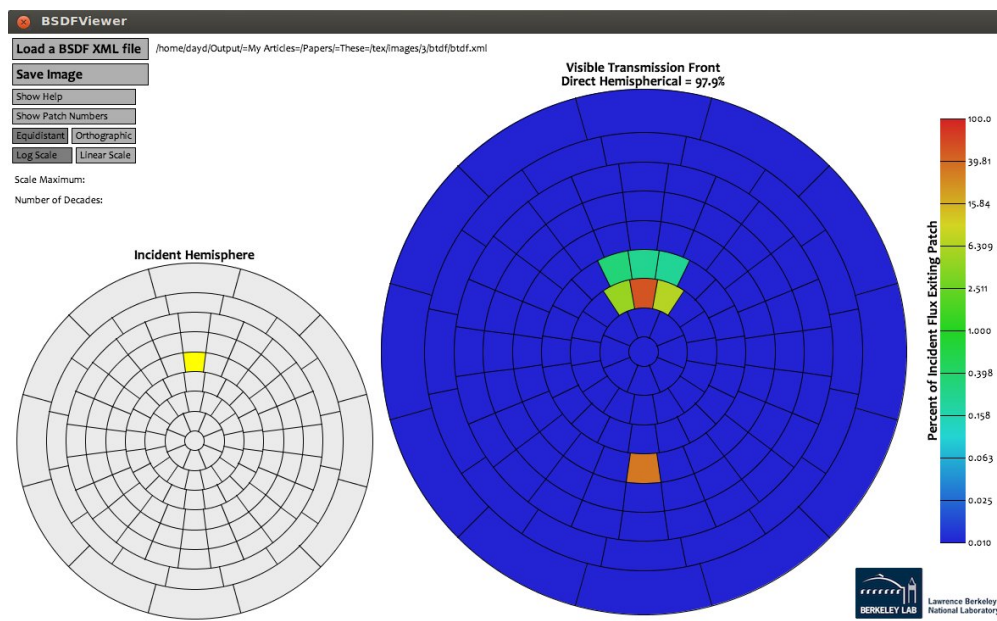
Figure 3.8 – LBNL Visualiser for BSDF, an incoming zone can be selected (in yellow in the left hand side hemisphere), the transmittance distribution for this zone is given along with a colour map and quantitative transmittance for each outgoing patch. If reflection information is available, the reflectance can also be visualised.

As described in the next section, the calculation of separate BTDFs for direct and diffuse components can be used for an accurate computation of the solar gains. These BTDFs can

also be employed to compute hourly illuminance maps, create daylight rendering in office spaces and to study glare risks.

3.4 Advanced daylighting and thermal modelling

Designing or selecting a CFS is an intricate task that depends on many factors. The location, orientation, climatic conditions, usage of the building are important factors. The energy savings and user comfort should also be considered. Some objectives can seem contradictory: in winter solar gains should be large to reduce heating loads but they should be mitigated in summer to avoid overheating and cooling loads. Daylight provisions should be high to increase the visual comfort and the quality of lighting while reducing electricity demand. But on the other hand glare should be avoided by all means. These design objectives are coupled with energy related considerations. Current policies target energy savings; the residential and office spaces are large consumers for heating, cooling and lighting. Maximising the passive solar gains can reduce the energy consumption. In particular the choice of the most appropriate fenestration system and its appropriate sizing for a particular situation can make a difference, but this task can be delicate. CFSPro was developed to assist this process and to design new CFSs. The performance indicators for thermal and daylighting performances enable the optimisation, scaling of such CFSs. For thermal performances, heating and cooling loads are considered whereas for daylighting, metrics such as the daylight factor (DF) and others such as the daylight autonomy (DA) and useful daylight illuminance (UDI) are computed. Glare risk can also be assessed using the unified glare rating (UGR), daylight glare probability (DGP), visual comfort probability (VCP), daylight glare index (DGI) or CIE glare index (CGI). These indicators were described by Wienold who developed the DGP specially for rating glare caused by windows whereas the others are better suited for point source glare [Wienold, 2009, pp. 56-67].

The BTDFs computed as described earlier are used to compute thermal performance, daylight performance and glare risk indicators. Firstly, they are used in combination with Radiance simulations to render scenes and quantify task illuminance in an office space. Secondly, they are combined with irradiance distribution of the sky vault to provide an estimation of the hourly solar gains. The later can be fed to a nodal thermal model to derive the temperature evolution or the corresponding heating and cooling loads. To make the computations fast, a matrix approach is used whenever possible. It has to be reminded that some of these computations are done for a selected location, using the annual radiance distribution obtained with the Perez model as described previously. These aspects are descibed in more detail in the following sections.

3.4.1 Reference room

The reference room described in [Reinhart, 2014a] and [Reinhart et al., 2013] was used to assess these thermal and daylighting performances. The room was designed for the evaluation

of dynamic façade and lighting technologies; it was made deep (8.2 m) and is available for download from the LBNL website [Reinhart, 2014b]. The room has a height of 2.8 m and a width of 3.6 m, by default the window covers just below 40% of the façade area. The photometric properties of this reference office as they are found in [Reinhart, 2014a] are listed in Table 3.1; this seems tailored for this study. For thermal properties, the U-values were set to 0.365 W/m^2K for walls and 1.6 W/m^2K for windows. For the study of sun shading, a solar control glazing with a radiometric transmittance at normal incidence of 0.5 was used.

Window	Double glazing without low-e coating
Interior walls	Lambertian diffuser with 50% reflectance
Ceiling	Lambertian diffuser with 80% reflectance
Floor	Lambertian diffuser with 20% reflectance

Table 3.1 – Optical properties of the reference room

3.4.2 Radiance rendering and glare rating

Glare risks and workplane illuminance on the work plane are the critical values for the evaluation of daylighting performances. Glare can be evaluated using the UGR or the DGI. The illuminance is measured in *lux* and should be in the range of 300 to 10,000 *lux* depending on the task. For common office work, values between 300 and 500 *lux* are required. To assess these values for a complex fenestration system, it should be placed in a given context such as an office and a lighting simulation performed. Recent development in Radiance added the capability of accurately simulating CFSs using BSDF [Ward et al., 2011]. To avoid large datasets, the hemisphere is divided into zones and the scattering distribution can be given from one zone to an other in the form of a matrix. Typically, Tregenza or Klems subdivisions are applied; as defined earlier, such BSDF matrices can be generated with CFSPro. This data can be transformed into a Radiance compatible XML file (in the Window 6 format) that can in turn be loaded in Radiance. Only recently the possibility to simply define a new material with such complicated transmittance and reflectance distributions was added in Radiance by means of the new *bsdf* material type. This material can then be used to describe a glazing within a Radiance scene.

Once properly set up, the scene can be rendered using Radiance to obtain images such as the one given in Figure 3.9a. It shows a rendering of a room with microstructured fenestration systems. This rendering was first carried out separately using Geronimo, a graphical interface for Radiance developed at the LESO-PB to study complex fenestration systems [Kämpf and Scartezzini, 2011]. It has then been integrated in the interface of CFSPro and the required BTDF is directly generated in the appropriate XML format. The BTDF description of the CFS can be used for any window in any scene. As in Geronimo, the scene can be selected from a list of predefined environments. Further more, the parameters can be modified for the rendering of individual images. Hourly images over the course of a day can also be generated

(a) Radiance rendering of a scene with microstrucutred glazing under a clear sky on the summer solstice at noon. It was rendered using the *bsdf* primitive with the computed BTDF.

(b) False colour illuminance map obtained with the *-i* flag in the *rpict* Radiance command and post-processing to obtain the colour scale and convert to false colours.

(c) Glare as indicated by the *evalglare* post processing of the Radiance rendering for a scene with microstructured glazing shown in Figure 3.9a.

Figure 3.9 – Radiance analysis of a space with plain glazing covering 60% of façade area on summer solstice at 1pm local time.

and played as a movie. Rendered images are saved and the rendering parameters of each image is stored within the exchangeable image file format (EXIF) data for each generated image. For a more quantitative representation of a scene illumination, the renderings can be visualised with false colours indicating the illuminance values (Figure 3.9b) for the different surfaces. For glare analysis, the rendered image can be passed to the *evalglare* software to compute DGP, UGR and other glare metrics. As shown in Figure 3.9c, a false colour image is also given to provide information about glaring sources.

3.4.3 Daylight factor

The daylight factor (DF) is one of the earliest metrics to assess the capability of a designed space to provide daylight to the occupant. The DF at a given point is the ratio between the interior illuminance and the exterior horizontal illuminance. It must be computed under a standard CIE overcast sky for several locations within a room. Points at equal depths are then averaged to provide a DF profile along the depth of the room. Figure 3.10a shows the DF in the reference room for a clear double glazing compared to a daylight redirecting structure (laser cut panel).

3.4.4 Dynamic daylight metrics

To study daylighting performances of CFSs with more accuracy and to take into account location and orientation, two dynamic performance indicators were implemented: daylight autonomy (DA) and useful daylight illuminance (UDI). The DA is the relative fraction of annual office hours during which a defined daylight illuminance is reached at a given point, it was
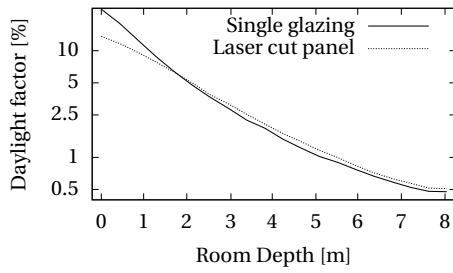
(a) Daylight factor compared between single glazed window and laser cut panel.
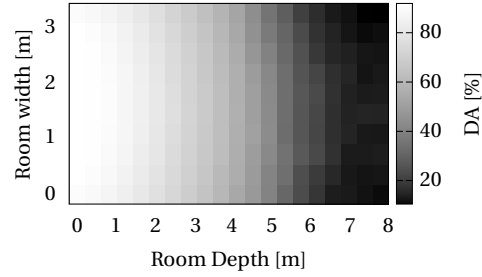
(b) Daylighting autonomy (300 lux) in a room with double glazing window for an occupation between 8am and 5pm

Figure 3.10 – Daylight indicators as simulated in the developed software. The daylight factor provides a good indicator for diffuse radiation whereas the daylight autonomy gives a location dependent characterisation of daylight performance.

first suggested by the "Association Suisse des Electriciens" in 1989 and later refined by others [Michel, 1999, Reinhart et al., 2006] to provide a dynamic, location and weather dependent evaluation of daylighting performance. Typically the 300 lux minimum task illuminance is often used to determine the DA. Areas within a space with a $DA_{300\,lux}$ value of 50% and more can be considered well daylit [Reinhart, 2014a]. The UDI is the relative fraction of time during occupancy hours where the task illuminance is within a certain range, typically between 150 lux and 2000 lux [Michel, 1999, Nabil and Mardaljevic, 2006]. Creating DA and UDI maps requires determining the illuminance maps at each time step: they can be obtained by a matrix multiplication method. As introduced in 3.3.4, this method is applied separately for the diffuse and the direct components. Both are computed considering their specificities and the results added afterwards. Hence the illuminance values for a virtual array of sensors are obtained by the following multiplication of V, D and T matrices:

$$E_v = V(T_d \cdot L_{v,d} + T_b \cdot L_{v,b}) \tag{3.12}$$

The $L_{v,d}$ and $L_{v,b}$ matrices specify the hourly (or other time step) values of luminance on the window from each direction of a given BTDF representation for the diffuse component and from the corresponding sun position for the direct component. The two T matrices give the transmission distributions from each incoming sky patch respectively sun position to the outgoing patches. The V matrix is the view matrix: it gives the contribution coefficient by each outgoing direction of the window to each virtual sensor in the plane of interest. The V matrix is computed with Radiance and needs to be recalculated only when the room or number of sensors is modified. The E_v luminance matrices depend on the orientation and location of the scene; the T matrices need to be updated each time the complex fenestration system is modified.

An example of DA map is given for a double glazing in Figure 3.10b. This result is for a south oriented office located in Lausanne, Switzerland.

3.4.5 Annual energy transmittance

To assess seasonal thermal control, the dynamics of solar gains were examined: they should be maximised in winter and minimised in summer. For each square meter of window, a portion of the incoming radiation is transmitted and heats up the space behind the window. To estimate this value, diffuse and direct transmittance factors are calculated separately with the ray tracing simulation tool as defined previously. They will be used in combination with radiometric data derived from the Perez model introduced previously, based on climatic data from the Meteonorm model. To combine these data, the representation of space and time has to be used consistently. The following operation can then be used:

$$Q_t = \sum_{k=1}^{k=p_s} \left(L_{ed,k,t} \cdot v_{d,k} \right) + E_{eb,t} \cdot \tau_{b,t} \tag{3.13}$$

where k is the sky patch index, p_s patches cover the hemisphere centred around the normal to the glazing. $L_{ed,k,t}$ is the diffuse radiance for the given patch and $E_{eb,t}$ the solar irradiance for this time step t. $v_{d,k}$ is the transmittance coefficient of the CFS for the set of incoming directions corresponding to the kth patch (including the solid angle for conversion to resulting irradiance) and $\tau_{b,t}$ is the energy transmittance for the direction corresponding to the sun position at this time step. All values are time dependent except $v_{d,k}$ which is constant for each patch of a given CFS. This calculus discards the radiative heat gains from the window due to heat absorption in the window.

3.4.6 Thermal modelling

Because thermal gains do not have identical effects on all types of builds, and in particular might have a strong effect in modern well insulated buildings [Enshen, 2005], a simple thermal model for an office with a façade and CFS was needed. This additionally gives an estimate of the thermal loads associated with a given CFS, the influence of design parameters and the potential energy savings. The ray tracing simulation tool was therefore extended with the functionality to compute the hourly temperature in a simple room using a resistance-capacitance thermal model and the Crank-Nicolson method. This method was based on the work of Daum [Daum, 2011] who developed a thermal model with low computational cost for the study of dynamic blind control. This model itself was based on previous work of Nielsen [Nielsen, 2005] and Kämpf [Kämpf and Robinson, 2007]. Such simplified thermal models consider the heat capacity of different elements as well as the thermal resistance among them, to determine the temperature at different nodes depending on the values at

the previous time step and eventual external excitations. They are widely accepted and give satisfying results for comparative studies. This computation is based on the hourly solar gains computed separately for diffuse and direct solar radiation as described above. If only fixed ventilation due to infiltration is considered, this model gives very fast results because the resistance and capacitance in the system do not vary over time. The evolution only depends on the temperatures and stimulations at each time step (heating, cooling, outdoor temperature and solar gains). Therefore for n temperature nodes, two square $n \times n$ matrices A and B can be defined containing the parameters of the model. They can be generated in a pre-process and applied to compute the temperature at each node for the next time step depending on the applied heating, cooling, thermal gains and exterior temperature (contained in a vector U of size n):

$$\vec{T}(t_0 + \Delta t) = A\vec{T}(t_0) + B\vec{U}\left(t_0 + \frac{1}{2}\Delta t\right) \tag{3.14}$$

The implementation of this nodal model was validated by comparing the simulation results with those given by an existing Matlab script for the same thermal model. More details about this thermal model and its implementation are given in Annexe B. An example of such thermal simulations for different types of glazing is given in Figure 3.11, the impact of solar energy transmittance on the thermal loads is very important: in this case reducing the solar gains strongly reduces the cooling loads during summer. The heating loads on the other hand are increased but the overall loads are still lower, for a solar transmittances at normal incidence below 0.35, the heating loads become too high and the overall loads start increasing again. This is valid for this particular window size, U-value, building type and with equal efficiency of cooling and heating; changing these parameters can greatly influence the outcome of the simulation.

(a) Temperature evolution with no cooling or heating.

(b) Corresponding thermal loads with a heating and cooling COP = 3.
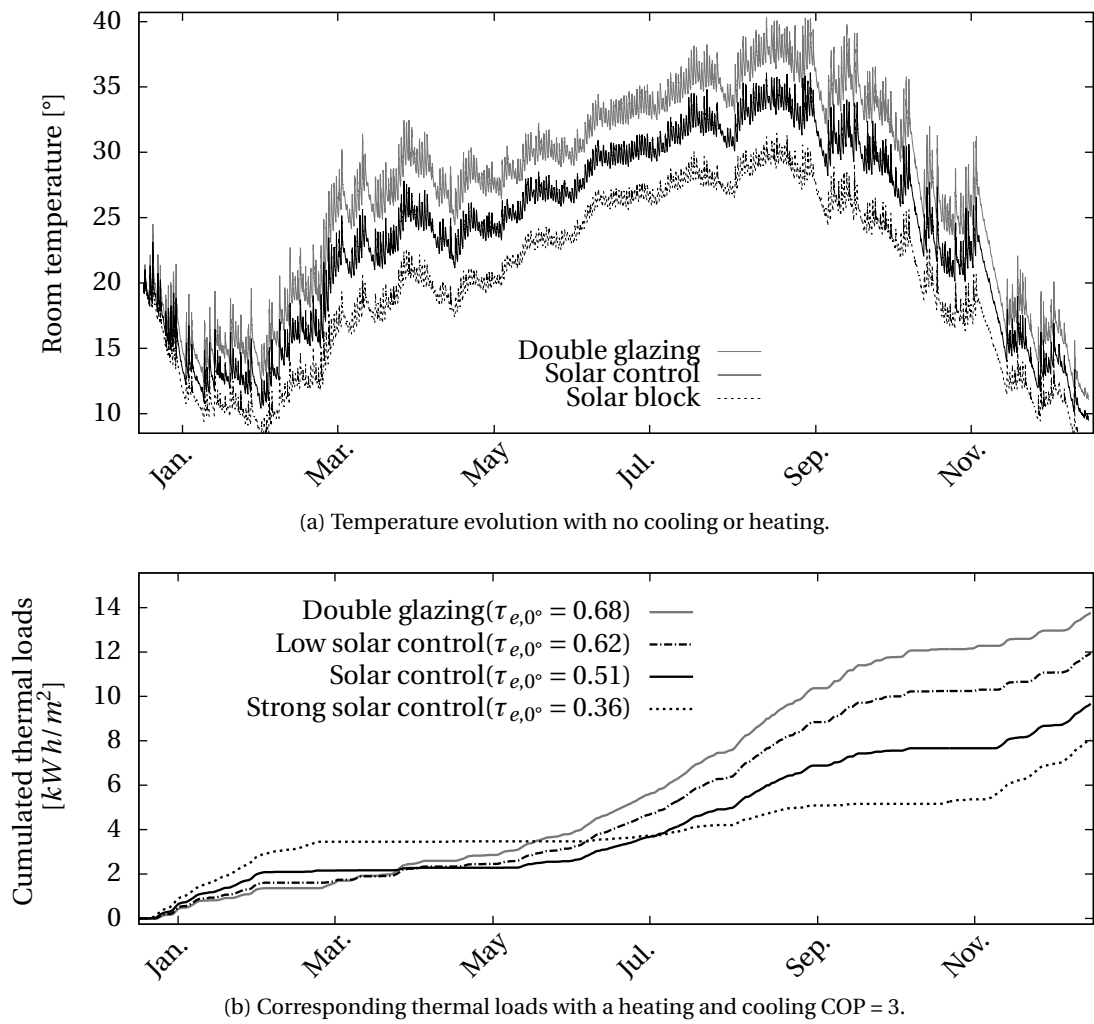
Figure 3.11 – Thermal simulations in the reference office for double glazed windows with different solar transmittances at normal incidence.

4 Experimental Methods and Tools

In this chapter the methods and tools that were investigated and realised for the fabrication of samples according to the simulated designs presented later are introduced. Firstly the sequence of fabrication steps will be briefly introduced. After this overview, the various methods and tools for each step will be discussed in more detail.

4.1   Fabrication of embedded mirrors

The designs proposed in the scope of this work are based on embedded micromirrors: their fabrication requires multiple steps. The number of steps increases if a second optical component needs to be included. The principles and advantages of such a complex optical device will be introduced in Chapter 6. As illustrated in Figure 4.1, five to seven steps are required to fabricate embedded mirrors. They can be grouped into six processes:

1. The substrate needs to be thoroughly cleaned and prepared, as detailed in Section 4.2.

2. If needed, periodical reflective stripes are realised by lift-off lithography: this technique is explained in Section 4.3.

3. The desired shape for the embedded mirror has to be carried-out on a support which is used as a stamper for replication into a transparent medium. If it can not be directly obtained in such a material, it may be duplicated in polydimethylsiloxane (PDMS) from a mould made of virtually any material. Multiple approaches and their propitiousness for this step are discussed in Section 4.4.

4. The structure then needs to be replicated onto the substrate. This is done by ultraviolet nanoimprint lithography (UVNIL), as defined in Section 4.5.

5. The selected facets of this structure then have to be coated with a reflective material, as described in Section 4.6

6. Finally the mirrors have to be embedded: the specificities of this in appearance rather simple step are enunciated in Section 4.7

45
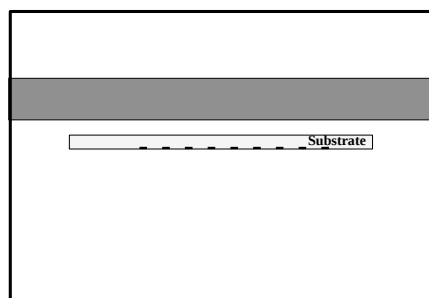
(a) Clean and prepare substrate
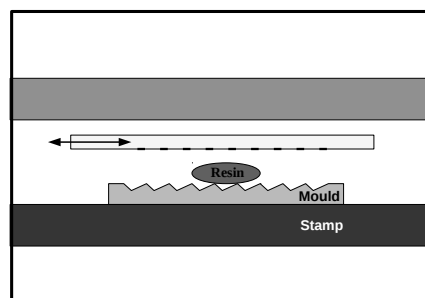
(b) Align the stripes with structures if required
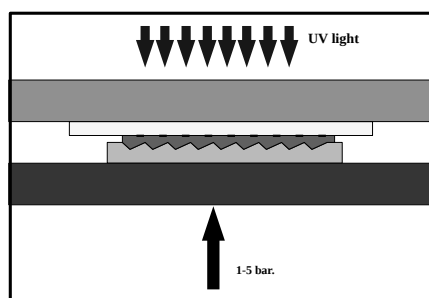
(c) Replicat microstructure into resin by UVNIL
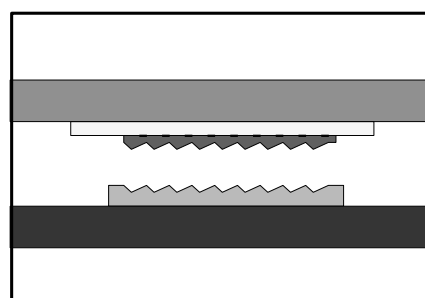
(d) Unmould the structure
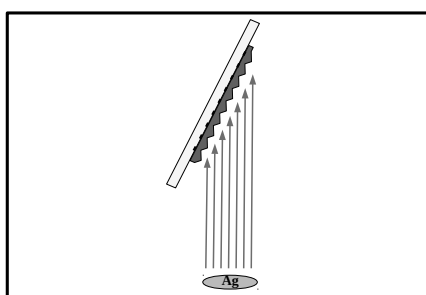
(e) Reflectively coat selected facets
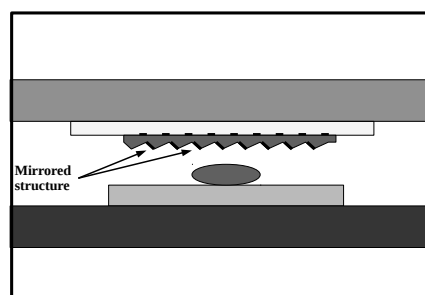
(f) Use same resin as in 4.1c
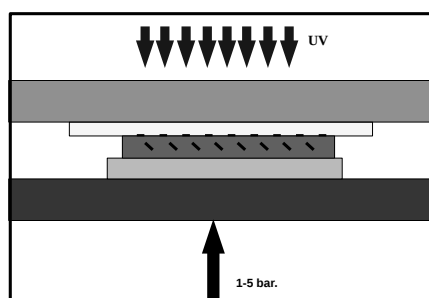
(g) Embed the mirrors using the same resin
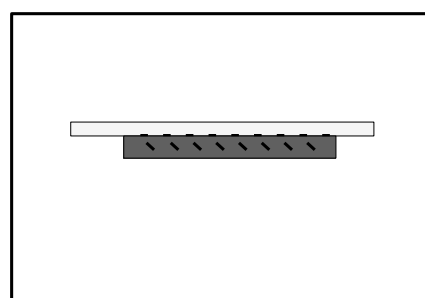
(h) Finally embedded mirrors

Figure 4.1 – Schematic of the fabrication process for embedded micromirrors.

4.2 Sample preparation

To produce repeatable results, a constant and clean starting point is essential. This is the main purpose of a well defined cleaning procedure. For thin films coating, a clean substrate also improves adhesion of the first layer and removes impurities such as dust that may create defect in the film, especially when depositing thin films of a thickness below that of a dust particle. The used cleaning process is as follows:

- In order to remove the most severe stains, the substrate is mechanically wiped with a soft cloth soaked with ethanol.

- The substrate is then placed in an ultrasound bath of ethanol for 20 minutes.

- The substrates are cleaned in an industrial washing machine using laboratory grade washing powder for glassware.

4.3 Lift-off lithography

Lift-off lithography is a common process in microfabrication to deposit a material only on selected areas of a substrate. It can be done by etching away the coating in unwanted areas or by depositing the coating only in the selected areas. In both cases a patterned sacrificial layer is required, either to protect or to remove the coating. This layer is generally a resin patterned by lithography. The steps of photo lithography and lift-off lithography will be introduced along with the different tools that were used in this thesis to obtain striped mirrors.

4.3.1 Photo lithography

For the fabrication of microstructures, photo lithography is a common process. A photo-sensible material can be patterned with a shape by exposing it to a certain light dose. Such light sensitive materials are called photoresist (PR), they can then be developed and only the exposed areas will remain (or the non exposed areas in case a negative resist is used). Photo lithography is generally done with a mask; it is possible to reproduce patterns down to tens of nanometres. Using a photo resist patterned by photolithography as a template, the surface of many materials can be modified in selected areas. The PR may be used as protective mask on the substrate that can then be etched chemically or physically. It may also be used as a mask for the deposition of material on selected areas of the substrate. The former process may also be used to structure a material in depth; this usage of lithography will be discussed in 4.4.2. In both cases, the six steps of a photo-lithographic process are:

1. **Clean** and prepare the substrate. The surface needs to be clean, dry and prone to good adhesion with the chosen resist. A heating step is required to dehydrate the substrate.

2. **Deposit** a thin layer of photoresist on the substrate, this is mostly done by spin coating.

3. **Bake** the PR to evaporate remaining solvents, improve adhesion and release from the internal stress due to spinning.

4. **Expose** the PR to some source of radiation (adapted to the type of PR) with a mask to protect parts of the resist from the latter. Generally a UV lamp with constant intensity is used and exposure time is varied.

5. **Develop** the PR to remove exposed (positive) or unexposed (negative) photoresist. The developer depends on the chemistry, it is an alkali for most positive resists.

6. **Rinse** abundantly to stop the reaction between developer and PR.

7. **Inspect** the result and check if the obtained pattern is conform to the mask. Optically, one might check if the contrast is sufficiently high between regions were the resist was removed and region were it remained. The quality of the edges is also important.

This process is typical repeated by varying the bake temperature, exposure dose and development time until an optimal solution is found for each pattern. Some further insight on the materials and apparatus used for the different steps are introduced in the following subsections.

4.3.2 Mask fabrication
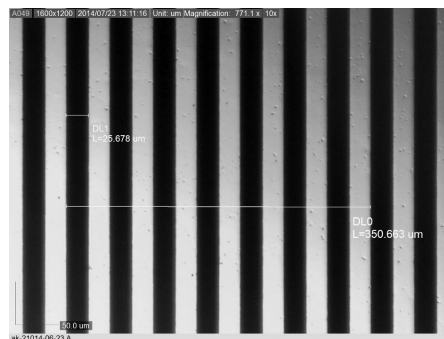
Figure 4.2 – Micrograph of a mask for lithography with alternating stripes of $25\,\mu m$ every $50\,\mu m$ obtained by photoplotting.

In the MEMS and CMOS industry, laser writing of chromium in a clean room environment is the most common process for the production of a mask. The resolution required in this project is however not as high and other, coarser methods can be considered. After failed tests using laser cutting of thin metallic sheets, photoplotting was selected for the fabrication of masks. The mask is printed onto a transparent plastic sheet with a laser photoplotter. This technique is often used for the production of masks required in the fabrication of electronic circuitry. The used plotter is a FIRST EIE RP-212 NT available on campus at the STI workshop. The spot size of this plotter is $8.5\,\mu m$; maximal resolution is $12,000$ dots per inch (dpi). The limiting factor on this printer is the minimum feature size of $25\,\mu m$, a mask with such stripe

width is illustrated in Figure 4.2. This was sufficient in most cases for this work, however masks with smaller lines were produced by Selba SA using a plotter with a resolution $of\,50,800\,dpi$, spot size of $2\,\mu m$ and minimal feature size of $4\,\mu m$.

4.3.3 Resin coating

The photoresist is coated on the substrate using a WS-650Mz-23NPP spin coater from Laurell Technologies corporation. Spin coating is a technique used to apply uniform thin film coatings. The substrate is maintained by vacuum on a holder designed specifically for microscope slides (27x76mm). The spin coater can then be programmed to rotate at speeds up to 12'000 rpm for a given time. The coating material is either applied before rotation (static dispense) or at low rotation speed (dynamic dispense) and the substrate is then spun at maximum speed for a defined duration. The centrifugal force uniformly spreads the material on the substrate and forces any excess material off the edges. By changing the rotation speed and the viscosity of the material, the thickness of deposited films can be controlled precisely. The obtained thickness is typically between few hundred nanometres and several microns for photoresists. In this project the S1818, a positive PR from DOW Chemical was used.

4.3.4 Baking

Before exposition, the resist needs to be baked to evaporate remaining solvent, improve adhesion and free from the internal stress due to spinning. The samples are baked on Ika laboratory hot plates; the temperature is controlled with the built in thermostat or an external thermostat applied directly to the hot surface. Too high temperatures can trigger chemical reaction and weaken positive resist all together. Other, non photochemical resists need to be heated at high temperatures for curing.

4.3.5 Exposition

As mentioned earlier, the PR needs to be exposed to UV light in order to reproduce the master geometry. To obtain optimal results, substrate and mask are put in contact for optimal shading of the unexposed resist. The contact method reduces any source diffraction and produces the optimal achievable resolution. The chemical properties of exposed parts will change depending on the type of used PR. In positive resists, photochemical reaction weaken the resist and brake chains, the exposed part will become more soluble in the developer and be removed in the next step. In negative resists, photochemical reaction harden the resist, cross-linking occurs and the exposed part will be insoluble in the developer. The right dose of exposure has to be found in order not to overexpose, nor underexpose the PR. A custom source shown in Figure 4.7a and described in detail in 4.5.3 was built. The main reason to fabricate such a custom made device was to obtain a UV source that has a low thickness and can easily be moved and oriented. This makes it usable in the imprinting step described later

(4.5) where the source needs to be placed in the limited space available below the stage of an optical microscope to polymerise a UV curable resin after alignment.

4.3.6   Development

The S1818 PR can be developed with the generic mr-Dev300 provided by Micro Resist Technology GmbH. The development time needs to be refined since even unexposed resist are slowly dissolved by the developer. It has to be mentioned that the efficiency of the developer is reduced when exposed to ambient air from which it absorbs carbon. The development times also increase when the bath is polluted with dissolved resists, certain resists affecting the developer efficiency more than others. After suited development time, the substrate has to be thoroughly rinsed to stop the reaction. This is done with a bath of distilled water followed by a second rinsing pouring distilled water onto the sample.

4.3.7   Lift-off

To create ribbons of reflective aluminium or silver, they are two types of processes. One where the desired coating is applied first and a PR is used to protect selected areas of the coating in an etching step. In an other approach, the coating is applied on top of the patterned resist and when the resist is dissolved, part of the coating is also removed. The latter approach was selected because no etching device was available in the laboratory. Using this approach, to increase the quality of this lift-off, two resists are used in combination as illustrated in Figure 4.3. The different chemistry implied enable to create an overhanging structure and distinctively separate the coating on the substrate from the coating on the resin stack. The first layer is a resist (LOR5A from MicroChem) that has to be baked at higher temperature and that is not a PR. The second layer is a common PR, the S1818 introduced previously. The exposed area of the top layer reacts strongly during development and the resist is removed very fast. Selected areas of the bottom layer are now in contact with the developer and slowly dissolved in an isotropic way. This isotropic etching creates an under etching as illustrated in step 4 of Figure 4.3. Care has to be taken that the dissolution rate of the underlying resist is faster than that of the protective, unexposed photo resist. To reach this objective the baking temperatures need to be fine tuned and the thickness of the lift-off layer needs to be lower than that of the PR layer. With a overhanging top layer, the dissolution of the resist layers is easier and the removal of the unwanted coating cleaner.

4.4   Mould fabrication

The required dimensions for the designed microstructures (50-300 microns for period and respectively 112-700 microns depth) are well above the nano scale and at the lower limit of micro scale. Few techniques are suited to produce structures in this range; an aspect ratio above one is typically difficult to obtain with those techniques. The importance of this

1. Coat and Soft-bake PMGI or LOR.   2. Coat and Soft-bake Imaging Resist.   3. Expose Imaging Resist.

4. Develop resist and PMGI/LOR.   5. Deposit film.   6. Lift-off Bi-layer stack and residual deposition.
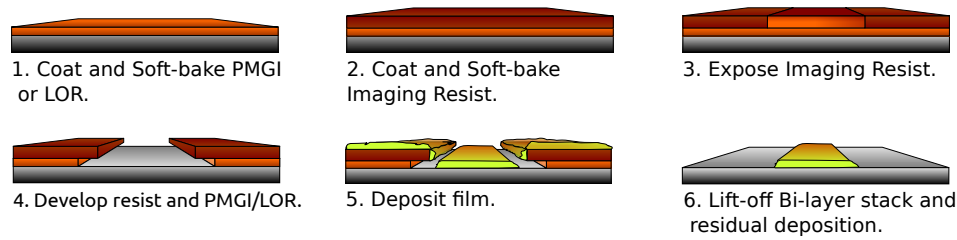
Figure 4.3 – Principle of lift-off lithography as illustrated in the manual provided by MicroChem.

limitation is emphasised when the functional surface only represents a fraction of the period. In addition, the produced surfaces need to be of optical quality. Given these challenging objectives, the high level of expertise required for the production of structures with such scale and properties, and the limited time available for this thesis, partnership solutions have been preferred:

- Mechanical diamond milling (Fraunhofer Aachen) revealed to be impossible at the required micro-metric dimension because of the high aspect ratio. The angle and depth of the grooves is incompatible with the smallest diamond milling tools.

- Electrical discharge machining (EDM) can be used to fabricate structures with features sizes down to ten micrometers. The possibilities and limitations for this method will be detailed in Section 4.4.1.

- Conventional lithography for high aspect ratio structures (CMi) is optimised to produce vertical pits. Curved surfaces could be produced but with very low control and predictability: this is detailed in Section 4.4.2.

- Lithography using grey scale masking to obtain gradients in the exposition of photoresists is an exclusive technique that could possibly yield satisfying results but was not accessible for this project. Section 4.4.3 explains this approach.

- Interference lithography offers limited control on shape but some parabolic shapes could be produced with lower dimensions. Published results are discussed in Section 4.4.4.

- 3D printing would work for larger structures or optical structures with an aspect ratio lower or equal to one. Stereo lithography was also discarded because of the steps created in this layer by layer approach. But since the beginning of this thesis, huge progress was made in these fields: they are presented in Section 4.4.5.

- Laser ablation (EMPA Thun) can be used to create structure with an aspect ratio of up to 2-3 and a depth of some 100 microns; the produced surfaces are of optical quality. This technique is introduced in Section 4.4.6

4.4.1 Electrical discharge machining

EDM was considered the most appropriate technique at the beginning of this thesis. It is at the edge between millimetre and micrometer scale and often used in the watch industry to cut very small and complex gears and pieces. In this process, rapidly recurring current discharges between two electrodes separated by a dielectric liquid remove material from the work piece. One of the electrodes is the tool (a thin metal wire, down to $20\,\mu m$) and the other one is the work piece. The wire is positioned with a micrometer accuracy and shapes down to a couple tens of μm can be cut into any conducting material. It is however not possible to obtain sharp corners in concave cuts because of the wire geometry. First satisfying moulds were cut using the Fanuc Robocut α - 0B, a wire EDM available on campus. Because the wire removes material along its path and that two or three iterative cutting runs are required for a good surface finish, the design has to take into account that the cutting wire will create a gap twice its diameter. The final surface finish is not optically perfect so a polishing step has to be planned. Finally certain materials such as stainless steel cannot be used below a certain scale because the internal stress would be to strong. If only little material is left, the smaller tips may bend under internal forces. Tungsten carbide can be used for very small structures. Different companies were contacted: Derwa SA in Switzerland, Mecasoft in Belgium and Elefil in France. Derwa was retained for the quality of surface, proximity and rapid delivery. Figures 4.4 and 4.5 show SEM micrographs of surfaces obtained by electrical discharge machining suporting this choice.

(a) Stainless steel surface after EDM with a $200\,\mu m$ wire in the EPFL workshop.	(b) Tungsten carbide surface after EDM with with a $50\ \mu$m wire by Derwa SA.	(c) Tungsten carbide surface after EDM with a $30\,\mu m$ wire by Mecasoft.
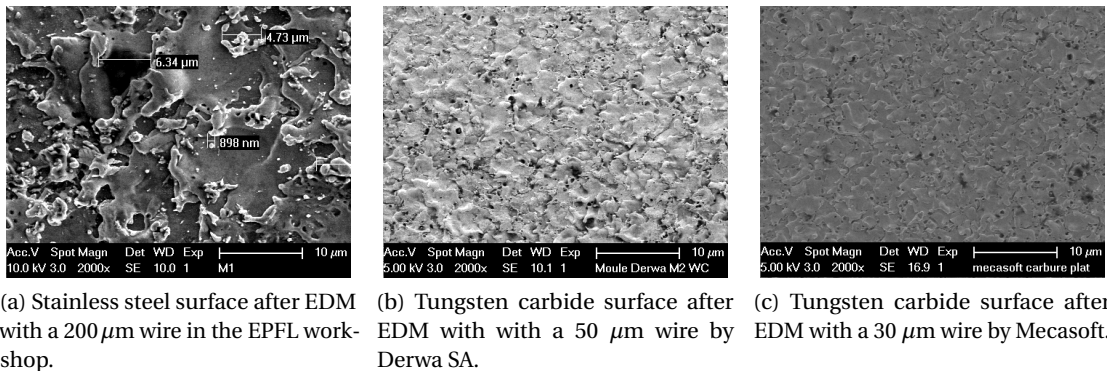
Figure 4.4 – SEM Images of stainless steel and titanium carbide surface cut by electrical discharge machining. All images are at 2000x magnification, the size of the roughness is decreased along with the wire diameter.

4.4.2 Lithography

The clean room at the Center of MicroNanoTechnology (CMi) offers cutting edge lithographic processes for micro fabrication, the available tools are however mostly dedicated to the fabrication of electronic devices. As introduced above, they uses a mask to replicate a pattern onto a photosensitive material, the result is a binary form were some areas are coated with
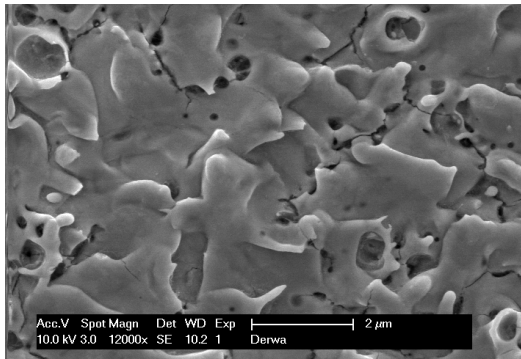
(a) Tungsten carbide surface for EDM with with a 50 μm wire as obtained from Derwa SA.
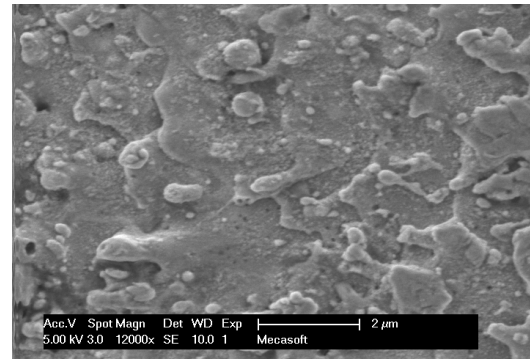
(b) Tungsten carbide surface for EDM with a 30 μm wire as obtained from Mecasoft.

Figure 4.5 – SEM Images of titanium carbide surface cut by electrical discharge machining with different wire diameters by different companies. All images are at 12000x magnification, it seems like going from a 50μm to a 30μm wire does not decrease roughness any more. The process used by Derwa SA however seems to provide a cleaner surface.

the PR and others are not. Uncoated areas can then be etched to shape the substrate. Etching is the process of removing material with an etchant; they are three main processes used in micro fabrication: dry etching, isotropic wet etching and anisotropic wet etching. The pattern of the deposited photo resist is hereby transferred to the substrate and the material is etched only where it is unprotected. Wet etching uses chemical etchant like hydrofluoric acid (HF) to remove material from the substrate. If it is isotropic, material below the protective resist layer is also removed and a so called undercut is obtained. This undercut is round if the etching is perfectly isotropic. Anisotropic etching such as potassium hydroxide (KOH) etching of <100> silicon will create slopes tilted at 54°. This is due to the strong difference of etching rate (1:400 ratio) along the different crystallographic planes. Dry etching or plasma etching is widely used in micro fabrication processes, it is an anisotropic process were energetic free radicals react with the surface of the wafer. It is a plasma process and somewhat similar to a sputtering process were the target is replaced by the substrate. The "sputtered" material is taken from the substrate and not redeposited. The used gas is chosen for its chemical reaction with the substrate and (non reaction with) the resist. This process is both a chemical and physical removal of material, the balance between both can be chosen and depend on the application. Using advanced techniques like the deep reactive ion etching Bosch process, aspect ratios up to 22 can be reached with steep walls being very close to vertical [Hermersdorf et al., 2011]. With these techniques, it is however difficult to create controlled slopes and curved shapes in materials in a reproducible manner.

4.4.3 Greyscale lithography

Grey-scale lithography uses masks with changing opacity or direct laser writing of the photo resist and can only be produced with specialised high-end equipment. Such equipment is

not only unavailable on campus but each mask is expensive and time consuming to produce. The Institute of Microstructure Technology (IMT) at the Karlsruhe Institute of Technology (KIT) is equipped with such material [Waldbaur et al., 2012] and was contacted to inquire for feasibility. It turned out fabricating the desired structure by grey-scale lithography is not a simple application of known recipes. Because the profile scale and shape is very unusual, an optimisation process and some research would have to be performed. The main challenge in this approach would then be the large height of structures. Smooth parabolic surfaces could be realised, to obtain them on heights of a couple hundred micrometers would however be very challenging.

4.4.4 Interference lithography

Laser interference lithography is an other feasible approach that could yield interesting results, even though working with laser interferometry also limits the possible designs. The interference of two incoming laser beams can be projected on large areas of photo sensible material; this allows the creation of a variety of shapes [Bühler, 2003, Wolf et al., 2012]. Amongst these shapes, parabolic surfaces were realised to fabricate miniature CPC. The specialised laboratory using this technology at the Fraunhofer ISE was contacted to obtain feedback about the feasibility of the desired structure using this technique. Again the scale was a major challenge along with the high aspect ratio of the parabola. Stronger curvature with a height of $30\mu m$ can be obtained easily with an irregularity of 2% maximum using existing recipes. Larger, steeper parabolic surfaces with controlled curvature however cannot be obtained without a significant research effort.

4.4.5 Stereo lithography and 3D printing

At the beginning of this thesis, stereolithography and other 3D printing techniques were emerging technologies [Bertsch et al., 2004]. In stereolithography, polymer or ceramics are shaped using a laser in a layer by layer process, the continuity between layers is therefore not perfect. In 3D printing, material droplets are directly deposited and hardened. Because of the high aspect ratio in the functional surface and the resulting high resolution required along both vertical and horizontal directions this was not an option. In the meantime, significant progress was made and new companies propose solutions to print small object with high resolution. LUXeXcel namely prints optical devices down to some hundred micrometers directly in a transparent polymer. Micro lenses and small Fresnel lenses are typical realisation, the limiting factor is the low achievable aspect ratio, below one. Another company sells a 3D printer named Nanoscribe capable of printing very small structures with high resolution. Such a printer is available at the Laboratory for Micro- and Nanotechnology of the Paul Scherrer Institute in Villigen. This device would be suited to print structure up to $300\,\mu m$ high; the drawback being the limited printed area ($300 \times 300 \times 300\,\mu m$). Larger areas require stitching of several smaller areas together. This can however introduces a slight discontinuity in the structures that cannot be perfectly aligned. This may be a disadvantage in the case where

the structure needs to be aligned with a second optical component. However progress is continuously made in this field and this solution has to be kept in mind for future trials.

4.4.6 Laser ablation

Pulsed lasers are well established in industry where these are used as tools to machine materials. Lasers with picoseconds pulses and deep UV radiation allow direct ablation of material with little heat affected zones (HAZs). The use of excimer lasers (at 193nm for example) allow very high resolution especially in polymers. This technology is used at the laser centre of the Empa in Thun to produce optical devices on large areas [Boehlen et al., 2005, Pedder et al., 2007]. The laser is used to structure polymers directly; typical individual feature sizes are in the range of 2 to 200 microns. The first significant advantage is that the machined structures directly present optical quality. The second main advantage of this technique for application to glazing is that well engineered micro geometries can be machined over large areas up to 3 m2. Hence an attempt was made with this technology to machine light guiding structures, the results will be presented in Section 7.5.

4.4.7 Polydimethylsiloxane formwork

The mould obtained by most of the above techniques are simple 2D extruded profiles on small areas. Because of the material they are made of, they cannot be used directly for replication, unmoulding would be difficult and resin might pollute the mould. By reproducing the microstructure into an intermediate moulding material, a negative mould is created. This intermediate step makes it possible to chose a material well suited for moulding of the final material: a UV curing resin developed at the Laboratory of Polymer and Composite Technology (LTC) introduced in Section 4.5.2. PDMS is a silicone based organic polymer that is known to work well as a mould for most resins and has been tested at LTC. PDMS is prepared by mixing a silicone based solution with a curing agent in 10:1 proportions. After mixing, this preparation has to be left to degas in vacuum. A water pump is used to reach this vacuum and after 20 to 40 minutes, the PDMS solution is ready for moulding. To cure, the PDMS has to be left at ambient temperature for at least 48 hours, 24 hours at 40°C, for 2 hours if heated at 80°C and 15min if heated at 140°C. Dow Corning DC 184 Silicon was used in this work. An interesting feature of PDMS is its low, temperature dependent shrinkage. At about 55°C it is slightly above 0.5% and raises almost linearly to 3% at 140°C [Krogh, 2003].

The shape of the microstructured part can either correspond to the desired final shape or be its negative. In both cases, this master mould will be referred to as father. To reproduce the shape of the father, a negative can be used as mould for the substrate, this negative will be named mother. In case the shape of the father is already the moulding shape, a negative of the mother has to be taken. Interestingly, it was observed that a negative of a PDMS shape can be obtained in PDMS by curing it at 140°C [Krogh, 2003].

(a) Added features in a mould, profile view. The mould is illustrated in dashed pattern and the resin in dotted pattern. The first column shows the initial replication step, the second the embedding step. In A only the feature for alignment with mould is shown. In B the thickness below the structure is controlled. In C, the total thickness is controlled and no contact is made between substrate and structures during both the replication and embedding step.

(b) Formwork with interchangeable core element (in light gray), the channels for excess resin to escape are pointed by D. The resulting PDMS stamp is a negative of this structure. The reference surfaces for vertical alignment are next to the draining channels. The surface created in the PDMS mould will be in contact with the substrate to control the thickness of resin below the microstructures. Their edge provide the alignment reference. Finally the total thickness of resin in the embedding step is controlled by the two surfaces at each side of the structured part of the insert.

Figure 4.6 – Illustration of extra features required in the formwork for PDMS mould and CAD of such a formwork. The formwork is needed in the replication step to fabricate a PDMS stamp. It adds the features required for alignment the structures with the substrate and to evacuate excess resin (pointed by D).

Furthermore, the replication step requires some extra features in the mould. The first feature is required to align the structures perpendicularly to the glass substrate. This can be obtained by including a reference that has the width of the substrate: $26\,mm$ for microscope slides. Secondly, as illustrated in Figure 4.6a, reference surfaces need to be present to control the thickness of resin below and above the structure. If no such reference is present as in row A of the figure, the tips of the structure in the mould will touch the substrate during the replication: this would induce deformation during stamping (because PDMS is soft) and the obtained structure is weakened by the absence of linkage between the stripes of resin. By adding a first reference as illustrated in row B, these problems are eliminated and the total height of the structure relative to the substrate is controlled. In the final embedding step, yet an other reference (as illustrated in row C) is required to provided control on the total thickness and spacing between the microstructure and the second interface. Finally, the PDMS mould also has to be designed to drain the excess resin that must escape the mould during both replication and embedding (D in Figure 4.6b).

To provide an alignment reference, the reference surfaces, draining channels and include the micro structured surface, a formwork needs to be fabricated. It can simultaneously provide all these extra features and a container for the PDMS in liquid state. With this type of more

complete mould, shown in Figure 4.6b, the metallic insert with the microstructured area (shown in lighter grey) can be interchanged.

4.5 Replication

4.5.1 Micro imprint lithography

UVNIL is a well-established process for the replication of micron and sub-micron scale features into photopolymerizable resins. Different shapes, namely gratings or stellar like structures with dimensions between $30\,nm$ and $100\,\mu m$ have been successfully transferred on silicon wafers with good dimensional stability [Vratzov et al., 2003]. To produce samples from the mother mould, a miniature pressure replication setup available at LTC is used as detailed in [González Lazo et al., 2012, Geiser et al., 2010]. The substrate, resin and mould are placed on a piston, the piston pushes against a quartz window above which a UV lamp is switched on to cure the resin. The pressure is applied using a pressure-controlled pneumatic movable stamp to which the master is attached. The quartz glass is used here for its strong scratch resistance and high transmittance down to $170\,nm$. Because of the soft character of the PDMS mother mould, limited pressure is used. Since pressure was not making a difference in the results, this step was later performed without piston by simply using a thick slab of glass as transparent weight.

4.5.2 Resins

There are many different types of UV-curable resins, amongst them two types were used in this project: an epoxide resin with a cationic polymerisation mechanism and an acrylate with a free radical polymerisation mechanism. The epoxide was rapidly abandoned because of its yellow colouration and because it was harder to unmould with high aspect ratios.

Amongst UV-curable resins, hyperbranched polymers (HBP) were found to be well suited for nano and micro-replication due to their low polymerisation shrinkage and internal stress [Schmidt et al., 2007]. Acrylated HBPs were previously used to fabricate polymer micro- and nano-structures with high accuracy [Schmidt et al., 2008, González Lazo et al., 2012]. The HBP used in this study was a polyester acrylate oligomer (from Sartomer) with functionality of 16 and a glass transition temperature in cured state equal to 165°C (by dynamic mechanical analysis (DMA)). The shrinkage rate of this resin is in the order of 9% [Sartomer, 2008]. The photoinitiator was Esacure trimethylbenzoyl phosphine oxide (TPO) (Lamberti) at a concentration of 6 wt%. The photoinitiator has an activation wavelength between $360\,nm$ and $420\,nm$ [Green, 2010]. Unlike the cationic polymerisation which can be self sustained by temperature, free radical polymerisation stops when it is no longer photo-induced.
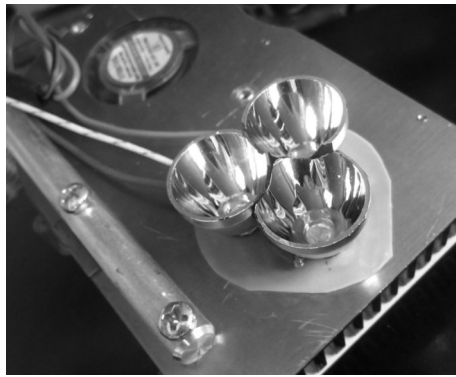
(a) UV source

(b) UV Control

Figure 4.7 – Photograph of the fabricated UV source. The LEDs are placed on a ventilated heat sink and three parabolic reflectors are used to concentrate light. The exposure time and intensity can by controlled with the control unit shown in 4.7b.

4.5.3 UV source

At LTC, a 200 W mercury bulb UV lamp (Omnicure 2000, Exfo, Canada) was used for initial experiments. Later, a custom UV source was built using a timer, a controllable power source, three power UV light-emitting diodes (LEDs) with a narrow peak centred at 375 nm and a cooling board from a computer graphical card (Figure 4.7a). The LEDs are fabricated by Seoul Semiconductors (P8D2 275) and have an optical power output of approximately 250 mW each with a full width at half maximum (FWHM) of 11 nm, it is important that they are cooled properly. For cooling the LEDs were glued onto a heat sink with a thermally conductive but electrically insulating glue before being soldered together. A thermocouple was placed close to a LED to monitor temperature during first operations. Because the LED slug (bottom part) is connected to the anode, and to avoid contact between the anode and the conducting metallic heat sink, a Teflon sheet was perforated and used as a space keeper. The light from the LEDs was collimated using optical reflectors designed to provide a narrow, 6° wide cone of light. To fit the source within the available area under the alignment setup, the cones were cut to bring the LEDs closer together. The resulting distribution of intensity was measured with a UV watt meter in a plane at 12 cm distance, taking measurements every 0.5 cm. The intensity distribution for the area of interest is shown in Figure 4.8a. the distance was increased to 15 cm and an etched Fällander glass was added to increase the uniformity of the distribution as shown in Figure 4.8b.

4.5.4 Alignment

In case a two component device is produced, the structure is replicated on a substrate with striped mirrors. The stripes and structures have to be positioned relatively to each other and the resin cured only once the mould and substrate are properly aligned. Such an alignment
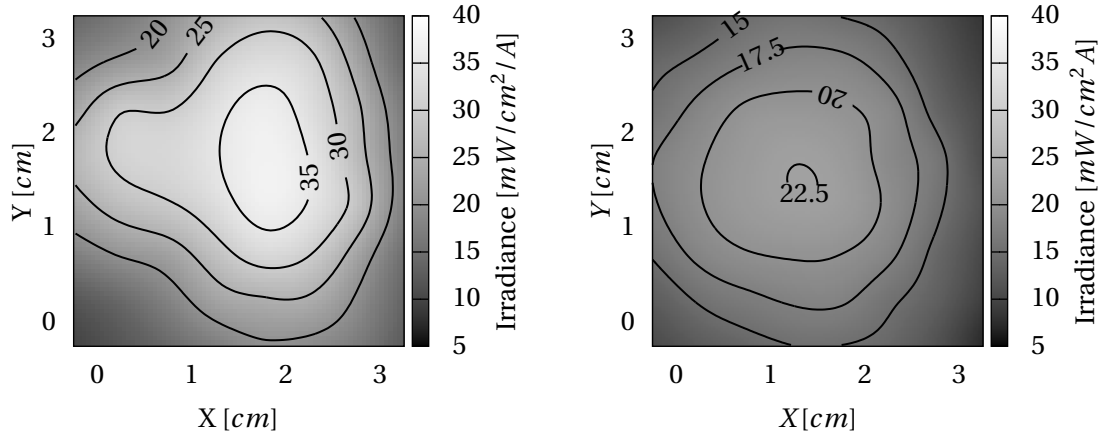
(a) Homogeneity at $12\,cm$

(b) Homogeneity at $15\,cm$ with diffuser.

Figure 4.8 – Characterisation of UV source homogeneity with and without diffuser. The figure shows interpolated values from an array of 7 by 7 measurement points. The irradiance was normalised with the current supplied to the LEDs. With a diffuser, the maximum variation of intensity is in the order of 10 % in the central square centimetre whereas it is above 30 % without diffuser.

can be carried out with an optical microscope; the UV source has been designed specially to provide sufficient intensity and to be fitted below the sample, replacing the normal light source. The light source can be inserted once the elements have been placed accordingly.

4.6 Reflective coatings

The objective of this study is to fabricated embedded micromirrors, as mentioned in the introductory section of this chapter: they are directly deposited on a structured surface and then embedded. There are several means of deposition to create thin films, chemical vapour deposition (CVD) and physical vapour deposition (PVD) are the two main techniques. Film thickness reach from atomic monolayers for most advanced CVD to few micrometers for PVD. The later was available in the laboratory for this thesis (and also best suited as explained in this section). In this section the used deposition techniques are introduced.

4.6.1 PVD

PVD is a family of technologies commonly used to produce thin films where the material to be deposited is heated until melting point; its vaporised form then condensates on the substrate. Several methods exist to evaporate the material: it may be heated directly by an

electron beam, it can also be sputtered using various techniques such as magnetron sputtering or ion-beam sputtering. In this case an electric field is applied in order to bombard the target with ions created in a plasma and dislocate atoms. Some of these will coalesce on the substrate and form a thin film. These atoms have relatively high kinetic energy, in the order of several eV. Lasers may be used to evaporate material in pulsed laser deposition (PLD). Finally, in thermal evaporation, the technique used for this work, the material is placed in a crucible mounted between an anode and a cathode. When a high current is applied (several hundred amperes), the crucible is heated to several hundred degrees until the pellets of material placed in it melt and evaporate. To obtain a good film quality, the chamber for such evaporations needs to be in vacuum, the quality of vacuum depending on the used technique. A controlled atmosphere can be used to deposit oxides or nitrides. This technique is sometimes also called evaporative deposition and the kinetic energy of the atoms arriving on the surface is lower than for sputtering, typically in the order of $0.1eV$.

4.6.2 Balzers BA 510

In the solar nanotechnology laboratory of LESO-PB, a Balzers BA 510 vacuum evaporator is available for deposition of various materials on organic and inorganic substrates. The chamber possesses a relatively large bell that can be lifted with a pneumatic system and fitted with substrates of consequent size. The substrates may be rotated and heated; these option were however not used in this work for reasons explained in the following section. The thickness of the deposited film can be monitored using a quartz crystal oscillating at a given frequency. Because the quartz is also exposed to the vapour, its frequency changes with the thickness of deposited material. According to Sauerbrey [Sauerbrey, 1959], there is a direct link between the mass of the deposited film and the decrease in frequency:

$$\frac{m_F}{m_Q} = \frac{\rho_F * d_F}{\rho_Q * d_Q} = \frac{\Delta f}{f_Q} \tag{4.1}$$

where m is the mass, ρ the material density, d the thickness, Δf the frequency change and f the eigen frequency. The subscript $_F$ are for the film and $_Q$ for the quartz. The deposited thickness Δd can therefore be linked to the frequency change as follows:

$$\frac{\Delta f}{\Delta d} = \frac{\rho_F}{(\rho_Q * d_Q)/f_Q} \left[\frac{Hz}{nm} \right] \tag{4.2}$$

It can be mentioned that this relatively early technique for the monitoring of the deposition rate has since been improved to increase the range and accuracy of the measurement [Benes et al., 1989]. It has also to be kept in mind that depending on the used deposition technique and chamber configuration, the measured thickness is not always equal to the deposited thickness. With a calibration step for a given configuration and technique, this method is however sufficient in most cases.

4.6.3 Thickness study

Unlike other applications such as interferometric thin film coatings, the exact thickness of deposited films in this project is not crucial. Silver (*Ag*) and aluminium (*Al*) are deposited to obtain reflective coatings that only need to be thick enough to reflect most of light. Different thicknesses were deposited; their transmittance was measured using a Perkin-Elmer Lambda 2 spectrometer. Because the effective thickness is not known yet, these different samples are identified by the frequency change on the quartz after the coating, their transmittance is shown in Figure 4.9a. For aluminium, completely opaque films were obtained at a $800\,Hz$ frequency change whereas for silver height variations in the quartz frequency are required. This is both because of the increased density of silver and the higher thickness required for an opaque coating.
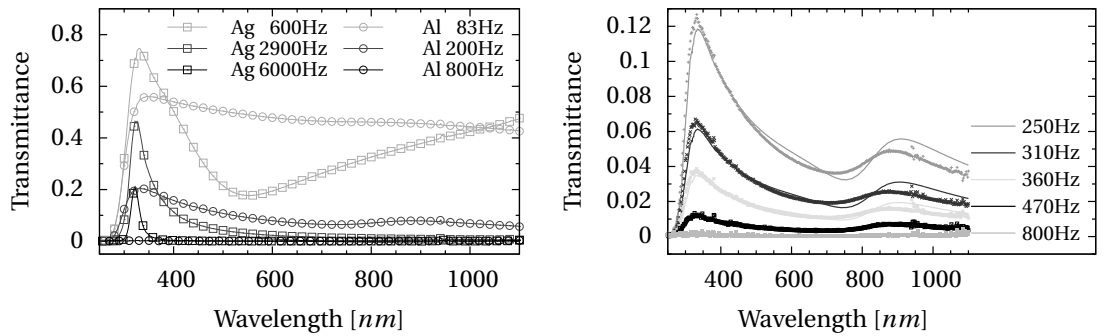
(a) Measured transmittance for various Al and Ag coatings with different thickness.

(b) Measured transmittance of aluminium thin films compared to the calculated transmittance for the best fitting thickness.
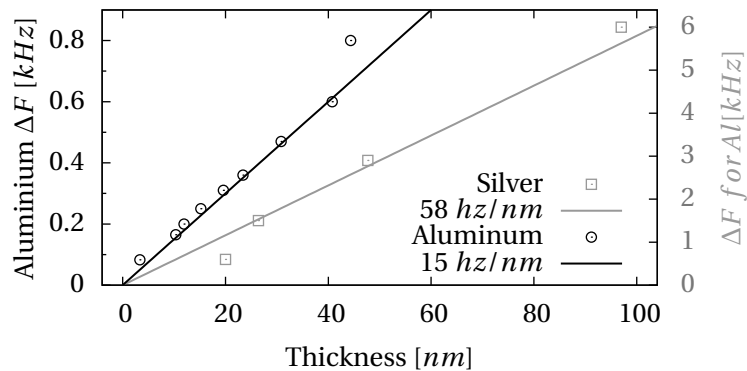
(c) Theoretical deposition rate (line) for aluminium and silver compared to the effective deposition rate obtained by fitting of the optical characterisation with theory (points).

Figure 4.9 – Characterisation of deposition rate on Balzers BA 510 for aluminium and silver reflective coatings.

These transmittances can also be used to fit a thickness with a thin film software such as TFCalc. For aluminium, the optical constants where taken from the work of Rakic *et al.*

[Rakic et al., 1998]. The transmittances computed using the best fitting thickness are compared with the measured ones in Figure 4.9b; the associated thickness is shown in 4.9c. In this last figure the theoretical deposition rate of $15\,Hz/nm$ is also shown as derived by applying (4.2) to aluminium with a density of $\rho_{Al} = 2.7\,g/cm^3$ and the properties of the used quartz ($\rho_Q = 2.6$, $d_Q = 350\,\mu m$ and $f_Q = 5\,MHz$). Like wise this process was applied with silver ($\rho_{Ag} = 10.5\,g/cm^3$) to obtain a theoretical deposition rate of $58\,Hz/nm$. The last point is a little far of the curve in both cases because at this thickness the film is almost fully opaque and the relative error in the measured transmittance therefore is very high. The first point is also slightly off the curve because for very thin films, the coating is not perfect and other phenomena come at play (oxide layer, droplet formation, etc.).

4.6.4 Angular setup for partial coating
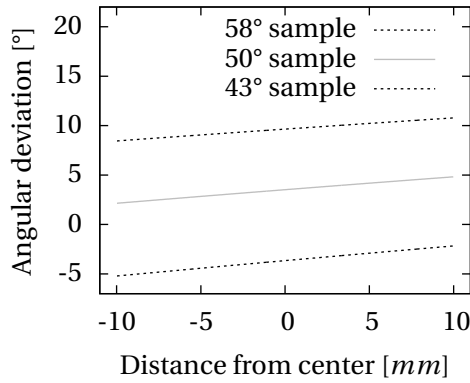
(a) Variation of the effective deposition angle on the sample depending on the distance from the centre. The centre of the sample is aligned vertically with the point evaporation source and is also the rotation axis. Results are shown for a source to sample distance of $30\,cm$.
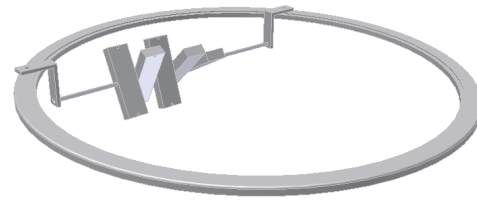
(b) CAD drawing of the sample holder. Several holders are placed on an axis and can be individually rotated as desired. The axis was fitted into the chamber so that it is positioned above the crucible.

Figure 4.10 – Study of deposition angle variation and schematic of the sample holder for angular deposition.

In the scope of this work, reflective coating were deposited on selected facets of a microstructures. The most general way of coating selected areas is by masking or removing unwanted areas. The former is not straight forward in the present case because the substrate is not flat. A lithographic approach of the later technique was introduced earlier, however it is also difficult on non flat substrates. The chosen approach relies on the directionality of the evaporation source and shading from neighbouring peaks. The evaporative deposition can be considered directional because the distance between the source and sample is larger than the feature size. The inclination angle of the sample however varies along the sample because the distance to the source is variable and the source does not emit particles in a parallel beam. This slight variation of the impinging angle depending on the location on the substrate was computed for a source to centre of sample distance of $30\,cm$ and tilt angle of 45° (Figure 4.10a).

In order to apply this directional coating principle, it was necessary to design a device to hold the samples at a give angle. The sample holder was designed and built to fit the Balzers evaporating machine (see Figure 4.10b & 4.11a). It comprises an axis and six relatively thick aluminium pieces dimensioned to hold microscope glass slides ($26\,mm \times 86\,mm$) and to better evacuate the eventual latent heat from the deposition process. The axis was placed as high as possible in the chamber and each sample holders can be fastened into a given position by a screw.

A macroscopic 90° polymethyl methacrylate (PMMA) prism was placed in this sample holder and coated to demonstrate the possibility to coat only exposed surfaces (see Figure 4.11b). The first visual check confirmed that only one prism side was coated: normally those prisms duplicate objects into a left and right displaced images; the coated prism shows only one image. The different coating angles along the sample create an observable variation in the uncoated prism faces. The coating is not fully facet selective all over the sample, for certain facets, the hidden face of the prism is also slightly coated and shows a brownish colour. This enabled to identify an ideal tilt angle of 52° for this configuration. At larger angles, the coated ratio of the exposed facet decreases, at lower angles the shading effect is not perfect and the hidden facet is slightly coated. It is therefore important to chose the proper angle.
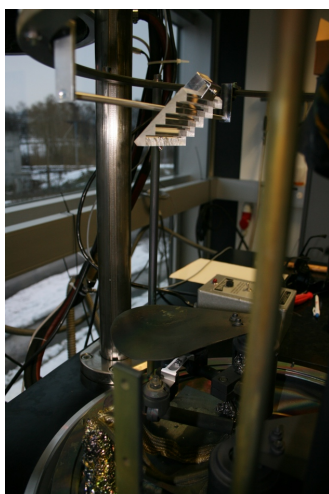
(a) Photograph of the sample holder installed on the Balzers Evaporator with a macroscopic prism fitted and ready for coating.

(b) Photograph of an uncoated and a coated (left) macroscopic prism. The lines below the prism disappear on the coated facets. Some of the uncoated facets on the left prism appeared very slightly brown; this can hardly be distinguished in the photographs but enabled to define the ideal tile angle for this deposition. On a coated facet, the reflection of a pen can be seen.

Figure 4.11 – Photograph of angular coating device and coated macroscopic prisms.

Finally, on the topic of angular coating it has to be mentioned that the film thickness is decreased when increasing the angle for the same variation of quartz frequency. The flux of deposited material remains constant, but the projected surface of the sample in the plane perpendicular to the deposition direction decreases with the cosine of the tilt angle. In practice because the distance to the source also varies, this effect is emphasised for the area that is

moved away from the source and reduced for the part moved closer to the evaporation source. This induces an inhomogeneous film thickness; for a $76\,mm$ sample placed at $300\,mm$ of the source and tilted at 45° the film will be approximately 30% thinner in the uppermost part than in the closest extremity. This should be considered when depositing a material and when choosing the location on the sample to measure film thickness.

4.7   Encapsulation

For encapsulation, the UV curable polymer used for replication is used one more time in order to have virtually no interface at the structure surface. A modification of material would create extra refraction and make the system less transparent and more diffusing. Light rays passing through the system without interacting with the embedded mirrors have to pass without any other interaction to avoid direction changes and to keep the system imaging and transparent at normal incidence. As introduced previously, to create parallel back and front interfaces, the mould has two reference levels next to the structured area. These are also used to ensure that during encapsulation, the glass slide placed on top of the structures is parallel to the substrate and does not crush the fragile structures. The embedding process is a delicate step where polymerisation time and intensity have to be controlled to avoid dislocation from the glass slide and creation of air pockets on the microstructured side. This practical difficulties as well as others are discussed further in Chapter 7.

5 Characterisation Methods

In this chapter the methods and tools used for the physical characterisation of produced moulds, replicated structures and other samples are introduced. A spectrophotometer was used to measure optical properties of materials, the methodology being introduced in Section 5.1. Moreover, optically functional samples with angular dependent transmittance require angular optical measurements to assess their performance and measure both the transmittance and the transmission distribution depending on the incoming angle. Such an apparatus was designed and built, it will be presented in Section 5.2. In the fabrication processes introduced in the previous chapter, each step requires appropriate methods to be assessed. Surface roughness and profiles needs to be measured and sometimes observed. The associated profilometry and microscopy techniques are described in Sections 5.3 and 5.4.

5.1 Spectral characterisations

Spectral measurements of transmittance and reflectance can be used to derive optical properties of thin films. The theory is briefly discussed in this section along with the spectrophotometer available and used for this thesis.

5.1.1 Theory

The main properties of a thin film are the thickness d, the refractive index n and the extinction coefficient κ; they all affect the transmittance of the thin film. The refractive index directly influences the reflected and refracted components of the light beam at the interfaces between materials as described in 3.2.1. The measured transmittance and reflectance however is the total contribution of all interfaces and inter-reflections.

κ contributes to reduce the transmittance exponentially with the distance in the material as given by the Beer Lambert law (Section 3.2.2). Using measurements of transmittance and reflectance, the absorption can be derived, and from there on κ can be estimated. For an accurate result the refractive index should be included and the optical quantities should be

expressed as series considering all possible path (light rays are also absorbed when traversing the layer after being reflected at the back interface).

Finally for thin films, interference effects have to be considered. In quarter wave layers, with a thickness equal to one quarter of the wavelength, the distance travelled by the reflected radiation at the second interface is half a wavelength longer than that of the radiation reflected at the first interface: they are hence out of phase and will interfere destructively. To calculate the exact quarter wave thickness the refractive index should be considered since it influences the speed of light. Such interferences are wavelength dependent and the induced variations can be measured in the transmittance and reflectance spectra.

Using specific software such as TFCalc, unknown quantities can be approximated by fitting the theoretical transmittance and/or reflectance spectra to the measured ones.

5.1.2   Spectro-photometry

For the spectral measurements, a Perkin Elmer Lambda 2 spectrophotometer was used. It provides rapid measure of transmittance from $190\,nm$ to $1100\,nm$. After taking the reference intensity without sample, the latter was placed in a black box and transmittance measured by the means of a spectral light source transported to the sample and back to the sensor by fibre optics. Care has to be taken not to move the optical fibres after the reference was measured.

5.2   Development of a miniature goniophotometer
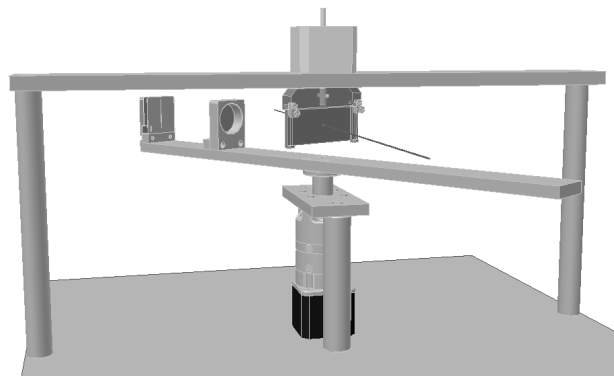
Figure 5.1 – CAD drawing of the goniometer setup. The top motor moves the sensor, the bottom one (black) is attached to a planetary gear and moves the sample.

Because the embedded mirrors studied in this work are designed to obtain specific transmission distributions and a strongly angular dependent behaviour, their measurement is absolutely required. This measure has to provide the angular distribution for a set of incoming angles: such a device is called a goniophotometer. A large scale goniophotometer is available at the LESO-PB but is not adapted to characterise samples smaller that $10\,cm$ in diameter.

Furthermore, it does not provide spectral information which is necessary to characterize thin film coatings. And finally, the maximal angular resolution of this device is 5°, such a resolution is too low for the purpose of this thesis. Indeed as it will be exposed in the result sections, the energy transmittance may double for a change of one or two degrees in the angle of incidence. Because the studied geometries are extruded profiles, a single angular variation is sufficient to provide a significant amount of information on laminar structures. Therefore the measurement can be done in a single plane, changing only the angle relative to the normal and measuring in the plane of the profile, perpendicular to the sample. The complexity of the measurement is hereby considerably reduced and a custom setup has been designed and built; it is presented in this section. A computer aided drawing of the design and a view of the assembled apparatus are shown in Figures 5.1, respectively 5.3.

5.2.1 Measurement setup

For an automated, precision goniophotometer the following elements are required:

- A collimated light source

- A monochromator

- An angle selective sensor

- An accurate signal monitoring provided by the sensor

- A data acquisition method to store this measure on a computer

- A set of motors with a computer driven control to set the incoming and outgoing angles.

The working principle of such a device is schematically drawn in Figure 5.2.
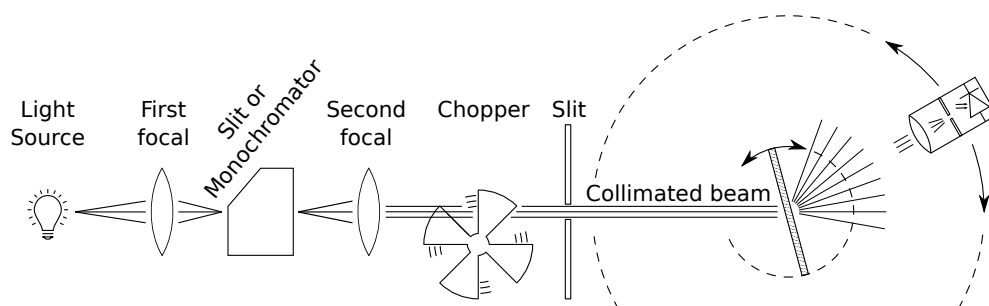
Figure 5.2 – Schematic drawing of the working principle of the goniophotometer.

Sensor

For the sensor, a focusing lens and a slit accept light rays from a small angular range, parallel to the sensor axis. Behind the slit, a silicon photo diode with an electronic circuit converts

light into current. The current is amplified and converted to a voltage by the means of two operational amplifiers. This voltage is then acquired through the sound card based lock-in described below.

Development of sound card based lock-in amplifier

To measure accurately even very small signals and eliminate the surrounding noise, a lock-in amplifier was used. A lock-in amplifier uses a reference to distinguish signal from noise, integrates the signal over time and amplifies it if necessary. Cutting edge lock-ins work at Ghz frequencies and can measure pico volts buried in noise. For the measures of the samples in this thesis, lower frequencies and smaller amplifications are sufficient. A digital lock-in was developed using only a pre-amplifier and a sound card. The line in of a sound card has two channels and can monitor voltages between 0 and 1 V at $92\,kHz$. Using one channel for the signal and one for the reference, the signals are synchronised and can be used in a digital lock-in software. To make the best use of the 24 bits encoding of the sound card over the $[0,1]\,V$ range, the pre-amplifier can be set to four distinguished amplifications. The magnitude of this amplification is controlled by a computer through the frequency sent to the line out of the sound card by means of a microcontroller converting the frequency into a 2 bit logical output that triggers two miniature relay and activates or bypasses two amplifying circuits. More details about the lock-in principle and its implementation can be found in Annexe C.
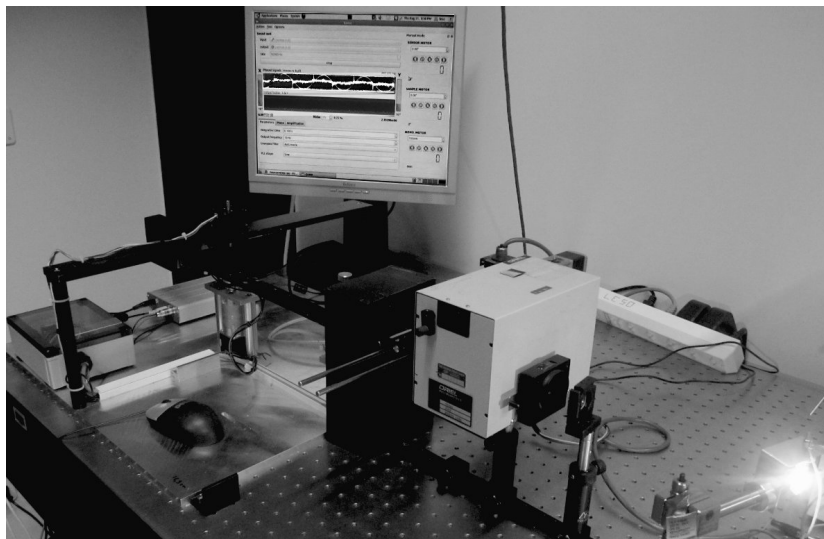
Figure 5.3 – Photography of the miniature goniometer and associated control screen.

Computer control

This digital lock-in amplifier was then integrated to a program that simultaneously controls the two stepper motors to rotate the sample and the sensor. The motors are driven by a controller card to which the program sends its orders. A calibration step is needed to align the two motor

(a) Measurement of the distribution for a diffusing glass provided by Fällander compared to those of samples fabricated at LESO-PB by Jolissaint and Paone.

(b) Spectral measure of a 3M prismatic sheet at 0° incidence on the prismatic side. The spectral variation of the refractive index changes the angle of refraction depending on wavelength of light.
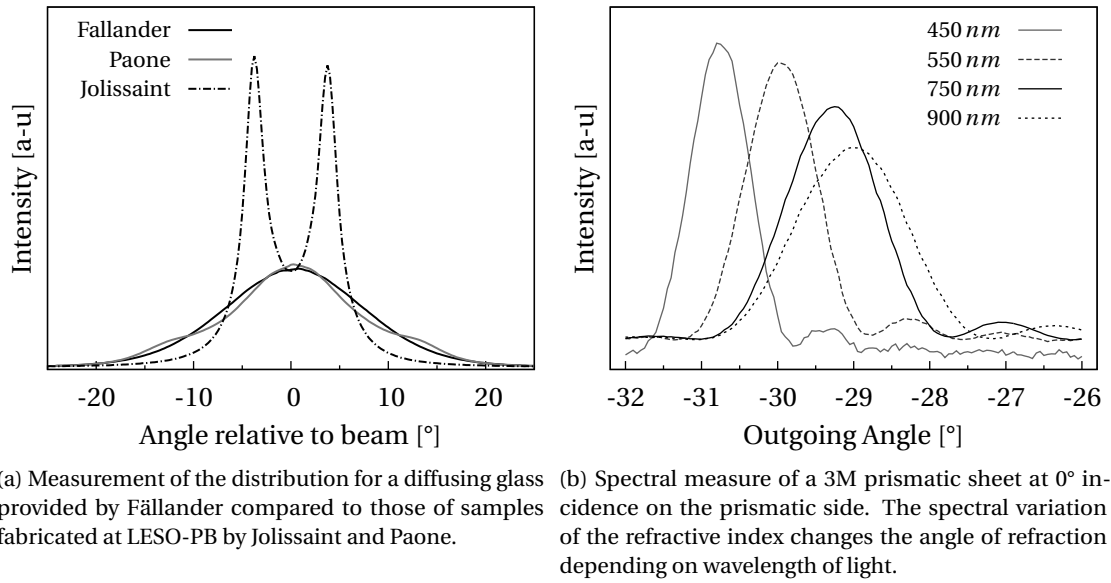
Figure 5.4 – Illustration of goniophotometer measurements

axis with the zero reference before measuring any data. For the sensor, an angular resolution lower than one tenth of degree was reached using a 54:1 planetary de-multiplication: with 200 steps per revolution on the stepper motor this provides 30 steps per degree. Additionally, microstepping can be used to add intermediate steps and increase resolution. An illustration of such a measurement is shown in Figure 5.4a where the transmission distribution of an etched glass provided by Fällander was measured. The diffusion of glass etched in the laboratory was also measured; the two peaks in some measurements are most likely due to pyramidal structures with relatively flat facets that refract light.

5.2.2   Spectral measurement

The Goniophotometer was extended with spectral capabilities. A monochromator was added in the light path and a third stepper motor used to control it. Since the monochromator strongly decreases the intensity of the source, this was only possible because the sensing process uses a lock-in amplified approach and can measure very small signals. This modification also required to control the polarisation of light because grating based monochromators such as the Oriel monochromator used in this setup create a polarised beam with a polarisation state dependent on the incident angle on the grating. To avoid measuring polarisation dependent behaviours, the beam is *s* polarised regarding the sample. It is polarised perpendicularly to the plane of incidence and generally has less influence on the measurement: there is no Brewster angle and generally a more linear behaviour. The spectral measurements of the goniophotometer was automatised through a control software. Some existing prismatic structure such as the one of a 3M film illustrated in Figure 5.4b and diffusing sample were characterised (Figure 5.4a).

5.2.3 Accuracy and validation

For validation of the goniophotometer, the transmittance of a clear glass sample was measured depending on incoming angle. This measurement was performed in the non spectral mode with a halogen source; the correspondence with theoretical transmittance is shown in Figure 5.5a. The transmittance is accurately measured until 83° of incidence. For greater angles, the light beam becomes too large on the sample. Likewise, the validation was performed for s-polarised spectral transmittance of a glass coated with an interferometric coating. In Figure 5.5b the measurement of the coated glass is compared to a measurement performed using an integrating sphere with an Oriel spectrophotometer. This comparison is only possible at normal incidence when the transmittance for polarised and depolarised light beam is equal.

The goniophotometer was also tested for repeatability and after replacing the power supply with a supply independent from the mains voltage fluctuation, variations lower than 0.1% were measured. The linearity of the sensor was tested over five orders of magnitude by comparison with a luxmeter. Using an absolute calibrated spectrometer, it was confirmed that the used silicon photo diode has a specific spectral response with a peak at about 900nm. This was accounted for in the spectral measurement since the sensor is calibrated in intensity for each measured wavelength. For samples with a strong spectral behaviour this however makes measurements in the non spectral mode irrelevant. The spectral distribution of the light source cumulated with the spectral response of the sensor emphasises variations in the high range of the spectrum, towards the red and infrared.
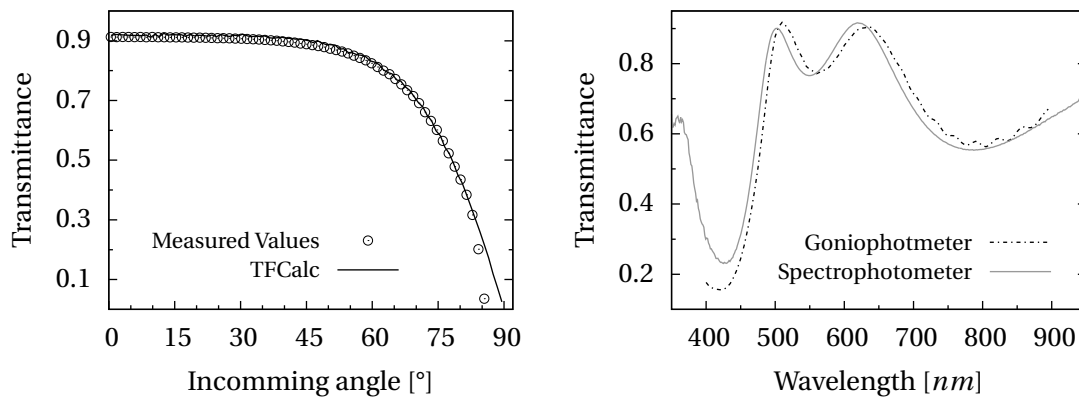
(a) Validation of angular measure with goniophotometer by comparison with theoretical transmittance of a $1\,mm$ glass with $n = 1.52$ as computed with TFCalc.

(b) Validation of spectral measure with goniophotometer by comparison with a spectral measurement using an integrating sphere an Oriel spectrophotometer.

Figure 5.5 – Validation measurements of the fabricated goniophotometer.

5.2.4 Protocol for measurement of structures

In this section the protocol to perform accurate and reliable measurements is introduced.

- Firstly the equipment might be set to spectral or non-spectral mode. This has to be done manually by setting the appropriate light source: white or passing through the monochromator. In both cases, the source should be turned on an hour before measuring to allow it to stabilize.

- As in most optical measurements, once stable, the reference intensity has to be set. This is done by measuring the signal at zero degrees. If the measure is spectral, this value has to be taken for the whole range of measurement ($400 - 900\,nm$). By default this spectral reference is taken every $25\,nm$, but this interval may be modified in the software properties.

- Last but not least, stepper motors do not have an intrinsic position information, only relative movement is known. Hence the initial position of all three (two if measuring in non spectral mode) motors needs to be known. This can be done manually; to ensure repeatability and make it simpler for the user, a routine was implemented in a wizard dialogue. This wizard goes through three steps:

  - Firstly, the sensor motor is calibrated, this is done using the left and right stop switches wired to the control board and the known position of the zero relative to then. In case this interval is not known or has changed after a modification of the optical path or movement of some element in the setup, the maximal value of the transmission peak can be used to set these values and determine the zero position.

  - Secondly, the sample motor is calibrated; this is done manually after moving the motor to the zero position. The sample holder is loosened from the motor axis and a special gauge is then used to aligne it with the main axis of the setup before tightening the mounting screw.

  - Thirdly, if in spectral mode, the monochromator motor is calibrated; this is done by setting the grating to $555\,nm$ using the computer control of the stepper motor and the display on the monochromator. Other wavelength can then be found using this position and the known relation between steps and wavelength. A full rotation of the motor counts 200 single steps whereas a full rotation of the monochromator axis shifts the wavelength by $25\,nm$. Depending on n_m, the number of selected micro-steps, a single nanometre therefore corresponds to 8×2^{n_m} motor steps.

After appropriate calibration of the device, different measurement modes are possible. The outgoing distribution can be measured for a selected incoming angle or a range of angles at regular intervals. The range of the transmitted and/or reflected distribution can be specified; it may be absolute (relative to the light source axis) or relative to the sample. By changing the incoming angle only, transmittance in a given direction can be measured. The wavelength may also be changed to obtain spectral measurement if the monochromator is in the light path. More details about the interface and measurement possibilities can be found in Annexe D.

5.3 Profilometry

In this section two techniques to directly measure the profile of a surface are introduced. The first is a non contact method using optical properties to measure the height variation. The second uses a stylus in contact with the sample to measure the latter. Atomic force microscopy (AFM) is another more elaborate and high resolution method to measure the surface profile, but this technique is not adapted to features with sizes above one micron.

5.3.1 Optical profilometry

Optical profilometer typically use a laser to measure the variation of height in structures. The sample is placed on a 2D stage and is moved to obtain profiles or maps of heights. In this thesis, the profilometer from UBM available at the Tribology and Interfacial Chemistry Group (TIC) was kindly put at disposal of the candidate. This profilometer works with a laser diode that is first collimated and then focused on the sample. A set of photodiodes then measure the focus error in the reflected signal and correct the distance between the objective and the sample to keep the sample surface in focus. The displacement of the objective is measured with a light barrier measurement system [Stemp and Stemp, 2001]. The TIC group discussed the opportunity to purchase another more refined optical profilometer relying on the fixed depth of field in optical microscopy to reconstruct surface profiles.

5.3.2 Contact profilometry

Alpha step profilometry is a contact method to measure profiles. It is typically used to measure the coating thickness in a location where coated and uncoated areas are neighbouring. A small stylus is dragged along the surface of the sample and follows the surface topography. The stylus applies a constant force in the range of the milligrams and the heigh variation can be measured (along one direction only). The surface roughness can also be computed for a given range by doing a mathematical average of the variations to compute the roughness arithmetic average. Such a device was kindly put to the disposal of the candidate by the Laboratory of Physics of Complex Matter (LPMC). It has been used to measure film thicknesses but was unfortunately not suited to characterise the profile of structures since the depth of structures are in the order of several hundred micrometers, well above the range of this device.

5.4 Microscopy

Beside optical characterisation, some type of microscopy had to be used to visualise the structures shape and the coating location. Different types of microscopy techniques are suited depending on the seeked information. Scanning electron microscopy (SEM) is an advanced technique that provides a great depth of field in the image and great magnification. It is however time consuming and cannot easily provide information about the third dimension.

To have a more rapid observation method than SEM images and because SEM requires sample preparation (especially for organic, non conduction samples) other methods were also considered. Optical microscopy is ideal to provide rapid information about a sample for micro metric features that are not three dimensional. Confocal microscopy is somewhat slower since it requires some acquisition time but gives information about the third dimension accurately in the micron range.

5.4.1 Optical microscopy for substrate analysis and lithography

The optical microscope images were acquired by fitting the *Zeiss Laborlux* microscope with a specialised *Dino* digital camera. The rapid observation of planar features using an optical microscope was useful to optimise parameters in lithographic processes and in particular the results of lift-off lithography. The mask printed on a photoplotter as described in Section 4.3.2 was illustrated in Figure 4.2; the corresponding patterned PR is illustrated in Figure 5.6b. In Figure 5.6a, the surface of the transparent PDMS mother mould is shown. The roughness created by the wire electro-erosion process in the EDM transferred during the replication process.
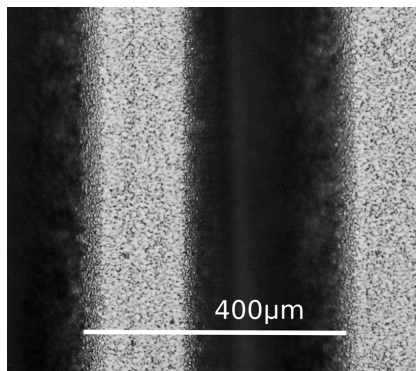
(a) Image of roughness on a PDMS mould obtained by Optical microscopy.
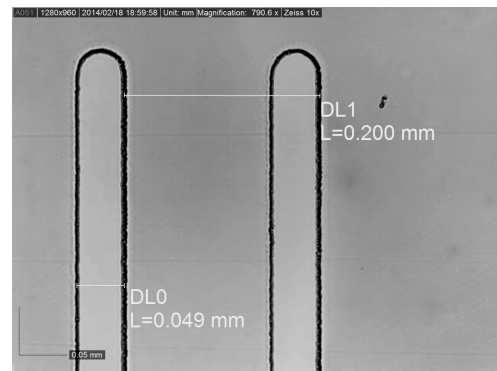
(b) Image of patterned photoresist.

Figure 5.6 – Micrographs of PDMS mould, lithographic mask and patterned photoresist.

5.4.2 Confocal microscopy for coating location

Because confocal microscopy gives greater resolution than traditional optical microscopy and allows to create 3D profiles, it was selected as an alternative to SEM. Confocal microscopy is an optical imaging technique using point illumination with a focalised laser and on the sensor side, a focal combined with a pinhole to increase optical resolution and contrast. The measurement point scans the sample in the x, y and z directions. This point by point acquisition of reflected signal enables the reconstruction of three-dimensional structures from the obtained images. This particular aspect is very interesting to reconstruct the profile of created microstructures. Images were obtained at the BioImaging and Optics Platform (BIOP)

using a LSM 710 Zeiss confocal microscope with a 405nm laser. The two samples illustrating this technique are microstructures of the first generations. It was possible to observe the shape of the structure and the roughness of the surface (see Figure 5.7). This method however requires a water immersed objective; it was observed that water swells some types of resins and progressively destroys the structures. Because the signal strength varies a lot depending on the inclination of the observed surface, the figure of the uncoated profile shown in Figure 5.7b was constructed from three different image stacks obtained at different amplifications. This method also proved to be useful to identify coated areas, the coated facet appearing clearly in Figure 5.7c: one face is bright and clear, the other one is almost invisible. The brightness of the peak is an artefact probably due to light scattering and the brighter bottom is due to higher signal. It seems that the steep faces of the structures are slightly deformed, this is probably due to the swelling of the resin this sample was made of.

(a) Top view image of the bottom of a groove obtained by confocal microscopy with a 405nm laser.

(b) Topography of an uncoated microstructure obtained by assembling three z-stack confocal scans.

(c) Topography of a coated microstructure obtained by z-stack confocal imaging.
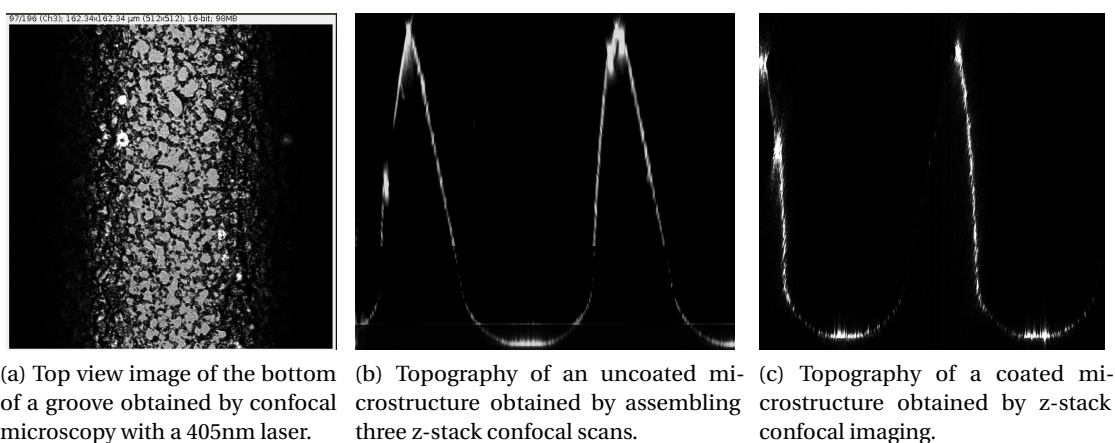
Figure 5.7 – Confocal microscopy images of replicated structures.

5.4.3 SEM for surface analysis

SEM is a powerful microscopy technique using an electron beam to overcome the limitations due to the large wavelength of visible light and to generate images with much higher magnifications. A XLF30-FEG SEM available at the Interdisciplinary Centre for Electronic Microscopy (CIME) of EPFL was used to observe the sample surface and its profile. An example of SEM micrograph for an etched glass surface is shown in Figure 5.8a. The scale of the roughness can be identified; it is however hard to identify the valleys the hills; it does not provide any information about their relative heights. This is a major limitation of this technique for the observation of three dimensional (3D) structures. For the observation of non conductive materials such as polymer or glass, a preliminary coating with a conducting material is nescessary. This can be done by evaporating a metal in the laboratory or at the CIME using a carbon coater for the deposition of a few nanometres of carbon.
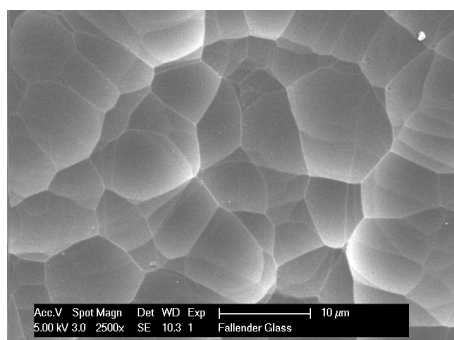
(a) SEM image of an etched glass surface as provided by Fällander.
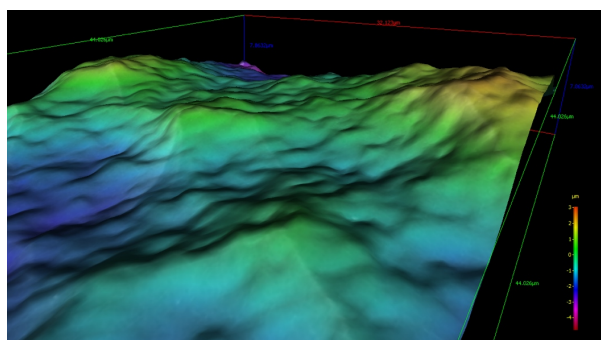
(b) 3D SEM image of an etched glass obtained by the processing of images taken from three different angles.

Figure 5.8 – Scanning electron microscopy images.

5.4.4   EDX for surface analysis

EDX spectroscopy in an other powerful application of electron microscopy where electrons are ejected from inner-shell atomic orbitals by a high energy electron beam hitting the sample. X-rays are then emitted during the transitions of electrons from higher energy shells to fill the created vacancies. The energies of these X-rays are characteristic of the atomic species and the X-ray spectrum allows to identify the sample composition to some extent. To obtain not only the count of electrons hitting the sensor but also their energy, the XLF30-FEG SEM is fitted with a Si(Li) nitrogen cooled sensor. When an X-ray photon passes through, it causes a swarm of electron-hole pairs to form, causing a voltage pulse. Depending on this voltage, the electron energy can be derived. This technique was attempted to identify coated and uncoated areas. Results using this technique will be presented in Section 7.4.

5.4.5   3D SEM for topography

Finally a third application of SEM was attempted to observe the topography. Using three images of the same area taken at different angles, the 3D profile can be derived. This technique from the field of photogrammetry is widely used in image analysis; results can be obtained using image processing software such as 3DMex. Using this software a 3D image for an etched glass could be obtained and is shown in Figure 5.8b; for high aspect ratio and large features, the method reaches its limits (due to important shading from the high peaks), the image quality is reduced (less pixels on close to vertical surfaces) and the software could not provide satisfying results.

6 Simulation Results

In this chapter results regarding simulations are presented. First, the validation results will be presented. An optimised design with embedded mirror for light redirection will be described followed by a novel design fulfilling the set of objectives pursued in the scope of this thesis. The corresponding design will then be introduced and discussed. Following a systematic study of daylight and thermal objectives, the novel design will be optimised further. Annual thermal and daylighting performances will be computed for such an optimised design using climatic data for Lausanne, Switzerland. Finally other applications of the simulation toolbox will be introduced.

The results presented in the "Daylighting performance" and "Energy performance" sections are given (unless specified) for the standard reference office of Reinhart, with a south orientation. The location was set to Lausanne (46.52°N, 6.63°E) and Meteonorm was used to generate hourly outdoor temperatures, as well as diffuse and direct horizontal irradiances. The reference window used for comparison is a double glazing with slightly reduced transmittance for solar protection: its transmittance at normal incidence is 0.7.

6.1 Validation

The developed software was validated using inter-model comparisons with other software. The thin films interference calculations for reflectance and transmittance were compared to those computed with TFCalc for two complex stacks. For geometric validation, a complex system was simulated and the results compared with that of a well established geometrical ray tracing software widely used for lamp and lens design. Finally, the embedded implementation of the Perez sky model (Section 3.2.4, Annexe A) was compared to the implementation available in the Radiance suite. All these validations were successful.

6.1.1   Thin film model validation

Transmittance and reflectance coefficients in thin film optical systems are directly influenced by the thickness of the thin films, their refractive indices and the considered wavelength. This was implemented as described in Section 3.2.3 and results were validated by comparison with TFCalc, a well established software for the design of thin films coatings. Firstly, the model was verified with a theoretical stack of four layers alternating low and high refractive indexes to compose an anti-reflective coating. The design of this anti reflective coating is shown in Table 6.1. For the layers of Sol-Gel TiO_2 and MgF_2, constant refractive indices of 2.2 and 1.38 respectively were used with no absorption.

Glass	TiO$_2$	MgF$_2$	TiO$_2$	MgF$_2$
	17.66	50.52	25.0	122.47

Table 6.1 – Materials and corresponding thickness in nm for the simulated anti-reflective design.

Secondly, a more complex solar control thin film coating similar to those described in recent literature [Mack, 2008, Oelhafen, 2007] was simulated. These original designs create an M shaped transmitted spectrum with a very low τ_e/τ_v ratio but keep a relatively high τ_v and a reasonable colour rendering. A theoretical 7 layers design was obtained by optimisation with TFCalc. The target transmittance spectrum for the optimisation step was taken from [Mack, 2008]. The material and thickness of each layer in this coating are described in Table 6.2; the same design was then modelled in CFSPro for comparison.

Glass	Ag	TiO$_2$	SiO$_2$	Ag	TiO$_2$	Ag	TiO$_2$
	19.73	27.68	53.87	11.11	66.53	25.59	38.65

Table 6.2 – Materials and corresponding thickness in nm for the simulated low emissivity coating design.

In this case, spectral values were used for the refractive indexes with an non zero extinction coefficient for the silver coating. In Figures 6.1a and 6.1b the resulting reflectance, respectively transmittance of these designs as issued from CFSPro are compared with those obtained from TFCalc. For the M coating, the incidence angle was also modified to fully validate the used model. Such designs are theoretical and in practice other materials (ZnO, Si_3N_4) are used; additional layers such as an initial adhesion layer and blocker layers are also required. These designs were used for validation only.

It can be pointed out that Monte Carlo simulation is normally not the most adapted method to compute such transmittance spectra, since they can be derived directly from the equations described in Section 3.2.3. However in systems including diffusing elements, prismatic surfaces or discontinued coatings, these calculations can not be performed with conventional

(a) Reflectance of a glass with anti-reflective coating at normal incidence as simulated by Monte Carlo ray tracing and by calculation with TFCalc.

(b) Transmittance of a glass with low-e coating at 0° and 70° incidence as simulated by Monte Carlo ray tracing and by calculation with TFCalc.
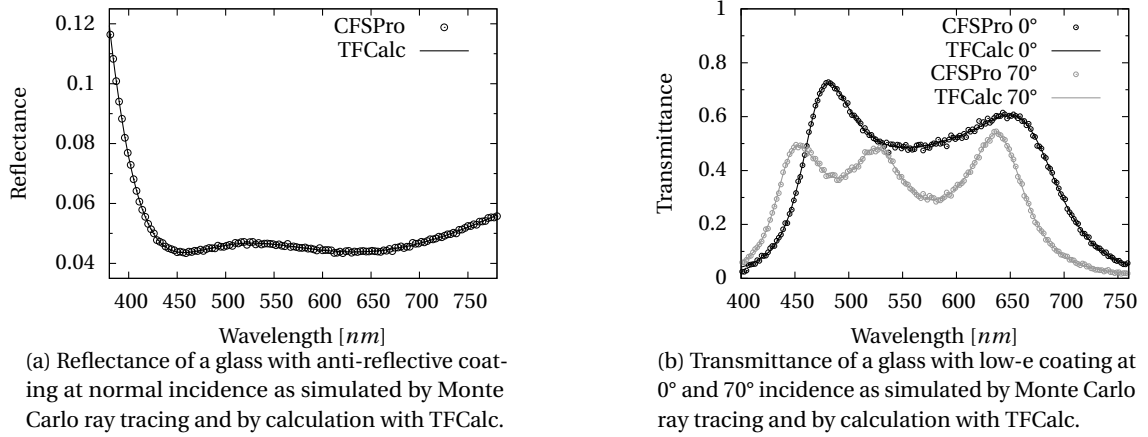
Figure 6.1 – Comparison of TFCalc simulation with CFSPro simulation for validation of thin film model.

thin film analysis tools such as TFCalc or the Essential Macleod. In this case the Monte Carlo approach gives a valuable computation of transmittance and angular distribution depending on the wavelength. By computing the mean energy transmittance of a zone, this method enables the calculation of the energy transmittance of a glazing under a certain sky type, taking into account the location and climatic dependent sky illuminance distribution. However, because of the large set of events due to changing refractive index for each wavelength, a sound statistical estimate of these values requires a large number of rays to be drawn. This is well illustrated in the M coating example where some statistical noise remains even for 500.000 rays traced at a single angle of incidence. This however is not a major problem since the time to trace 500.000 rays on a laptop (2.26Ghz Intel Core 2 Duo) is about 5 to 10 seconds.

6.1.2 Comparison with an other ray tracing software

For the validation of the geometric ray tracing, the Photopia software was selected for comparison. Photopia is a commercial software that enables the modelling of reflective surfaces and refractive materials. It is described as a fast and accurate photometric analysis program that produces comprehensive performance evaluations for non-imaging optical designs [LTIOptics, 2014]. Some simulations were kindly performed by Mark Jongewaard from LTI Optics. The design selected for comparison is an embedded parabolic mirror with an additional backside mirror as described later in Section 6.2.2 and illustrated in Figure 6.2. The purpose and specificities of this design will be explained later, it is presented here as a complex geometry used for validation. In both cases, the embedded parabolic mirrors were modelled using a subdivision into 39 flat mirrors with a purely specular reflectance of 95% and a thickness of $2\,\mu m$. They were embedded in a transparent medium also referred to as resin with a constant refractive index $n = 1.47$ and an extinction coefficient $\alpha = 0.4\,cm^{-1}$. A substrate with a constant refractive index of 1.52 and no absorption was also included in the model. No
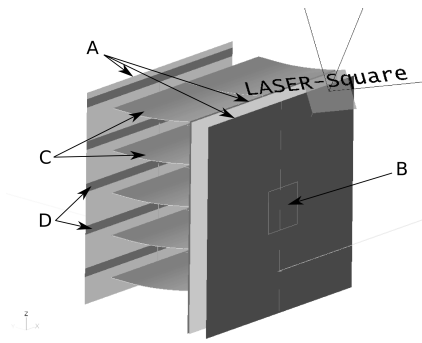
Figure 6.2 – 3D view of the model as simulated with Photopia. The laser source is depicted, simulating a sun at 50° elevation and 30° azimuth. A points towards the interfaces, from right to left between air and substrate, substrate and resin, resin and air. B points towards the aperture in the system, through which light passes. C points toward embedded parabolic reflectors and D towards the backside reflector stripes.

wavelength dependent properties were used because this specific validation focuses on geometrical interactions. The tracing was performed for a light beam impinging at 50° elevation and 30° azimuth. The modelled source was a cone with a half angle of 0.01° hitting a square area of $200 \times 200\,\mu m$ at the centre of a $1,000 \times 1,000\,\mu m$ sample.

Comparing the distributions of transmitted light rays in Figure 6.3 demonstrates that the developed software accurately traces the path of light in a geometrical model. The distributions present some statistical noise (inherent to the stochastic nature of Monte Carlo ray tracing) but are globally identical over six orders of magnitude. The only minor difference between both models was found to be in the rounding. Because the embedded mirror is not modelled as a real parabola but as a set of 39 flat mirrors, the collimated beam generates well defined spots on the transmitted side. Some of these spots are very close to the bounding limit of a bin and a difference in rounding modifies the bin it is counted in. In this particular situation, both software estimated that 77.8% of the light flux is transmitted by the system. This specific angle was chosen for incoming light because at this angle it is reflected by the parabola and concentrated very close to the edge of the backside mirror. Therefore a slight change in the ray tracing has a strong impact on transmittance and reflectance values. This sensibility of the design was demonstrated as initially the thickness of the mirror was not modelled in CFSPro, it created a $2\,\mu m$ shift of the reflecting surface. This minimal shift of 1% of the period height increased the transmittance value by 4.8% points.

6.1.3   Validation of the implemented Perez sky model

The implementation of the Perez sky model has been validated using a series of specific tests. The first most trivial test was to check if the integral of the obtained sky distribution equals the input horizontal irradiance: this test was successful. The implementation was then compared with the validated Perez distribution used in Radiance and implemented in
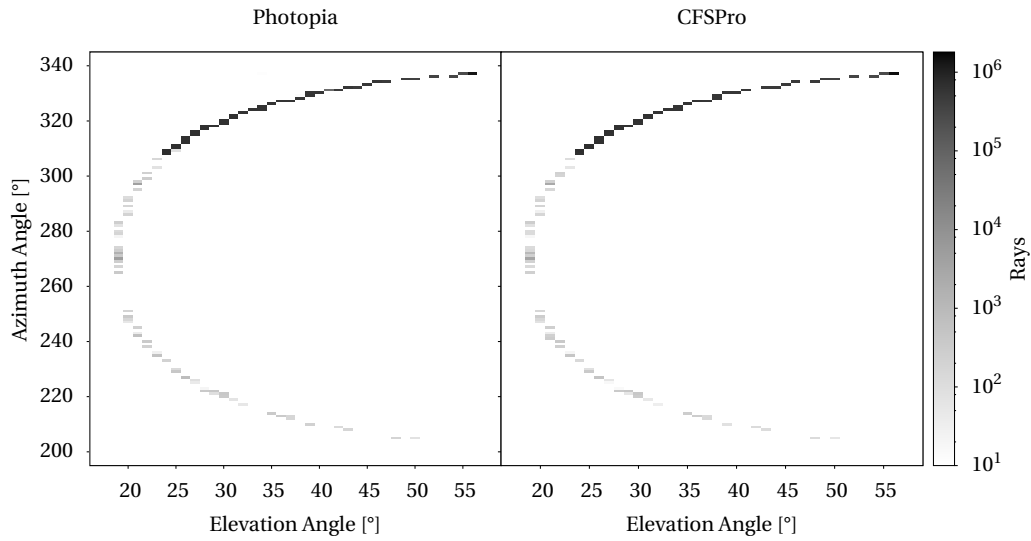
Figure 6.3 – Comparison of transmission distribution by a complex geometry for a single incoming angle as simulated by Monte Carlo ray tracing in CFSPro and Photopia. The simulation was performed at a single incoming angle, simulating a sun at 50° elevation and 30° azimuth. 250 Millions rays were traced in both cases, the figure shows the excellent agreement of the ray count in each 1° bin.

the *gendaymtx* command. The *gendaymtx* command generates an annual series of Perez distributed patches in the Tregenza distribution based on the location and a climatic file. This comparison was conclusive as shown in Figure 6.4a for three selected patches over the course of four summer days. Finally in order to validate the combination of sky radiance distribution, ground contribution and of the patch subdivision performed relatively to the studied orientation, the resulting radiance values were compared with those obtained by the combination of Radiance commands used in the three phase method to obtain the intensity distribution of the hemisphere visible from the window in a Klems representation. In this combination, the results from the *gendaymtx* command are multiplied by a contribution coefficient matrix to obtain the radiance values in each patch of the Klems distribution for the given surface orientation. This contribution coefficient matrix is obtained by the *rcontrib* command, using *genklemsamp* to sample rays in the Klems patches relative to the given surface normal, and the *reinhart.cal* file to bin them into the appropriate sky patches in the Tregenza distribution. The validation was successful for various orientation, in particular the comparison for a random orientation of 121° from north to the east and a vertical tilt of 31° is shown in Figure 6.4b for all patches on three selected days at noon. These comparisons were performed for all days of the year at the location of Lausanne, using an albedo of 0.2 and a climatic data file issued from Meteonorm in Lausanne. The luminance values can be estimated from the radiance with the luminous efficacy given by the Perez model: they depend on the sky clearness. A clear sky has a luminous efficacy of approximately $105 \, lm/W$ whereas an overcast sky has a luminous efficacy of approximately $140 \, lm/W$. More details about these validation are given in Annexe A.
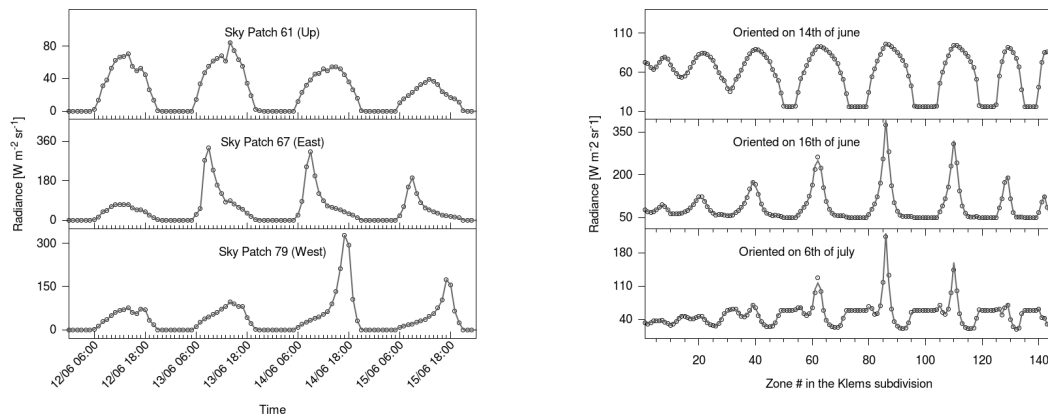
(a) Validation of the Perez radiance distribution implementation by comparison with Radiance (*gendaymtx*). For different sky patches (north, east and west), the good correspondence over 4 summer days is shown.

(b) Radiance distribution over the 145 patches of a Klems subdivision of the visible hemisphere. The window has a 121° eastwards from north orientation and a vertical tilt of 31°. Validation of the implementation by comparison with results from Radiance (combination of *gendaymtx, rcontrib* and *genklemsamp*).

Figure 6.4 – Validation of the sky model implementation by comparison with the implementation in Radiance. The values of the implementation in CFSPro are marked with circles and the results from Radiance with lines.

6.2 Novel design

To find a suitable design reaching a complex set of objectives (daylighting performance, glare protection, seasonal thermal control and transparency) existing products were studied as presented in the state of the art chapter. These products rely on the redirection of light rays to distribute them more evenly in a room and increase the light flux into the depth of the room. For thermal control, static systems use the changing elevation of the sun over the year: for high elevations - in summer- the radiation is reflected or blocked to reduce cooling loads whereas for lower elevations -in winter- it is transmitted to reduce heating loads. The aim was to propose a microstructure achieving these angular dependent behaviours. One of the main challenges was to design a transparent system conserving the view outside and combining the said advantages.

Like many discoveries, the main result discussed in this section started with an observation. During the design of a complex fenestration system with embedded mirrors, it was observed (graphically in the GUI of CFSPro) that the light flux and area of interaction on the backside of the device was changing with the shape of the embedded mirror but most importantly with the incoming angle. This observation led to the development and optimisation of a novel system geometry that simultaneously redirects light rays and blocks a range of selected elevation angle. This geometry was then studied for a certain location and regarding a given meteorological situation. Before introducing this novel two component design, the optimised

embedded mirrors will be compared to an optimised laser cut panel.

6.2.1   Optimisation of redirecting daylighting devices

The first objective was to replace large anidolic daylighting systems and other existing light redirecting devices such as the laser cut panels and Lumitop™ windows with smaller miniaturised embedded mirrors. This further miniaturisation of light guiding devices should reduce production cost, increase transparency and possibly improve performances. Using CFSPro, the tilt angle and periodicity of cuts in a laser cut panels have been optimised for increased light redirection and compared to optimised embedded micromirrors. Results are shown in Table 6.3 as well as in Figures 6.6a and 6.6b.

(a) Ray tracing of a laser cut panel for an incident angle of 65°. The tilted rectangles represent the cuts, light rays are reflected at the interface due to total internal reflection. Because of the large width of cuts, for such elevated incidence angles, light rays are reflected twice and hence not redirected.

(b) Ray tracing of an embedded parabolic mirror for an incident angle of 65°. The changing curvature of the parabola overcomes the problem faced with flat reflective surfaces such as in the laser cut panel.

Figure 6.5 – Ray tracing of embedded parabolic mirrors compared to a laser cut panel at equal angle, the aspect ratio of embedded parabolic mirrors can be larger without encountering the limitation of double reflection.

Assuming a fixed cut width of $0.5\,mm$ and $6\,mm$ depth, it was found that the best design for a laser cut panel is a 3° tilted cut with a $4.5\,mm$ periodicity. As stated in Table 1, 74.0% of the light flux incoming between 50° and 70° is redirected at $4.5\,mm$ interval against 68.7% at $5\,mm$ interval. The custom microstructure (labelled MS in the graph and tables) with parabolic micromirrors reaches 84.8%. The transmittances depending on the incoming angle for this MS and a 3°/$4.5\,mm$ laser cut panel are compared in Figure 6.6a. In such redirecting devices, the increase in the redirected fraction is linked to a larger aspect ratio. For laser cut panels this increase of aspect ratio reaches its limit when light rays starts being reflected twice; as illustrated in Figure 6.5a. By hitting the straight cut once on the way down and a second time on the way up, light rays are no longer redirected. With changing curvature, the parabola overcomes this limitation: higher tilt angle on the admitting side of the system reflect light

	SG	LC0°	LC1°	LC2°	LC3°	LC5°	LC2°/ 3.5mm	LC2°/ 4mm	LC2°/ 4.5mm	LC3°/ 3.5mm	LC3°/ 4mm	LC3°/ 4.5mm	MS
Mean Transmittance	78.0	75.0	76.8	77.7	78.4	78.8	76.0	76.7	77.3	76.2	77.0	78.0	81.7
Mean T_{up} Quadrant	0	41.7	42.9	42.9	42.2	39.7	42.0	44.3	44.6	42.3	44.4	44.4	56.2
Redirected $20° < \theta_{in} < 70°$	0	55.6	54.8	54.1	52.7	50.0	58.7	59.9	57.7	59.4	59.9	56.9	74.7
Redirected $50° < \theta_{in} < 70°$	0	68.5	69.2	69.5	68.7	67.5	57.8	70.8	73.5	62.6	73.7	74.0	84.8

Table 6.3 – Mean percentages for different glasses and different laser cut panels. SG is a standard single glazing with BK7 glass. LC stands for laser cut with different tilts angles and a 5mm periodicity. The periodicity is specified when different. MS stands for the optimised microstructure developed using the ray tracing tool.

rays more horizontally and reduce double reflection for high incidence angles; this can be seen in Figure 6.5b. The reduced thickness of embedded mirrors compared to that of cuts also increases performance slightly. Finally, it was observed that besides impacting the mean angle of transmission, a tilted reflecting surface increases the overall transmittance by reducing the angle of incidence at the second interface and hereby the reflectance at the glass-air interface.
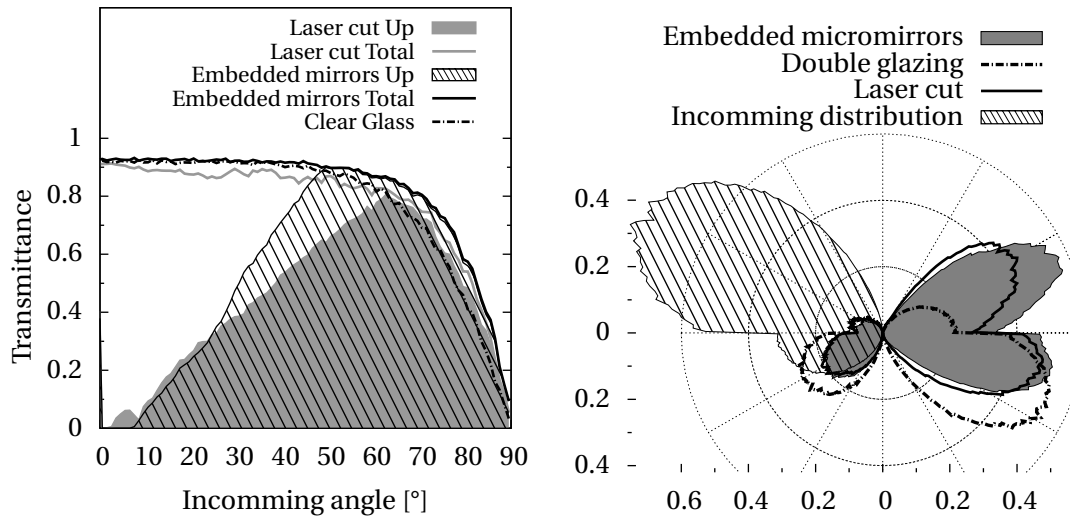
(a) Comparing transmittance for a Lasercut Panel and an optimised custom microstructure.

(b) Polar plot of the transmission distribution under an overcast CIE sky for a laser cut panel and embedded micromirrors.

Figure 6.6 – Comparing performances of an optimised laser cut panel and an optimised embedded parabolic mirror.

The embedded microstructures are also superior for overall transmittance, overall redirection and most important, the "useful" redirection between 20° and 70°: the span of solar elevation during a year in Lausanne and the span with most diffuse irradiance. The redirected light

beam is mainly distributed around 20° for the MS when it is distributed around 30° for the laser cut panel: this is well illustrated in Figure 6.6b, showing a polar plot of the transmitted light beam under a CIE overcast sky. This lower direction in the transmission distribution is better suited for daylighting; moreover, a parallel beam is effectively diffused by the curvature of the parabola. This diffusion is enhanced by the refraction at the rear interface were the angular difference is increased. In conclusion, the use of parabolic embedded mirrors was shown to be superior to laser cut panels for light redirection.

6.2.2 Two component design
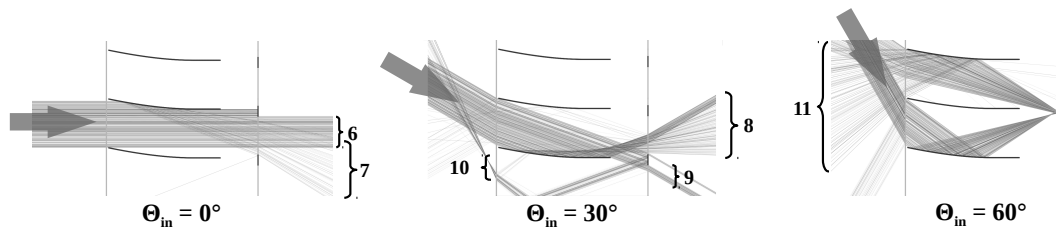
Figure 6.7 – Structure as proposed with incoming beam at 0°, 30° and 60 ° elevation simulated by Monte Carlo ray tracing. The black lines on the right surface of polymer are mirrors. Illustration of focused light and of the resulting reflection on these back surface reflectors. Illustration of light redirection for daylight at lower elevations

With embedded parabolic micromirrors, three of the four objectives set for an ideal glazing were reached. By redirecting light rays, daylighting performance should be increased and glare risks reduced. Transparency is increased by reducing the size of features. In order to add a seasonal thermal control, a second optical element is needed to block light rays from angles corresponding to the summer position of the sun. By using the parabolic mirror to focus light from a given angular interval onto a second mirror placed vertically at the rear side of the system, this angular dependent blocking of solar radiation can be reached. The working principle of this novel design is illustrated with rays incoming at 0°, 30° and 60° elevation in Figure 6.7.

Care has to be taken to arrange the two components in a way that minimizes further interactions and efficiently reflects the light flux out of the system. A careful choice of the blocking angle in correspondence with the summer elevation of the sun at the specified location can create seasonal thermal control as it will be verified in Section 6.5. For Lausanne for example, it is suited to block a large portion of rays incoming with an elevation angle between 50° and 67°; these angles correspond to the sun's elevation at solar noon in September and June respectively. For angles out of the specified blocking range, the reflection on the parabolic shape distributes parallel beams over a range of angles (marked 8 in Figure 6.7). This redistribution of a direct beam is similar to that obtained with anidolic systems [Courret et al., 1998] and is suited for daylighting. To achieve clear view, direct transmission without interaction for close to normal angles is maximised: the two elements have a minimal height and a maximal
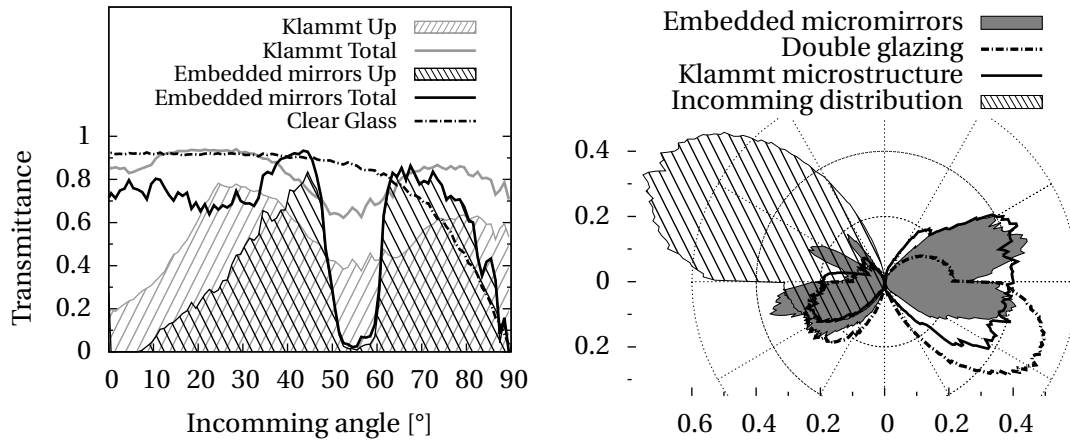
(a) Simulated transmittance depending on the incoming angle for embedded micromirrors and a daylighting device proposed by Klammt *et al.* [Klammt et al., 2012]. The solid line represents total transmittance and the patterned area represents the fraction of transmission that is transmitted upwards and will thereby contribute more significantly to daylighting. The transmittance of a clear glass is shown for reference.

(b) Polar plot of transmission distribution for an standard CIE overcast sky. The embedded microstructures are compared to the daylighting device developed by Klammt *et al.* The transmission distribution of a clear glass is shown for reference.

Figure 6.8 – Performances of an optimised embedded parabolic mirror with backside blocking mirror for focusing range in comparison to an other microstructured light redirecting device.

overlap. In the illustrated design, for normal and near to normal incidence, the mirrors cover less than one third of the area (marked 6 in Figure 6.7). Also, in this design the first and last interfaces are parallel to avoid distorting the image. A patent application for this novel design was filed under the Patent Cooperation Treaty (PCT).

The performance of the proposed structure compared to that of a state of the art microstructure proposed by Klammt *et al.* [Klammt et al., 2012], introduced in Section 2.3.1, is illustrated in Figure 6.8a. The latter microstructure has a large transmittance for angles of incidence up to 85° and is very efficient at redirecting light from all angles; about 75% of the transmitted light flux is redirected upwards. The large transmittance at high incoming angles is explained by the geometry of the first interface (see Figure 2.6). It is not flat and the curved quarter circles strongly decrease the angle of incidence relative to the surface, and hereby the reflectance; this also destroys the imaging properties as interfaces are not parallel. After the first interface, embedded mirrors also increase transmittance at high angles of incidence when compared to double glazing by reducing the angle of incidence on the remaining interfaces. The former redirects 64% of the transmitted light flux but can be seen through in the near to normal range were it has low redirection rate (14%). For the remaining angles (25° to 90°) both systems redirect 85% of transmitted light flux but the mean transmittance of the device proposed by Klammt is larger. The microstructure proposed by the author additionally has a low mean transmittance (26.2%) in the targeted blocking range (between 55° and 70°). It can

be mentioned that this device surpasses many earlier daylighting devices relying on light redirection, such as laser cut panels.

Regarding the distribution of transmitted radiation, the performance of the proposed structure compared to that of the geometry proposed by Klammt *et al.* is illustrated in Figure 6.8b. The overall transmittance for a CIE overcast sky is 83% for the Klammt microstructure and 65% for the proposed microstructure; in comparison a single pane of clear glass transmits 79% of the light flux.

In conclusion, the defined two components system creates strong variation of transmittance (respectively reflectance) depending on the incoming angle of light rays: for a selected interval of angles, the incoming light beam is mainly reflected; for angles close to the normal, most of the light beam is transmitted with no significant deviation and for the remaining angles, most of it is redirected in the opposed direction, in a diffuse way. This design provides both a strong light redirection and angular dependent transmittance required to satisfy the complete set of objectives set for this thesis. It was assumed that a seasonal thermal behaviour would be created by a strong reduction of transmittance for elevations close to those of the sun during the hot season. For daylighting it was assumed that the light redirection extends the daylit area within the space. Based on the results obtained in this section, it is however not possible to quantify how the workplane illuminance in a space is really increased and whether or not the thermal comfort is really improved over the year. By adding an extended thermal and daylighting study as described in Section 3.4, it will be verified that these assumptions are correct (Sections 6.4 and 6.5). Also with the related thermal and daylighting performance indicators, the design will be further optimised. But before performing this optimisation, the structure needed to be better understood and the different parameters defining the geometry were studied to be able to understand their effect on angular properties. This will be useful to adapt a geometry to provide an ideal transmittance depending on the location specific, annual incoming radiance distribution and an ideal transmission distribution (specific to the room).

6.3 Parameters study

The shape and the parameters defining the novel geometry introduced previously are introduced in Figure 6.9. As introduced above, the light-path through this design depends strongly on the incoming angle. Depending on the objectives, the geometry might be modified to meet the needs accordingly. In this section, the implications of each parameter will be studied as well as the interconnection between them.

6.3.1 Terminology and parameters

Light rays transmitted through the system without hitting any of the two components will be referred to as direct transmitted light flux. Light rays reflected by the parabola but passing by
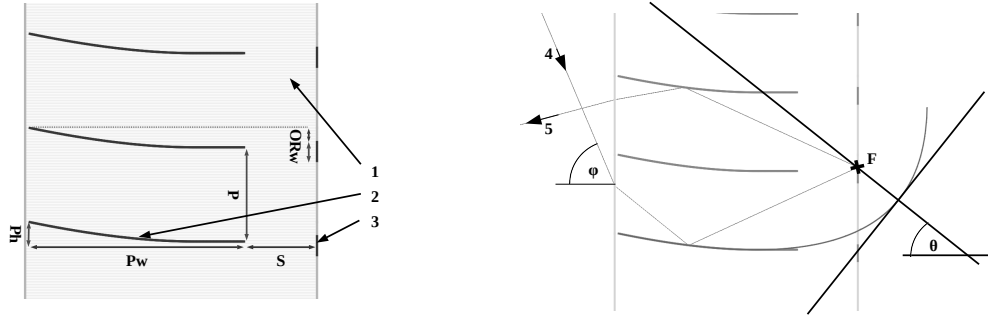
(a) The generic sizing parameters of the design: period, width, spacing, etc. The grey area (1) corresonds to the resin embedding the mirror (2).

(b) The parameters of the parabola defining its curvature. The path of a ray illustrates the effect of refraction on the parabola main axis angle to horizontal (θ).

Figure 6.9 – Parameters of the proposed design.

the second component will be referred to as redirected light flux. Finally light rays focused onto the second element will be referred to as selected light flux. The material or resin (1) refers to the medium the mirror is embedded in, it has a given refractive index n_r. First surface, first mirror, parabolic mirror or parabola refer to the component noted (2) in Figure 6.9a, likewise back mirror, blocking mirror, vertical mirror refer to component (3). The front side refers to the left-hand side interface; back side or rear to the right hand side surface. Projected obstructed ratio (POR) refers to the ratio of surface obstructed by some non transparent element when looking at normal incidence.

The following symbols are used in Figure 6.9:

- P is the period between two parabolic mirrors
- The focal point (F) is placed on the back side of the system
- P_w is the parabola width
- P_h is the parabola height
- O is the vertical offset between the focal point F and the parabola starting point.
- S is the horizontal offset between the focal point and the parabola ending point
- R_w is the width of the blocking mirror
- ϕ is the angle for which light will be focused at F
- θ is the parabola main axis angle (it is the angle at which the incoming light rays are focused)
- r_m the mirror reflectivity

6.3.2 Effects of parameters on light path

- The period P is chosen as the reference parameter, a smaller period will decrease the overall size of the structure and hereby increase the perceived transparency. The angular behaviour will however not be affected since changing the period will scale other elements accordingly.

- The focusing angle (ϕ) is the main parameter, it has to be chosen according to the desired application of the system.

- The parabola tilt angle θ is directly dependent on (ϕ), the refraction at the first interface has to be accounted for to calculate it:

$$\theta = \arcsin(\sin(\phi)/n_r) \tag{6.1}$$

- The focal point F is generally located on the back surface, it may however be shifted by changing the offsets S and O.

- Reducing the horizontal offset S, increases the curvature of the parabola, the redirected light is hence diffused more.

- Increasing the horizontal offset S, decreases the curvature of the parabola and increases it's tilt, the redirected light is hence diffused less and more horizontally.

- Reducing the vertical offset O increases the parabola tilt and affects the main direction of redirection.

- The width of the first mirror P_w determines the aspect ratio of the structure.

- The vertical dimension of the embedded mirror P_h is modified indirectly by changing O, S, P_w and ϕ.

- The aspect ratio and (P_h to some extend) determine the range of angles for which the parabola redirects light. Depending on these values the shading angle θ_s can be defined:

$$\sin(\theta_s) = n_r \cos\left(\tan^{-1}\left(\frac{P_w}{P + P_h}\right)\right) \tag{6.2}$$

Above this angle, all the light flux transmitted by the first interface will hit the parabola. Below this angle, the portion of light rays hitting the parabola gradually declines.

- The width of blocking mirror R_w influences the blocking range. The wider the mirror, the higher the blocking range. The rear mirror generally starts at the focal point and goes down, so maximal blocking efficiency will be reached at ϕ. The blocked proportion remains maximal for some degrees, when lowering the incoming angle and then gradually decreases.

- The reflectivity of the mirrors r_m defines the fraction of reflected light beam. Generally it is maximised and the remaining light beam is absorbed.

6.3.3   General design guidelines

Parameters should be chosen in a way to avoid multiple reflections. The path of most of blocked rays should have two reflections, at most three. This reduces the absorption in the system and therefore reduces overheating risks. The tilt of the parabola in its left most part should be strong enough to avoid inter-reflections.

To obtain a transparent design, the influence on light rays impinging with normal incidence has to be minimised. The total height of the embedded mirror P_h and the back reflector height R_w should not be too large and overlap to a certain extent. The parallel arrangement and smooth surface of the front and back interfaces can than preserve the view through the system.

Since the focus effect should be achieved for angles corresponding to the summer sun elevation, and not for lower winter elevations, the region of the surface useful for focusing does not include the part of the parabola towards the inside of the glazing. This surface can be left flat or tilted and serve only for daylighting purpose.

With the effect of parameters understood, a proper objective needs to be set regarding blocked angular range for thermal control, as well as distribution and orientation of redirected light rays for optimal daylighting contributions.

6.4   Daylighting performance

Because it can be treated as a general, not so location specific characteristic, the daylighting aspect will be studied first. Using the Radiance based approach described in Section 3.4.4, the contribution of the different outgoing directions of a window can be studied for different locations in the room. The results of this study will be presented first along with preferred directions to reach a maximal mean task illuminance with a minimal variance. These insights will then be applied to suggest a better microstructure which will be assessed using the daylight factor. Finally a climatic dependent analysis is presented and the design compared to a double glazing with low-e coating and to a daylighting system.

6.4.1   *V* matrix study

As introduced in Section 3.4.4 and equation (3.12), to compute dynamic daylight metrics, researchers introduced a matrix approach to derive the illuminance for various sensor points. In this approach a contribution coefficient matrix, generally referred to as *V* matrix, quantifies the contribution of each outgoing direction of the window to each sensor. In order to define in which direction it is preferable to redirect light rays to improve illuminance in the depth
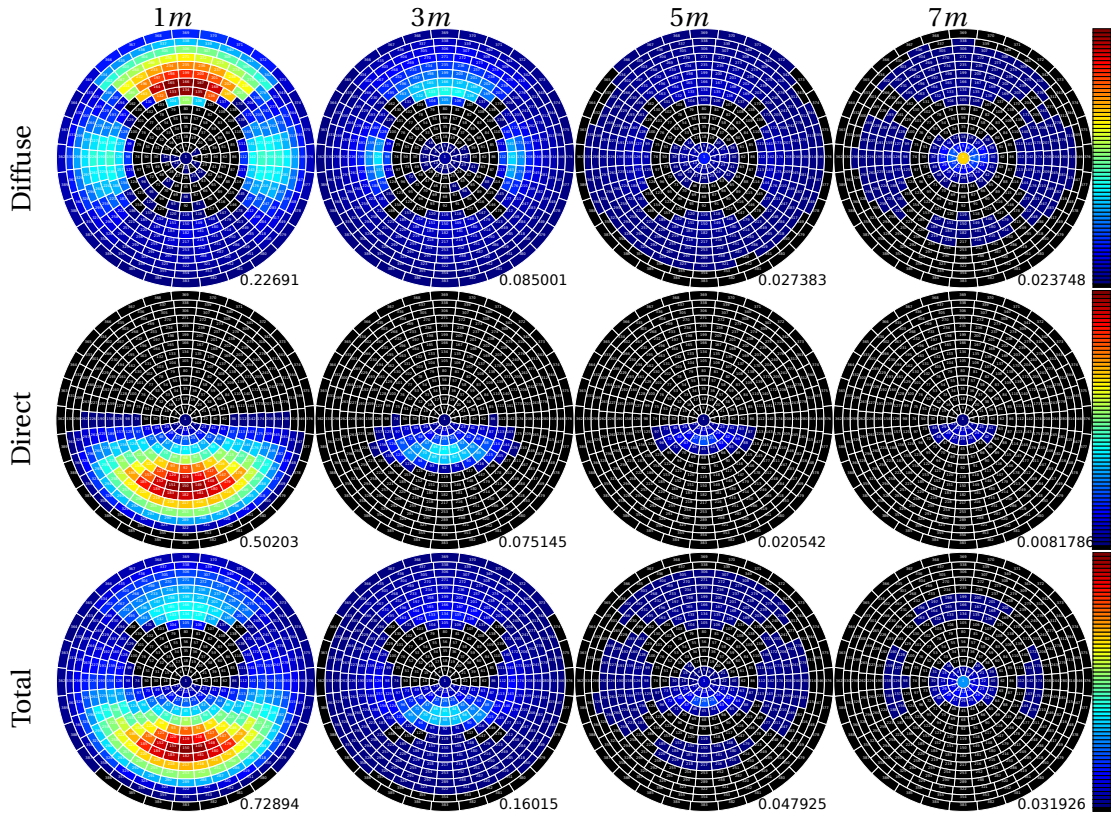
Figure 6.10 – Study of V matrices obtained with Radiance for the comparison of window contribution to illuminance for different directions depending on the depth into the room. Each patch in the circles gives the mean contribution to illuminance for the corresponding direction. Looking at the first column, for a distance of $1\,m$, the direct contribution is mainly due to downward directions whereas the diffuse contribution at this depth is mainly do to directions that are reflected by the ceiling and walls. In the last row, the total contribution gives an information about the relative importance of direct and diffuse contributions (each row has its own scale relative to the maximum value in the row). The room is the standard room from Reinhart with no furniture. The value on the bottom right hand side of each circle gives the mean irradiance level at this depth for a window with a Lambertian radiance of $1\,W \cdot sr^{-1} \cdot m^{-2}$

of a room, the V matrix obtained by Radiance simulation for a standard room as described in [Reinhart et al., 2013] was considered. This standard room used to study daylighting and electric lighting has a depth of $8.2\,m$ to outline the daylight contribution of CFSs far from the window. Arrays of sensors were first placed, centred at distances of 1, 3, 5 and 7 meters. Each array was composed of 7x7 sensors placed at regular intervals of $15\,cm$ along the y axis (depth of the room) and equally spaced along the room width in the x axis. The V matrices obtained by *rcontrib* for each of these arrays were then averaged. The resulting mean V

91

matrices give an averaged contribution from each direction of the window at 1, 3, 5 and 7 meters. To differentiate direct and indirect contribution, a simulation was run with fully absorbing surfaces everywhere; this simulation yields V matrices for direct contribution only. By subtracting the latter to the global V matrices obtained with reflecting materials, the contribution of light rays reflected once or several times upon walls, ceiling and floor can be obtained (later referred to as diffuse component).

The results presented in Figure 6.10 for the standard office room (window to wall surface ratio (WWR) of 0.4) confirm that the most important light rays direction to enhance task illuminance deep into the room are those illuminating the ceiling and walls. This includes the wall located in the back for the area in the depth of the room. The contribution of direct light rays however is also of significant importance, even deep into room. At seven meters, the direct contribution of 15 zones in the subdivision of the hemisphere is approximately one third of the 120-130 zones contributing indirectly. These directions, close to horizontal have however to be used sparingly to increase daylight illuminance because they can also induce glare: they are typically the one looked at when entering a room.

A few parameters of the room were then studied: ceiling specularity, room depth, WWR and window position. Regarding the WWR, findings of [Reinhart et al., 2013] were confirmed, the illuminance in the room strongly increases when the WWR is raised from nil to $0.4 - 0.5$. Further increase only mildly raises workplane illuminance. It can be noticed that for this room configuration, at approximately $5\,m$ depth, the diffuse contribution overtakes the direct contribution for all WWRs.

Modifying the height of the window centre displaces the maximum of direct contribution; this contribution obviously decreases with the distance from the window. As illustrated in Figure 6.11c for diffuse contribution, the optimal solution at all distances is a centred window. The specularity of the ceiling was also studied: as expected when increasing specular reflections, the diffuse illuminance increases significantly (almost double) in the back of the room and decreases slightly close to the window. This effect is illustrated in Figure 6.11b.

6.4.2   Optimal target

Using a V matrix for an array of equally spaced points in the reference room, the optimal distribution among the outgoing patches was searched. This distribution, when multiplied with the V matrix, yields the most homogeneous possible illuminance distribution among the sensor points. The mean value of the resulting illuminance should be maximised. To reach this objective, two approaches were attempted. The first used the *optimize* command in Matlab with the constraint of a maximal total radiant exitance of $1\,W \cdot m^{-2}$ and objective to maximise the average minus the standard deviation of irradiances at the sensor points. The second used a genetic algorithm (GA) to search for an optimal distribution with a merit function targeting a minimal value above a certain threshold and a mean value as large as possible but not larger than double the lowest value. This minimal threshold illuminance
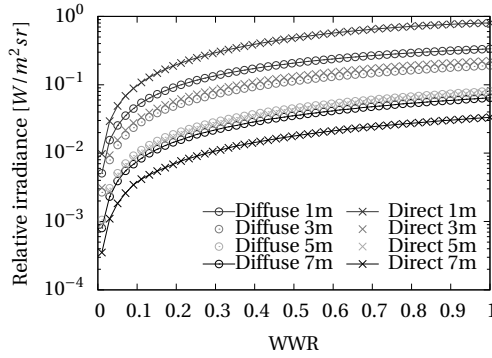
(a) Influence of WWR on irradiance in standard room. The irradiance increases exponentially at first but above 0.5 the increase is moderate.
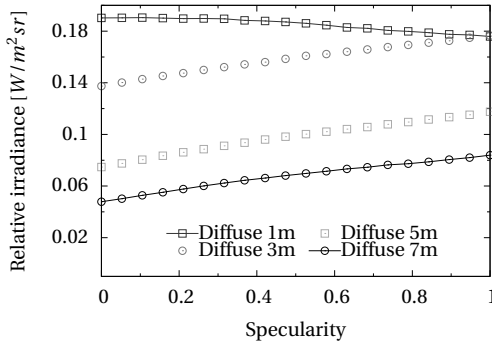
(b) Influence of ceiling specularity on irradiance in standard room. It is not shown for the direct contribution because it has no influence on direct contribution.
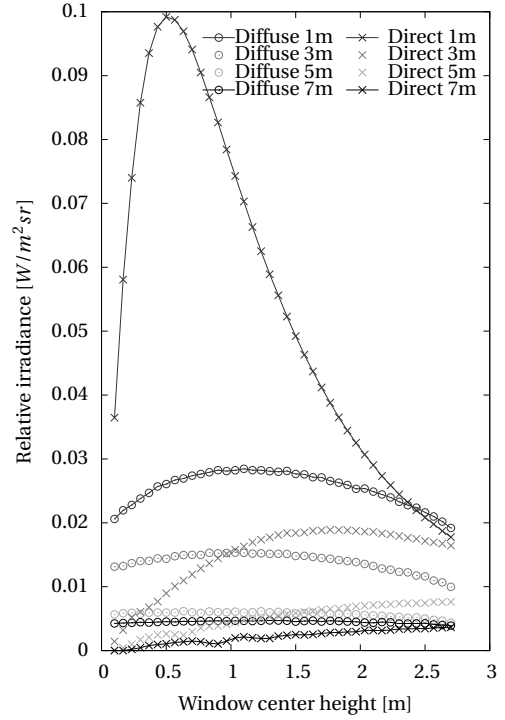
(c) Influence of window position on irradiance in standard room with a constant window height of $0.2\,m$.

Figure 6.11 – Window size and position parameter study, influence of WWR and window heigh on irradiance depending on the depth in the room for diffuse and direct. The irradiance is given for a window with a Lambertian radiance of $1\,W \cdot sr^{-1} \cdot m^{-2}$.

for sensors was set at $0.06\,W \cdot m^{-2}$, given a radiant exitance of $1\,W \cdot m^{-2}$; this would roughly corresponds to a minimal illuminance of $100\,lux$ for a window with a transmittance of 0.7 under a sky with a vertical illuminance of $2,000\,lux$. The later distribution over patches is presented in Figure 6.12a; the corresponding irradiance for a window with a radiant exitance of $1\,W \cdot m^{-2}$ is illustrated in Figure 6.12. The results from the Matlab approach are very similar.

6.4.3 Adapted geometry

The conclusion of this study on the V matrices was applied to the embedded parabolic mirrors. In order to redirect light more horizontally, the structures where tilted a bit more by increasing the distance to the focal point and the vertical offset. Too much tilt is however not possible
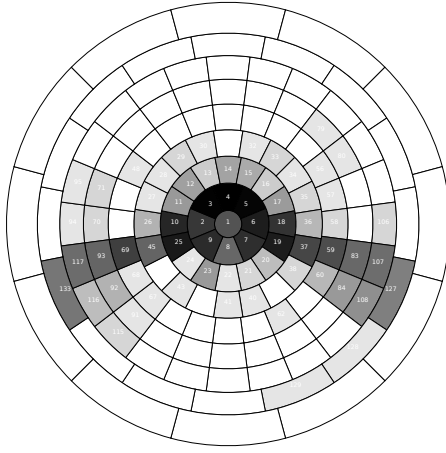
(a) Selection of optimal outgoing directions for a uniform daylight level. Importance of patches is illustrated by the grey levels on a logarithmic scale.
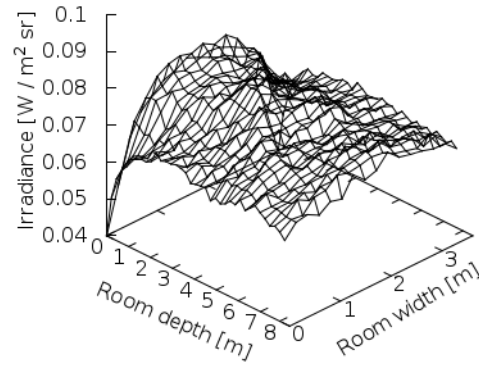
(b) Corresponding irradiance as computed by multiplying the outgoing distribution shown in Figure (a) by the V matrix.

Figure 6.12 – Optimal directions for daylight and corresponding irradiance.

because it decreases the transmittance and impacts the view through the device. The related improvements are presented in the next subsection.

6.4.4 Daylight factor

The DF was simulated with Radiance in the reference office for the different dayighting systems. Like for the *V* matrix computation (using *rcontrib*), this computation (using *rtrace*) required an appropriate choice of Radiance parameters. Radiance is a very powerful tool with the potential to provide physically sound results. But as illustrated by the recent withdrawal of the "Understanding *rcontrib*" tutorial from the web [Jacobs, 2014, Jacobs, 2010], inappropriate use of this tool can provide irrelevant results (which in this case led to wrong policies according to Jacobs). To choose the proper parameters, they were modified one by one and the DF in the reference office was computed for a CFS with redirecting properties. For each parameter a convergence was targeted and the least computationally expensive parameter providing this convergence was chosen. Figure 6.13a illustrates the impact of the chosen parameters on the result, DF in this case. Table 6.4 lists the parameters used for the DF results presented in this section.

In Figure 6.13b, the DF profile of a double glazing is compared to embedded micromirrors. For a fair comparison, the device with embedded micromirrors is associated to a second glass pane with a spacing between the two elements. This way the number of interfaces is identical and the devices can be compared. With such optimised embedded mirrors, the DF

Daylight factor	-u+ -ab 9 -ar 30 -aa 0.15 -ad 4096 -as 256
V matrix	-ab 10 -ad 65536 -lw 1.52e-5
Basic rendering	-ab 2 -ar 32 -aa .2 -ad 256 -as 128

Table 6.4 – Radiance parameters for daylight factor, V matrix calculations and set of parameters for different rendering settings.

at 8 *m* is increased of about 50% relative when compared to the double glazing. The DF is strongly decreased close to the window, the contrast in illuminance within the room is hereby decreased and with a lower maximum illuminance level, the eye of the occupant can better adapt to lower illuminances. This has a positive impact on the user comfort beyond the minor increase in the DF. It can be noticed that in comparison, the device proposed by Klammt and laser cut panels have a lower performance. Using the insight from the daylighting objective study, the geometry of the embedded mirrors was improved to redirect light in a direction closer to horizontal by tilting the mirrors. This however reduces transparency as the POR of the mirrors is increased. In addition, when tilting the mirror strongly, contribution from the ground are severely cut since the convex curvature of mirror when reached from the bottom reflect light rays at a different angle; this leads to several inter-reflection between adjacent mirrors and to rays reaching the backside interface with an incident angle beyond the critical angle.
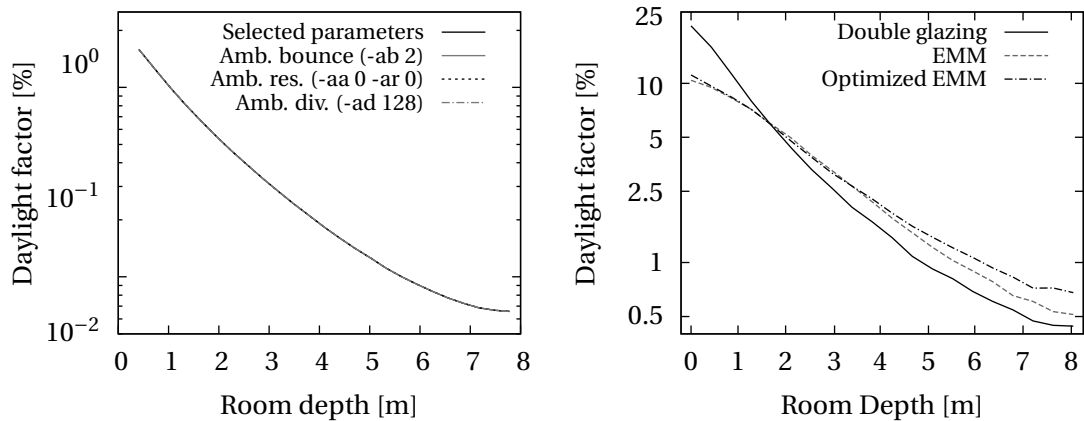
(a) Parameter study for computation of DF with Radiance. With inappropriate parameters, the daylight factor in the depth of the room can be underestimated by a factor of 2 to 3.

(b) Daylight factor for embedded micromirrors (EMM) before and after optimisation compared to a double glazed window.

Figure 6.13 – Daylight factor Radiance parameters study and resulting DF curves for various fenestrations.

6.4.5 Daylight autonomy and useful daylight illuminance

As introduced previously the DA and UDI metrics were implemented to assess daylighting performances. The large window of the reference office room (40% WWR) is already a relatively optimal solution from a daylighting point of view. From a quantitative point of view, a large window admits a large light flux into the space. But the distribution and the strong variations in illuminance are not very advantageous from a qualitative point of view. The comparison of DA_{300lux} profile between a double glazing and the embedded mirrors associated to a single pane of glass is shown in Figure 6.14.
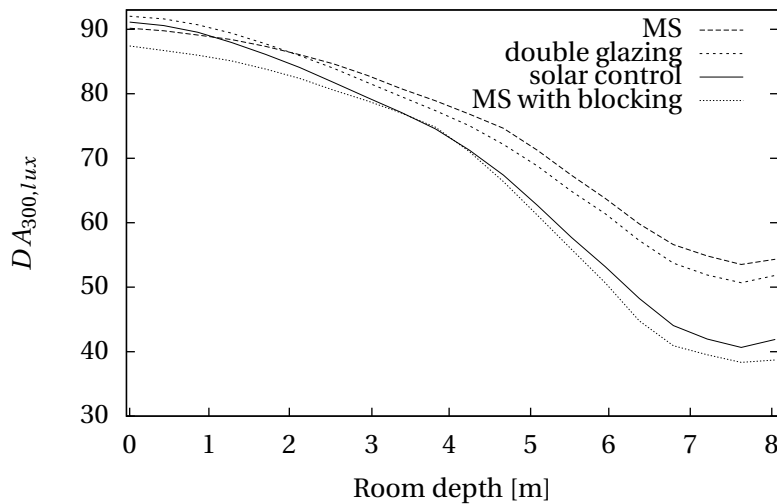
Figure 6.14 – Daylight autonomy ($300\,lux$): when comparing a double glazing with embedded micromirrors, the micromirrors achieve superior DA at $8\,m$ by a few percent points. When adding 35% of reflective surface and comparing to an equivalent (in hemispherical transmittance) solar protective glazing, the DA values are a few percent points below but still comparable. As it will be mentioned in Section 6.7.1 this lower performance can be increased by the use of selective coatings. With a high transmittance in the visible range, microstructures with such coating can reach a DA close to that of the structure with no blocking mirror and therefore about 10% above that of the solar control glazing. The low energetic transmittance of the coating replacing the blocking mirror on the other hand conserves the seasonal thermal behaviour of the microstructured glazing, and thus the increased energetic performances studied in the next section.

In conclusion, embedded mirrors increase the daylight provision in the depth of the room: the DF is increased by 50% and most importantly the ratio between the minimum and maximum DF is reduced from 47 for a double glazing to 16 for the optimised embedded mirrors. The latter reduction induces a more homogeneous workplane illuminance. The DA is increased by a few percent points at $8\,m$ depth in the room; when adding a back mirror covering 35% of the glazing surface, the DA is lowered a bit along the depth of the room but comparable to that of a solar control glazing with equivalent transmittance. If the back mirror is replaced by a selective coating with high visible transmittance and low energetic transmittance, the increase in DA can be as high as 10% when compared to a solar control glazing, yet the seasonal dynamics

of the microstructured glazing is partly conserved. This back mirror or selective coating is present in stripes and provides a cut in the transmittance for selected incoming elevation angles as illustrated previously in Figure 6.8a. The effect of this reduced transmittance will be assessed by a thermal analysis of the office room in the following section.

6.5 Energy performance

Now that it is known how to ideally distribute daylight within a given office room to obtain an elevated and homogeneous task illuminance, the question remains about which directions in the sky for a given orientation are most suited for winter solar gains and which are unfavourable in summer: the later should be blocked and the former admitted as much as possible. To clearly identify these, the annual irradiance values of the 145 Klems patches for a given orientation were computed using the implemented Perez sky model. This hourly data was then analysed in correlation with the hourly temperature evolution. At first this was carried out in a static manner and later dynamically, using the reference room with its thermo-physical properties and the corresponding nodal thermal model. For a south oriented reference office room located in Lausanne, the results are presented in this section. The initial design was improved based on these learnings and the new thermal loads were computed.

6.5.1 Optimal target

The repartition of irradiance over the visible hemisphere were summed and weighted using a method suggested by [Wirth, 2000] to weight the g-value over the year and propose a winter g-value that should be larger and a summer g-value that should be low. The factors were computed for Lausanne (Switzerland), based on the mean daily temperature with a maximum for the summer coefficient when the temperature is the highest and a maximum for the winter coefficient when the temperature is the lowest. The reference temperature was set a $12°C$; resulting coefficients are illustrated in Figure 6.15b. When applied to irradiance data, this yields a distribution of the most undesired directions for solar gains in summer and the weighted mean of their contribution. It also provides a weighted mean irradiance information about the direction best suited for thermal gains in winter; these two distributions are shown in Figure 6.15a. By subtracting these two distributions, the patches with a positive thermal impact can be identified; they are greyed out in Figure 6.15c. The slight asymmetry in this figure between east and west might be linked to the statistical distribution of the climatic data or to a more sound meteorological effect such as overcast mornings and clear evenings in winter or vice-versa in summer. Also it has the be pointed out that this boolean representation provides no information about the amplitude of the difference between summer and winter contributions. In deed, the difference between winter and summer distribution for patches 91, 116 and 126 is smaller than 1% of the maximal difference (for patch 22).

In the original approach of Wirth, monthly values were taken and resulted in coefficients that are both nil or low in the spring and autumn period. In the hourly calculation of the

(a) Weighted mean of irradiance distributions in summer (left-hand side) and winter (right-hand side) for a south oriented façade in Lausanne. A horizontal diametrical line in the hemispheres would represent to horizon. The two scales are different, the available, weighted radiation in summer is higher than in winter.
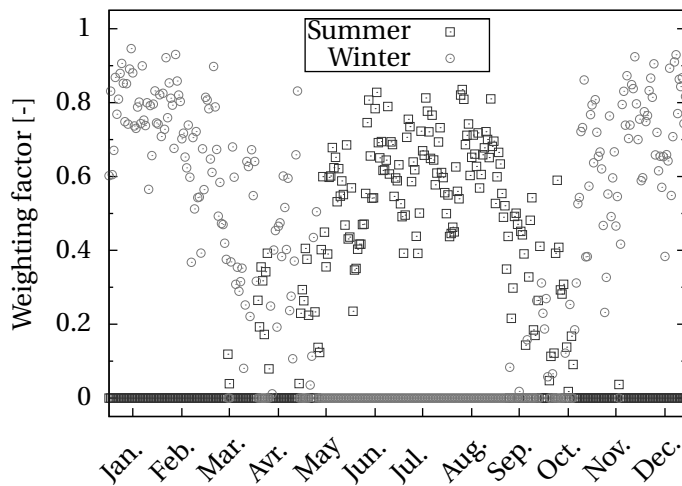
(b) Daily winter and summer weighting factors for Lausanne (Switzerland) as proposed by Wirth. The factors were computed based on the mean daily temperature and its difference with a reference temperature of 12°C. In spring and autumn, heating and cooling days can alternate.
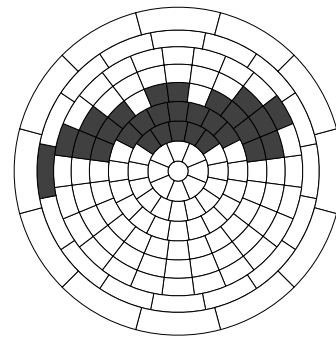
(c) Patches with advantage to have thermal gains in winter: patches where winter - summer > 0 using the values from figure (a).

Figure 6.15 – Study of annual thermal gains, selection of most favourable direction for lowest thermal loads.

coefficients performed for this study, illustrated in Figure 6.15b, the coefficient are not zero but both reduced in the spring season with the winter coefficient slightly above the summer coefficient. This is in contradiction with what was observed in the initial thermal simulations (Figure 3.11): the strongest raise in temperature for a solar protective glazing is in spring. During spring, the elevation of the sun is low and the solar gains per unit of vertical surface area are not yet reduced by a strong cosine factor. Additionally with modern construction that are well insulated, the solar gains in spring are "stored" by the thermal mass and the

temperature overshoots in summer. The combination of the annual thermal dynamic and distribution of available radiation was not taken into account in the approach inspired by the method of Wirth to propose seasonal *g* values. A GA approach was attempted to minimise the annual thermal loads (heating and cooling treated equally.) based on the nodal thermal model described earlier, the temperature data and the hourly irradiance distribution. The resulting ideal transmittance for each zone are illustrated in 6.16 along with the resulting annual thermal loads and temperatures.

(a) Ideal transmittance values for each patch (regarding the incoming direction) as obtained by GA optimisation to minimize thermal loads.

(b) Results of thermal simulation using an ideal transmittance as shown in figure (a). The temperature evolution with no cooling or heating is shown in black and the annual cumulated thermal loads in case of cooling and heating in grey (target room temperature between 18°C and 26°C, COP of 3).

Figure 6.16 – Genetic algorithm optimisation of the transmittance depending on the incoming direction (annual irradiation distribution for Lausanne, Switzerland) to find the optimal annual thermal gains distribution for reduced annual thermal loads.

6.5.2 Dynamic solar gains

The annual thermal gains due to direct and diffuse solar radiation of the novel design were computed and compared to those of a double glazing with an energy transmittance $\tau_e = 0.7$ at normal incidence. This glazing was selected because the hemispherical transmittance with uniform irradiance of the two devices are comparable (0.42 and 0.46). Using the lessons learnt from the above GA optimisation, the structure was adapted to better reach the objective of seasonal thermal dynamics. Daily values for diffuse and direct components are shown in Figure 6.17a and 6.17b. The total energy transmittance of direct solar radiation by the designed microstructured glazing is 40% lower than that of the double glazing during the summer period (21st of June to 22nd of September) and only 7% lower during the winter period (22nd of December to 20th of March). Considering the diffuse contribution only, it transmits 20% less heat during summer and 17% less during winter. On a clear summer day,

direct sunlight accounts for about half of the incoming solar radiation and therefore this strong variation in transmittance of the direct component should have notable impact on the temperature evolution.
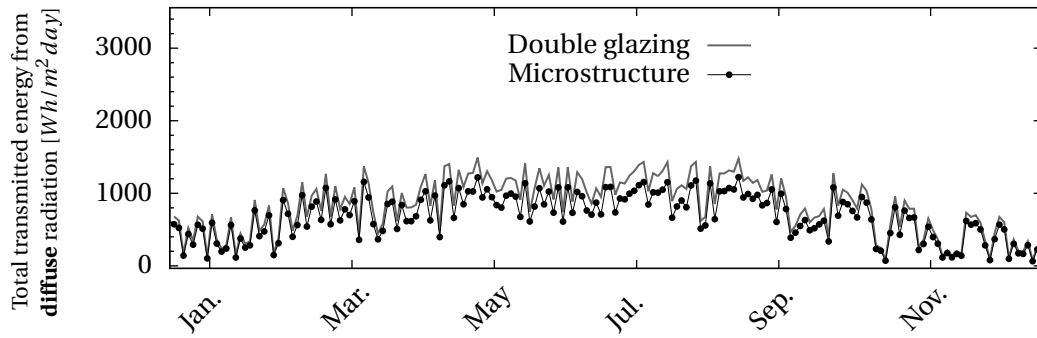
(a) Daily gains from diffuse radiation in Lausanne for a microstructured glazing and a double glazing.
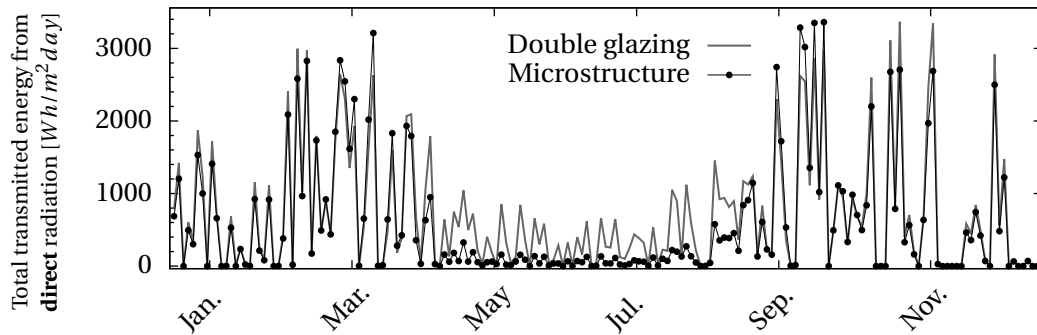
(b) Daily gains from direct radiation in Lausanne for a microstructured glazing and a double glazing.

Figure 6.17 – Thermal gains in Lausanne considering a $8.2\,m \times 3.5\,m \times 2.8\,m$ south oriented office.

6.5.3 Heating - cooling

Thermal simulations were then performed for an office room using these dynamic solar gains, an infiltration rate of $0.5\,ac/h$, a well insulated façade ($20\,cm$ wood and $20\,cm$ insulation layer providing $U = 0.15[\frac{W}{m^2 K}]$) and a reasonable U value for the window ($U = 1.1[\frac{W}{m^2 K}]$). For the double glazing in the extreme case were no cooling, heating or ventilation is used except for the infiltration rate, the temperature rises too high values of nearly $40°C$ as show in Figure 6.18a. Because the space is well insulated and the surface of the window amounts to nearly $6m^2$, the mean daily solar gains are about 9kWh (mean of $1.5kW/m^2$ per day during summer) whereas the losses are comparatively very low (approximately $2kWh/m^2$ per day during summer, considering a mean temperature difference of 10 degrees). In fall the temperature for the room fitted with a microstructure catches up with that of the solar control glazing because the back mirror is out of focus and solar gains become more important again and are superior to those allowed by the solar control glazing. When adding an angular selectivity

and blocking the incoming solar radiation from an angular interval around 60°, the gains are mitigated as shown in Figure 6.17. This reduction of solar gains reduces the temperature during summer by 5°C. The required energy to keep the room temperature between 18°C an 26°C considering a heating, ventilation, and air conditioning (HVAC) system with a coefficient of performance (COP) of 3.0 for both heating and cooling is pictured in 6.18b. The heating loads are slightly increased during the heating season because solar gains are also slightly mitigated during winter. The cumulated annual energy demand however was reduced by 25%, from 10.3kWh/m^2 to 7.7kWh/m^2. This result demonstrates that a static system with an angular selectivity can create seasonal thermal dynamics.
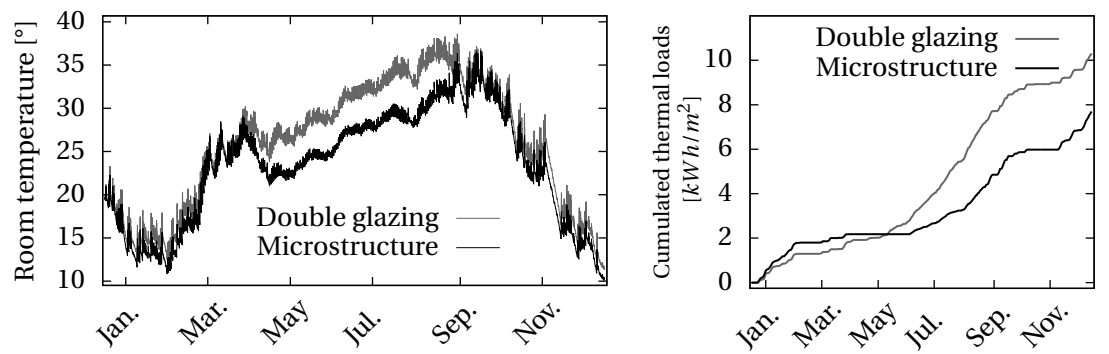
(a) Temperature evolution with no cooling, heating or ventilation except an infiltration rate of 0.5ac/h.

(b) Thermal loads for heating and cooling with a COP of 3.0 for a target temperatures between 18°C an 26°C.

Figure 6.18 – Thermal study considering the computed thermal gains for a double glazing and a microstructured glazing.

The effect of angular dependent transmittance on seasonal variation of solar gains was shown. The resulting thermal gains were applied in a simple nodal model to estimate the corresponding thermal loads. When large windows areas are used, the proposed microstructure can significantly reduce thermal loads compared to a solar protection glazing. This is in particular true when the heating COP is larger than than the cooling COP which is generally the case when a reversible heat pump is used for cooling and heating ($COP_{heating} = COP_{cooling} + 1$): using a COP of 4 for heating in the example above, the energy saving increase to 30%.

6.6 Rendering

For the optimised embedded parabolic mirrors combined with a blocking back mirror, an XML description of the CFS was generated to be used in Radiance. The office room was then rendered to get an impression of the indoor environment with such a system. It is compared to a double glazing with a visible transmittance at normal incidence of $\tau_\nu = 0.7$, corresponding to a double glazing with a low-e coating. The scene was also rendered for a laser cut panel and for an embedded mirror with no back reflector; all these renderings were performed on the spring

equinox at noon (21st of march) for a clear CIE sky; they are presented in Figure 6.19. When looking at the illuminance levels on the desk placed further from the window and comparing the embedded mirrors to a double glazing, the maximum level is decreased (no bright area on the desk) but stays high (approximately $5,000\,lux$). The minimum levels on the other hand is increased form about $700\,lux$ to $3,000\,lux$. The mean illuminance level is hereby increased, further more the ratio between minimum and mean is decreased to a reasonable level which signifies more comfort and reduced need for artificial lighting to homogenise illuminance levels.

(a) Double Glazing

(b) Laser cut panel

(c) Embedded mirror with back reflectors

(d) Embedded mirror without back reflectors
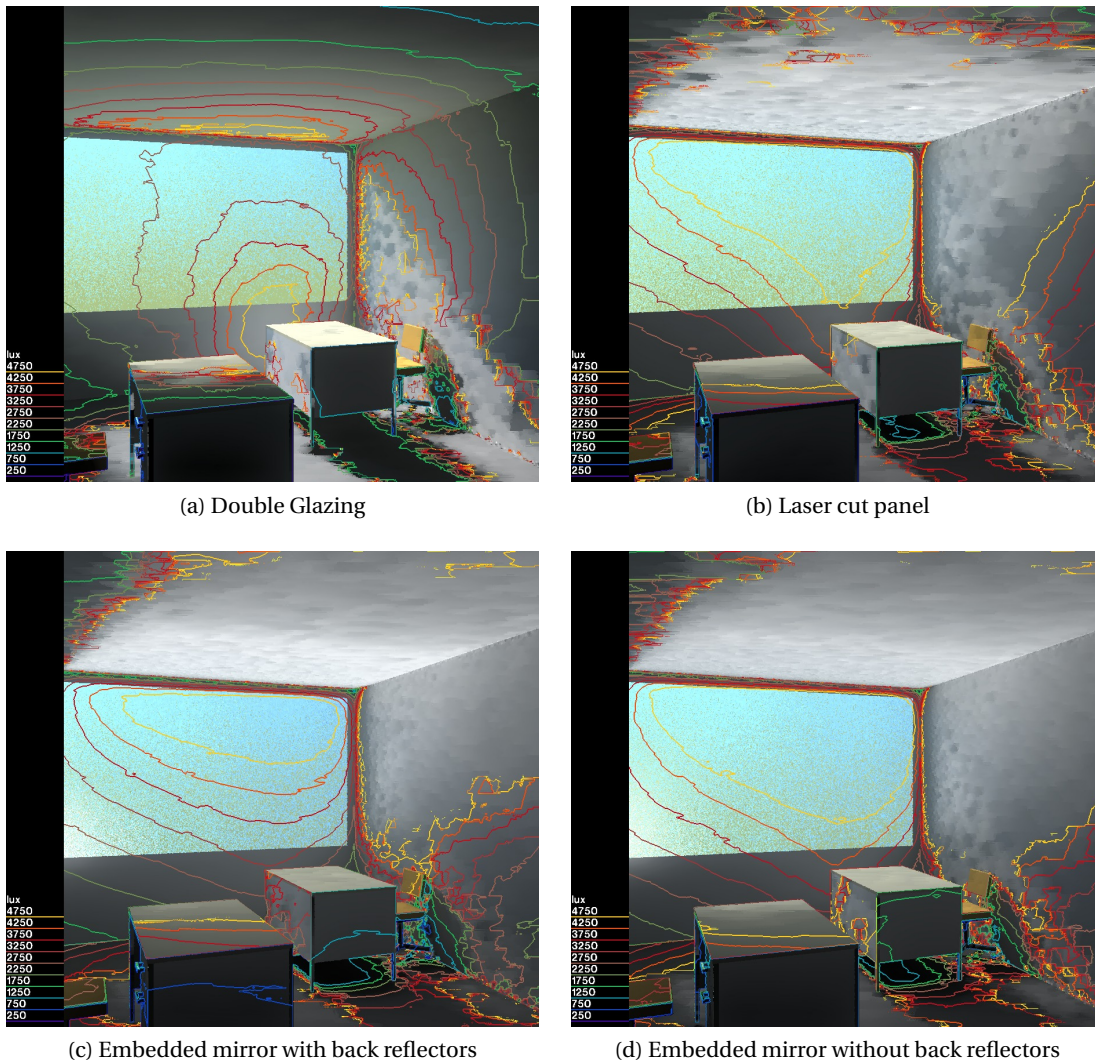
Figure 6.19 – Radiance rendering of various systems based on the computed BTDF. All renderings were carried out on the spring equinox at noon (21st of march) for a clear CIE sky. Isolines for illuminance levels were overlayed to facilitate quantitative comparison.

The complete device was then rendered hourly from 8 am to 1 pm on the summer (Figure 6.22) and winter (Figure 6.20) solstice as well as on the spring equinox(Figure 6.21). In winter there

is more scattering and one might think that this could cause glare; but using *evaglare*, it can be verified that the DGP for the rendering at 1 pm is 0.
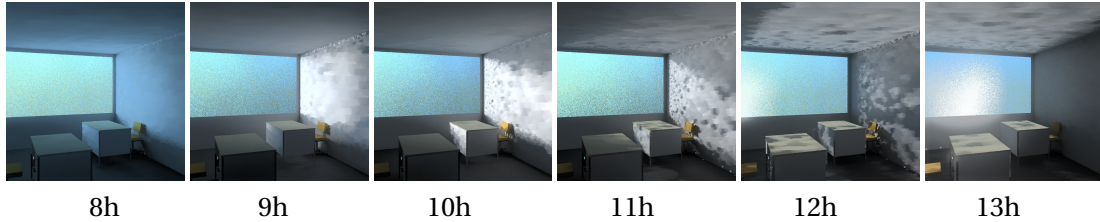
Figure 6.20 – Time series of renderings on the winter solstice for a clear sky.
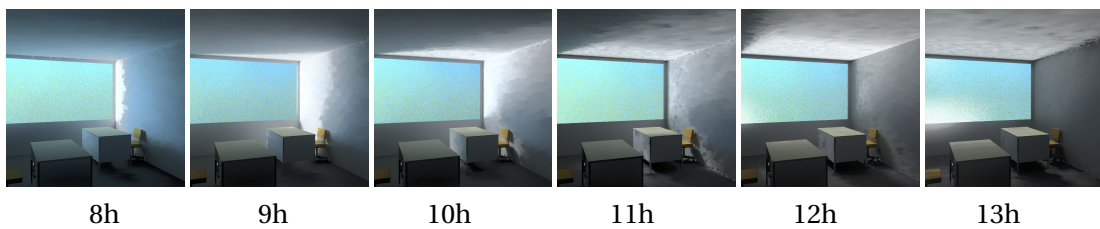
Figure 6.21 – Time series of renderings on the spring equinox for a clear sky.
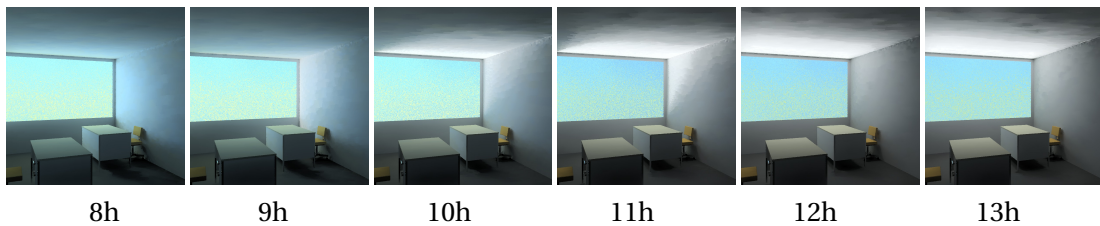
Figure 6.22 – Time series of rendering on the summer solstice for a clear sky.

6.7 Other simulation results

6.7.1 Combination of structure with selective NIR-reflective coating

Following the above described study, it was found that solar gains need to be minimised in spring and summer. This requires large blocking ranges that are obtained with larger mirrors on the backside (40% of the surface area). These mirrors reduce transmittance and transparency as they represent the largest fraction of POR and hence decrease the workplane illuminance in consequence. This can be improved by the usage of selective solar coatings instead of reflective coatings. The seasonal thermal dynamic is maintained to some extent and the visible transmittance increased, hereby only the POR of embedded mirrors affect visual transmittance and daylight availability is conserved.
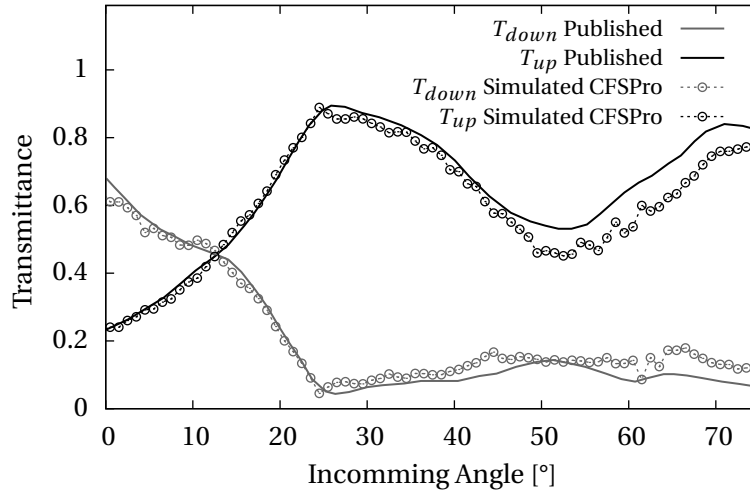
Figure 6.23 – Transmittance of the microstructure proposed by Klammt *et al.* as simulated by CFSPRo by the author and by TracePro [Klammt et al., 2012]

6.7.2 Simulation of Klammt microstructure

The structure proposed by Klammt et. al. was discussed several times in this thesis, The geometry was modelled from the micrographs available in the literature illustrated in Figure 2.6. The script describing this design introduced five parameters: device thickness, period, lens radius, prism depth and material refractive index. In this section, the simulated transmittance of this model is compared with one published by the authors. In Figure 6.23, the good agreement of corresponding values with those issued by the CFSPro simulation. The CFSPro model of the system is based on the dimensions measured on the micrograph.

6.7.3 Modeling spectral dependent diffusion of fibre glass

The developed software was also used in collaboration with C. Pascual to study optical properties of fibreglass reinforced resin [Pascual et al., 2013] such as the one illustrated in Figure 6.24. In such typical samples several hundred fibres of few micrometers diameter were modelled, arranged in four equally spaced layers of $290\,\mu m$ thick bundles with 4300 fibres/mm^2. The software is able to simulate the importance of index matching in this application. It was shown that when a large number of fibres are embedded in the resin, even a mismatch of 0.01 in refractive index can lead to strong diffusion of light. The importance of this diffusion was linked to the quantity of fibres in the laminate. In the case of the used fibres, and in the blue range of the spectrum, the mismatch is much stronger than in the red range, therefore the fibreglass diffuses blue light much stronger than green or red light. This was observed experimentally, Figure 6.25a shows how the simulation recreates the same spectral variation of diffusion. This simulation also shows how important the absorption in the UV range can be. In these simulations and measurements, diffusion was defined after measurement of direct and diffuse components in the experimental setup. In the integrating sphere, total transmittance
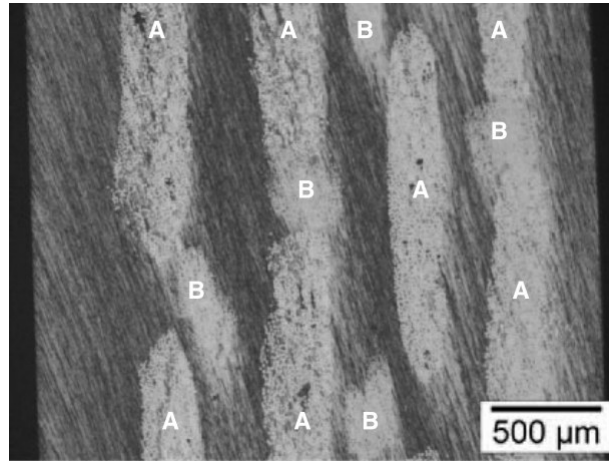
Figure 6.24 – Micrograph by optical microscopy of a fibreglass reinforced resin sample. Through-thickness optical microscopy image of a fibreglass reinforced resin sample with four layers of fibres. A: rovings, 12.8 μm diameter, B: yarns, 8.9 μm diameter [Pascual et al., 2013].

was measured when the backside aperture of the sphere is closed. When it is opened, the diffuse transmittance is measured and the direct transmittance escapes the integrating sphere. For the direct transmittance, a light beam within a given cone is considered. This cone angle is defined by the geometry of the measurement apparatus (exit aperture diameter and distance to sample), its angle and orientation changes slightly depending on the position on the sample. In the simulation this angle was set to a mean value of 4.5°, centred around the normal to the sample. Air bubbles were also added to the model to conform with the measured samples. The model gave a reasonable estimate of the optical properties; remaining discrepancies between model and simulation are explained by the strong sensibility of many variables.
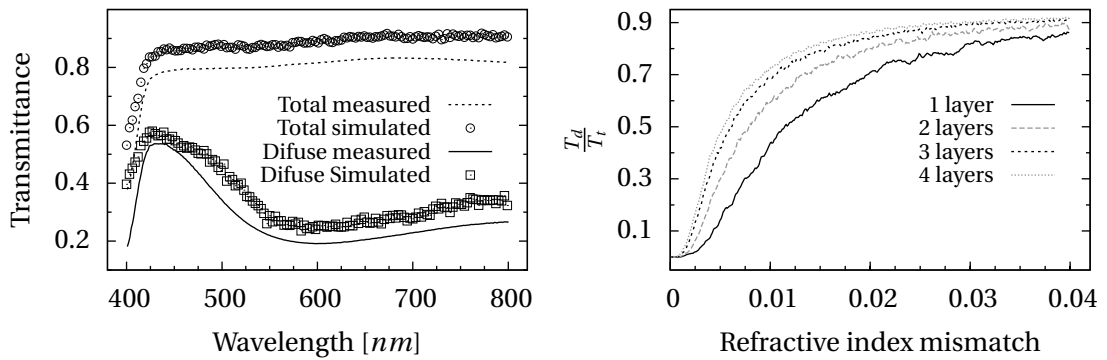
(a) Comparison of transmittance as simulated by Monte Carlo ray tracing and measured with an integrating sphere. Direct and diffuse spectral transmittance are plotted.

(b) Simulated effect of index mismatch on diffusion. $\frac{T_d}{T_t}$ is the ratio between diffuse and total transmittance; light within a cone of aperture 4.5° centered around the normal to the sample is considered direct.

Figure 6.25 – Comparison of simulated and measured diffusion in fibreglass reinforced resin and study of the refractive index mismatch effect.

7 Experimental Results

The software toolkit was used to design an optimised optical system blocking light rays within a selected angular range, redirecting light beams over a broad range of incoming angles and offering reasonable transparency at normal incidence. To materialize this design, the fabrication process introduced in Section 4.1 was applied; the results for each step are presented in this chapter. To conclude, the optical characterisations of key samples by the way of goniophotometric measurements are presented and discussed.

7.1 Substrate with reflective stripes

Using the methodology and experimental setup presented in Section 4.3, striped reflectors were produced on a glass substrate. These mirrors act as back-reflectors for light rays within the selected blocking range. Depending on the size of the structures, different geometries were created to produce these reflectors. The period of stripes has to match the period of structures, so masks with periods of $200\,\mu m$ and $50\,\mu m$ were printed. The width of the unobstructed part of the mask determines the width of the produced reflective stripe. For the masks with a period of $200\,\mu m$ different width of unobstructed stripes were realised between $25\,\mu m$ and $50\,\mu m$. For the smaller structures with a $50\mu m$ period, masks were printed with stripe width of $10\,\mu m$, $15\,\mu m$, $20\,\mu m$ and $25\,\mu m$. A selected mask for each periodicity is illustrated in Figure 7.1.

7.1.1 Lithography

Before using a combination of two resists for proper lift-off lithography, the S1818 PR was used alone and lithography parameters optimised to obtain stripes with equal width. To achieve this goal, it appeared that the exposure dose should be uniform over the sample: a diffuser was used accordingly to make the exposure more uniform as described in Section 4.5.3. By trial and error experimentation, it was confirmed that the bake temperature also influences the curing process significantly. To obtain clean and repeatable results, the temperature must be uniform over the sample and matched with the exposure and development time. A thick
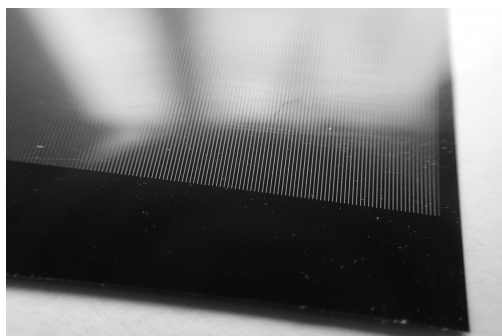
(a) Mask for photolithography with $50\,\mu m$ wide stripes every $200\,\mu m$; printed on a photoplotter at EPFL.
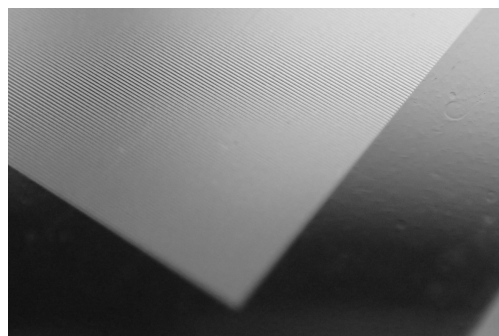
(b) Mask for photolithography with $25\,\mu m$ wide stripes every $50\,\mu m$; printed on a photoplotter by Selba SA.

Figure 7.1 – Photographs of two types of masks for lithography, one with $25\,\mu m$ wide stripes every $50\,\mu m$ and one with $50\,\mu m$ wide stripes every $200\,\mu m$.

metal slab ($25\,mm$) was added on top of the hot plate to obtain a more uniform temperature. Results of unsuccessful patterning are shown in Figures 7.3a and 7.3b, insufficient exposure or too short development time produce ill defined structures and partial removal of the resist. Over-exposure and lengthy development remove too much resist. The contact method applied on dedicated exposure tools was also applied here by placing the mask between the substrate and a glass slide and pressing then together mechanically in the sample holder. This decreases slightly the exposure dose but guaranties good shading by the mask, it hereby reduces diffraction effects and increases the spacial resolution. The optimal process parameters to obtain well defined and regular stripes in the PR are as follows:

- Dehydrate the sample at $125°C$ for $60'$
- Cool the sample for $30'$ on a cold metal plate
- Spin-coat $1\,mL$ of S1818 at $6000\,rpm$ for $45'$ after $5'$ at $500\,rpm$ with the PR deposited before spinning (static dispense). According to the documentation, this yields a film approximatively $1.5\,\mu m$ thick
- Bake at $125°C$ for $30'$
- Expose the resist for $20'$ with the potentiometer set at 250. This corresponds to approximately $100\,mJ/cm^2$
- Develop the PR for $30'$ in mr-Dev300
- Rinse well with deionised (DI) water in two steps and blow dry with nitrogen

Once the parameters were optimised for the S1818 PR, the LOR5A PR was added in the process in order to create a proper lift-off sacrificial layer with an overhang as required in the process (Figure 4.3) and illustrated in Figure 7.2. This resist requires higher backing temperature for the process to work; otherwise it is completely dissolved within seconds during the developing step. The process parameters were quasi-optimal when the developer solution was renewed and strongly modified the chemical kinetics of development. With this new developer bath,
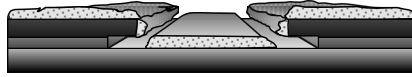
Figure 7.2 – Coating ready for lift-off. The dual resist coating with underetch permits clean lift off.

even when baked at 180°C, the LOR5A resin spun at 3500 is removed within few seconds. After a failed attempt to dilute the developer 1:1 with DI water, the developer was slightly diluted at 10:1 with DI water to slow down the reaction. With the same parameters, a LOR5A layer was dissolved completely in approximately 45′. The unexposed S1818 resist layer prepared as detailed above is removed within 60′ in the diluted developer; with such a small difference the lift-off process will still be imperfect. To increase the difference, a thicker S1818 layer was coated by slower spin speed and baked at lower temperature since a high backing temperature increases removal rate. Likewise, the LOR resin was spun faster and baked at high temperature. In this process, optical microscopy was performed to measure the stripe width. For a two layer coating with both resists, a micrograph of a successful patterning is shown in Figure 7.3c. A photograph of the corresponding sample is presented in Figure 7.4a.

(a) Underexposed photo resist stripes in S1818 photoresist.

(b) Partly developed stripes in S1818 photoresist.

(c) Successful patterning of S1818 resin on top of LOR5A layer.
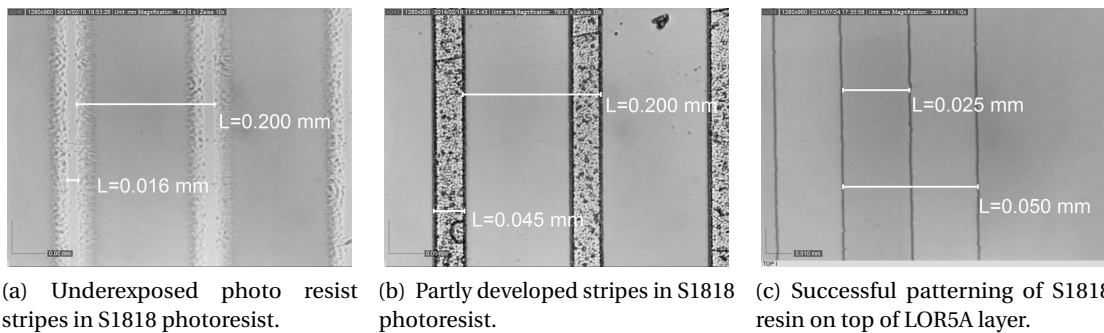
Figure 7.3 – Micrographs by optical microscopy of lift-off patterns in photoresist.

After a systematic optimisation of parameters, the following process parameters were identified to work properly:

- Dehydrate the sample at 160°C for 120′
- Cool the sample for 30′ on a cold metal plate
- Spin-coat 1.5 mL of LOR5A at 4000 rpm for 45′ after 4′ at 400 rpm with the PR deposited during spinning (dynamic dispense). According to the documentation, this yields a film approximatively 0.5 μm thick
- Bake at 160°C for 60′
- Cool the sample for 30' on a cold metal plate
- Spin-coat 1 mL of S1818 at 3500 rpm for 30′ after 5′ at 500 rpm with the PR deposited before spinning (static dispense). According to the documentation, this yields a film approximatively 2 μm thick

- Bake at 100°C for 30'
- Expose the resist for 20' with the potentiometer set at 250. This corresponds to approximately 100 mJ/cm^2
- Develop the PR for 30' in mr-Dev300 diluted at 10:1 with DI water
- Rinse well with DI water in two steps and blow dry with nitrogen

7.1.2 Lift-off
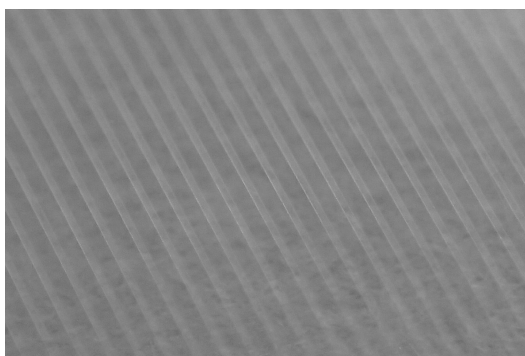
(a) Photograph of a pattered dual layer resin for lift-off lithography. Stripes have a period of 50 μm and width of 25 μm.
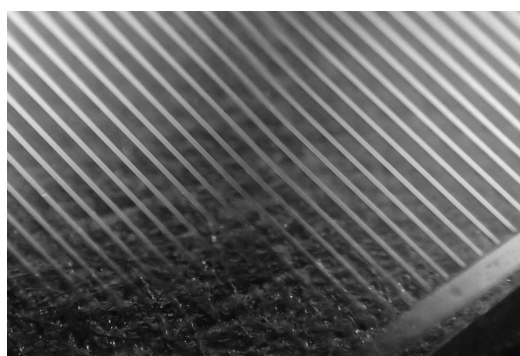
(b) Photograph of a pattered reflective coating. Stripes have a period of 200 μm and width of 50 μm.

Figure 7.4 – Photographs of a patterned lift-off coating (S1818 + LOR 5A) and striped reflective coating (Aluminium) as obtained by lift-off.

Once the pattern in the mask was successfully reproduced in the S1818 PR, the substrates were coated with Ag or Al. The remover (Rem400 from MichroChem) was used to remove the PR and the coating deposited on top of it. It was found that even without using the two resists to obtain a proper overhang and cleaner lif-off, satisfying results could be reached. However, the sample had to be placed in an ultrasonic bath for one to two minutes to remove the coated resist completely. This longer process sometimes removed the coating partly in places where it should remain or failed at removing all parts to remove (Figure 7.5a). Any variations in the stripe width is reproduced during lift off and this is not the critical step. The removal step is however not compatible with Ag since the used remover is acidic and oxidises the silver surface (Figure 7.5b). A photograph of a sample with striped aluminium coating is shown in Figure 7.4b. With the proper lift-off coating, the removal is faster and the result cleaner. However any remaining LOR 5A resist prevents proper adhesion of the coating and it is removed completely.

7.2 Fabrication of a mould

The realisation of a mould with the desired shape is certainly a critical step in the fabrication process. As introduced in Section 4.4, numerous fabrication methods exist; initially EDM

(a) Failed removal of aluminium after single layer lift-off, uneven edges and partial removal of coating.

(b) Oxidised Silver stripes obtained by single layer lift-off, clean edges and complete removal.
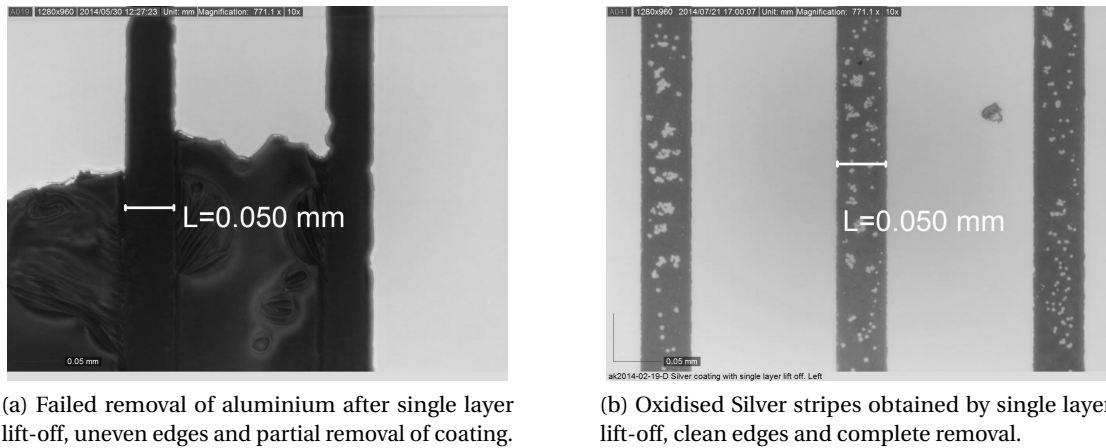
Figure 7.5 – Micrographs of striped reflectors obtained by evaporation and subsequent lift-off.

was selected because it seemed most promising. Later the limitations of this process pushed for the exploration of other techniques. The best suited and most available technique was found to be direct laser ablation at Empa. The moulds produced using these two fabrication processes are introduced in this section followed by results associated with the improvement of the surface quality of EDM moulds.

7.2.1 Electrical discharge machining

As introduced in Section 4.4.7 a mould was designed to hold different inserts fabricated by electrical discharge machining. A first insert for the fabrication of flat tilted integrated mirrors with a $400\,\mu m$ period and 1.5 aspect ratio was cut in stainless steel by electrical discharge machining at the EPFL workshop. Figure 7.6a is showing the profile obtained by this technique; it can be observed that some tips are bent and how rough the sample surface is in comparison to the vertical edges (in the forefront). The roughness on the structures surface was created by the EDM process, the relative flat surface on the other hand was produced during the preliminary milling step for the sizing of the insert before EDM cutting.

A mould with parabolic surfaces, increased spatial resolution, $200\mu m$ period, increased aspect ratio and lower surface roughness was cut by Derwa SA following the surface quality study of Section 4.4.1. In order to create these smaller structures with a periodicity of $200\mu m$ and an aspect ratio of 2.25, tungsten carbide had to be used to avoid deformations. With ductile materials such as stainless steel, the internal tensions deform the workpiece after cutting, and the thin remaining tips would bend and snap off after the cutting. Tungsten carbide which is a refractory carbide is harder to deform and has lower internal stress than stainless steel; it is possible that the bending of corners and the slight curvature along the tips seen in Figure 7.6a are due to these internal tensions. The resulting tungsten carbide mould is shown in Figure 7.6b where it is overlaid with the corresponding design. In the latter, the reflective

(a) SEM micrograph of the EDM mould cut at EPFL in stainless steel using a $200\,\mu m$ wire showing the bending of tips.

(b) Overlapped image of the parabolic design and a SEM micrograph of the EDM mould cut by Derwa SA in tungsten carbide using a $50\,\mu m$ wire
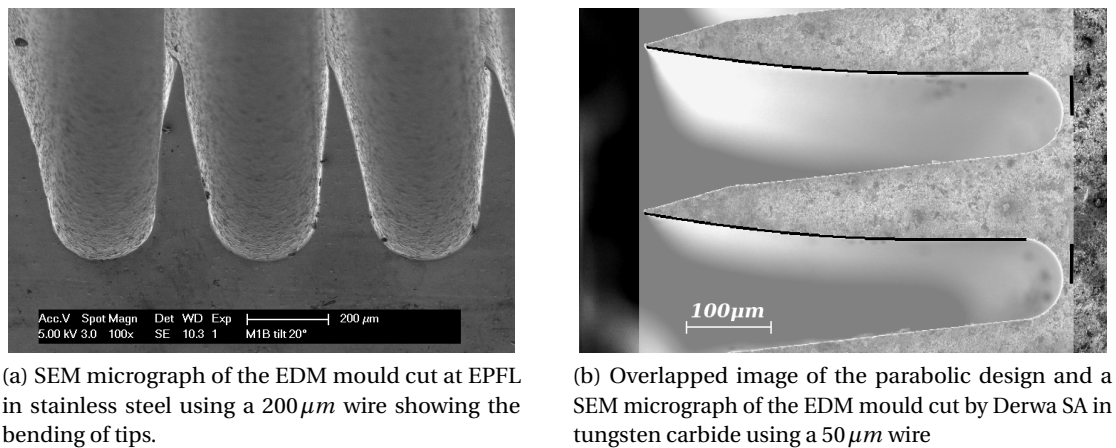
Figure 7.6 – SEM micrographs of metallic inserts cut by EDM with different wire diameters and materials.

surfaces are marked by black lines.

7.2.2 Electropolishing of metalic moulds

(a) Unpolished stainless steel surface after EDM with a $200\,\mu$m wire.

(b) Stainless steel surface after 6 minutes electropolishing.
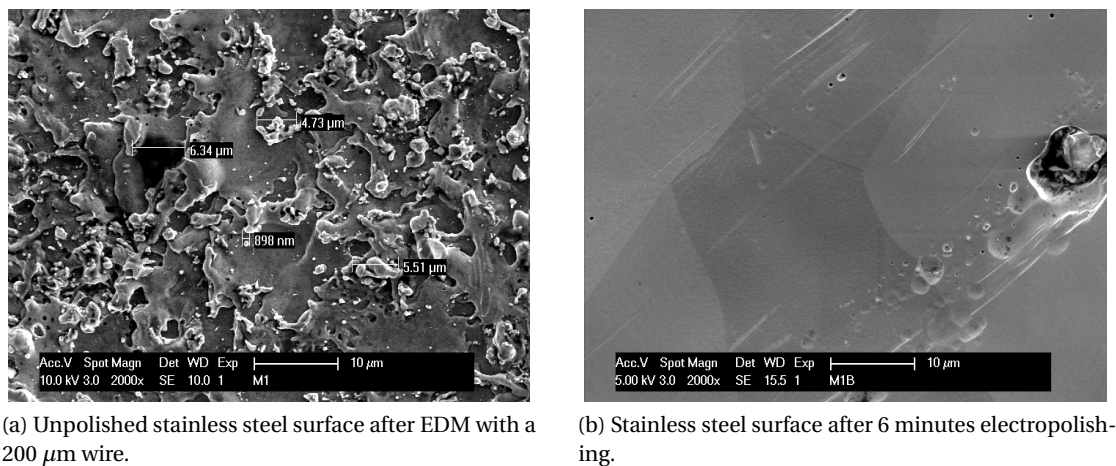
Figure 7.7 – SEM Images of different electropolishing times for a stainless steel surface cut by electrical discharge machining.

To eliminate the surface roughness of metallic mould inserts, a treatment in an ultrasonic bath with diamond micro particles was attempted but not successful. Stainless steel moulds were then electropolished during 2, 4 and 6 minutes. The surface roughness of the metallic mould inserts due to the EDM fabrication process was hereby successfully removed and observed by SEM imaging of polished and unpolished surfaces (Figures 7.7a and 7.7b). The optical improvement was measured with the goniophotometer; Figure 7.8a shows the associated reduction in the width of the reflection distribution. The reflection became less diffuse yet

far from being specular. To explain this, the surface roughness was measured with a laser profilometer on the flat area of the samples; a roughness arithmetic average of $1.48\,\mu m$ was measured, after polishing it was reduced to $0.81\,\mu m$. Surfaces with a roughness in this order of magnitude are still diffusing. To explain this diffusion despite the smooth aspect of surfaces observed by SEM, the profile was scanned before and after polishing, the results shown in Figure 7.8b indicate that the small scale roughness was removed but that a wave like roughness remained. This remaining roughness is most likely due to the imprecise movement of the wire during the cutting.
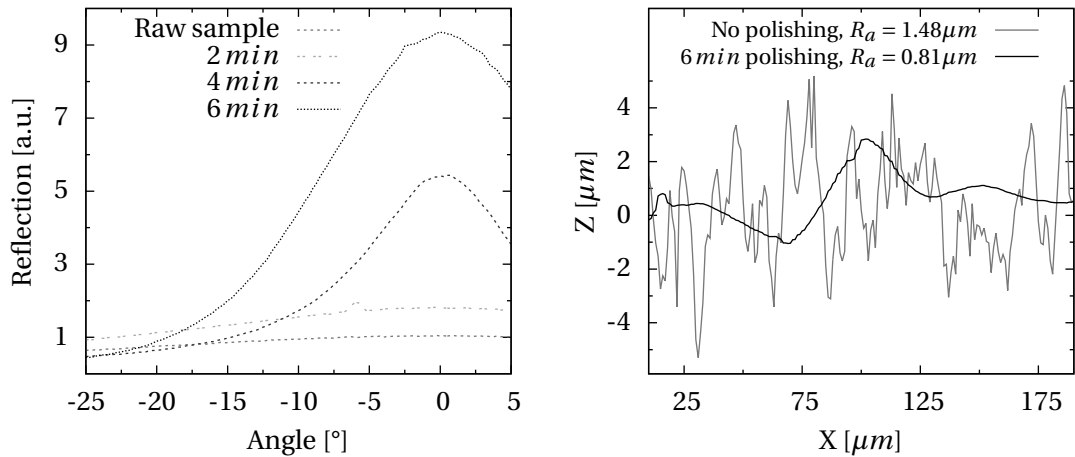
(a) Diffusion profile for different polishing times as measured by goniophotometry.

(b) Stainless steel surface profile before and after 6 minutes of electropolishing measured by laser profilometry.

Figure 7.8 – Study of the effect of electro polishing on surface diffusion and surface profile.

7.2.3 Smoothing by spin coating of resin

The tungsten carbide insert was fabricated on a machine with increased spacial resolution, the roughness induced by the tool's position had therefore bene reduced. However, a certain roughness due to the localised plasma process of EDM cutting remains and tungsten carbide cannot be electropolished. To obtain a smooth surface, spin coating with a resist was attempted. When applying the resist, it is viscous and covers the surface. Once spun the quantity of resist is rather uniform on the surface of the rough insert. Before drying, surface tension in the resist should create a smooth surface as long as there is enough resist to fill the spaces between the peaks of the surface. Once dry, the smooth resist surface can be replicated into the PDMS stamper because this replication involves no mechanical and very little thermal constraints. The mould was spun with $1\,mL$ of S1818 resist at $1500\,rpm$ and baked on a hot plate at low temperature ($60°C$) to slowly evaporate the solvent and harden the resist. It was then replicated to a negative PDMS stamper, the resulting surface was observed with an optical microscope. In Figure 7.9a the roughest area of the mould is shown where the insert was partially coated with resist. The high roughness is still present at the surface in areas where the mould was covered with resist. In Figure 7.9b the moulds roughness (which is

smaller due to enhanced setting in the cutting process in this area) is completely immersed in the resin and the surface appears very smooth. Once again the roughness due to the cutting process can be observed along the cutting direction (horizontal lines). Its dimension seems very small and when observing the reflection in the coated area of the tungsten insert, it is imaging and appears to be fully specular to the naked eye. Furthermore, looking through the PDMS stamp, transmission seems non diffusing and fully specular. This approach was successful at reducing roughness on flat surfaces, but the vertical surfaces of the structures could not be smoothed successfully. When cutting the PDMS mould and observing vertical surfaces under the microscope, some roughness remains.
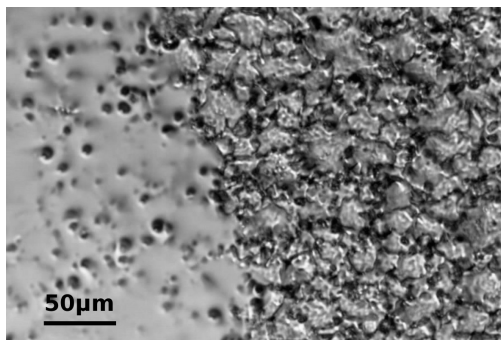
(a) Smoothing of areas with high surface roughness.
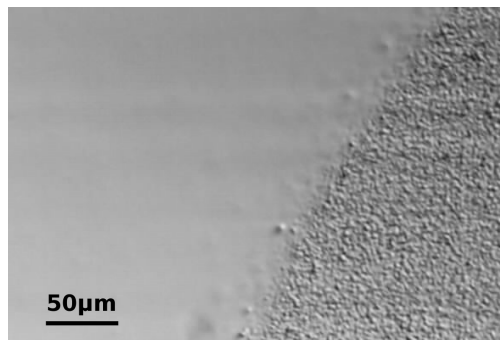
(b) Smoothing of areas with lower surface roughness.

Figure 7.9 – Micrographs of a PDMS stamp obtained from a tungsten carbide mould "polished" by spin coating of a resin.

A light beam is focused by a parabolic mirror only if its surface is smooth enough for specular reflection and if its geometry is precise enough to focus light at the desired angle. Regarding these objectives, the EDM technique reached its limits and other techniques had to be envisaged. The results of direct laser ablation are presented in the following section.

7.2.4 Direct laser ablation
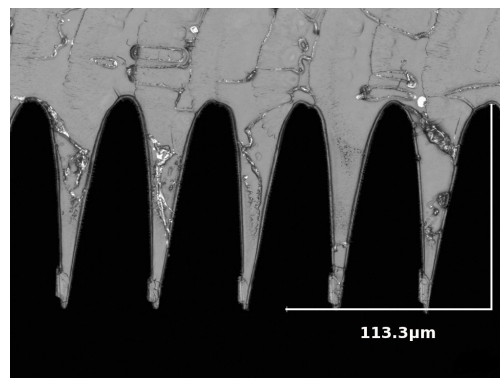
Figure 7.10 – Confocal imaging of the laser ablated mould profile.

Following the difficulties and limitations found using a mould cut by EDM, other techniques were investigated. Amongst these, direct laser ablation was attempted. First trials using the $248\,nm$ excimer laser setup at Empa resulted in a sample of parabolic like structures engraved directly in polycarbonate (PC) with a period of $50\,\mu m$. The short pulse duration of about $20\,ns$ limits the heat affected zone (HAZ) in polymers to some tens of nanometers. Initially the grooves were $113\,\mu m$ deep; after a cleaning process this depth was reduced to about $93\,\mu m$. polycarbonate (PC) was used because of the absorption at the laser wavelength and for the good predictability of structures due to the broad experience at Empa with this material. To provide the required alignment of structures, perpendicular to the substrate, a new holder was fabricated using this PC sheet. As for the other moulds, an extra reference was added to the mould holder in order to provide a constant and controlled thickness in the replicated structure. This reference also prevents contact (and hence deformation of the soft mould) between the mould peaks and the substrate during the UVNIL step. A confocal microscopy image provided by Erdem Siringil at Empa illustrates the profile of this sample (Figure 7.10), the structure is asymmetric and provides two different facets, on tilted at appropriately 4° and the other one at 12°. These facets will later be referred to as F_4 and respectively F_{12} facet.

This surface geometry is not parabolic and does not perfectly focus light, the process would have to go through fine tuning of to obtain a parabolic geometry conform to the design. It was however used to produce promising light redirecting samples with embedded mirrors. The laser ablation was performed on an area of approximately $2\,cm^2$, this can easily be extended to larger areas.

7.3 Replication

PDMS mother moulds were then produced. These moulds were used to create structured surfaces on glass substrates using an UV polymerising resin as described in Section 4.5. A good adhesion between substrate and resin was not reached immediately. An optimisation of the process parameters and a suitable choice of the used resin resulted in satisfying samples. The results for this work are presented here.

7.3.1 PDMS stamp

PDMS stamps made from various types of moulds were successfully obtained. It was found that once prepared, the PDMS mix should be used within the hour, later the mould presents signs of incomplete curing or strong weakness upon unmoulding. The main challenge in this step was to provide the extra features for thickness control, as discussed in section "Polydimethylsiloxane formwork". This was achieved by fabricating a formwork out of aluminium using a milling cutter. The accuracy of the used cutter is in the order of $10\,\mu m$ to $50\,\mu m$, making it possible to create references with dimensions of several tenth of a millimetre. This is sufficient and satisfying for structures that have similar dimensions as the first inserts produced by EDM, illustrated in Figures 7.11a. For the structure fabricated by direct laser ablation in PC
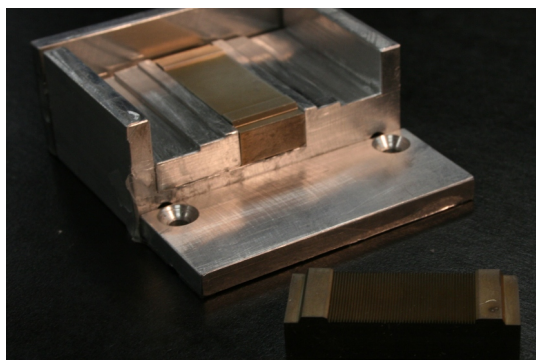
(a) Aluminium formwork for the fabrication of PDMS mould with stainless steel microstructured inserts (one in the formwork and one in the forefront).
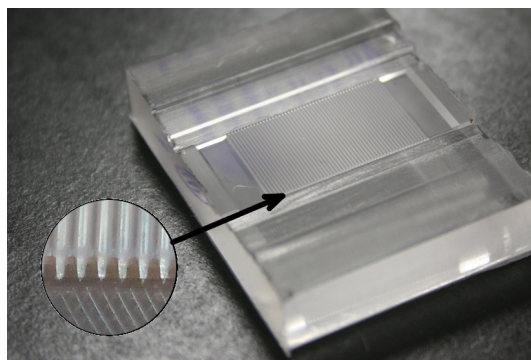
(b) Corresponding PDMS Mother mould with zoom on structured area.
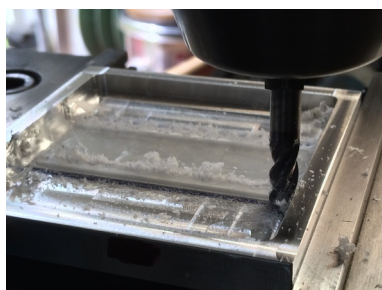
(c) Milling of $0.15\,mm$ into the PC insert to provide reference step.
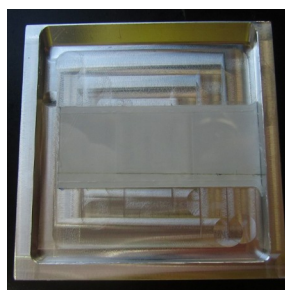
(d) Stainless steel microstructured father mould and formwork for the fabrication of PDMS mould.
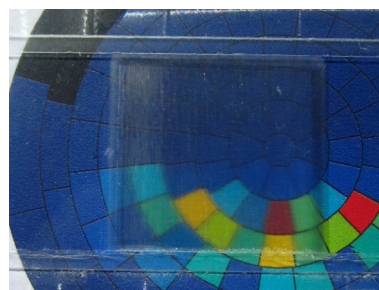
(e) Corresponding PDMS Mother mould with diffusion effect on transmission

Figure 7.11 – Photographs of mould inserts and resulting PDMS mother moulds

however this limitation was at the edge of what was required. $0.15\,mm$ grooves were milled in the PC to provide a separation between the structures and the substrate (Figure 7.11c). The reference required to provide and control the gap during the embedding step could not be fabricated. Because of its limited thickness ($0.5\,mm$), the structured PC part could not be maintained mechanically and was fixed with double sided tape in the bottom of a flat container. The resulting father mould is pictured in Figure 7.11d.

The resulting PDMS mother moulds are illustrated in Figures 7.11b and 7.11e. The reference border for the vertical alignment of structures can be seen on both moulds. The draining channels for the excess resin on the other hand are only present in the first mould. In Figure 7.11e, the non imaging effect of the obtained mould can be visualised. Even though the image is close to the stamp, it is blurred by the structured surface.

7.3.2 Resin choice and properties

To achieve a satisfying optical performance, the used resin needed to be transparent and colourless: for this reason the epoxide resin (which has a yellow tint) was eliminated. Using the acrylate HBP, flat layers of resin below 450μm thickness showed sound optical properties, a transmittance of 91% was measured in the visible range. Above this thickness, a haze can appear at some viewing angles when looking through the sample. With such thicknesses, the resin blocks UV light and polymerisation can no longer continue below the first couple hundred micrometers. The haze might therefore be caused by varying refractive indexes between polymerised and unpolymerised resin. It was observed that the acrylate resin also shows a slight yellowish tint for thick samples. This tint disappears after some time, it is likely that this is also an effect of unpolymerised or partially polymerised resin. With time, the resin fully polymerizes under ambient UV and the tint disappears.
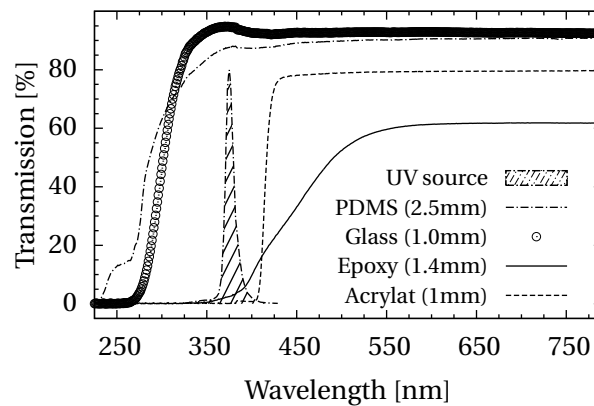
Figure 7.12 – Transmittance of acrylate and epoxide resins compared to that of glass and PDMS. The acrylate resin is fully transparent in the visible range. The spectrum of the LED taken from the data sheet is shown for comparison.

7.3.3 Process parameters

It was found that by putting the PDMS stamp first in the path of a light beam, the flux of the source was not reduced significantly despite its high thickness. This can be verified in the transmittance measurement shown in Figure 7.12. The polymerisation process however then starts on the structured side, this enables easier unmoulding and better finish of the replicated structure. Furthermore the interface between resin and glass polymerises last; it is likely that this reduces internal tensions that are responsible for delaminations in case the substrate is placed first. This delamination of the structured resin from the substrate happens in particular if the UV doses is large and the polymerisation fast. Using a UV luxmeter, the attenuation of the UV radiation remaining after half a millimetre of resin was found to be larger than 300 fold and the transmittance through $1\,mm$ of resin could not be measured with the spectrophotometer. This strong absorption in the UV range makes it hard to replicate

thick structures because the resin no longer polymerises. The thin structure fabricated by laser ablation was easily replicated without any particular process optimisation (potentiometer set to 500, $120'$ exposition at $10\,cm$ distance with a single diffuser). The thicker structure of the second generation EDM mould was harder to replicate. The polymerisation had to be carried out slowly and at moderate doses to avoid delamination and obtain a fully polymerised surface. On the setup at LTC, the resin was exposed at 6% of maximal intensity through the glass substrate for $180'$.

7.4 Coating

To obtain embedded micromirrors, only a part of the structure needs to be coated with a reflective material. For the latter, aluminium was selected for its high reflectivity, the ease of deposition and low cost. Silver coatings were also realised as it was found that for angles around 50°, the reflectance on aluminium is reduced and strongly polarised. The thin-films were deposited by physical vapour deposition in an Balzers BA 510 vacuum evaporation chamber. The thickness was controlled using the frequency variation on the quartz during deposition (see Section 4.6.3 for methodology); the likewise obtained coating thickness was verified using optical methods described in 5.1 and some times measured with contact profilometry when it was fully opaque. To obtain the coating of selected facets only, thin-films were deposited at a given angle and the tilt angle of samples was controlled with a special sample holder, as described in Section 4.6.4.

7.4.1 Partial coating

After validation on macroscopic samples (4.6.4), aluminium was deposited on prismatic films (3M BEF II, 90° prisms with $50\,\mu m$ period) with different tilt angles. The first evaporation was too long and the plastic substrate suffered from heat but with optimised parameters, a rapid evaporation (less than 10 seconds) caused no visible damages to the substrate. In Figure 7.13 it can be observed how a beam hitting the sample at normal incidence on the side with the prisms is redistributed. For an uncoated prism it reveals how such prisms split a light beam and redirect light rays towards −30° and +30°. The coated prism almost completely suppresses one of the redirected beams.

Structured samples obtained from the various PDMS stamps were also coated with an aluminium layer using this setup. The resulting samples were effectively facet selectively coated. Without embedding the mirrors these devices do not provide a significant distribution of transmission. Confocal microscopy was used to create 3D profiles of the surface and characterise how the angular deposition affected the coating location as described in the following subsection.
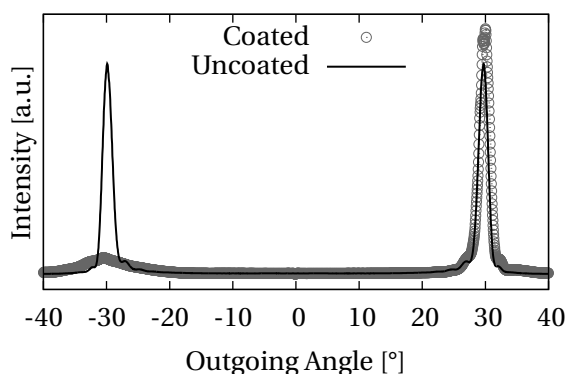
Figure 7.13 – Comparing transmission distribution for a coated and uncoated 3M prism.

7.4.2 Angular study of deposition

Confocal microscopy micrographs were taken for different deposition angles on microstructures with flat surfaces. There were taken on samples made out of the epoxy resin since the acrylate resin tends to swell when exposed to water. Water was required with the objective that yielded the best images. The images were processes with Fiji Is Just ImageJ (Fiji), an image processing package based on ImageJ [Fiji, 2014, Collins, 2007]. The Figures are created from a stack of 2D images taken from the top with a 10 μm width and the length equal to the period. These "slice" images were taken every 0.5 μm along the z axis and averaged along the width to generate a line. The lines are stacked and the resulting 2D image is therefore a view of the profile where the roughness of the reflective surface is shown statistically. The result is illustrated in Figure 7.14, the relation $\beta = \gamma * 1.17$ was derived as the closest fit of a linear function with this result (β the effective deposition angle as pictured in Figure 7.14 and γ the tilt angle of the substrate).

After the deposition of a thin film of carbon for the electrical conductivity of the polymer surface, EDX spectroscopy was also used to localise the metallic coating and derive the deposition angle on polymer samples. However, due to the high aspect ratio of structures, the vertical location is imprecise when projected into the horizontal observation plane; a slight tilt of the sample transforms this projections. Additionally the height of the structure is above the depth of field, it was therefore hard to clearly identify the deposition angle. Finally, the relative positioning of the electron source, the sample and the EDX detector greatly influences the signal strength and therefore the interpretation of results. Because these parameters are hard to control, this technique could not be used to observe the effective coating angle. A map obtained by EDX is however shown in Figure 7.15. This map is useful to show that the shadowing of the structure is not perfect and some amount of material (in this case aluminium) is deposited on the back side of the structure tips.

(a) $\gamma = 90°$ (b) $\gamma = 55°$ (c) $\gamma = 50°$ (d) $\gamma = 45°$
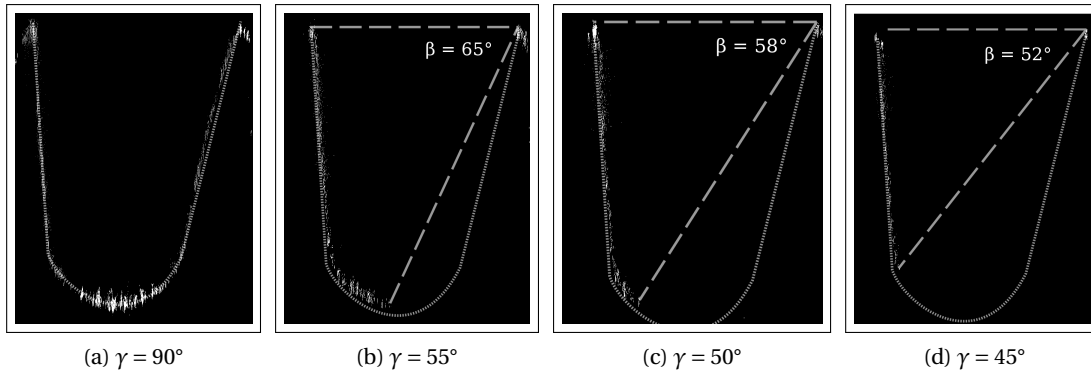
Figure 7.14 – Confocal microscopy images of embedded mirrors deposited at different sample tilt angles (γ) on microstructures with flat surfaces. The white image points indicate where the coating was deposited. A stack of images was taken by confocal microscopy and treated with an imaging software (Fiji) to create 2D profile images. To do so the points along the y axis were summed and the surface roughness is therefore shown statistically. The dotted line indicates the supposed interface i.e. the surface of the microstructure before coating and embedding. The dashed lines indicate the effective deposition angle β measured on the image.

7.5   Encapsulation

In this section we present how coated samples were encapsulated to fabricate embedded micromirrors. Because the encapsulation was a challenging process, plain structures with no coating were encapsulated first to understand the specificities of this process. The results for such "plain encapsulation" are presented first followed by actual embedded mirrors.

7.5.1   Plain encapsulation

Regarding the embedding step of structures with total heights in the range of one millimetre ($540\,\mu m$ structure plus additional thickness above and below), two challenges were faced. First, during embedding and probably due to resin shrinkage, voids appear at the very bottom of the structures. Second, even when no voids are present, the sample is not fully transparent.

The voids disappeared after further optimisation of parameters and slowing down the polymerisation. It is supposed that to rapid polymerisation from one direction only favours curing on the side which is exposed to the UV source. Because the polymer shrinks during the curing process, lack of material and higher constraints are created on the opposite side towards the end of the curing process. The sample were therefore first cured at a 2% of the maximal intensity for 90 seconds on each side then at 7% of maximal intensity for 90 seconds on both sides. Finally, to ensure complete curing of the polymer, the samples were exposed for 90 seconds at maximal intensity. However, it was observed that bubbles can be formed overnight due to ageing processes in the resin during the first days. This is possible linked to the shrinkage of resin that was not fully polymerised. Reducing the thickness of samples should reduce this
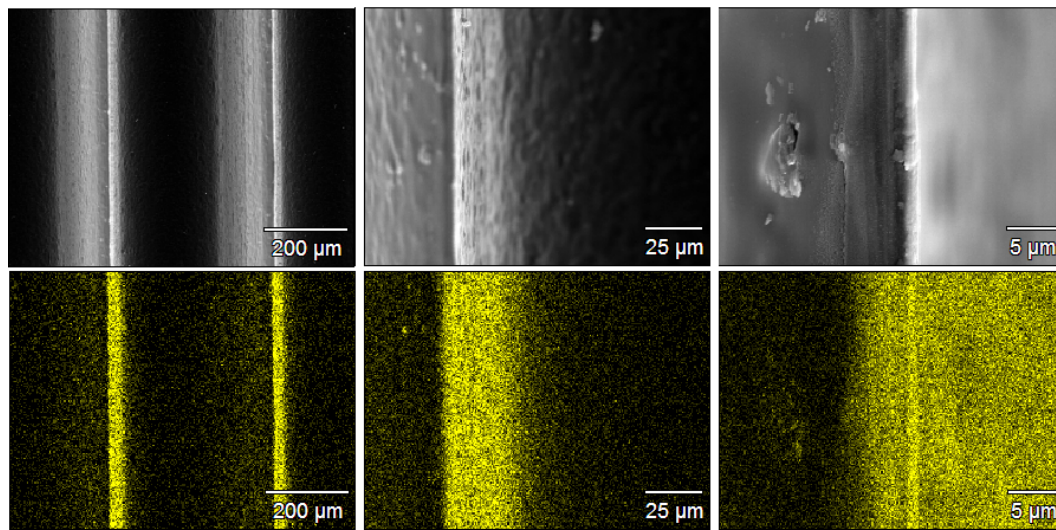
Figure 7.15 – EDX analysis of microstructured sample with angular deposited coating. The coating was deposited from the right hand side and the bottom row shows the map for aluminium.

problem.

The partial transparency can be explained if the interfaces do not disappear completely when a resin structure is filled with the same material. This creates a certain diffusion and reduces overall transparency. A small index mismatching combined with the strong roughness of the interface enhances this effect. Reducing roughness should dramatically decrease this effect. Various other samples with no coating (3M prism, flat shape with rough surface) were also encapsulated in order to verify if the embedded surface becomes invisible. These experiments confirmed that the roughness of the embedded surface highly influences its invisible integration. In particular, the significant roughness due to the EDM mould is still visible once embedded and creates a slight haze in transmission.

When embedding the smaller structures with surfaces of optical quality, as those produced by laser ablation at Empa, both problems disappeared as illustrated in Figure 7.16c. In this case the total resin thickness is only $180\,\mu m$; in comparison, the first samples had a total thickness of $880\,\mu m$ and the sample originated from the mould fabricated by Derwa had a total thickness of $540\,\mu m$. The polymerisation was carried out through the mould in the replication step and through the structured sample in the embedding step. When polymerising through the flat mould, from the side where resin is added to embed the structure, bubbles appear. This confirms on the one hand that during embedding it is advantageous to expose the side in contact with structures first and that total thickness and surface roughness are key parameters for a clean encapsulation.

(a) Encapsulation of first microstructure fabricated by EDM at EPFL.

(b) Encapsulation of second microstructure with increased aspect ratio.

(c) Encapsulation of structures as fabricated from the mould produced at EMPA.
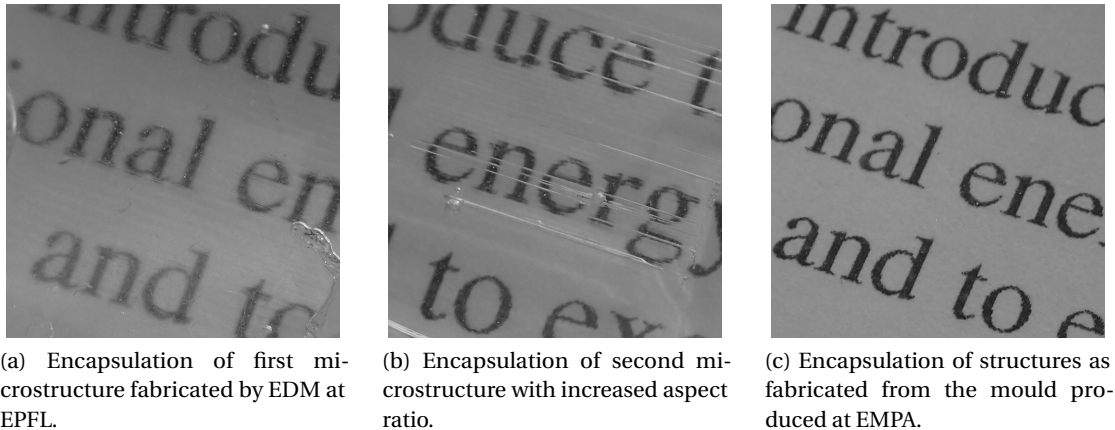
Figure 7.16 – Photographs of plain encapsulated structures showing the influence of surface roughness and thickness.

7.5.2   Encapsulation of mirrors

Various samples of coated microstructures were also embedded. For the samples of the second generation (with the high aspect ratio and parabolic mirrors) this was however not done successfully due to the bubble formation problems mentioned above. The samples from the first generation were successfully embedded after slight optimisation of parameters. Figure 7.17a and 7.17b show the view through such samples and their redirecting effect for direct sunlight. The reduced aspect ratio (approximately 1) results in partial redirection even for high angles of incidence. The occurrence of bubbles in samples of the second generation was a systematic problem that could not be overcome, no samples of embedded mirrors were produced without some bubbles. The structures from the third generation could be embedded in a successfully way, the coating was first attempted with silver and the unoptimised deposition parameters resulted in a slight golden colouration of the samples. As illustrated in Figure 7.17c when coating with aluminium, this coloration is not present and the result is very convincing. The transparency is preserved but a ghost image is created. This ghost image is most likely due to a reflection on the embedded mirror. The redirection of this sample is illustrated in Figure 7.18, where a flashlight is used to illuminate the sample from a given angle. The light beam is mostly redirected upward on the transmitted side (right hand side), and a small part is directly transmitted. Regarding redirection, samples of this generation are more effective than the first samples. This will be confirmed by goniophotometric measurements in the following section. With the aluminium coating, the samples had a cleaner appearance and no colouring.

7.5.3   Aligned encapsulation

The striped substrate were produced and parabolic shaped structures were coated with mirrors. To combine these two elements, a setup for the last fabrication step was prepared. For the alignment of the structure and the stripes, an optical microscope was adapted to provide x,

(a) View through a sample fabricated from the 1st generation mould.

(b) Light redirection by aluminium mirrors embedded in resin (1st gen).

(c) View through a sample fabricated from the laser ablated mould (3rd gen).
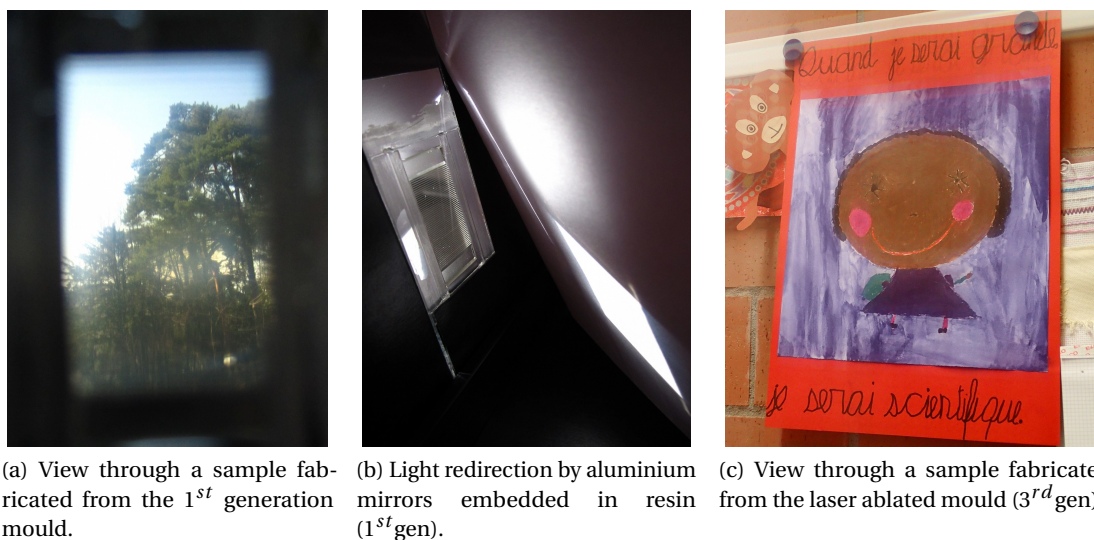
Figure 7.17 – Photographs of samples with embedded micromirrors.

y and z relative positioning as well as mould rotation to align the reflecting stripes and the mould. This setup is illustrated in Figure 7.19a, the optical filter holder normally placed on the path of light was replaced by a hollow support for the mould (A). The holder is hollow to provide a light path for the UV source that is placed underneath after the optical alignment. This alignment can be performed during the initial structure fabrication as it is shown in the original schematic (see Section 4.1); it may also be performed during the embedding step depending on the orientation of the fabricated mirrors. In the first case, the mould is placed on the holder and aligned with the stripes; in the second case the coated structures are aligned with the striped reflector. In both cases, the striped reflectors can be moved latterly on the stage and the transparent PDMS mould (or structured sample) sample enables optical alignment before curing. The digital camera and associated software are used to help in the alignment procedure. As shown in Figure 7.19b, the knobs from the sample stage (B and C) can be used to position the stripes relatively to the mould (or structured sample). The knobs from the filter holder (D) can be used to rotate the mould (or structured sample) in the horizontal plane before pressing it against the striped sample using the z position knob of the filter holder.

This step was however not used because the latest mould requires a control of the distance between the embedded mirrors and the striped mirrors on one of the surfaces to produce angular selective transmittance. No reference surface for this alignment or other mean of controlling the total thickness could be added to the mould.

(a) 30°

(b) 45°

(c) 60°

(d) 70°
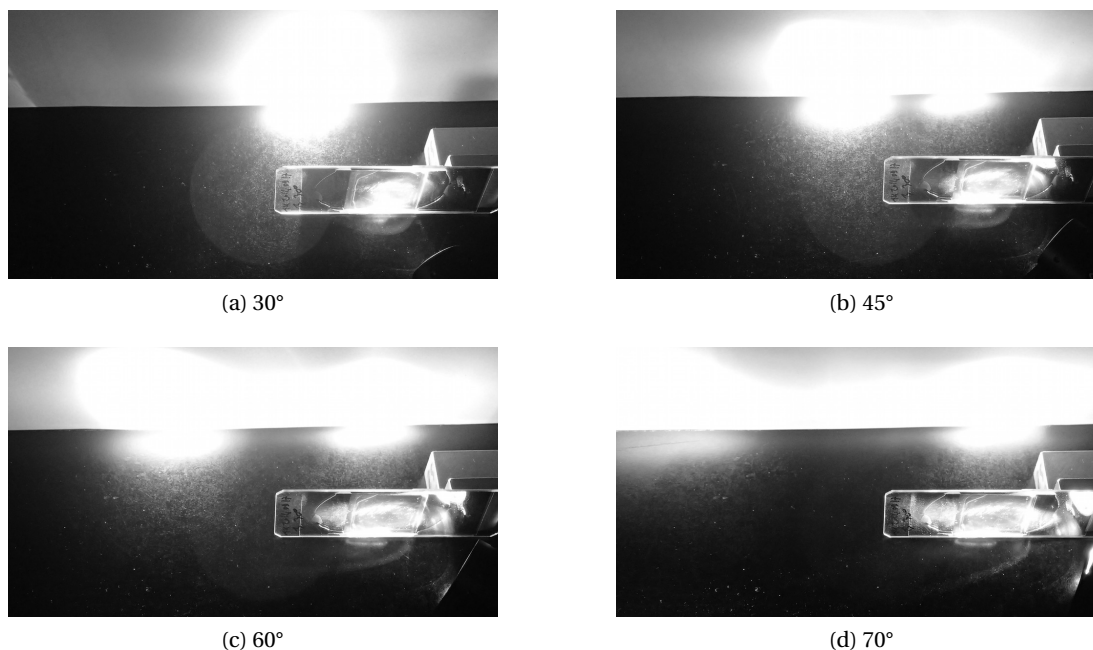
Figure 7.18 – Light redirection by curved aluminium mirrors embedded in resin (3^{rd}gen) when illuminated with a flashlight. The flashlight is placed in the bottom right quarter and the light beam angle is gradually changed. Despite the clear view through the sample at normal incidence (Figure 7.17c) the impinging light beam is strongly redirected for higher incidence angles.

7.6 Goniophotometer measurements

Two types of goniophotometric measurements were performed on the samples with embedded micromirrors to characterise the light transmission: the direct transmittance for different sample angles (Figure 7.20a) and the transmission distribution for different incoming angles (Figure 7.20b).

7.6.1 First generation samples

The various samples with integrated mirrors were monitored using the goniophotometer. The first samples obtained from the mould with straight, tilted surfaces were measured and despite the very strong diffusion due to surface roughness, the angular dependent behaviour was characterised. In Figure 7.21a the direct transmittance is characterised for various incoming angles. It is strongest at about 20° when the incident beam is refracted in the sample, parallel to the structures. The direct transmittance is minimal at incidences above 40° when the structure redirects most of the light beam. For incident angles of 40° and 60°, the distribution of transmitted radiation was measured (Figure 7.21b). Direct transmittance (not shown in this figure) is observed as a narrow peak whereas the redirected light flux is measured as a very low

(a) Alignment setup on optical microscope with digital camera and computer connection.
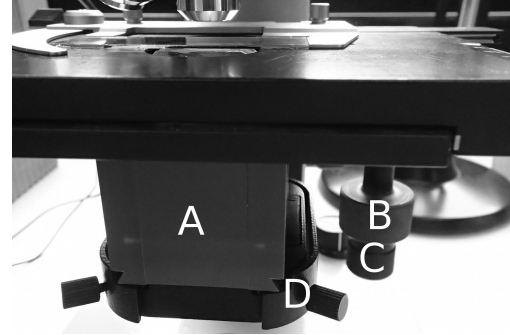
(b) Detail of holder and knobs for alignment.
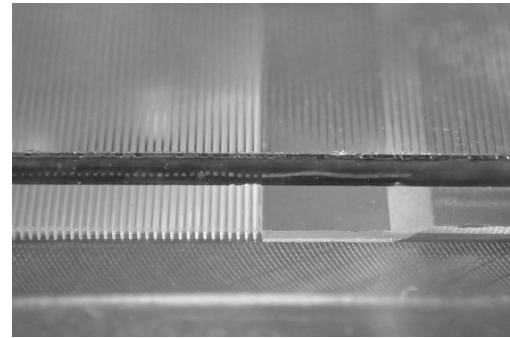
(c) Detail of striped substrate and mould for alignment.

Figure 7.19 – Photographs illustrating the alignment setup.

signal over a broad range of angles.

7.6.2 Samples of latest generation

Similar measurements where performed for the samples obtained from the laser ablated mould.

In the three rows of Figure 7.23, goniophotometric measurement are shown for several depositions angles $\gamma = 15°$, 20° and 25°. With such a positive tilt angle, the steeper, less tilted facet (F_4) of the structure is coated. The plots in the left hand side column present the transmission distribution for incoming beams at $\theta_i = 0°$, 30° and 55°. In the right hand side column, the integral of the total transmitted light flux for a serie of transmittance distribution measurements at $\theta_i = 0°$ to 75° in 5° intervals was computed. Depending whether θ_o was negative or positive, two other quantities were integrated: T_{up} respectively T_{down}. The obtained values are comparable to the T_{tot}, T_{up} and T_{down} quantities computed in the ray tracing simulation.

In the transmittance distribution plots (left hand side column), the reduction of direct transmittance can be observed as well as the broadening of the redirected peak for higher angles of
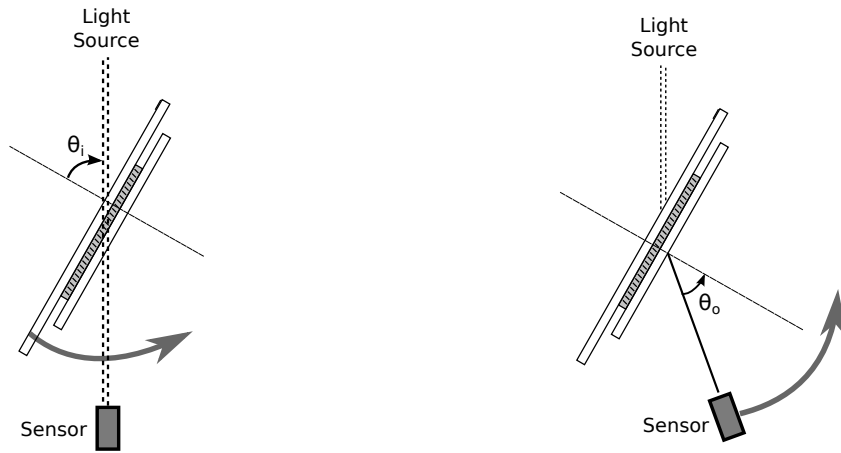
(a) Measurement principle for direct transmittance depending on the incident angle. Fixed sensor in the axis of light source, sample is rotated

(b) Measurement principle for transmission distribution with fixed incident angle. Sensor is rotated, sample is fixed.

Figure 7.20 – Two possible goniophotometer measurements: fixed sensor position for direct transmittance depending on incoming angle (a); fixed sample for transmission distribution at fixed incoming angle (b).
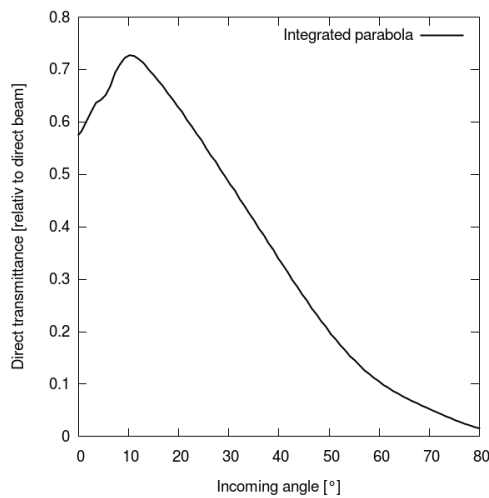
(a) Intensity of direct transmitted light for changing angles of incidence in an sample with embedded parabolic mirrors.
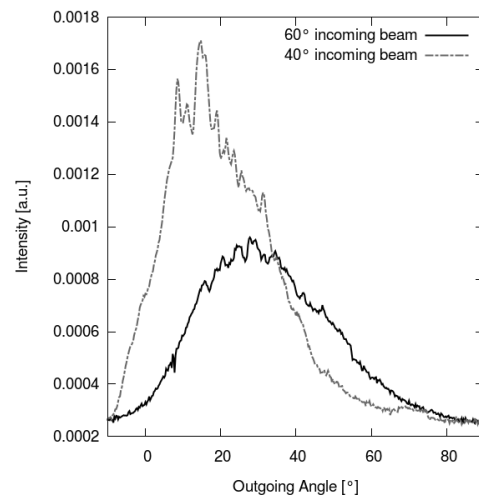
(b) Distribution of transmitted light by embedded parabolic mirrors for 40° and 60° incident beam.

Figure 7.21 – Goniophotometer measurements of first embedded mirror.

incidence. The main direct transmittance angle is always equal to the incident angle, other smaller well defined peaks can be seen on each side of this direct beam. The main angle of redirection is shifted further from the normal to the sample for larger θ_i, this shift is not linear.
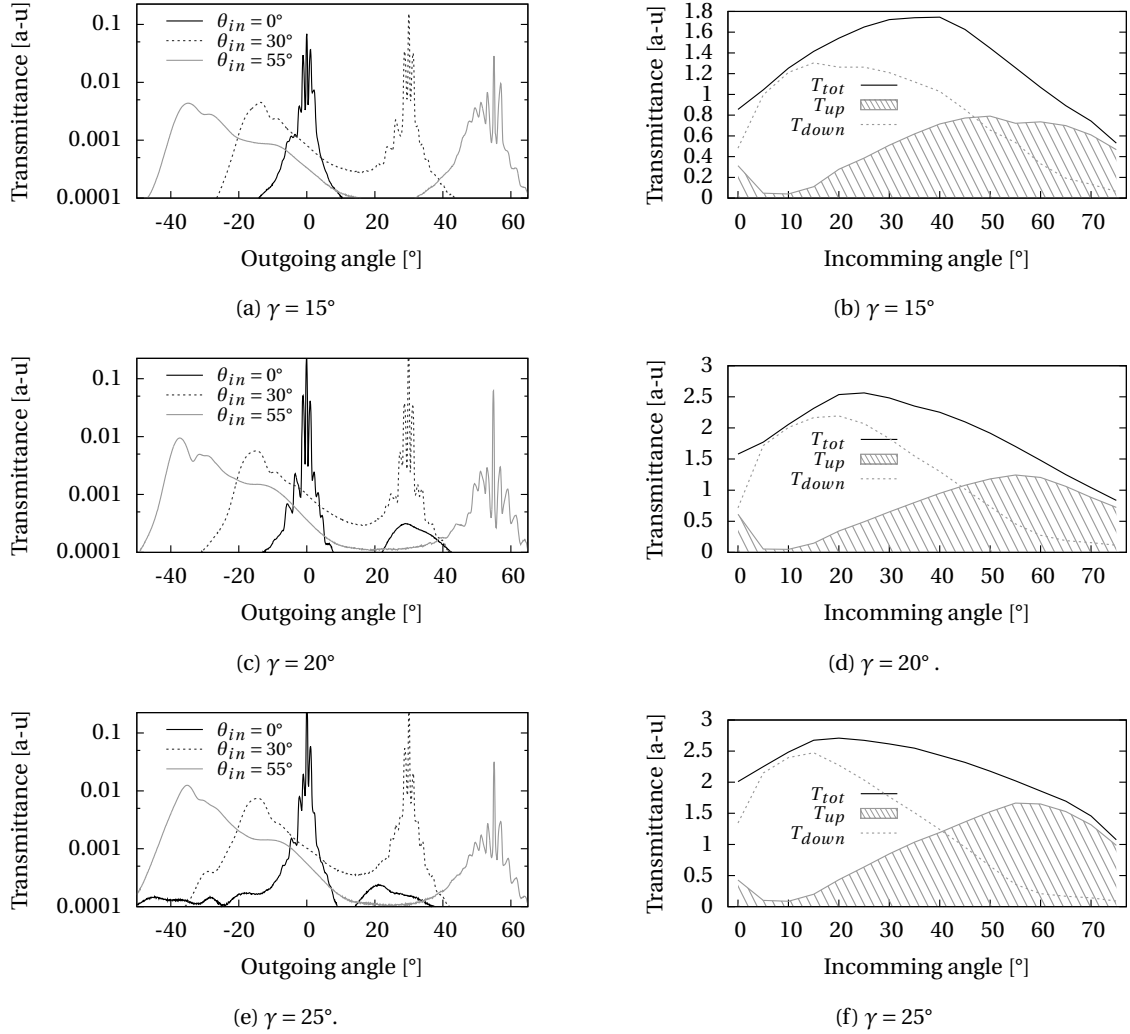
Figure 7.22 – Goniophotometer measurements for sample of the latest generation with different deposition tilt angles γ. The transmission distribution is given for three incoming angles: 0°, 30° and 55° and the outgoing angle is given relative to the sample normal. The dashed areas in the transmittance plots illustrate the proportion that is redirected in the opposite quarter. In the right hand side column, the transmittance distributions for different θ_i were integrated into three quantities: T_{tot}, T_{up} and T_{down} depending on θ_o.

If it was linear, based on the peak location for $\theta_i = 30°$ at approximately $-12°$, it should be located before $-30°$ and not close to $-40°$ for a $\theta_i = 55°$).

From these observation it can be concluded that some ghost image is created around the direct transmission direction. The broad redirected peaks confirm that the embedded mirror is not flat (it diffuses light). For elevated angles of incidence, the stronger shift of the peak can be explained by the refraction at the exiting interface, because of the sinus in Snell-Descarts Law, this evolution cannot be linear. The stronger diffusion is also partly explained by refraction:

angular distributions are emphasised by refraction, they are emphasised more with larger incident angles.

From extra data analysis on the importance of the "side peaks" (not plotted here), it can be deduced that the θ_i angle generating the least ghost image for $\gamma = 25°$ is around 5° to 10°. In this direction the refracted light (with $n = 1.48$, the corresponding refracted angles are 3.5° to 6.9°) is parallel to the embedded mirror therefore the ghost images can be attributed to reflections. In addition for $\gamma = 20°$ the "side peaks" are not reduced, indicating that the coating was not optimal; more surface than only that of the desired facet was likely coated.

In the right hand side column, it can be observed that the transmittance increases with the coating tilt angle and that the angle where T_{up} and T_{down} cross decreases from 46°, to 44° and finally 42° with increased γ. For larger γ, the redirected fraction also increases gradually. From the observations in the right hand side column, it can be concluded that the ideal angle of deposition is certainly not 15° for which is it likely that the bottom of the structure is coated (lower total transmittance). Because the redirected fraction increases gradually, it is imposible to tell if the maximal redirection is reached between 20° and 25° or above 25°, additional coating angles should be studied to define the optimal deposition tilt angle. The minimal value of redirection at an incident angle of approximately 5° to 10° is justified by the tilt angle of the embedded mirrors: with a refractive index of roughly 1.48 the resin refracts light from these angles at 3.5° to 6.9°; this range corresponds to the tilt angle of mirrors.

Coatings were deposited with sample tilt angles of 30° and 35°; because no reference is visible on the structure to define its orientation they were tilted the wrong way and the F_{12} facet was coated. For one evaporation batch, visual observation of transmitted image was used to chose the tilt angle direction consistently. Visually, the transmitted image of an object just behind the transparent structure is seen differently at close to normal incidence depending on the orientation of the sample (i.e.±10°). The result for these sample are discussed below.

With the same mould a different embedded mirror can be produced. Because it is asymmetrical, depending on the selected facet, the coating may be deposited to form a more or less tilted embedded mirror. An attempt was made with aluminium on the more tilted surface (F_{12}) and with a stronger deposition tilt angle (−30° and −35°). The result is a more important light redirection (downwards) at normal incident angle and a redirection angle closer to the horizontal. For low incoming angles, the redirection is in the same quarter as the direct transmitted beam.

(a) $\gamma = -30°$.

(b) $\gamma = -35°$.
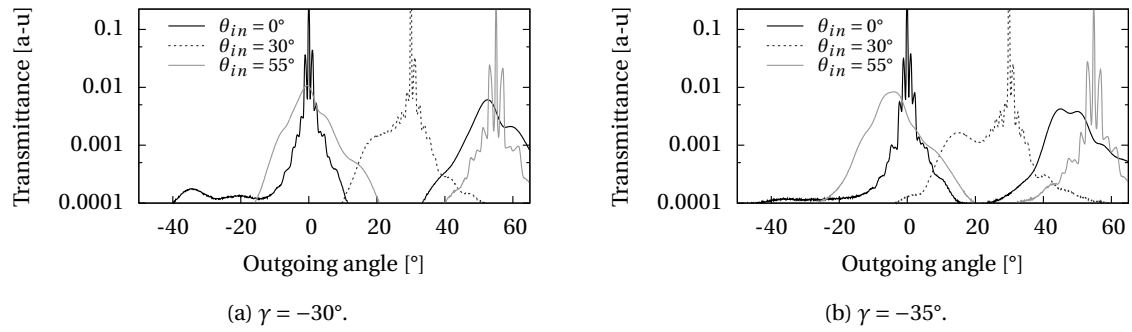
Figure 7.23 – Goniophotometer measurements for sample of the latest generation with the more tilted surface coated. The transmission distribution is given for three incoming angles: 0° and 60° and the outgoing angle is given relative to the sample normal.

8 Discussion

In this chapter side issues in the areas of simulation tools, design optimisation, and fabrication techniques that were only partly answered will be discussed. Limitations and challenges that are still faced and future perspectives will also be mentioned.

8.1 Simulation

8.1.1 Scattering

When fabricating optical structures it is only possible to approach the perfection of a described shape. Surface quality can vary depending on the fabrication process and each one has a limited resolution, in particular EDM machining produces rough surfaces. A miniature goniophotometer was therefore used to characterise how the moulds surface quality can be improved by electro-polishing. In this process two orders of magnitude of surface roughness were identified. One caused by the accuracy of the wire displacement, the other by the localised plasma generated in the cutting process. Such light diffusing processes should be included in the simulation to analyse the importance of well finished surfaces in a design and the sensibility to fabrication defaults. In such an extension, previous work from the field of light scattering by random surfaces can be used [Nayar et al., 1991, Oren and Nayar, 1993, Oren and Nayar, 1994, O'Donnell, 2001]. The diffusion of rough surfaces is generally a function of the incoming angle; for high aspect ratio geometries in particular, at grazing angle, the appearing roughness of a surface is strongly lowered as the fraction of flatter surface increases. The wavelength also has some influence on light scattering. All these considerations add up to a complex problem. For accurate modelling it might be easier to reproduce a measured angular dependent diffusion distribution. This distribution can be measured with the goniophotometer developed in this thesis and associated to integrating sphere measurements for a precise quantitative measure of the total reflectance.

8.1.2 Polarisation

Light is polarised, its electrical field oscillates perpendicularly to its direction of propagation. It may oscillate along only one direction, in this case light is said to be linearly polarised, or the electric field may rotate around the direction of propagation, in this case light is circularly or elliptically polarised. To define polarisation, especially when studying its effects at interfaces, the electrical field is often split into s and p components. The plane of incidence is then defined by the direction of propagation and a vector perpendicular to the considered interface. P polarised component of the electrical field is in this plane, whereas the s polarised component is perpendicular to that plane (from the German *senkrecht*). The p and s fields can have different amplitudes and might be out of phase. The amplitude ratio and phase shift are named ψ and δ respectively. For simplicity, polarisation was not taken into account in the developed ray tracing tool, but it was verified that this is an acceptable approximation: to estimate the effect of polarisation for embedded mirrors, the special case were the azimuth angle is 0° was chosen. At this angle, for any elevation angle, the plane of incidence does not change. Hence, in this situation, the polarisation state remains identical between two interfaces. In the presented example, the light rays are incoming at 55° ± 5°, corresponding to the case of direct sunlight in the blocking range. After refraction at the first interface, the light rays are reflected by the embedded mirror, focused onto the backside mirror where they are once again reflected to finally be reflected on the bottom surface of the embedded mirror and refracted at the first interface to exit the system (as illustrated in the right most part of Figure 6.7). The angle of incidence at each interface was computed with CFSPro and the transmittance t and reflectance r at these angles were computed for both polarisations states using TFCalc. Assuming the incident light beam is depolarised, as direct sunlight is, two computations were made to compute the fraction of light flux following this path. In the simplified approach, equivalent to the one used in CFSPro, the reflectance resulting from these five interactions was computed by directly multiplying the mean values:

$$r_{path} = t_{55} \cdot r_{67} \cdot r_{23} \cdot r_{67} \cdot t_{23}. \tag{8.1}$$

where the subscript is the mean angle of incidence for each interface and the t and r values are the mean of $t_\perp$ and $t_\parallel$, respectively of $r_\perp$ and $r_\parallel$. A more rigorous computation was then made, by multiplying the weighted average for each interaction depending on the evolution of the polarisation state.

The results for aluminium and silver embedded mirrors are presented in Figure 8.1. The dots represents the rigorous approach and the continuous line the approximate approach. For aluminium mirrors, the greatest difference, at 820 *nm*, was found to be below 2% relative; for silver the difference was below 1% relative. This low difference is surprising, especially for aluminium since the transmitted light is strongly p polarised because the incoming angle is close to the Brewster angle and the reflected light at the mirrors is strongly s polarised. Despite these strong changes in the polarisation state, in this special case and for the presented design with embedded parabolic mirrors, taking into account polarisation does not make a strong
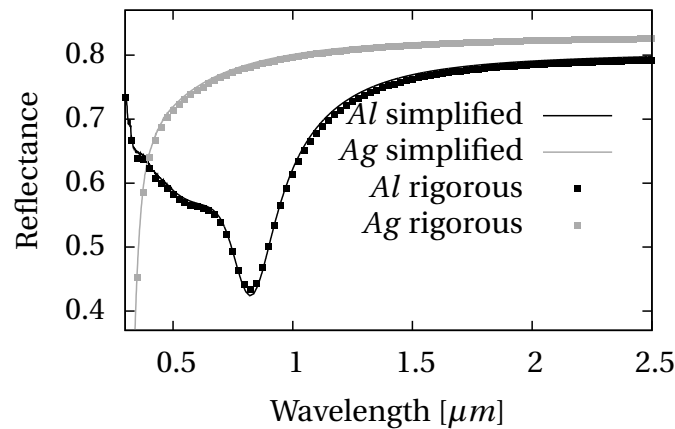
Figure 8.1 – Polarisation effect in reflectance for an embedded parabolic mirror at an incoming angle of 55° ± 5°.

difference on overall reflectance and transmittance. It can be noticed that for cumulated reflections, aluminium mirrors are not very efficient reflectors in the visible range for high angles of incidence; in this particular configuration, a large part of the light beam is absorbed.

The final polarisation state may however vary significantly after several polarising interactions. In the studied case the final change is moderate because the reduced transmittance at interfaces for s polarised light beam is balanced out by the reduced reflectance on the mirrors for p polarised light. These cancelling events might not happen in all designs, and successive interaction may strongly affect the polarisation state if they add up. Adding polarisation is possible but not straight forward since it requires to compute and keep track of the polarisation state at each interface, this was successfully carried out by the author in the past to study luminescent planar concentrators [Schuler et al., 2008]. Considering polarisation would be useful to study polarisation based designs using the Brewster angle, the effect of the design on the polarisation state or to account accurately for the polarisation of the diffuse contribution of the sky. As defined by the Rayleigh scattering law, unlike the depolarised direct sunlight, the light flux of a clear sky is polarised dependent on the angle with the sun.

8.1.3 Optimisation by genetic algorithm

Before the thermal and daylighting performance metrics where implemented as they currently are, it was hard to define an appropriate fitness function. For this reason, the genetic algorithm (GA) could not be applied to find new design alternatives. With the annual daylight metrics and the annual thermal loads, it becomes possible to implement a very objective fitness function, such as "maximize illuminance and minimize thermal loads". An alternate, more direct (because it does not require complete daylight and thermal simulations) fitness function can be implemented based on the ideal distributions derived in Section 6.5 and 6.4. During the development of the simulation toolkit, some new functionalities were added and others modified but the GA was not adapted accordingly.

8.1.4 Annual glare study

Using an approach similar to the matrix multiplication for the computation of annual illuminance values on a set of sensors, it is possible to compute a contribution to each pixel from the scene and to apply annual sky luminance values to directly obtain an approximated rendering for each time step. These renderings can in turn be used to rate glare with *evaglare*. Such annual glare value have been introduced recently in the Diva-for-Rhino plug-in for Rhinoceros. The later is a CAD program for architects and the plug-in enables the "users to carry out a series of environmental performance evaluations of individual buildings and urban landscapes including Radiation Maps, Photorealistic Renderings, Climate-Based Daylighting Metrics, Annual and Individual Time Step Glare Analysis, LEED and CHPS Daylighting Compliance, and Single Thermal Zone Energy and Load Calculations" [Sollema, 2014].

8.1.5 Reach of CFSPro

Beside the study and development of complex structures for CFSs, the software was also used to study the effect of mismatch in refractive indexes on diffusion in fibreglass [Pascual et al., 2013]. When designing thin films for interferometric filters as described in [Mertin et al., 2014], this software could easily be adapted to obtain more precise solar transmittances depending on the location, orientation and tilt of glazing. These are just two of many other fields of optics were CFSPro could be applied. This tool is very contemporary and was developed in its time: the *bsdf* Radiance primitive was developed in parallel and CFSs characteristics are slowly taken in account in energy simulation tools, such as EnergyPlus (from V8.0 on)[Dartevelle et al., 2013].

8.2 Design consideration

8.2.1 Non constant geometry

If the embedded mirrors are used over the whole surface of a window, redirection from the bottom part of the glazing might induce glare. This can be avoided, and performance potentially increased further, by adapting the structures depending on their location in the window. The tilt angle, parabola shape and blocking mirror size can easily be modulated in the design. If such a design is modeled in CFSPro, the resulting BTDF however is an average BTDF and cannot be used directly in Radiance with the *bsdf* material type. The window would have to be defined as several elements with different BTDFs.

8.2.2 Location dependence

The desing principles are based on a static structure: to be efficient it has to be adapted to the location where it will be installed. Depending on the latitude, the solar course changes and the parabolic surface has to be optimised to block radiation for the summer elevations of the sun and transmit radiation from the winter sun. As a preliminary study, the optimised

transmittance distribution obtained as described in Section 6.5.1 was computed for Rome and Berlin. Initial results are promising and a systematic study should be performed.

8.2.3   Structure tilt on east and west facing windows

So far, only the question of south orientation was considered in this work. East and West orientations offer different solar radiation distribution. However as discussed in [Lorenz, 2001b] and pictured in Figure 8.2, by tilting the structures, a similar angular dependent behaviour of the same design can be reached for other orientations. In deed, when changing the orientation, the region of the hemisphere occupied by the sun's position over the year changes. For an East orientation for example, the sun will never be in the left-hand side of the visible hemisphere; it will rise around the centre and move towards the upper, right-hand side. Unlike for a south orientation where the sun covers a rainbow like area of the hemisphere, the sun will then cover half of a diagonal like area. When rotating the structure in the right direction, the sun's path can therefore again be "more parallel" to the extrusion direction of the profile. The seasonal variation of the sun elevation angle relative to the plane described by the latter direction and the window normal direction is therefore conserved.
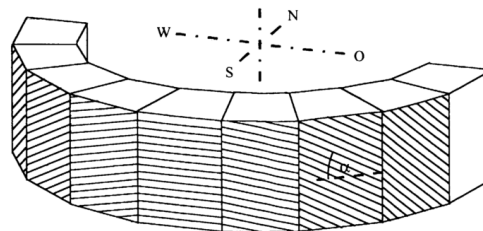
Figure 8.2 – Structure rotation for different orientations as described by [Lorenz, 2001b].

8.2.4   Climatic evolution

In this work the heating and cooling loads have been treated equally, this is justified by the fact that modern HVAC systems use a reversible heat pump to generate both heat and cold. In the future, with global warming and climate change, the cooling loads in office building are likely to increase and become more important in the annual thermal balance [Struck et al., 2014]. It is important to look ahead and consider this aspect when designing an ideal fenestration system.

8.3   Microfabrication

8.3.1   Engraving techniques for mould fabrication

The production of a suitable mould with precise dimensions, smooth surfaces and large surface capabilities remains a challenge. The fabrication process of vinyl masters in the record industry could possibly be adapted as it offers good surface quality and the record grooves are within the required dimensional range. This technique would require engraving of a soft material with a tool shaped to the profile of the desired structure. Such a tool can be fabricated by standard UV-LIGA technique. This seems a promising novel technique suited for extruded geometries, in particular within the $50 - 500\,\mu m$ scale range and for structures with high aspect ratio. But such a new method would required extensive research to produce results, unfortunately time was not available for that during this thesis.

8.3.2   Replication problems

For the next mould fabricated by laser ablation, a reference mark should be added to the mould in order to clearly identify the orientation of structures. To resolve the replication problems faced when imprinting thick structures, the quantity of photo initiator might be modified or the type of resin adapted. This requires further study with difference concentrations of photo initiator and even changed completely. It is likely that a mean to better polymerise thick structures can be found.

8.3.3   Alignment

The alignment of two optical elements was only partly studied and requires further experimentation. The setup was tested without applying the resin because the available samples are not yet fully focusing and the references for thickness control were not available on the latest samples. Because of the micrometric scale of the latest samples, mechanical machining techniques such as milling could not be used to produce these required references and to enable a control of the total sample thickness. In future designs, these reference will have to be included in the mould like it was done for the EDM machined inserts. This may however not be straight forward in the case of laser ablation.

8.4   Perspectives

8.4.1   Improvement of the laser ablated mould

The goniophotometer measurements of the samples produced using the laser ablated mould can be used to define the optimal deposition angle and, in correlation with simulations performed on basis of the profile characterisation, a proposition for an improved profile can be made. As it was already mentioned, reference surface have to be added in future

designs. The vertical and tilt alignment can be performed during the embedding step but such reference surfaces are required to guarantee the horizontal alignment of the two optical components.

8.4.2 Roll to roll

An interesting technique for industrialisation in the scope of the thesis is the roll to roll replication. The substrate is rolled from one roll to the other, in between it may undergo different steps of structuring with a master roll holding the pattern and pressing against the substrate, embossing the shape it carries. The substrate may also be coated along the process. Some companies like Wavefront Technology Inc. produce large areas of microstructured film this way; the LTC lab at EPFL has an experimental setup for such processes.

8.4.3 Energy production

The back reflector could be replaced by a thin film solar cell, adding on more functionality to the CFS and making it both a passive and active solar system. The back reflector area represents 20-40% of the window surface and receives 20 to 80% of the direct solar radiation impinging on the CFS. This fraction depends on the time of the year, the mean is at 35% and in total, the annual irradiation on the blocking stripes is $200kWh/m^2$ in Lausanne, Switzerland. Further more, light concentration slightly increases the open circuit voltage, therefore the efficiency of a solar cell. With a concentration of 10 times, the open circuit voltage is increased by $60mV$ for an ideal $n = 1$ junction at $300°K$ [Friedman et al., 2011]. Because the efficiency depends linearly on the short circuit current, this represents an increase in efficiency of roughly 7% for an initial open circuit voltage of $0.8V$ (typical value for J_{SC}). However, temperature raise would most likely counteract this increase in efficiency. Such striped thin film solar cells could be realised with amorphous silicon ($a − S_i$), hydrogenated amorphous silicon ($a − S_i − H$), coper indium galium selenide (CIGS) or cadmium teluride (CaTd). All these technologies are suited for thin stripes of solar cells. In all cases the film could be deposited using lift-off lithography. Using a thin film solar cell with a typical efficiency of 8% would produce $16kWh/m^2$ annually. With an annual energy consumption for lighting in the order of $2kWh$ per m^2 of surface, light self sufficiency can be reached with one square meter of window for 8 square meters of surface.

9 Conclusion

In this chapter, the key achievements and findings of this research are summarised. A simulation tool was developed for the study and optimisation of microstructured glazing with the combined functions of daylighting, glare reduction, seasonal thermal control and clear outside view. Using this tool, a novel geometry was designed and a fabrication process suggested; the different steps of this process were studied, samples were fabricated and a measurement setup was established to characterise the resulting samples.

Summary

- **Software Development.** CFSPro, a ray tracing simulation software was developed and validated. Angular dependent transmittances were studied and compared between designs. This software was also used to generate complete BTDFs and visualise the task illuminance distribution in a standard office room using Radiance. A matrix multiplication method was implemented to assess daylight availability based on hourly workplane illuminance over the year. To obtain this result, a matrix containing hourly luminance values from different directions is first multiplied with the BTDF. The luminance values are derived from a Perez sky model based on climatic data for this location; the BTDF is obtained by ray tracing with CFSPro. The resulting contributions in different direction on the interior face of the CFS are then multiplied by a so-called "view matrix" obtained by ray tracing of the office room with Radiance to compute the illuminance values on a set of sensor points in the scene. Likewise, a matrix multiplication based on the BTDF was used to calculate the solar gains depending on the hourly diffuse and direct irradiances. The effect of these thermal gains on the hourly temperature and corresponding heating and cooling energy demand were estimated with a resistance-capacitance thermal model that also takes into account the outdoor temperature and construction properties (U value, thermal mass, etc.). In both cases, extra accuracy was reached by performing these matrix operation for direct and diffuse contributions separately, using time step sun positions and an appropriate discretisation of the visible vault respectively.

- **Novel structure.** This simulation tool enabled the study of current designs and the invention of a promising design for multifunctional glazing. The light scattering properties of this novel design were compared with those of state of the art daylighting redirecting devices; it was shown that it offers sound light redirection capabilities with an added angular dependence of transmittance and increased clear vision. The angular dependent transmittance has the particularity to "cut-down" transmittance for a selected range of incoming elevations: this interval can be modulated to some extent. After optimisation, the BTDF of the corresponding design was computed and the above described performances calculated.

- **Experimental methods.** In order to fabricate the novel device designed with the ray tracing software, a process was proposed. This process requires a mould for the fabrication of the structure. This mould was first fabricated by EDM, because of limited surface quality, several other techniques were considered and studied. A mould with optical surface quality was produced by direct laser writing in a collaboration with Empa. Negative stamps were fabricated in PDMS, this step was required to produce a mould compatible with UV curing resins used in the replication step and to provide the required additional features for alignment. After replication by UVNIL, samples were coated by evaporation under a certain angle to coat only one facet of the structures. Finally, the deposited mirrors were embedded using the same resin. The experimental apparatus required for each of these steps were identified and those that were not available were fabricated. Challenges remain however in the fabrication of an appropriate mould.

- **Experimental results.** The principles of each step in the fabrication process were validated. Directional evaporation of material was shown to be effective, the PDMS stamper fabrication and UVNIL replication were successful, although the parameters for the UVNIL required some optimisation. In particular for thick samples, delamination and air pocket formation posed problems. Flat diffusing mirrors were successfully embedded and measured using a "home made" miniature goniophotometer. Diffusing parabolic mirrors were also obtained at a much smaller scale. Finally a mould with parabolic like optical surfaces with a period of $50\,\mu m$ was obtained, replicated, and the resulting structures coated and successfully embedded. Reflective stripes were deposited using a lift-off process.

Advantages

Compared to conventional windows, blinds or complex fenestration systems, this optical design has several advantages:

- It achieves simultaneous angular dependent transmittance and redirection of light rays.

- Because of the small dimension (sub-millimeter), the structures are almost invisible and the resulting system is close to transparent.

- The redirected light beam is distributed horizontally in a diffuse way, hereby suitable for daylighting purposes.

- The system is thin and could be fabricated in a roll to roll process or web process and produced as a sheet. This sheet can easily be placed within a standard double glazing.

- Unlike external blinds or shades, the system is static and protected, therefore not sensible to strong winds.

- It can be placed on the first glass of a double glazing; this reduces unwanted solar gains in the cooling period.

- Because it can be part of the glazing, architectural integration is facilitated.

- Cost in the case of roll to roll production can be relatively low.

- There are no mobile parts therefore more robustness.

Outlook

In the future, new techniques for the production of moulds can be studied. The adaptation of existing techniques, such as laser ablation, can be considered. For the simulation, additional physical models for diffusion and polarisation can be added and the glare rating can be made dynamic to provide location and time dependent information. The designs can be optimised for several locations and more advanced orientation dependent study performed.

The potential for such complex fenestration systems is high since they can simultaneously increase daylight provision, reduce glare risks and mitigate energy consumption by lowering heating, cooling and electric lighting loads. With miniaturised structures, these functionalities can be provided whilst conserving a view to the outside, an essential property for glazing elements.

A Sky Model

A.1 Motivation

To study daylighting provision and solar gains it is necessary to understand and know the source of radiation: the sky. In particular, for the simulation of complex fenestration system (CFS) performances, a model of the distribution of radiation / luminance over the sky was required for two reasons:

- Firstly in CFSs, the g value can show strong variations depending on the angle, therefore a detailed description of the sky is useful for energy related computations such as solar gains. In Complex Fenestration System Ray tracing Profile Optimisation (CFSPro), the sky radiance is multiplied by the glass transmittance and summed to give time series of solar gains at each time step t:

$$Q_t = \sum_{k=1}^{k=p_s} \left(L_{ed,k,t} \cdot v_{d,k} \right) + E_{eb,t} \cdot \tau_{b,t} \;\; + \;\; Q_i \tag{A.1}$$

where k is the sky patch index, p_s patches cover the hemisphere centred around the normal to the glazing. $L_{ed,k,t}$ is the diffuse radiance for the given patch and $E_{eb,t}$ the solar irradiance for this time step, $v_{d,k}$ is the transmittance coefficient of the CFS for the set of incoming directions corresponding to the kth patch (including the solid angle for conversion to resulting irradiance) and $\tau_{b,t}$ is the transmittance for the direction corresponding to the solar position at this time step. All values are time dependent except $v_{d,k}$ which is constant for each patch of a given CFS:

$$v_{d,k} = \frac{\Omega_k \cdot \sin(\theta)}{2 \cdot \pi} \;\; \cdot \;\; \sum_{j=1}^{j=p_{in}} \Omega_j \cdot \tau_{d,k,j} \tag{A.2}$$

The $v_{d,k}$ coefficient contains the solid angle Ω_k of the concerned sky patch k and the effect of the angle relative to the surface normal to convert the radiance values to irradiance values. The hemisphere subdivision of the sky and inside window contribution (as described later) may differ; the solid angles Ω_j of the p_{in} inside patches has to be considered to weight each patch accordingly. $\tau_{d,k,j}$ is the transmittance from a patch k to a patch j.

- Secondly, the distribution of illuminance is useful for the assessment of daylighting performance. An approach similar to the five phase method [McNeil, 2013] used with Radiance command line tools can be applied to obtain time series of illuminance on a plane in a chosen space. In matrix notation:

$$E_v = V(T_d \cdot L_{v,d} + T_b \cdot L_{v,b}) \tag{A.3}$$

where V, the view matrix as defined in the three and five phases methods, is obtained from Radiance to compute the contributions of each outgoing direction from the window to each location in the test room. The T matrices links the inside and outside of the window, for the diffuse, each element τ_{ij} of the matrix T_d gives the energy transmittance from patch i on the outside to patch j on the inside. This transmittance is weighted with the cosine of the angle between the patch i and the normal to the glass. For the direct, τ_{hj} give the energy transmittance for a given time step h to each patch j on the inside. Finally the L_{vd} and L_{vb} matrices hold the luminance of the diffuse and direct sky at hourly interval. They are derived from the L_e matrices as described later.

It can be noticed that in both cases, diffuse and direct radiation are considered separately. The transmittance for an incoming direction corresponding to the sun position is computed accurately and not averaged by the mean transmittance of the patch the sun is in. This strongly increases the accuracy of the computation when the direct contribution is significant (under clear skies) and especialy if the studied CFS has sharp, angular dependent transmittance. The luminance and radiance of the different sky directions and of the direct component are derived from hourly horizontal irradiance measurements using the Perez Model. Figure A.1 illustrates how such a model can be used to compute the monthly distribution of radiance over the sky vault in Lausanne, Switzerland.
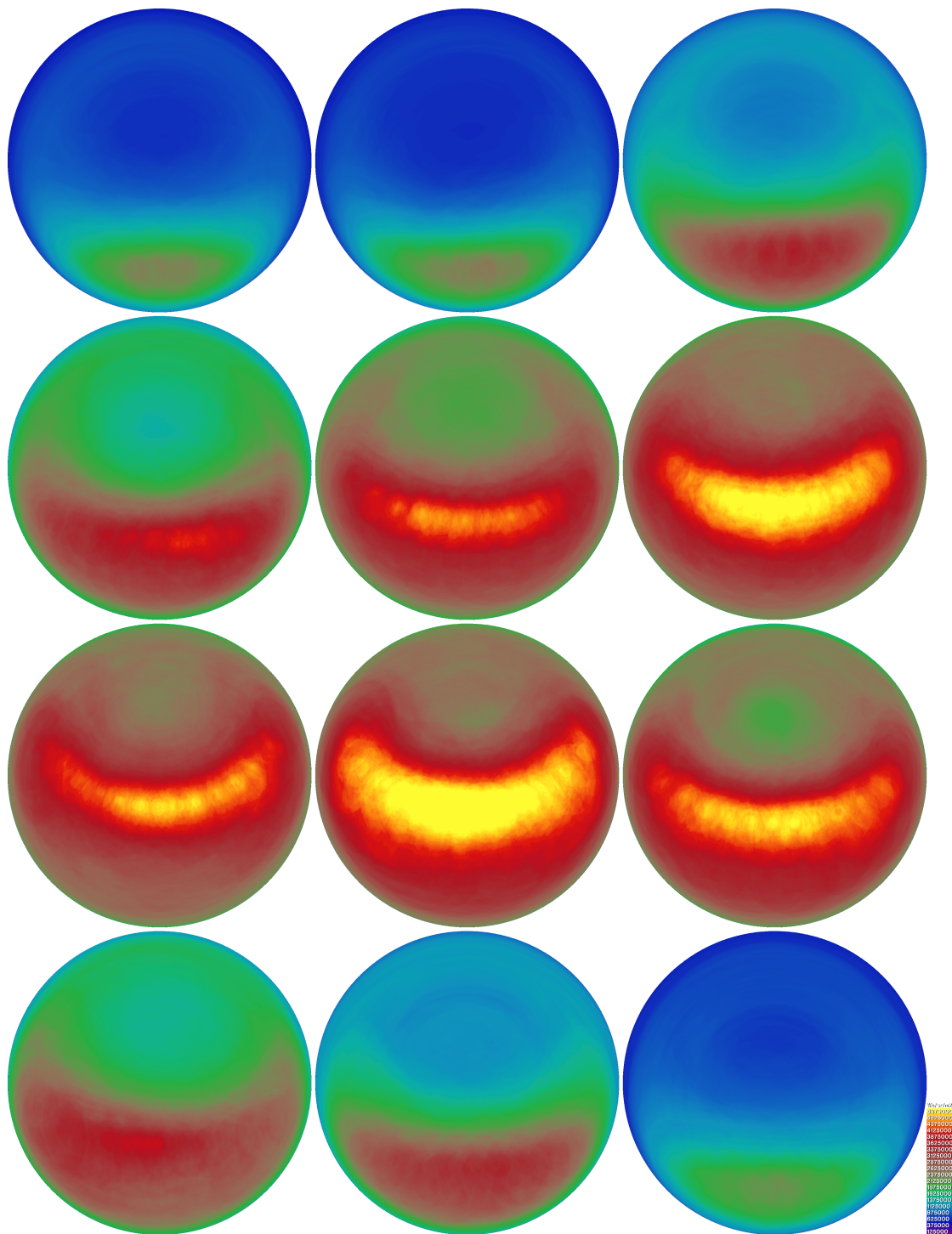
Figure A.1 – Monthly radiance distribution of the sky for Lausanne, Switzerland as obtained from an annual simulation with Radiance using the Perez model.

A.2   Theory

A.2.1   Perez model

The Perez model for all weather sky luminance distribution was described by Perez *et al.* [Perez et al., 1993]. It is a widely used model for the determination of sky luminance. It is used amongst others by Radiance and Meteonorm. The mathematical expression for the sky luminance is a generalisation of the International Commission on illumination (CIE) standard for clear sky. It includes five critical coefficients that can be adjusted to render sky conditions ranging from completely overcast to very clear. As defined by Perez *et al.*, the relative luminance is the ratio between the luminance for a considered sky element and an arbitrary reference. In this implementation of the model, the recommendations of the authors were applied and the luminance is normalised by the diffuse horizontal illuminance divided by the integral of relative luminance over the hemisphere. So as described in [Perez et al., 1993], the relative luminance of a patch is given by:

$$l_v = f(\zeta, \gamma) = \left(1 + a \cdot e^{\frac{b}{\cos(\zeta)}}\right) \cdot \left(1 + c \cdot e^{d \cdot \gamma} + e^{\cos^2(\gamma)}\right) \tag{A.4}$$

where ζ is the zenith angle of the considered sky element and γ is the angle between this sky element and the position of the sun at a given time. And the luminance of a patch is then given by:

$$L_v = \frac{l_v \cdot E_{vdh}}{\int l_v(\zeta, \gamma) \cdot \cos(\zeta) d_\omega} \tag{A.5}$$

where ω is the solid angle of the differential elements over which the sky is integrated and E_{vdh} is the diffuse illuminance on the horizontal plane and is computed from the diffuse horizontal irradiance E_{edh} by applying the luminous efficacy described by Perez *et al.* in [Perez et al., 1990]:

$$E_{vdh} = E_{edh} \cdot (a_i + b_i W + c_i \cos(Z) + d_i ln(\Delta)) \tag{A.6}$$

where W is the atmospheric precipitable water content and depends on the surface dew temperature; in this implementation, the W parameter was set to be constant and equal to $2\,cm$ (dew temperature at 11°C). Z is the solar zenith angle in radians and Δ is the sky brightness and depends on the relative optical airmass, horizontal diffuse irradiance and the extraterrestrial irradiance. The a, b, c and d coefficients were fitted by Perez *et al.* following several measurements. They are eight different sets of values for these coefficients, the appropriate

set of values depends on the sky clearness ϵ:

$$\epsilon = \left(\frac{E_{edh} + E_{ebn}}{E_{edh}} + \kappa Z^3 \right) \cdot (1 + \kappa Z^3) \tag{A.7}$$

where E_{ebn} is the direct irradiance at normal incidence and κ a constant equal to 1.041. This description of the sky can also be used for the estimation of radiance values when based directly on the diffuse horizontal irradiance.

A.2.2 Solar path

The Perez model relies on the diffuse and direct irradiance data. They can easily be found for hourly steps in climatic data (taken from Meteonorm for example). The Perez model also relies heavily on the solar position. To determine this position, the latitude Φ and longitude λ have to be known. Solar time is defined as 12:00 when the sun is at it's highest point, the solar time angle h is between 0 and 2π and equal to π at solar noon. The flowing equation is used to calculate the elevation of the sun depending on the solar time

$$\sin(\theta) = \sin(\Phi) \cdot \sin(\delta) - \cos(\Phi) \cdot \cos(\delta) \cos(h) \tag{A.8}$$

where δ is the declination, the angle between the ecliptic plane of rotation around the sun and the equatorial plane of the earth. It is between 0° and 23.27° and changes for each day of the year. For the solar azimuth:

$$\sin(\phi) = \frac{-\cos(\delta)}{\cos(\theta)} \cdot \sin(h) \tag{A.9}$$

The solar azimuth is zero at solar noon, when the sun is at the south. Attention! This is converted to angles from north as defined in the coordinate system of the sky. The Perez model then uses only relative angles and uses the point coordinates. In this description of the solar path, the time is given in solar time. The relation between solar (h_s) and local time (h_l) depends on the time zone, localisation on earth and time of year:

$$h_l = h_s - 4\lambda + F - \Delta_h \tag{A.10}$$

where F is the shift between h_l in the considered time zone and at Greenwich and Δ_h is the time equation.

A.2.3 Ground contribution

The method for the computation of sky luminance was described above, the ground luminance is computed in a more simple fashion. The ground has a reflectance, the albedo, the reflection

is assumed to be fully specular and Lambertian; the ground has a constant radiance no mater what direction it is looked at. Both direct and diffuse irradiance are reflected so the Illuminance from the ground is :

$$E_{vg} = \frac{(E_{vdh} + E_{vbh}) \cdot albedo}{2\pi} \tag{A.11}$$

A.3   Space time and Coordinate Systems

A CFS is defined by the way it scatters light for different incoming angles, this distribution is called bidirectional scattering distribution function (BSDF). More specifically, the transmission part of the BSDF, the bidirectional transmission distribution function (BTDF) is required to compute the illuminance at specified points in a space and the thermal gains trough a window. This distribution function is central in the CFSPro simulation tool and so is the spherical coordinate system it is defined in. Because a patch division can be insufficient for some CFSs that have strong changes of transmittance or reflectance distribution for a small change in the incoming angle, a second coordinate system is used for the computation of the direct component. This coordinate system uses yearly time steps and the associated solar positions. It is therefore location dependent. Additionally, for the definition of the sky and the scenes a third coordinate system is used. Finally a last system is used for the ray tracing of the CFS. The later two orthographic coordinate systems have to be converted to the spherical BSDF coordinate system to enable the matrix multiplications used to derive thermal gains and illuminance values through the window and under a give sky. Likewise for direct contribution, the hourly solar positions have to be computed relatively to the orientation of the window surface.

A.3.1   BSDF dome

The sky values are used in combination with a transmittance matrix to compute transmitted energy and its distribution. When adding a V matrix computed with Radiance, the contributions from each direction of the interior vault can be weighted to compute luminance values for a series of points in a scene. To make this calculations work in a simple matrix multiplication, the indexes have to match. Because the central element in this calculations and in the CFSPro tool is the window, The reference coordinate system is the spherical coordinates system centred on the window. A window is defined as a flat system, oriented with its normal $\vec{n}$ pointing inside. The sphere around the window is separated in two hemispheres: on the inside the transmission side, on the outside the reflection side. $\vec{h}$ defines the directionality of the window, it is in the horizon plane if the window is not rotated around the normal vector. The up direction for the window is then defined as $\vec{n} \times \vec{h}$.

These three vectors define the origin of a spherical coordinate system relative to the window ($x = h, y = up, z = n$). Theta is the angle with the n vector, it is between 0° and 180° and

smaller than 90° for transmittance and larger for reflectance. Phi is the angle from h towards up vector and is between 0° and 360°. In order to describe BSDFs, the two hemispheres on each side of the glass are subdivided in angular patches. Multiple standard subdivision of a hemisphere exist: Tregenza, Klems, Illuminating Engineering Society (IES) lighting standard and more. They all reduce the infinite directions of a coordinate system to a list of patches. A patch is generally defined by two angular intervals (in elevation and azimuth) and these intervals are of different sizes to obtain patches with similar solid angles. Particularly, as defined in the extensible markup language (XML) standard for windows from the Window 6 software from Lawrence Berkeley National Laboratory (LBNL), patches are defined on both side of the window. Attention, the patch index is always defined considering the direction of propagation; for clear glass, the patch number is the same for transmission as for incoming, the transmission matrix is a diagonal matrix.

Depending on the representation, the angular ranges change:

- **Tregenza** is defined by a 6° half angle zenith patch and seven 12° bands. This representation was designed to represent sky distributions, the bands are divided in order to obtain patches with roughly similar solid angle. Starting from the horizon band, they are successively divided into : 30, 30, 24, 24, 18, 12 and 6 patches

- **Klems** is defined by a 5° half angle zenith patch and seven 10° bands and a 15° horizon band. This representation was designed to represent BSDFs, the bands are divided in order to provide a good representation of transmittance/reflectance. Because reflectance and transmittance are less important for low angles (the projected area for these angles is much lower) the solid angle for these patches are greater. Starting from the horizon, the bands are successively divided into : 12, 16, 24, 24, 24, 20, 16 and 8 patches.

- **IES** is defined as regularly subdivided azimuth and elevation angles. The subdivision angles may change and can be different for elevation and azimuth. It was designed for the description of luminaries with no intent of optimised data storage. The solid angle of patches close the zenith are much smaller than that of patches at the horizon. Regardless of the chosen subdivision, the order of patches can change. They may then be counted starting from the top or at the horizon. For a new band, counting always starts centred in the x direction and usually done in the normal direction: from x direction to y. However in some cases, the direction is reversed.

These representations and their directions were implemented in the BSDF Representation class. This class takes a normal (inside) and an up vector from the coordinate system it is in. The patch number can then be computed for a given direction in the considered orthonormal coordinate system. Likewise, the vector pointing at the centre of a patch can be obtained in the orthographic coordinate system. This representation therefore effectively links the CFSPro coordinate system with the general sky / scene coordinate system.

A.3.2   Sun coordinate system

For the direct contribution, the solar time with defined time steps (1 minute to 1 hour) is used as a simplified coordinate system. Depending on the location, the associated solar position is computed and used if visible. The time can be given in solar or local time and the solar position is computed as described in the theory part. This subdivision has to be recalculated for every location. The associated direct radiance / luminance values of the sky and BTDF of the considered CFS have to be recalculated as well. However the resulting precision for direct radiation is crucial.

Special care has to be take when reading weather files, they often provide average data for certain time intervals and the time value may be the centre or bounds of these intervals. If they represent the end on an interval (as in Meteonorm), the solar time for an interval has to be centred on the interval and the solar position computed accordingly. The solar position at a give time is computed once in the sky coordinate system and once in the window coordinate system.

A.3.3   Sky and Radiance

An orthographic coordinates system is used in the Perez model and in Radiance. In Perez it is used for the computation of solar positions along the year and the associated illuminance/irradiance. Likewise it is used to compute and average illuminance/irradiance for the sky patches. In this coordinate system:

- The $+x$ axis is in the east direction.

- The $+y$ axis points in the north direction.

- The $+z$ axis is the up direction or zenith and any vector with z < 0 points below the horizon.

- The elevation angle is defined from the horizon upwards to the zenith = $asin(z)$.

- The azimuth is defined as the angle from the north in clockwise direction = $atan2(x, y)$.

The Tregenza zones of the sky generated with `genskyvec` start at North and are counted clockwise and patch 0 is the ground. To generate a corresponding BSDF representation as defined in 1.2.1, the normal is (0,0,-1), the horizontal is (-1,0,0) and the up direction is (0,-1,0). This coordinate system is also used to draw the scene for which the daylighting will be evaluated in Radiance. Scene are however always drawn with the studied façade facing south and at y = 0. If the façade needs to be studied with an other direction, the radiance scene is rotated to obtain accurate rendering. This however does not affect the V matrix which is only dependent on changes in the scene itself.

A.3.4 V matrix

The V matrix is required to compute the contributions to different points in a room from each transmission direction. It is computed with radiance using the `rtrace` command for a series of sensor points and for a set of sampled Klems directions. The scene is the same than when studying illuminance values but the window is replaced by a glowing source.

A.3.5 CFSPro

n CFSPro the *x* and *y* axis only are used to define the profile. The x axis is the normal to the window towards the inside and the *y* vector points up. If relating to the BSDF coordinate system defined earlier, the x axis corresponds to the normal to the window and *y* to the up vector. To generate a corresponding BSDF representation as defined in 1.2.1, the normal is (1,0,0), the horizontal is (0,0,-1) and the up direction is (0,1,0).

A.4 Implementation

This sky model was implemented in C++ in the QT Framework and partly based on work previously done by J. Kaempf. It was implemented in an object oriented paradigm to provide flexibility. The sun, vault, patches, location, climate and BTDF representations were all implemented as objects that can be sub-classed if needed. To be computed, a Perez sky needs to be given a location, a climatic data file, a normal vector and an up vector. Additionally, the desired time step for direct and diffuse output as well as the BTDF representation need to be specified. To provide consistent coordinates system within the Perez mode, the `GENPoint` class was inherited from an other project at Solar Energy and Building Physics Laboratory (LESO-PB) and is used in the Perez model. It provides transition from spherical to cartesian coordinates. The `GENAngle` class was also overtaken to guarantee the consistency of angle and avoid mistakes due to the mix of radians and degrees.

A.5 Validation

A.5.1 Sky model

This sky model has been validated using a series of specific tests. The first most trivial test is to find if the integral of the sky distribution corresponds to the imputed total diffuse and direct horizontal irradiance. This test was concluding. Secondly total irradiance for vertical walls with different orientations were compared to total irradiances for the same situation obtained with Meteonorm. This comparison was un conclusive because Meteonorm uses a simplified approach to compute this total irradiance (as defined in the Meteonorm theory manual for version 7 on pages 28 and 29). The Perez implementation was then compared with the validated Perez distribution used in Radiance and implemented in the `gendaymtx`
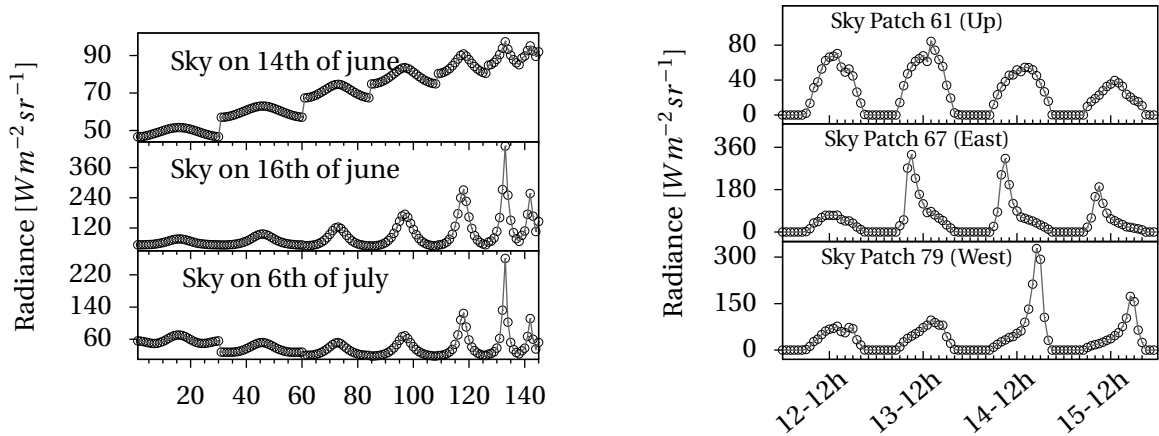
(a) Radiance value of sky patches at noon for three selected summer days.

(b) Hourly radiance values from the 12th to the 16th of june for three selected patches of the sky.

Figure A.2 – Comparing *gendaymtx* and QT implementation of the Perez sky model for selected days at 1 pm as well as for selected patches over the course of four days. The empty circles are values from the present implementation and the lines from the Radiance implementation.

command. In the QT implementation of the sky, the surface of interest was specified to be horizontal and the subdivision to be Tregenza to provide identical patches. This comparison was conclusive as shown in Figures A.2a and A.2b.

Finally in order to validate the combination of sky distribution, ground contribution, and the patch subdivision performed relatively to the studied orientation, the obtained irradiance (and illuminance) values for different orientations were compared with those obtained by the combination of radiance commands used in the three phase method to obtain. The surface was first oriented south with no ground contribution, then with ground contribution and finally for a random orientation of 121° from to the east north and a tilt of 31° and a ground contribution. These comparisons were performed for all days of the year at the location of Lausanne, using an albedo of 0.2 and a climatic file from Meteonorm obtained for Lausanne . The set of Radiance instructions were as follows:

- Generate a diffuse only sky using the weather file. This is done with the following command:

```
1  gendaymtx -m 1 -c 1 1 1 -g 0.2 0.2 0.2 -s -O1 lausanne.wea > skyDiffuse.smx
```

  where -m specifies the subdivisions. -c the sky colour -g the ground colour. The colours are deliberately set to be in grey levels. -s is the option to generate a the diffuse component of the sky only. -O1 is to output the result in radiance. For this command the weather file had to be converted to the *daysim* weather format. This implied adding a header and correcting the hour value of the time stamp. In Meteonorm the hour value indicates the beginning of a time slot whereas in *daysim* it specifies the centre of the
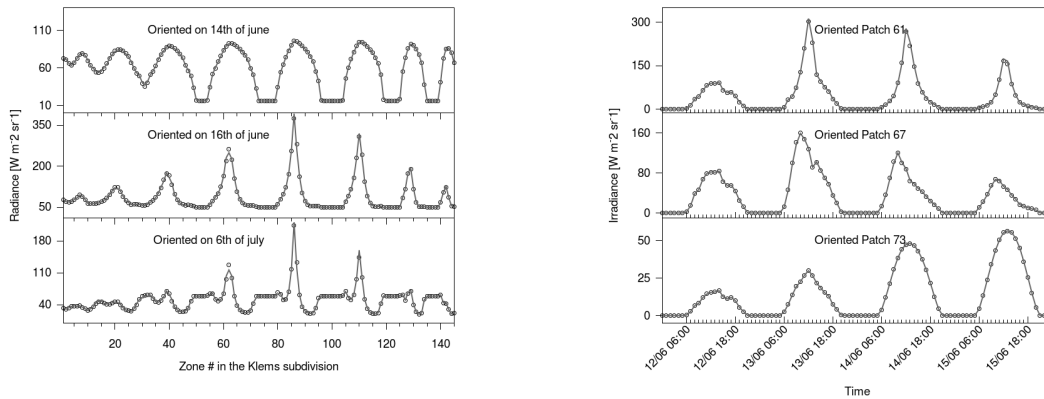
(a) Radiance value for the patches visible from an oriented surface, the ground patches all have the same value. Values are given at noon for three selected summer days.

(b) Hourly radiance values from the 12th to the 16th of june for three selected patches of the sky.

Figure A.3 – Comparing $S \cdot D$ from the Three phase method and the QT implementation of the Perez Model for an oriented surface on selected days at $1 pm$ as well as hourly values for selected zones over four days. The empty circles are values from the present implementation and the lines from the Radiance implementation.

       time slot.

- Generate a sampling with 1000 points for each Klems zones seen from the give surface with a specific orientation (described in a window.rad file) and no obstructions:

```
1  genklemsamp -c 1000 -vd 0 -1 0 -vu 0 0 1 window.rad > dPts.pts
```

- And calculating the contribution from the each direction in the sky vault distribution (a Reinhart subdivision of Tregenza patches as in the first step) to each of this sampled directions.

```
1  rcontrib < dPts.pts -c 1000 -e MF:1 -f reinhart.cal -b rbin -bn Nrbins -m
     sky_glow -faa window.oct > rad.dmx
```

- Transform the sky contribution to contribution from the Klems zones in the given orientation by multiplying the obtained matrices (S in skyDiffuse.smx and D in rad.dmx).

This comparison was conclusive for all orientation and with or without ground contribution. The comparison can be seen in Figure A.3. The slight difference in values is due to the fact that Radiance considers the real surface of the considered window whereas the QT sky implementation uses the Origin as unique reference point. The ground / sky ratio is therefore slightly different for large surfaces or surfaces set above or below the horizons (which is the case in this example).

A.5.2 BTDF XML file

The generation of BTDF XML files was validated by comparison with the output from `genbsdf` for a set of flat blinds generated with `genblinds` in radiance. Once again it was important to get all directions to be equivalent in order to compute the same thing. The BSDFViewer developed at the LBNL was also used in this process to verify the validity of generated XML files and to visualize if the resulting BTDF was oriented in the correct direction.

B Nodal Thermal Model

The nodal thermal model used for thermal simulations described in this annexe, is based on an analogy with electrical circuits. The elements of the system (wall, air, window, etc.) are represented by nodes, they have a certain capacitance and can be connected to each other with given resistances. The system can therefore be described by a set of equations which can be solved using a Crank Nicolson method. It was previously implemented and validated by others [Nielsen, 2005, Kämpf and Robinson, 2007, Daum, 2011].

B.1 Principles

B.1.1 Room definition

In a general application of this model, if there are n nodes and the nodes 0 to m are the nodes for which the temperature is unknown; then the nodes $m+1$ to $n-1$ are the nodes for which the temperature is known. In this application, the room is described by 13 nodes as picture in Figure B.1. Only one temperature is known: the exterior air temperature (node 13) taken from the climatic file. Additional stimuli such as heating, cooling, thermal gains from solar radiation and losses due to infiltration are applied to the remaining nodes if appropriate. The temperature of each of the other nodes, their interaction with each other are considered to calculate the temperature evolution. Node 0 is the indoor ambient air temperature node. This is the temperature that needs to be defined, depending on stimulations to the system. As it is illustrated in Figure B.1, the walls are not connect to the exterior except for the façade.

The heat flux between two nodes i and j is given by:

$$q_{ij} = h_{ij} \cdot (T_i - T_j) [W] \tag{B.1}$$

where h_{ij} is the equivalent conductance from node i to node j considering the conductivities of the different elements at play and their spacial definition (thickness). All nodes can have a thermal capacitance C_j that defines how they can store heat, it depends on the material and
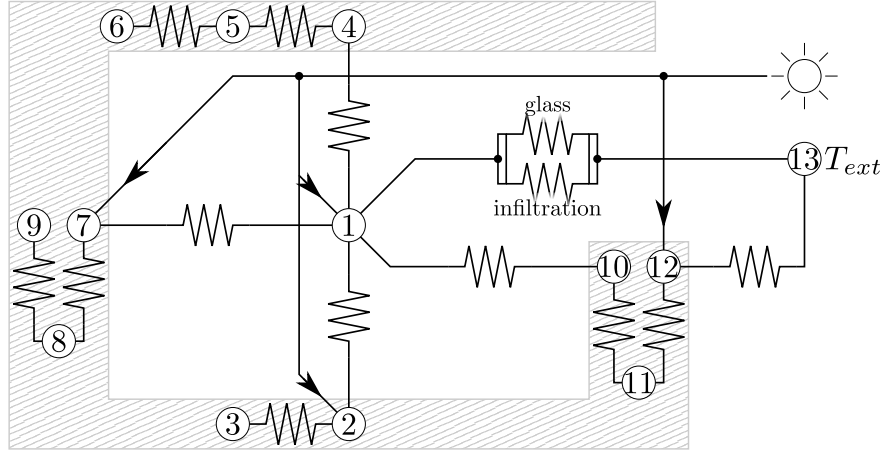
Figure B.1 – The differnet nodes of the thermal model and their interconnections. the capacitance is not shown in this representation but most nodes have an associated capacitance.

its volume. Additionally, each node 0 to m might receive a certain stimuli noted S_j. For each node, the equations for the conservation of energy can be then defines as:

$$C_j \cdot \frac{dT_j}{dt} = \sum_{i=0}^{n-1} h_{ij} \cdot (T_i - T_j) + S_j \tag{B.2}$$

Which can be re-written for the temperature by separating 0 to m and $m+1$ to $n-1$:

$$\frac{dT_j}{dt} = \frac{1}{C_j} \sum_{i=0}^{m} h_{ij} \cdot T_i + \frac{1}{C_j} \sum_{i=m+1}^{n-1} h_{ij} \cdot T_i - \frac{T_j}{C_j} \sum_{i=0}^{n-1} h_{ij} + \frac{S_j}{C_j} \tag{B.3}$$

or in matrix form:

$$\frac{dT}{dt} = A \cdot T + B \cdot U \tag{B.4}$$

where:

- T = vector of temperatures.

- U = vector of exterior excitations to each node (stimuli and exterior temperature.)

- A, B = Matrices defining the system computed from the resistances linking different nodes and their capacitances. A is $n \times n$, whereas B is $m \times m$. In a rigorous application,

some resistivity values used to define these matrices might change in time (for example night ventilation, window opening, closing of exterior shutters), in this study such changes where not considered. As it will be seen later, this accelerates computations.

The matrix form of the equation was used in the implementation. For each time step, a new temperature vector T is computed depending on temperatures at the previous step, solar gains, exterior temperature and eventual heating or cooling.

B.1.2 Solving the equations

The equation (B.4) needs to be solved to obtain the temperature evolution at each time step for the given stimuli. The time step Δt is defined by the available data for temperature and thermal gains. The temperature vector at the next times step $T(t + \Delta t)$ is found using an expansion in Taylor series around the current value $T(t_0)$:

$$T(t_0 + \Delta t) = t_0 + \Delta t \cdot T'(t_0) + \frac{(\Delta t)^2}{2} \cdot T''(t_0) + ... \tag{B.5}$$

In this resolution only the first derivative is used and the equation can be rewritten:

$$T(t_0 + \Delta t) = t_0 + \Delta t \cdot T'(t_0) \tag{B.6}$$

The first derivative needs to be evaluated, to do so, the Crank-Nicholson method is used. Crank-Nicholson is a combination of forward Euler and backward Euler resolution, it consists in evaluating the derivative by taking the mean between the time step $t - \frac{1}{2}\Delta t$ and $t + \frac{1}{2}\Delta t$.

$$T'(t_0) = \frac{T(t_0 + \frac{1}{2}\Delta t) - T(t_0 - \frac{1}{2}\Delta t)}{\Delta t} + \epsilon(\Delta t^2) \tag{B.7}$$

This expression of the derivative can be inserted into equation (B.6) using the following approximation:

$$T(t_0 + \frac{1}{2}\Delta t) = \frac{T(t_0 + \Delta t) + T(t_0)}{2} \tag{B.8}$$

Finally:

$$T(t_0 + \Delta t) = (I - \tfrac{1}{2}\Delta t \cdot A)^{-1}((I + \tfrac{1}{2}\Delta t \cdot A)/\cdot T(t_0) + \delta t \cdot B \cdot U(t_0 + \tfrac{1}{2}\Delta t)) \tag{B.9}$$

This method has a good convergence and is precise. It however requires a costly matrix inversion. Given that the conductivities and capacitances do not change in the described situation (i.e. no modification of the façade, building elements or ventilation rate) this inversion needs to be performed once only and does not change between time steps. Therefore the A and B matrices need to be computed only once. The subsequent matrix multiplication to obtain the temperature at each time step are fast.

C Lock-In Amplifiers

In this annexe, the principle of lock-in amplifiers is briefly presented along with the physical realisation of a sound card based lock-in as well as the related computer program implementation. The work presented in this annexe is the fruit of a collaboration with Mario Geiger during an internship. He has designed and assembled all the electric circuits for amplification and programmed the initial QT software to use the sound card from a computer as an acquisition card for low voltage in an *AC* circuit.

C.1 Principles

The principle of lock-in amplifiers is to isolate small signals buried in noise by means of a reference signal. This reference signal can also be referred to as carrier wave, because it has a fixed frequency, the other signal which are not in phase can be eliminated. This principle has been in use for many years and has since its invention become one of the basic measurement instrumentation in laboratories for all kind of application [Temple, 1975]. For optical phenomenons, a chopping wheel can be used to provide the reference. Because the light source and the reference are "chopped" by the same wheel, they have the same frequency even if the motor rotation speed varies slightly.

One of the basic components of a lock-in amplifier is the phase locked loop (PLL), it generates a well defined wave (square, sinus or triangular for example) with a frequency equal to the input signal. The reference signal passes through such a PLL to provide a clean reference. This reference can then be shifted to have it perfectly in phase with the measured signal. The signal of interest is then multiplied by the reference, this eliminates all signals that are not in phase and at the same frequency than the reference. Hereby only the signal is measured and any noise is discarded.

Dual phase lock-in have two outputs for a given reference that are out of phase by $\pi/2$. If the phase shift is set correctly, one of the signals should be zero, the other one is the signal of interest.
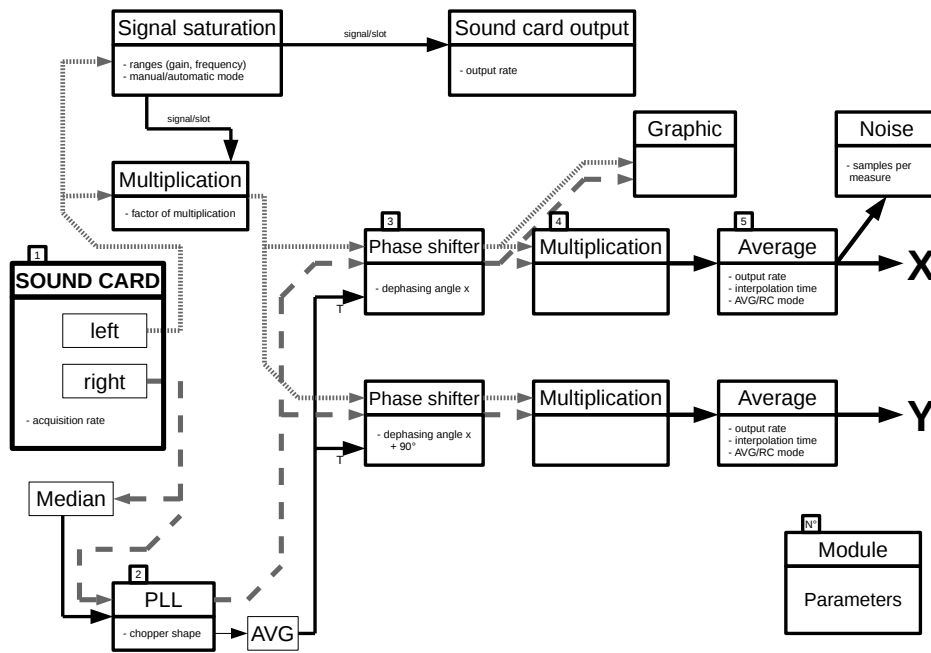
Figure C.1 – Block diagram of numerical dual phase lock-in amplifier.

C.2   Implementation and realisation

Analogical lock-in instruments can be purchased from several manufacturers and provide excellent signal acquisition over a broad range of acquisition frequencies ($100\,Hz$ to $500\,kHz$) and integration times (few μs to several ks). The sensitivity of such device is between a few nV and several hundred V. Recently digital lock-ins were introduced with even greater performance with frequencies up to $600\,Mhz$ and time constants as low a $30\,ns$. But such high end equipment are not required to measure a light flux with a photo diode. For this reason, a personal computer based method was implemented using the analogue to digital converter of the sound card. Such an approach has been applied successfully in the past [Probst and Jaquier, 1994] and presents the advantage to be low cost, universal and readily available.

C.2.1   Sound card as data logger

The line in of a computer can be used to read a voltage by means of the embedded analogue to digital converter, in basic sound card such as the ones embedded in mother boards, the acquisition rate is typically $96\,kHz$ with a 24 bit resolution over a $\pm1\,V$ range. With such equipment the maximal resolution in the measured voltage is in the order of $0.1\mu V$ and signals up to a few kHz can be measured. For a signal at $1\,kHz$, with a chopper turning at 300 rotations per minute (rpm), a single period has 300 points.

C.2.2 LabView

For a first validation, a lock-in was implemented in LabView using the computer sound card and an available lock-in library from the National Instrument website. This straight forward implementation was however slow and hard to interface with further equipment. For this reason, Mario Geiger developed the base for a numerical lock-in amplifier in $C++$.

C.2.3 C++ / QT

The numerical lock-in amplifier was developed in $C++$ using the Advanced Linux Sound Architecture (ALSA) library and the QT development framework. Namely QThreads were used to perform the different signal analysis simultaneously. The principle of the implemented dual phase lock-in amplifier is detailed in Figure C.1.

C.2.4 Electronic circuits

Because the purpose is to detect low signals, a pre-amplifier needs to be placed before the sound card line in. This pre-amplifier was build using an operational amplifier (OPA2134), which additionally has the advantage to convert the linearly changing current produced by the photo-diode into a linearly changing voltage that can be monitored by the sound card. In case very low signals are measured, an optional external amplifier module was also placed before the sound card line in. the amplification rate of this module can be controlled via the line out of the sound card. Depending on the produced frequency, a microcontroller activates two relays that select if the signal passes through the amplification circuit. With two relays and two amplification circuits in series, the amplifications can be selected amongst four values; in this case, 1, 7.5, 100 or 750.

C.2.5 Dual channel lock-in

By adding a second channel controlling an other sound card, two signals can be monitored synchronously because they have the same reference signal. From the implementation point of view this is simple but when this method was used in practise to measure the changing reflectance of a sample during evaporation, problems arrows. Two channels were required to precisely measure the variations in intensity of a reflected beam independently of the slight fluctuation of the source. This measurement was performed over long periods and yielded inconsistent results. After a lot of assumptions and modifications on the set-up it was found that two identical sound cards have slightly different acquisition frequencies. The difference is in the order of 30 samples per million but this small difference accumulates over time and the two signals are no longer synchronised. In addition, the ALSA library uses buffers that are read at equal rate, and one of the buffers slowly fills up; if it is not read, the data has to be dropped. The solution is to regularly purge the buffers once they were read to keep the signals synchronised.

C.2.6 Limits

The resulting lock-in is limited in precision, the electric circuits were optimised but still slightly affect the signal: the strong, oscillating reference can induce variations in the much lower signal by means of the electromagnetic waves produced by oscillation. To avoid this, the two channels (reference and signal) should be protected by a shielding. The bipolar $5\,V$ power supply generates noise, it had to be replaced by a better suited supply. The gains in the amplification circuits have limited precision (in the order of 0.1%).

D Goniophotometer Short Manual

The goniophotometer was introduced and described in Section 5.2 of this thesis. In this annexe, the graphical user interface (GUI) is rapidly introduced. Various procedures such as initialisation, calibration and measurement are also detailed.

D.1   Graphical user interface

Upon launch, the software GUI appears as illustrated by the screenshot in Figure D.1. To start the lock-in module, the correct in and out channels of the sound card have to be selected first (①) and then the *open* button (②) needs to be pressed twice. The area below the sound card setting ③ displays the reference and measured signal. The upper part displays the instantaneous signal read on the two channels while the bottom part displays the integrated signal as provided by the lock-in module described in Annexe C. On the right hand side of the GUI the different stepper motors can be controlled: the sensor ④, the sample ⑤ and the monochromator ⑥. Each motor can be moved using the arrows or a target position. The area marked with ⑦ provides control on the lock-in parameters (phase, amplification, integration time, output frequency and filter type). Finally the menu bar ⑧ in the top part gives access to the calibration and measurement operations as illustrated in Figures D.1b and D.1c.

Various calibrations are available. All should be performed if the device was shut down previously; the calibration has to be started only once the light source is stable. Two measurement modes are available: one in continuous mode, the signal is read continuously as the sensor moves at low speed. Or a stepping mode: the sensor moves step by step and waits for the signal to be properly integrated before moving to the next point. The angular intervals for the measurement can be specified (θ_i and θ_o) as well as the different wavelength if a spectral measurement is carried out.
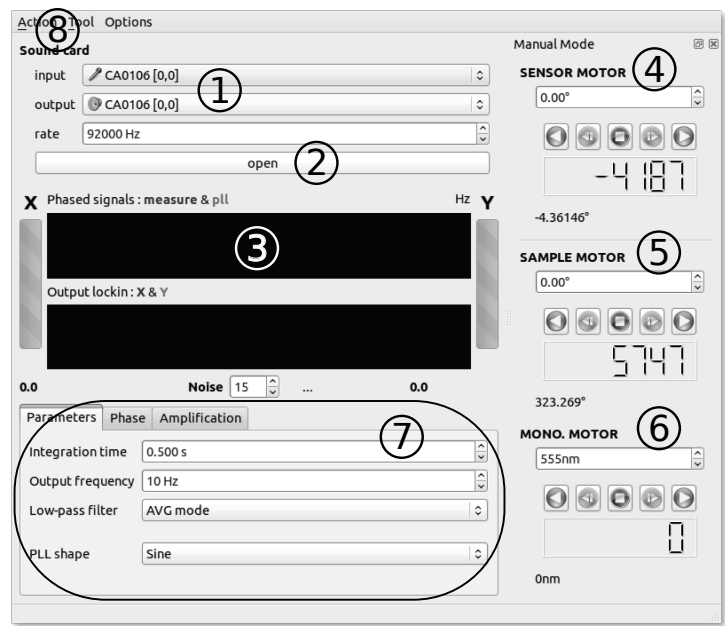
(a) Screenshot from the main interface in the goniophotometer software
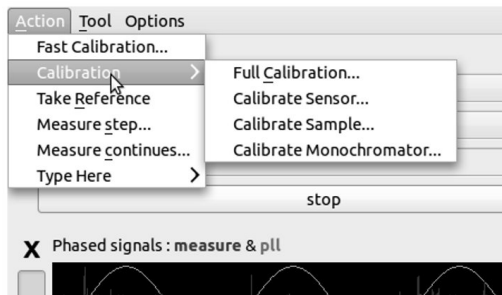
(b) Calibration menu.
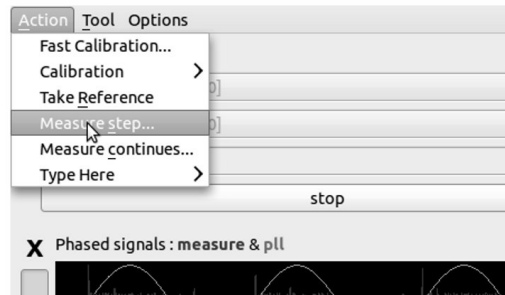
(c) Measure menu.

Figure D.1 – Screenshot from the goniophotometer GUI.

D.2 Implementation

The lock-in module was already described in Annexe C, the stepper motors are controlled via instruction sent to a control card over the RS232 serial port. The control card is a *Trinamic TMCM 310 V2.0* handling up to three stepper motors. The instructions are sent over QSockets in binary form as specified by the documentation from Trinamic. The measurements are performed in threads to avoid freezing the interface.

Bibliography

[Andersen et al., 2005] Andersen, M., Rubin, M., Powles, R., and Scartezzini, J.-L. (2005). Bi-directional transmission properties of Venetian blinds: experimental assessment compared to ray-tracing calculations. *Solar Energy*, 78(2):187–198.

[Bartenbach, 2014] Bartenbach (2014). http://www.bartenbach.com.

[Begemann et al., 1997] Begemann, S., van den Beld, G., and Tenner, A. (1997). Daylight, artificial light and people in an office environment, overview of visual and biological responses. *International Journal of Industrial Ergonomics*, 20(3):231–239.

[Benes et al., 1989] Benes, E., Schmid, M., and Thorn, G. (1989). Progress in monitoring thin film thickness by use of quarz crystals. *Thin Solid Filmsid Films*, 174:307–314.

[Bertsch et al., 2004] Bertsch, A., Jiguet, S., and Renaud, P. (2004). Microfabrication of ceramic components by microstereolithography. *Journal of Micromechanics and Microengineering*, 14(2):197–203.

[Boehlen et al., 2005] Boehlen, K. L., Stassen Boehlen, I. B., and Allott, R. M. (2005). Advanced laser micro-structuring of super-large-area optical films. In Johnson, E. G., Nordin, G. P., and Suleski, T. J., editors, *Progress in Biomedical Optics and Imaging - Proceedings of SPIE*, volume 5720, pages 204–211.

[Born and Wolf, 1999] Born, M. and Wolf, E. (1999). *Principles of Optics*. Cambridge University Press, 7 edition.

[Bourgeois et al., 2008] Bourgeois, D., Reinhart, C. F., and Ward, G. (2008). Standard daylight coefficient model for dynamic daylighting simulations. *Building Research & Information*, 36(1):68–82.

[Bühler, 2003] Bühler, C. (2003). *Mikrostrukturen zur Steuerung von Tageslichtströmen*. PhD thesis, Albert-Ludwigs-Universität Freiburg i. Br.

[Chang et al., 2005] Chang, P. C., Walker, J., and Hopcraft, K. (2005). Ray tracing in absorbing media. *Journal of Quantitative Spectroscopy and Radiative Transfer*, 96(3-4):327–341.

[Collins, 2007] Collins, T. (2007). ImageJ for microscopy. *BioTechniques*, 43(S1):S25–S30.

Bibliography

[Courret, 1999] Courret, G. (1999). *Systèmes anidoliques d'éclaireage naturel.* PhD thesis, EPFL - Ecole Polytechnique Federal de Lausanne.

[Courret et al., 1998] Courret, G., Scartezzini, J.-l., Francioli, D., and Meyer, J.-j. (1998). Design and assessment of an anidolic light-duct. *Energy and Buildings*, 28:79–99.

[Danny et al., 2008] Danny, H. L., Lam, T. N., Wong, S., and Tsang, E. K. (2008). Lighting and cooling energy consumption in an open-plan office using solar film coating. *Energy*, 33(8):1288–1297.

[Dartevelle et al., 2013] Dartevelle, O., Lethé, G., Deneyer, A., and Bodart, M. (2013). The use of bidirectional scattering distribution functions for solar shading modelling in dynamic thermal simulation: a result comparison. In *Proceedings CISBAT 2013*, pages 4–9.

[Daum, 2011] Daum, D. (2011). *On the Adaptation of Building Controls to the Envelope and the Occupants.* PhD thesis, EPFL - Ecole Polytechnique Federal de Lausanne.

[Daum and Morel, 2010] Daum, D. and Morel, N. (2010). Assessing the total energy impact of manual and optimized blind control in combination with different lighting schedules in a building simulation environment. *Journal of Building Performance Simulation*, 3(1):1–16.

[De Abreu and Labaki, 2011] De Abreu, L. V. and Labaki, L. C. (2011). Trees and heat fluxes: How much do they contribute to the energy balance at urban spaces? In *PLEA 2011 - Architecture and Sustainable Development, Conference Proceedings of the 27th International Conference on Passive and Low Energy Architecture*, pages 245–250.

[Edmonds, 1993] Edmonds, I. R. (1993). Performance of laser cut light deflecting panels in daylighting applications. *Solar Energy Materials and Solar Cells*, 29(1):1–26.

[Enshen, 2005] Enshen, L. (2005). Influence of inner heat sources on annual heating and cooling energy consumption and its relative variation rates (RVRs). *Building and Environment*, 40(4):579–586.

[Fiji, 2014] Fiji (2014). "Fiji is just ImageJ", image analysis software. http://fiji.sc/Fiji.

[Florides et al., 2002] Florides, G. A., Tassou, S. A., Kalogirou, S. A., and Wrobel, L. C. (2002). Measures used to lower building energy consumption and their cost effectiveness. *Applied Energy*, 73:299–328.

[Friedman et al., 2011] Friedman, D. J., Olson, J. M., and Kurtz, S. (2011). High-Efficiency III–V Multijunction Solar Cells. In *Handbook of Photovoltaic Science and Engineering*, pages 314–364. John Wiley & Sons, Ltd.

[Geiser et al., 2010] Geiser, V., Jin, Y.-H., Leterrier, Y., and Må nson, J.-A. E. (2010). Nanoimprint Lithography with UV-Curable Hyperbranched Polymer Nanocomposites. *Macromolecular Symposia*, 296(1):144–153.

[Glassner, 1989] Glassner, A. (1989). *An Introduction to Ray Tracing.* Academic Press.

[González Lazo et al., 2012] González Lazo, M. a., Teuscher, R., Leterrier, Y., Må nson, J.-A. E., Calderone, C., Hessler-Wyser, A., Couty, P., Ziegler, Y., and Fischer, D. (2012). UV-nanoimprint lithography and large area roll-to-roll texturization with hyperbranched polymer nanocomposites for light-trapping applications. *Solar Energy Materials and Solar Cells*, 103:147–156.

[Gooley et al., 2001] Gooley, J. J., Lu, J., Chou, T. C., Scammell, T. E., and Saper, C. B. (2001). Melanopsin in cells of origin of the retinohypothalamic tract. *Nature neuroscience*, 4(12):1165.

[Green, 2010] Green, W. A. (2010). *Industrial Photoinitiators: A Technical Guide*. Taylor & Francis.

[Grynning et al., 2014] Grynning, S., Time, B., and Matusiak, B. (2014). Solar shading control strategies in cold climates – Heating, cooling demand and daylight availability in office spaces. *Solar Energy*, 107:182–194.

[Hermersdorf et al., 2011] Hermersdorf, M., Hibert, C., Grogg, D., and a.M. Ionescu (2011). High aspect ratio sub-micron trenches on silicon-on-insulator and bulk silicon. *Microelectronic Engineering*, 88(8):2556–2558.

[Ize et al., 2008] Ize, T., Wald, I., and Parker, S. G. (2008). Ray Tracing with the BSP Tree. In Parker, S and Reshetov, A., editor, *IEEE/EG Symposium on Interactive Ray Tracing 2008, Proceedings*, pages 159–166, 345 E 47TH ST, NEW YORK, NY 10017 USA. IEEE Comp Soc, VGTC; EG; ACM, IEEE.

[Jacobs, 2010] Jacobs, A. (2010). Understanding rtcontrib. Technical report.

[Jacobs, 2014] Jacobs, A. (2014). rtcontrib tutorial withdrawl. Technical Report January.

[Jahan and Smith, 2007] Jahan, F. and Smith, G. B. (2007). Investigation of angular selective optical properties of silver / titanium oxide cermet thin films. *Thin Solid Films*, 333(1998):185–190.

[James and Bahaj, 2005] James, P. and Bahaj, A. (2005). Smart glazing solutions to glare and solar gain: a 'sick building' case study. *Energy and Buildings*, 37(10):1058–1067.

[Jelle et al., 2012] Jelle, B. r. P, Hynd, A., Gustavsen, A., Arasteh, D., Goudey, H., and Hart, R. (2012). Fenestration of today and tomorrow: A state-of-the-art review and future research opportunities. *Solar Energy Materials and Solar Cells*, 96(1):1–28.

[Jensen et al., 2001] Jensen, H. W., Marschner, S. R., Levoy, M., and Hanrahan, P. (2001). A practical model for subsurface light transport. In *Proceedings of the 28th annual conference on Computer graphics and interactive techniques - SIGGRAPH '01*, pages 511–518, New York, New York, USA. ACM Press.

[Kämpf and Robinson, 2007] Kämpf, J. H. and Robinson, D. (2007). A simplified thermal model to support analysis of urban resource flows. *Energy and Buildings*, 39(4):445–453.

Bibliography

[Kämpf and Scartezzini, 2011] Kämpf, J. H. and Scartezzini, J.-l. (2011). Ray-Tracing simulation of Complex Fenestration Systems Based On digitally Processed BTDF Data. In *Proceedings CISBAT*, pages 349–354.

[Klammt et al., 2012] Klammt, S., Neyer, A., and Müller, H. F. O. (2012). Microoptics for efficient redirection of sunlight. *Applied optics*, 51(12):2051–6.

[Klems, 1994] Klems, J. (1994). A new method for predicting the solar heat gain of complex fenestration systems II Detailed description of the matrix layer calculation. *ASHRAE Transactions*.

[Klems, 1993] Klems, J. H. (1993). New method for predicting the solar heat gain of complex fenestration systems - I. Overview and derivation of the matrix layer calculation. In *ASHRAE Transactions*, volume 100, pages 1065–1072. ASHRAE.

[Köster, 1995] Köster, H. (1995). Stepped Lamella for guiding light radiation.

[Köster, 2011] Köster, H. (2011). Light guiding venetian blinds with prism-shaped slat surfaces.

[Krogh, 2003] Krogh, M. (2003). My Little Guide to Soft Lithography.

[Kuhke, 1991] Kuhke, K. (1991). Einrichtung zur steuerung der transmission von licht einer strahlungsquelle.

[Lamontagne et al., 2009] Lamontagne, B., Barrios, P., Py, C., and Nikumb, S. (2009). The next generation of switchable glass : the micro-blinds. In *Proceedings of the Conference Glass Performance Days*, pages 637–639.

[Lamontagne and Py, 2006] Lamontagne, B. and Py, C. (2006). 11_359_421_Microblinds_and_a_method_of_f.pdf.

[Laouadi et al., 2007] Laouadi, A., Reinhart, C., and Bourgeois, D. (2007). The daylight coefficient method and complex fenestration. In *10th IBPSA Building Simulation Conference, Beijin, China, Sept 3-6*, pages 1–8, Beijin.

[LBNL, 2008] LBNL (2008). User Manual Window 6.2. A Program For Analyzing Window Thermal Performance. Technical Report January, Lawrence Berkeley National Laboratory.

[Leftheriotis et al., 2000] Leftheriotis, G., Papaefthimiou, S., and Yianoulis, P. (2000). Development of multilayer transparent conductive coatings. *Solid State Ionics*, 137:655–661.

[Linhart and Scartezzini, 2010] Linhart, F. and Scartezzini, J.-L. (2010). Minimizing lighting power density in office rooms equipped with Anidolic Daylighting Systems. *Solar Energy*, 84(4):587–595.

[Lorenz, 1998] Lorenz, W. (1998). Design guidelines for a glazing with a seasonally dependent solar transmittance. *Solar Energy*, 63(2):79–96.

168

[Lorenz, 2001a] Lorenz, W. (2001a). A glazing unit for solar control, daylighting and energy conservation. *Solar Energy*, 70(2):109–130.

[Lorenz, 2001b] Lorenz, W. (2001b). Eine Fensterscheibe fur Sonnenschutz, Raumausleuchtung und Energieeinsparung.

[LTIOptics, 2014] LTIOptics (2014). Overview of Photopia. http://www.ltioptics.com/Photopia/overview.html.

[Mack, 2008] Mack, I. (2008). *Development of Innovative Coatings for Sun Protection Glasses Based on the Theory of the Optimal Spectral Transmittance*. PhD thesis, University of Basel.

[Macleod, 2001] Macleod, H. A. (2001). *Thin-Film Optical Filters*. Taylor & Francis.

[Manz and Menti, 2012] Manz, H. and Menti, U.-P. (2012). Energy performance of glazings in European climates. *Renewable Energy*, 37(1):226–232.

[McNeil, 2013] McNeil, A. (2013). The Five-Phase Method for Simulating Complex Fenestration with Radiance. Technical Report August, Lawrence Berkeley National Laboratory.

[Mertin et al., 2014] Mertin, S., Hody-Le Caër, V., Joly, M., Mack, I., Oelhafen, P., Scartezzini, J.-L., and Schüler, A. (2014). Reactively sputtered coatings on architectural glazing for coloured active solar thermal façades. *Energy and Buildings*, 68:764–770.

[Meteonorm, 2012] Meteonorm (2012). Meteonorm handbook part II : Theory. (October).

[Michel, 1999] Michel, L. (1999). *Méthode expérimentale d'évaluation des performances lumineuses de bâtiments*. PhD thesis, EPFL - Ecole Polytechnique Federal de Lausanne.

[Morel et al., 2001] Morel, N., Bauer, M., El-Khoury, M., and Krauss, J. (2001). Neurobat, a predictive and adaptive heating control system using artificial neural networks. *International Journal of Solar Energy*, 21(2-3):161–202.

[Müller, 1994] Müller, H. F. O. (1994). Application of holographic optical elements in buildings for various purposes like daylighting, solar shading and photovoltaic power generation. *Renewable Energy*, 5(5-8):935–941.

[Münch and Bromundt, 2012] Münch, M. and Bromundt, V. (2012). Light and chronobiology: implications for health and disease. *Dialogues in Clinical Neuroscience*, 14(2):448–453.

[Nabil and Mardaljevic, 2006] Nabil, A. and Mardaljevic, J. (2006). Useful daylight illuminances: A replacement for daylight factors. *Energy and Buildings*, 38(7):905–913.

[Nayar et al., 1991] Nayar, S., Ikeuchi, K., and Kanade, T. (1991). Surface reflection: physical and geometrical perspectives. *IEEE Transactions on Pattern Analysis . . .* , 13(7):611–634.

[Nielsen, 2005] Nielsen, T. R. (2005). Simple tool to evaluate energy demand and indoor environment in the early stages of building design. *Solar Energy*, 78(1):73–83.

Bibliography

[O'Donnell, 2001] O'Donnell, K. a. (2001). High-order perturbation theory for light scattering from a rough metal surface. *Journal of the Optical Society of America. A, Optics, image science, and vision*, 18(7):1507–18.

[Oelhafen, 2007] Oelhafen, P. (2007). Optimized spectral transmittance of sun protection glasses. *Solar Energy*, 81(9):1191–1195.

[Oren and Nayar, 1993] Oren, M. and Nayar, S. K. (1993). Diffuse Reflectance from rough Surfaces. In *IEEE Conference on Computer Vision and Pattern Recognition (CVPR)*, pages 763—-764.

[Oren and Nayar, 1994] Oren, M. and Nayar, S. K. (1994). Generalization of Lambert's reflectance model. *Proceedings of the 21st annual conference on Computer graphics and interactive techniques - SIGGRAPH '94*, pages 239–246.

[Pascual et al., 2013] Pascual, C., de Castro, J., Kostro, A., Schueler, A., Vassilopoulos, a. P., and Keller, T. (2013). Diffuse light transmittance of glass fiber-reinforced polymer laminates for multifunctional load-bearing structures. *Journal of Composite Materials*.

[Pedder et al., 2007] Pedder, J. E. A., Holmes, A. S., Allott, R., and Boehlen, K. (2007). Pulsed Laser Ablation for Volume Micro-Optical Arrays on Large Area Substrates. In Maher, M.-A., Stewart, H. D., Chiao, J.-C., Suleski, T. J., Johnson, E. G., and Nordin, G. P., editors, *Proceedings of SPIE - The International Society for Optical Engineering*, volume 6462, pages 64620W–64620W–7.

[Perez et al., 1990] Perez, R., Ineichen, P., Seals, R., Michalsky, J., and Stewart, R. (1990). Modeling daylight availability and irradiance components from direct and global irradiance. *Solar energy*, 44(5):271–289.

[Perez et al., 1993] Perez, R., Seals, R., and Michalsky, J. (1993). All-weather model for sky luminance distribution - preliminary configuration and validation. *Solar Energy*, 50:235–245.

[Probst and Jaquier, 1994] Probst, P.-A. and Jaquier, A. (1994). Multiple-channel digital lock-in amplifier with PPM resolution. *Review of Scientific Instruments*, 65(3):747.

[Prognos et al., 2013] Prognos, Infras, and TEP Energy (2013). Analyse des schweizerischen Energieverbrauchs 2000 - 2012 nach Verwendungszwecken. Technical Report September, Swiss Federal Office of Energy SFOE.

[Rakic et al., 1998] Rakic, a. D., Djurisic, a. B., Elazar, J. M., and Majewski, M. L. (1998). Optical properties of metallic films for vertical-cavity optoelectronic devices. *Applied optics*, 37(22):5271–83.

[Reinhart, 2014a] Reinhart, C. (2014a). *Daylighting handbook I*.

[Reinhart, 2014b] Reinhart, C. F. (2014b). Reference room for daylight. http://web.mit.edu/SustainableDesignLab/projects/ReferenceOffice/index.html.

[Reinhart et al., 2013] Reinhart, C. F., Jakubiec, J. A., and Ibarra, D. (2013). Definition of a reference office for standardiezed evaluation of dynamic facade and lighting technologies. In *Proceedings of BS2013: 13th Conference of International Building Performance Simulation Association, Chambéry, France, August 26-28*, pages 3645–3652.

[Reinhart et al., 2006] Reinhart, C. F., Mardaljevic, J., and Rogers, Z. (2006). Dynamic daylight performance metrics for sustainable building design. *Leukos, Journal of the Illuminating Engineering Society of North America.*, pages 37–41.

[RetroSolar, 2014] RetroSolar (2014). Blind manufacturer website. http://www.retrosolar.de/.

[Ruck et al., 2000] Ruck, N., Aschehoug, O. y., Aydinli, S., Christoffersen, J., Courret, G., Edmonds, I., Jakobiak, R., Kischkoweit-Lopin.Martin, Klinger, M., Lee, E., Michel, L., Scartezzini, J.-L., and Selkowitz, S. (2000). 4. Daylighting Systems. In *Daylight in Buildings*.

[Sartomer, 2008] Sartomer (2008). Sartomer hyperbranched polyester acrylate. Data Sheet.

[Sauerbrey, 1959] Sauerbrey, G. (1959). Verwendung von Schwingquarzen zur Wägung dünner Schichten und zur Mikrowägung. *Zeitschrift für Physik*, 155:206–222.

[Scartezzini and Courret, 2002] Scartezzini, J.-L. and Courret, G. (2002). Anidolic daylighting systems. *Solar Energy*, 73(2):123–135.

[Scartezzini and Courret, 2004] Scartezzini, J.-L. and Courret, G. (2004). Experimental performance of daylighting systems based on non-imaging optics. In Winston, R., editor, *Nonimaging Optics: Maximum Efficiency Light Transfer*, volume 5185, pages 35–48.

[Schmidt et al., 2007] Schmidt, L. E., Schmäh, D., Leterrier, Y., and Må nson, J.-A. E. (2007). Time-intensity transformation and internal stress in UV-curable hyperbranched acrylates. *Rheologica Acta*, 46(5):693–701.

[Schmidt et al., 2008] Schmidt, L. E., Yi, S., Jin, Y.-H., Leterrier, Y., Cho, Y.-H., and Må nson, J.-A. E. (2008). Acrylated hyperbranched polymer photoresist for ultra-thick and low-stress high aspect ratio micropatterns. *Journal of Micromechanics and Microengineering*, 18(4):045022.

[Schuler et al., 2008] Schuler, A., Kostro, A., Huriet, B., Galande, C., and Scartezzini, J.-L. (2008). Monte Carlo simulations of quantum dot solar concentrators: ray tracing based on fluorescence mapping. In Tsai, B. K., editor, *Proceedings of SPIE - The International Society for Optical Engineering*, volume 7046, pages 704609–704609–12.

[Smith et al., 1997] Smith, G. B., Dligatch, S., Sullivan, R., and Hutchins, M. G. (1997). Thin film angular selective glazing. *Solar Energy*, 62(3):229–244.

[Sollema, 2014] Sollema (2014). Diva-for-Rhino website. http://diva4rhino.com/.

Bibliography

[Stemp and Stemp, 2001] Stemp, W. and Stemp, M. (2001). UBM Laser Profilometry and Lithic Use-Wear Analysis: A Variable Length Scale Investigation of Surface Topography. *Journal of Archaeological Science*, 28(1):81–88.

[Struck et al., 2014] Struck, C., Jurt, D., Seerig, A., Hangartner, D., Heim, T., Baschnagel, P., and Wouters, V. (2014). Einfluss des Klimawandels auf den Energiebedarf von Schweizer Bürobauten über den Lebenszyklus gebäudetechnischer Anlagen. In *Proceedings BRENET 2014*, number September 2014.

[Temple, 1975] Temple, P. a. (1975). An introduction to phase-sensitive amplifiers: An inexpensive student instrument. *American Journal of Physics*, 43(9):801.

[Tregenza, 1987] Tregenza, P. R. (1987). Subdivision of the sky hemisphere for luminance measurements. *Lighting research & technology*, 19(1):13–14.

[US Department of Energy, 2014] US Department of Energy (2014). EnergyPlus weather data. apps1.eere.energy.gov/buildings/energyplus/cfm/weather_data.cfm.

[Vieri, 1981] Vieri, N. G. (1981). Procede et dispositif pour arreter ou laisser passer la lumiere solaire selon la saison.

[Vratzov et al., 2003] Vratzov, B., Fuchs, a., Lemme, M., Henschel, W., and Kurz, H. (2003). Large scale ultraviolet-based nanoimprint lithography. *Journal of Vacuum Science & Technology B: Microelectronics and Nanometer Structures*, 21(6):2760.

[Waldbaur et al., 2012] Waldbaur, A., Waterkotte, B., Schmitz, K., and Rapp, B. E. (2012). Maskless projection lithography for the fast and flexible generation of grayscale protein patterns. *Small (Weinheim an der Bergstrasse, Germany)*, 8(10):1570–8.

[Wall, 2014] Wall, M. M. (2014). Genethic algorithm library (MIT). http://lancet.mit.edu/ga/.

[Walze et al., 2005] Walze, G., Nitz, P., Ell, J., Georg, A., Gombert, A., and Hossfeld, W. (2005). Combination of microstructures and optically functional coatings for solar control glazing. *Solar Energy Materials and Solar Cells*, 89(2-3):233–248.

[Ward et al., 2012] Ward, G., Kurt, M., and Bonneel, N. (2012). A Practical Framework for Sharing and Rendering Real-World Bidirectional Scattering Distribution Functions. Technical Report September.

[Ward et al., 2011] Ward, G., Mistrick, R., Lee, E. S., McNeil, A., and Jonsson, J. (2011). Simulating the Daylight Performance of Complex Fenestration Systems Using Bidirectional Scattering Distribution Functions within Radiance. *Leukos, Journal of the Illuminating Engineering Society of North America.*, 7(January).

[Webb, 2006] Webb, A. R. (2006). Considerations for lighting in the built environment: Non-visual effects of light. *Energy and Buildings*, 38(7):721–727.

[Wienold, 2009] Wienold, J. (2009). *Daylight Glare in Offices*. PhD thesis.

[Wirth, 2000] Wirth, H. (2000). *Richtungsselektive Steuerung von Sonnenstrahlung durch Fenster*. PhD thesis, EPFL - Ecole Polytechnique Federal de Lausanne.

[Wittkopf et al., 2010] Wittkopf, S., Oliver Grobe, L., Geisler-Moroder, D., Compagnon, R., Kämpf, J. H., Linhart, F., and Scartezzini, J.-L. (2010). Ray tracing study for non-imaging daylight collectors. *Solar Energy*, 84(6):986–996.

[Wolf et al., 2012] Wolf, A. J., Hauser, H., Kübler, V., Walk, C., Höhn, O., and Bläsi, B. (2012). Origination of nano- and microstructures on large areas by interference lithography. *Micro-electronic Engineering*, 98:293–296.

[Zhou et al., 2013] Zhou, J., Gao, Y., Zhang, Z., Luo, H., Cao, C., Chen, Z., Dai, L., and Liu, X. (2013). VO2 thermochromic smart window for energy savings and generation. *Scientific reports*, 3:3029.

Kostro André

Austrian,
Born on the 16th of July 1983 in Vienna, Austria.

Ch. d'Ondallaz 6
1807 Blonay SWITZERLAND
+ 41 76 616 19 43
andre.kostro@gmail.com

Innovative, Curious, Creative and Social
Fluent in French, German & English

OBJECTIVE

Acquire more experience in teaching and share knowledge with students. Wrap up the research project started during my PhD Thesis in closer collaboration with industrial partners.

EDUCATION

- 2010-2014: **Phd** at the Swiss Federal Institute of Technology (EPFL) *Microstructured glazing for seasonal thermal control, daylighting, glare protection and clear view.*
- 2005-2006: **Masters in computer Science** at the Swiss Federal Institute of Technology (EPFL) *Masters thesis work on a Monte-Carlo ray tracing of photoluminescent solar conentrators*
- 2004-2005: Year abroad at the **University of New South Wales** in Sydney, Australia (UNSW) *Semester project on the computation of extinction probability in small populations*
- 2001-2004: **Bachelor in Computer Science** at EPFL
- 1994-2001: French Baccalaureate at the Lycée Intrenational de Ferney-Voltaire.

EXPERIENCE

2010-2014 **Doctoral Candidate** on the subject of microstructured glazing for complex fenestration systems (CFS)
Solar Energy and Building Physics Laboratory, Swiss Federal Institute of Technology Lausanne.

- Developed a novel solution for the combination of seasonal thermal dynamics, daylighting, glare protection and clear view.
- Designed and implemented a simulation tool for CFS.
- Main assistant in the building physics III and IV class for the second year bachelor in Architecture.
- Supervised a trainee in computer science, a graduated bachelor in chemistry for a BNF contract and a graduated masters in microtechnology for his civil service.
- Participant in the IEA Task 50: Advanced Lighting Solutions for Retrofitting Buildings.

2009 **Participated in a web-based start-up**
Sophiagora, Lausanne

- Designed and developed a geo-localized and social web platform for classification, sharing and navigation of information.

2008-2009 Traveled in the Balkans, 6 month hitchhiking by myself to meet people and learn the basics of balkanian language.

2007-2008 **Scientific assistant**

Solar Energy and Building Physics Laboratory, Swiss Federal Institute of Technology Lausanne.

- Redesigned and rewrote the radiation algorithm in SunTool (now CitySim), a simulation tool for urban planers assessing the energetic consumption of suburbs. (energy coming from the sky, sun and reflections)

2006-2007 **Scientific assistant**.

Solar Energy and Building Physics Laboratory, Swiss Federal Institute of Technology Lausanne.

- Pursued the development and validation of PhotonSim and integrated polarization.
- Used PhontonSim and laboratory measurements to determine feasibility of large scale fluorescent planar solar concentrators.
- Assistant for the lecture of building physics I and II for the second year bachelor in Architecture.

2006 **Masters project**

Solar Energy and Building Physics Laboratory, Swiss Federal Institute of Technology Lausanne.

- PhotonSim: development of a Monte Carlo ray tracing software for the simulation of fluorescent planar solar concentrators

2006 **Student Assistant**
Applied Computing and Mechanics Laboratory, Swiss Federal Institute of Technology Lausanne. In the exercises for the "*fundamentals of computer aided Engineering*" lecture (2nd year Bachelor)

2005-2006 **Student Assistant**

Processor Architecture Laboratory, Swiss Federal Institute of Technology Lausanne. In the practical work sessions for the "*computer architecture*" lecture (2nd year Bachelor)

2005 **Semester Project** with Professor Bill Sherwin at the School of Biological, Earth and Environmental Sciences (BEES) at UNSW. "Computing probability of extinction in small populations using branching processes". In collaboration with the mathematics and computing departments.

2004 **Semester Project in software engineering:** developing a consequent Java software as a team using UML. (GUIs, Networking, databases).

AWARDS

Received the **Asea Brown Boveri (ABB) research award** for masters thesis (2007).
Received the best poster prize at CISBAT conference 2014.
Received the Doctoral Award for second best poster at ENAC Research Day 2014.

LANGUAGES

Fluent in French (native language)
Fluent in German (mother tong)
Fluent in English oral and written (Cambridge Advanced Certificate in English)

COMPUTER SKILLS

Strong ray tracing experience: wrote 2 applications for the study of complex optical systems
User of other ray tracing tools: Photopia, Radiance.
Bio inspired computing: artificial neural networks, Genetic algorithms, swarm intelligence.
Programming languages: C++, C, Java, Php, MySql, Qt framework, OpenGl.
Unix, OS X, Windows, Eclipse, Latex, OpenOffice, Matlab.

ACTIVITIES AND INTERESTS

Skiing, tennis, hiking, biking, climbing and swimming.
I try to live sustainably and enjoy music and good food as well as traveling.

PUBLICATIONS & CONFERENCES

Kostro A., Gonzales Lazo M.A., Leterrier Y., Siringil E., Hoffmann P., Schüler A. *"Replication and encapsulation of optical microstructures for light redirection."*. In preparation for Optical Materials.

Kostro A., Perrenoud M., Scartezzini J.-L. , Schüler A. *"CFSPro: Simulation of Thermal and Daylighting Performances of Complex Fenestration Systems."*. In preparation for Energy and Buildings.

Kostro A., Geiger M., Scartezzini J.-L. , Schüler A. *"CFSPro: Ray Tracing for Profile Optimisation of Complex Fenestration Systems using mixed dimensionality approach"*. Submitted to Applied Optics in Nov 2014.

Kostro A., Scartezzini J.-L. , Schüler A. *"Radiance rendering and thermal modeling for the design of complex fenestration systems with optimized performances"*. BRENET Status seminar 2014, Sept 4-5 2014, Zurich.

Carlos Pascual, Julia de Castro, André Kostro, Andreas Schüler, Anastasios P Vassilopoulos and Thomas Keller. *"Optomechanical investigation of glass fiber-reinforced polymer laminates for multifunctional load-bearing structures"*, Submitted to J Compos Mater in June 2014.

Carlos Pascual, Julia de Castro, André Kostro, Andreas Schüler, Anastasios P Vassilopoulos and Thomas Keller. *"Diffuse light transmittance of glass fiber-reinforced polymer laminates for multifunctional load-bearing structures"*, Journal of Composite Materials, November 2013

Kostro A., Scartezzini J.-L. , Schüler A. *"Mixed-dimensionality approach for advanced ray tracing of lamellar structures for daylighting and thermal control"*. CISBAT 2013 Conference, Sept 4-6 2013, Lausanne.

Kostro A., Scartezzini J.-L. , Schüler A. *"Conception d'un vitrage micro-structuré pour l'eclairage naturel et le contrôle thermique saisonnier"*. BRENET Status seminar 2014, Sept 13-14 2014, Zurich.

Kostro A., Geiger M., Jolissaint N., Gonzales Lazo M.A., Scartezzini J.-L, Leterrier Y., Schüler A. *"Embedded microstructures for daylighting and seasonal thermal control"*, SPIE Conf. Optics and Photonics, vol. 8485, San Diego, Aug 2012

Kostro A., Geiger M., Scartezzini J.-L., Schüler A. *"Towards microstrucutred glazing for daylighting and thermal control"*. CISBAT 2011 Conference, Sept 14-16 2011, Lausanne.

Robinson, D., Giller, C., Haldi, F., He, F., Kämpf, J., Kostro, A. *"Towards comprehensive simulation and optimisation for more sustainable urban design"*. PLEA 2008 , Conference Proceedings

Robinson, D., Giller, C., Haldi, F., He, F., Kämpf, J., Kostro, A. *"Towards comprehensive simulation and optimisation for more sustainable urban design"*. BRENET Status seminar 2008, Sept 11-12 2008, Zurich.

Schüler A., Kostro A., Huriet B., Galande C., Scartezzini J.-L. *"Monte-Carlo simulations of quantum dot solar concentrators: ray-tracing based on fluorescence mapping"*, SPIE Conf. Optics and Photonics, vol. 7046, San Diego, Aug 2008

Schüler A., Kostro A., Galande C., Valle del Olmo M., de Chambrier E., Huriet B.*"Principles of Monte-Carlo Ray-Tracing Simulation of Quantum Dot Solar Concentrators"*, ISES Solar World Congress 2007 Proc, Beijing, China, 18-21 Sept. 2007.

Kostro A., Huriet B., Schüler A.: *"PhotonSim: developing and testing a Monte-Carlo ray-tracing software for the simulation of planar luminescent solar concentrators"*, Proc. CISBAT 2007, Lausanne, 4-5th Sept. 2007.